ABSTRACT

Title of dissertation: SCANNING TUNNELING MICROSCOPY AT MILLIKELVIN TEMPERATURES: DESIGN AND CONSTRUCTION

Mark Avrum Gubrud,
Doctor of Philosophy, 2010

Dissertation directed by: Professor J. Robert Anderson
Department of Physics

This dissertation reports on work toward the realization of a state-of-the-art scanning tunneling microscopy and spectroscopy facility operating at milliKelvin temperatures in a dilution refrigerator. Difficulties that have been experienced in prior efforts in this area are identified. Relevant issues in heat transport and in the thermalization and electrical filtering of wiring are examined, and results are applied to the design of the system. The design, installation and characterization of the pumps, plumbing and mechanical vibration isolation, and the design and installation of wiring and fabrication and characterization of electrical filters are described.

SCANNING TUNNELING MICROSCOPY AT MILLIKELVIN TEMPERATURES: DESIGN AND CONSTRUCTION

by

Mark Avrum Gubrud

Dissertation submitted to the Faculty of the Graduate School of the
University of Maryland, College Park in partial fulfillment
of the requirements for the degree of
Doctor of Philosophy
2010

Advisory Committee:
Professor J. Robert Anderson, Chair/Advisor
Dr. Barry Barker
Professor Theodore L. Einstein
Professor Bruce E. Kane
Professor John Melngailis
Professor Johnpierre Paglione

Acknowledgments

I am hopeful that the members of my Advisory Committee will accept my sincere gratitude for their support in my completing this dissertation and graduating from the PhD program.

I owe special thanks to Prof. J. Robert Anderson for pushing me to finish, and to Dr. Bruce Kane and the Laboratory for Physical Sciences for support.

The work reported here was done in direct collaboration with Barry Barker, Michael Dreyer, Anita Roychowdhury, and Dan Sullivan. Notable contributions were made by J. B. Dottellis and Sudeep Dutta. Nolan Ballew, George Dearstine, Peter Krusen, and John Sugrue deserve thanks for their work as well.

Without listing more names, I wish to acknowledge the support, help, encouragement, collaboration, teaching, and friendship of many, many more persons over these past (too many) years.

Table of Contents

List of Tables

List of Figures

List of Abbreviations

ac	Alternating current, or the time-varying component
AMM	Acoustic mismatch model of thermal boundary resistance
atm.	Atmospheric pressure, 1.01×10^5 Pa
BCB	Benzocyclobutene, a polymer used in a family of negative photoresists
BCS	Theory of superconductivity named for its creators, J. Bardeen, L. N. Cooper, J. R. Schrieffer
CDW	Charge density wave, a state of nonuniform (periodic) charge density, generally observable in STM below some ordering temperature
CMN	Cerium magnesium nitrate, a paramagnetic salt used for thermometry
CNC	Computer numerically controlled machine tool
dc	Direct current, or the constant component
DMM	Diffuse mismatch model of thermal boundary resistance
emf	Electromotive force, or magnetically induced voltage
FEM	Field electron microscopy
FIM	Field ion microscopy
ID	Inner diameter
IVC	Inner vacuum can, the evacuated space of a fridge, where things get cold
lbf	Pounds force, i.e. 1 pound mass times the acceleration of gravity
LDOS	Local density of states, a measure of the number of electron states per interval of energy, around some given energy, weighted by the overlap of those states with some "local" volume
LHe	Liquid helium
LN_2	Liquid nitrogen
LPS	Laboratory for Physical Sciences in College Park, Md.
MVM	Metal-vacuum-metal tunneling
MXC	Mixing chamber, the coldest part of a dilution refrigerator
Pa	Pascal (unit of pressure)
PID	A control system in which the feedback signal is a sum of proportional, integral and derivative terms of the sensor data
PTFE	Polytetrafluoroethylene, the most common type of Teflon
PZT	Lead zirconium titanate, a strongly piezoelectric ceramic
OD	Outer diameter
OVC	Outer vacuum can, the vacuum space which insulates the LHe bath from room temperature
OFHC	Oxygen-free high conductivity, a moderate purity grade of copper metal
rf	Radio frequency
RRR	Residual resistivity ratio, the ratio of resistivity of a normal metal at room temperature to resistivity very cold

RT	Room temperature
SQUID	Superconducting quantum interference device
SS304	AISI 304 stainless steel
STM	Scanning tunneling Microscope or Microscopy
STS	Scanning tunneling spectroscopy
WKB	A method for approximate solution of Schrödinger's equation, named for its creators, G. Wentzel, H. Kramers, L. Brillouin

Chapter 1

Introduction

1.1 Overview

Experimental work at technological extremes is naturally difficult. Scanning tunneling microscopy (STM) and spectroscopy (STS) at milliKelvin temperatures (mK-STM) represents the intersection of several extremes: ultra-low temperatures (for physical instruments connected to the outside world), atomic resolution imaging, ultra-low electrical noise and high-gain amplification of low-level signals, ultra-high vacuum, and ultra-low vibration levels and/or high mechanical stability in a low temperature compatible instrument. Quantitatively, one seeks to work at temperatures around 30 mK, with voltage resolution of $\sim$10 μV, and current signals as low as 10 pA, under vacuum of 10^{-11} Pa or better, with tip-sample distance stable to $\sim$1 pm. The degree to which one can achieve these conditions simultaneously will determine the quality of experimental data obtained, and make the difference between significant findings and incomprehensible noise.

This dissertation reports progress toward realizing a state-of-the-art milliKelvin STM system at the Laboratory for Physical Sciences in College Park, MD. At the time of writing, the system is not yet operational, but the required "physical plant" infrastructure has been substantially completed. Initial testing, using an STM head that has demonstrated atomic resolution at room temperature (RT) is expected to

begin within weeks.

In undertaking the design and construction of this sytem, I have been guided by the experiences of a handful of other groups around the world who have built mK-STM systems and reported their results. I have also looked in depth at phenomena of heat transport at milliKelvin (mK) temperatures, and tried to apply what I have learned. In addition, I have surveyed the available literature on vibration isolation in STM and low-temperature STM, control of mechanical noise from the 1 K pot in a dilution refrigerator, cryostat wiring and thermal anchoring methods, and cryogenic low-pass filters. Some of this is reported here, but I do not claim to present comprehensive surveys.

I begin, in Chapter 2, with a review of the history and basics of STM.

Then, in Chapter 3, I review the basics of milliKelvin technology–how to design and build apparatus that operates at temperatures well below 1 K. I pay particular attention to issues of thermal transport, contact and insulation, thermalization of electrical wiring that connects the mK apparatus and the room temperature environment, and I estimate thermal performance parameters for particular materials and configurations that I used in this system. I also discuss low-pass electrical filters, an important consideration bearing in mind that 100 mK corresponds to 2 GHz, and that thermal or technological electromagnetic energy can be a significant source of heating and interference in mK experiments.

In Chapter 4, I describe the physical installation of the dilution refrigerator for our mK-STM and my design and construction of its vibration-isolated system of pumps and plumbing. I assess the performance of the vibration isolation system

both in the context of what was achievable in this installation and in comparison with more expensive facilities.

In Chapter 5, I describe and discuss issues related to the installation of an STM in the dilution refrigerator and my design and construction of an rf-shielded STM mount, electrical wiring of the cryostat, and two types of cold low-pass filters.

In Chapter 6, I state conclusions drawn from this work, and discuss further work to be done in completing the mK-STM system, studies we may be able to conduct with it, and issues related to Josephson phase STM.

1.2 A note on units and symbols

Because this dissertation reports and serves as a reference for experimental work, I have tried to be as consistent and explicit as possible about units, dimensions, and the meaning of particular symbols. Throughout the text I have used the logically consistent convention of treating the symbols for dimensioned physical quantities such as temperature and pressure as representing dimensions multiplied by numbers, rather than as pure numbers, and of displaying the dimension units used in the expression when mathematical consistency requires reducing the quantity to a dimensionless number, such as when raising to an arbitrary exponent in a power law or as the argument of an exponential function. Thus, one will see expressions such as "$(T/\mathrm{K})^{1.3}$," meaning "the temperature T (which may be expressed in any absolute units) divided by 1 K, (the result) raised to the power 1.3." Other conventions, such as treating the units as implicit, or canceling fractional exponents

elsewhere in an expression, are, I believe, more apt to lead to confusion about the units used or about the correct interpretation of an expression, or to doubt about whether it is stated correctly.

While I have preferentially used SI units, expressed in their conventional abbreviated forms, in practical work in our lab we specify machine parts in decimal inches, and we use many commercial components which are specified in whole or fractional inch units. While I could easily convert the latter to m or mm, it does not seem a reasonable thing to do, since anyone who uses the information in the future would need to convert back in order to obtain the useful specification–and might miss the fact that it is an inch specification. Also, I have sometimes expressed forces in both lbf and N because the former is familiar to Americans and provides an intuitive sense of force magnitude.

Chapter 2

Scanning Tunneling Microscopy

2.1 Seeing atoms

Atoms are much smaller than the wavelength of visible light, and therefore can never be imaged by ordinary light microscopy. They are comparable in size to the wavelength of free electrons with kinetic energies comparable to the potential that binds electrons within the atoms[1], suggesting (but see below) that electron microscopes able to resolve atoms would destroy them. Thus, although X-ray, electron and neutron diffraction, nuclear magnetic resonance, and the observations of chemistry are among the sources of data from which atomic crystal and molecular structures can be inferred and modeled (which might be called indirect imaging), the direct, real-space imaging, i.e. microscopy, of individual atoms and atomic lattice defects was once thought to be extremely difficult, perhaps impossible.

This view began to be challenged as early as the mid-1930s by E. W. Müller's development of field electron microscopy (FEM)[14], which exploits the particular geometry and physics of field emission from a sharp metallic needle (typically tungsten). As shown in Fig. 2.1 A, in FEM the tip of the needle (cathode) is placed behind an extraction anode at around 10 kV potential, inducing an electric field which could exceed several GV/m at the tip. Since the work function confining

[1]This follows from Bohr quantization, with the virial theorem.

electrons within metals is a few eV, electrons beyond about 1 nm from the tip surface have tunneled past the barrier and can be accelerated away from the tip by the field. Emission will occur most strongly where the barrier is narrow and low, that is, where the field is strongest, around surface asperities, and also where the work function is lowest. Modeling the tip as a hemisphere of 10-100 nm radius, the field around it is nearly radial and induces a radial acceleration of the emitted electrons, so that the direction of their radiation away from the tip corresponds to the location on the tip from which they were emitted. The electrons strike a phosphor screen (or microchannel plate in later versions), mapping a few μm of the tip to a few cm of the screen.

A tiny hemisphere cut from a crystal will have flat faces corresponding to the low-index planes, which show up as dark circles in FEM (Fig. 2.1 B) since the field is weaker above the flat faces than above the rounded and atomically rough surface between them. In the high field and typical temperatures in FEM of around 1000 K, atoms slowly desorb from the tip, causing the dark circles in the image to collapse as successive planes evaporate. By evaporating a low work-function metal such as barium onto the tip, emission can be enhanced, and as early as 1938 Müller noted the blurry images of isolated objects, which he interpreted as single adsorbed atoms [15] (Fig. 2.1 B). The FEM can also image single molecules decorating the tip, and can even reveal their symmetries (Fig. 2.1 C), but the molecules are not resolved. Resolution in the FEM is at best 1-2 nm, determined by the length scale of field emission (higher voltage will give better resolution but at too high a field strength the tip material will evaporate at too high a rate) as well as the curvature of the

field around emitting asperities, and the spread of electron initial velocities parallel to the surface.

By introducing a low pressure of helium gas and reversing the polarity, Müller created field ion microscopy (FIM), in which helium ions created by the field are projected to the screen, instead of electrons. The mechanics are somewhat complicated [16], but the main source of contrast is that ionization occurs most strongly within small regions of high field directly over atomic-scale asperities. By the mid-1950s, FIM had achieved resolution of 0.3 nm and could provide clear images of the atomic lattice of an FIM tip. In contrast to FEM, where the tip is often heated to enhance emission, in FIM the tip is often cryogenically cooled to enhance resolution and suppress field desorption of the tip atoms.

Although FEM and FIM provided the first direct imaging of atomic-scale features of a metal surface, and have been useful in the study of defects in metals [17], their application is limited by the requirement that the sample take the form of a sharp needle, and by the high field which can desorb surface atoms (Fig. 2.1 D), limiting the range of materials that can be studied mainly to hard metals. FIM is also used to examine tips in scanning tunneling microscopy (STM), where FIM can reveal the tip radius, shape and cleanliness, and field desorption can be used for further cleaning and smoothing of the apex. This requires that the FIM be integrated within a UHV STM system.

By the early 1970s, transmission electron microscopes (TEM) were also shown capable of imaging isolated heavy atoms [20, 21], and high-resolution TEM is today often used to image the atomic structure of inorganic crystals. The expectation

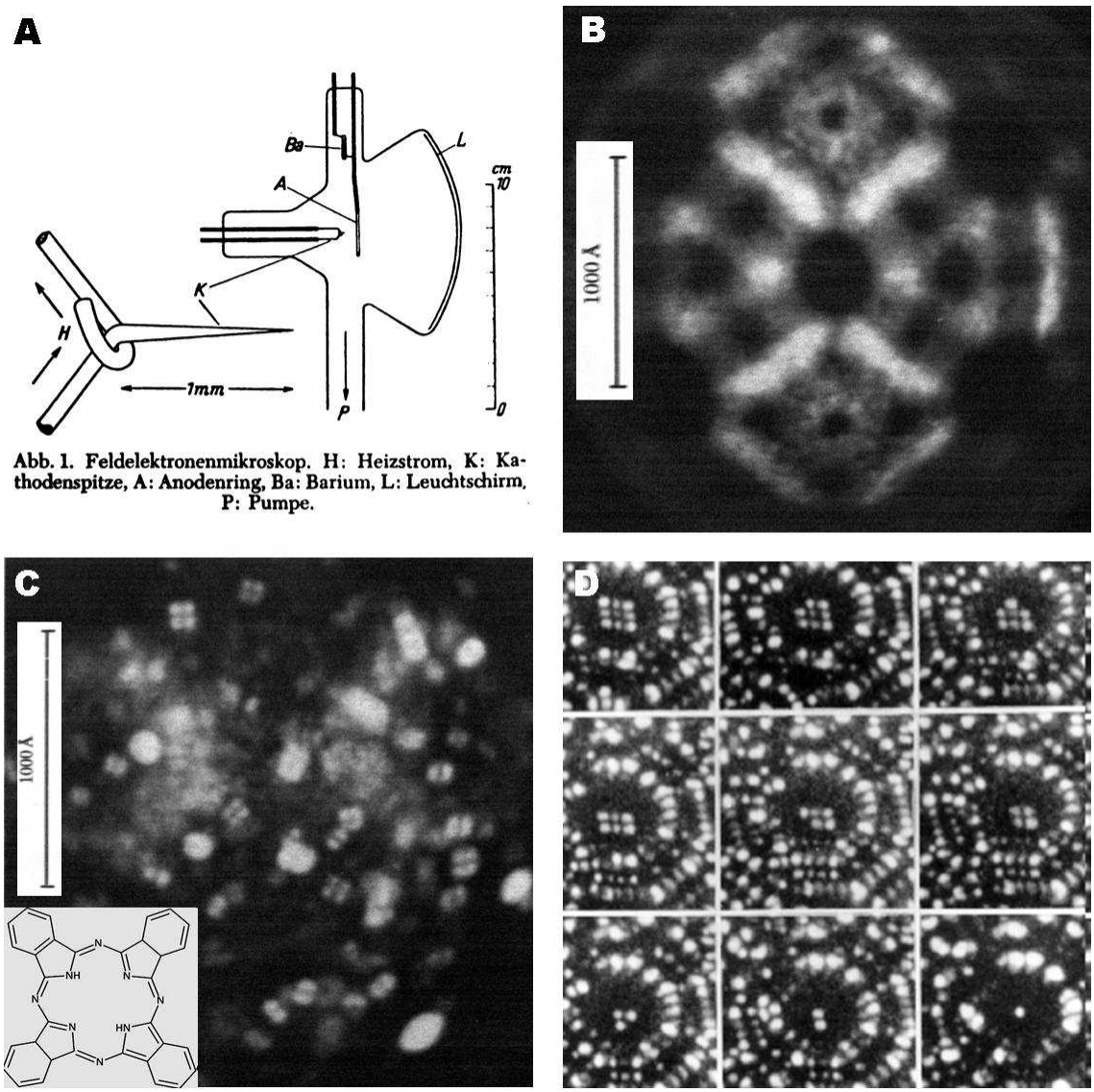

Figure 2.1: Field electron microscopy (FEM) and field ion microscopy (FIM). A. Principle of FEM: electrons emitted from the rounded apex of a sharp metal tip by a combination of thermal and field emission are accelerated radially away from the tip and towards a phosphorescent screen [18]. FIM is similar, except that the tip is kept cryogenically cold and a low pressure of helium gas is introduced; helium is ionized by the field and the ions accelerate away from the tip. Modern instruments replace the screen with electron-multiplying microchannel plates. B. Image made by FEM, circa 1950, reveals fuzzy images of individual Ba atoms on W tip [18]. C. FEM images display the fourfold symmetry of individual phthalocyanine molecules on W tip, although the molecules are not resolved (note scale) [18]. D. Sequence of images made with modern FIM shows 9 atoms in a plane at the apex of a Ni_7Zr_2 tip being removed one at a time by field desorption [19]. In the final frame, only a single apical atom remains. A similar technique can be used to sharpen STM tips.

that electrons of sufficiently short wavelength to resolve atoms would be energetic enough to ionize or dislodge them is correct; in fact electron optics requires energies of 100 keV and above to achieve atomic resolution. However, the interaction between one atom and one 100 keV eletron is usually very weak, with a small probability of a strong (ionizing) interaction. With a very low beam current, a phase contrast mechanism can be used to image the columns of atoms in ultrathin sections of properly aligned crystals [22]. Image interpretation can be complicated, and instruments capable of atomic resolution also have price tags in the $ million range.

2.2 Invention of STM

Like optical microscopy, FEM/FIM and TEM magnify an image by the geometry of projection. Our eyes do something similar, but another way we have to "see" things is to explore them directly with our hands. This is the principle used in scanning probe microscopies (SPM), which scan over the surface of the sample with a local probe having a sufficiently small region of sensitivity. Measurement of microscopic features by direct mechanical contact of a stylus probe is the principle of surface profilometers which have been in use for many decades [23]. The surprising thing is that it is not too hard to make a probe with a "spot size" small enough to resolve atoms.

The development of scanning tunneling microscopy (STM) during the 1980s provided a simple and relatively cheap method of imaging atoms, molecules, and lattices at the surfaces of electrically conducting samples. G. Binnig and H. Rohrer

announced STM in 1981 [24], and just 5 years later were awarded the Nobel Prize for their invention. STM quickly gained widespread use, producing images which captured headlines and dominated scientific journals, and contributing to the sense that a new age of nanotechnology was beginning. It turned out that the same "hands" that can "feel" atoms and molecules can also pick them up, move them around, and perform other actions at the atomic scale. Less than a decade after its invention, STM had enabled not only the imaging of a wide range of samples, but also the precise manipulation of individual atoms [25] and probing of electronic phenomena at the nanoscale.

STM involves bringing a sufficiently sharp conducting tip sufficiently close to a nearly flat sample surface that tip and sample electron states overlap, ideally within a region of atomic proportions. When a voltage (typically $\sim$1 V or less) is applied between the tip and sample, a measurable tunneling current (typically 10-1000 pA) can pass between them. The tunneling current will depend on the tip-sample voltage, tip-sample distance, and local (atomic-scale) features of the sample and tip electronic systems where they overlap. These features include information about the locations and identities of atomic nuclei, but may also reflect purely electronic phenomena, such as the long-range influence of impurities, trapped charge and defect states, charge density waves and superconductivity.

To record an image, the tip is raster scanned across the surface by a piezoelectric scanner capable of repeatable motion at the atomic scale. In the most common mode of imaging, the tunneling current, at constant voltage, is kept constant by varying the tip height as the tip moves over the sample surface. Even at

the considerable standoff distances of ∼0.5 nm typically used in STM, the exponential dependence of the current on distance is roughly a factor of e per Bohr radius (∼0.05 nm) [26]. Hence the tip height tracks the sample topography with high vertical resolution, subject to variations in the local density of states (LDOS) at different points on the sample surface. The images recorded in this way can appear almost like photographs, although their interpretation can be more problematic.

Ironically, Young *et al.* had come close to inventing STM more than a decade earlier, developing an instrument of almost identical schematic design (Fig. 2.2 B) which they called the Topografiner [27]. However, instead of direct tunneling between tip and sample at low voltage, they applied a high voltage (∼100 V) between tip and sample, with a vacuum gap of at least 2 nm, producing field emission from the tip – as in FEM, but in this case the tip is used as a probe, rather than being imaged as a sample.

According to the Fowler-Nordheim theory, field emission in the Topografiner can be understood as the tunneling of electrons from states in the tip to free states in the vacuum. A crude model is shown in Fig. 2.2 A. The space to the left of the E (energy) axis, $z < 0$, represents the tip. The work function $U(z)$ is the energy required to remove an electron from a state at the Fermi level E_F to a distance z beyond the (nominal) end of the tip; with the vacuum level defined as zero, $U(\infty) \equiv -E_F$. Field emission occurs when the tip is biased at a negative voltage V relative to the sample plate, located at a distance d from the tip. For electrons at E_F, a classical barrier exists for the region of $z > 0$ where $E_F + U(z) > |eVz/d|$. Fig. 2.2 A shows two cases, with $V_2 > V_1$ so that the barrier width $z_2 < z_1$. A simple

application of WKB theory [26] predicts that the current I will depend exponentially on the barrier width:

$$I \quad \propto \quad \exp\left(-0.68\,\phi^{3/2}\,\frac{d}{V}\right). \tag{2.1}$$

Given this exponential dependence of current on tip height, as in STM, holding the current constant while the tip is moved over the sample produces a topographic map of the sample, with a demonstrated vertical resolution in the Topografiner of 3 nm using fairly blunted tips. Young *et al.* expected that this could be improved by an order of magnitude with the use of sharp (10 nm radius) tips as in FEM/FIM, so that atomic steps might be observable. However, their expectation, based on field emission theory, was that horizontal resolution with the Topografiner would be no better than about twice the tip radius, so that about 20 nm ultimate horizontal resolution was expected. A key insight that was lacking was that at very close distances, in moving from field emission to metal-vacuum-metal (MVM) tunneling, the effective tip could be narrowed to as little as a single atom.

Unfortunately, the National Bureau of Standards (now the National Institute of Standards and Technology, NIST) did not see a compelling case for the Topografiner as a metrologic instrument, and work was soon terminated. Had development of the Topografiner been continued, the STM (and the nanotechnology age) might have been born a decade earlier.

Young *et al.* were actually quite close; they had begun exploring the transition from field emission to tunneling as the tip and sample were brought closer. As their data showed (Fig. 2.2 C), MVM tunneling exhibited much greater exponential

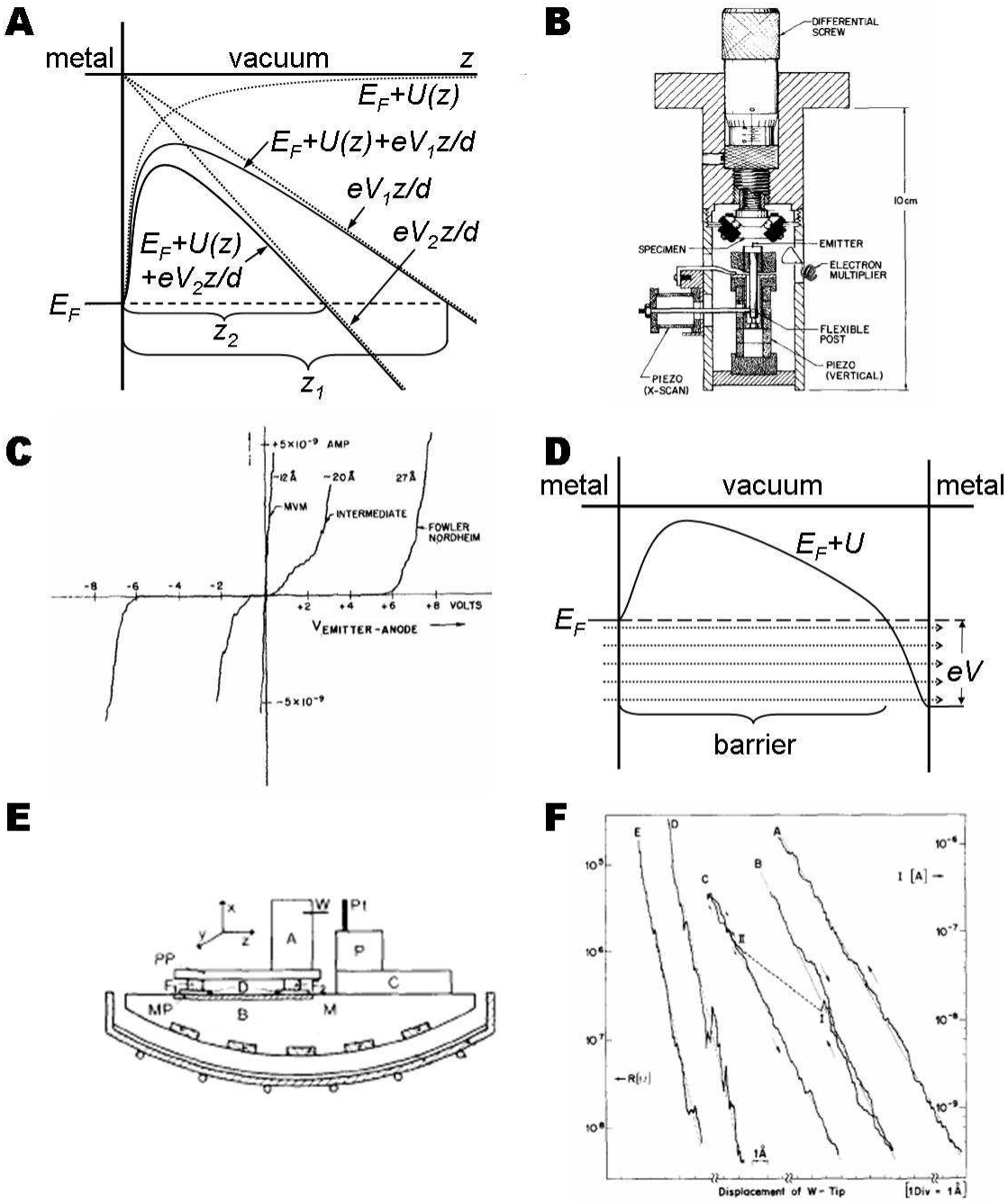

Figure 2.2: A. Illustration of field emission. Vertical axis is energy; electrons at Fermi level E_F in metal must overcome work function $U(z)$ but gain energy from electrostatic field V/d. Width of barrier is proportional to V^{-1}, hence $I \propto \exp(-d/V)$. B. Topografiner of Young, *et al.* [27]. C. Transition from field emission to MVM tunneling in Topografiner. D. Illustration of MVM tunneling between identical metals, with bias voltage V applied to metal at right. Barrier width is insensitive to V, but overlap between filled states at left and empty states at right (dotted arrows) is proportional to V, hence $I \propto V$. E. Apparatus used by Binnig and Rohrer [28] to obtain a controllable MVM tunnel gap. F. Data of Binnig and Rohrer shows exponential dependence of tunnel current on gap width.

sensitivity to tip height than field emission, with linear rather than exponential dependence on voltage. While noting this much higher sensitivity, they stated that "The instrument is never operated in this region due to the instability resulting from the high gain and because the emitter is only tens of angstroms from the surface...." [27].

Part of the problem was the electronics; Young *et al.* used a constant-current supply which both regulated tip-sample voltage to maintain a set current level, and generated a correction signal to adjust tip-sample separation. Adapted to the field emission regime, this control of two physical parameters simultaneously, based on feedback from a single measurment affected by both parameters, was needlessly complex and difficult to stabilize in the MVM tunneling regime. In STM, voltage is usually fixed, and tip-sample distance is controlled by feedback to maintain constant current. A logarithmic amplifier is usually inserted into the feedback loop to linearize the exponential dependence of current on distance.

Binnig and Rohrer picked up where Young had left off, using a very similar piezoelectric positioner to control tip-sample distance to subatomic precision and measure the exponential dependence of MVM tunneling current on distance (Fig. 2.2 F) [28]. They went to extraordinary lengths to isolate their apparatus from environmental vibrations, including the use, later seen to be unecessary, of magnetic levitation over a superconducting Pb bowl cooled by liquid helium (LHe) (Fig. 2.2 E). In addition, for coarse approach, bringing tip and sample within tunneling range, instead of a mechanical screw they used a piezoelectric walker, or "louse," a more stable and "hands-free" approach.

With the use of three matchstick-like piezoelectric elements to form an XYZ positioner, and a feedback loop to maintain constant current by controlling the Z piezo, Binnig and Rohrer's MVM tunneling device became the first STM [29], and its further refinement enabled them to obtain clear atomic-resolution images, including images of the Si(111) surface with its 7×7 reconstruction (Fig. 2.3 A), the first data by which it was possible to unambiguously determine which of several proposed structures was correct [30].

Development of the STM proceeded rapidly as more and more groups took it up. One of the most important early advances was the introduction by Binnig and Smith [32, 33] of the tube scanner to replace the piezoelectric "matchstick box" of the original STM. Tube scanners are simpler in construction, and have higher mechanical resonance frequencies and hence better vibration immunity.

In the usual mode of operation of piezoelectric elements made of ceramics such as lead zirconium titanate (PZT), an electric field applied in one direction causes the material to contract in a transverse dimension (Fig. 2.3 B), while reversing the polarity causes the material to expand in that dimension. Therefore, in the matchstick-type elements, as used in the Topografiner and in the first STMs, the electric field is applied transverse to the length of the stick, and the large aspect ratio serves to multiply the total change in length for a given applied voltage. To make an XYZ scanner, one such element is provided for each of the 3 directions.

The tube scanner uses a somewhat more clever mechanism (Fig. 2.3 C). A single electrode coats the inner surface of the tube, the outer surface is divided into four quadrant electrodes. The voltage applied to the inner electrode, relative to the

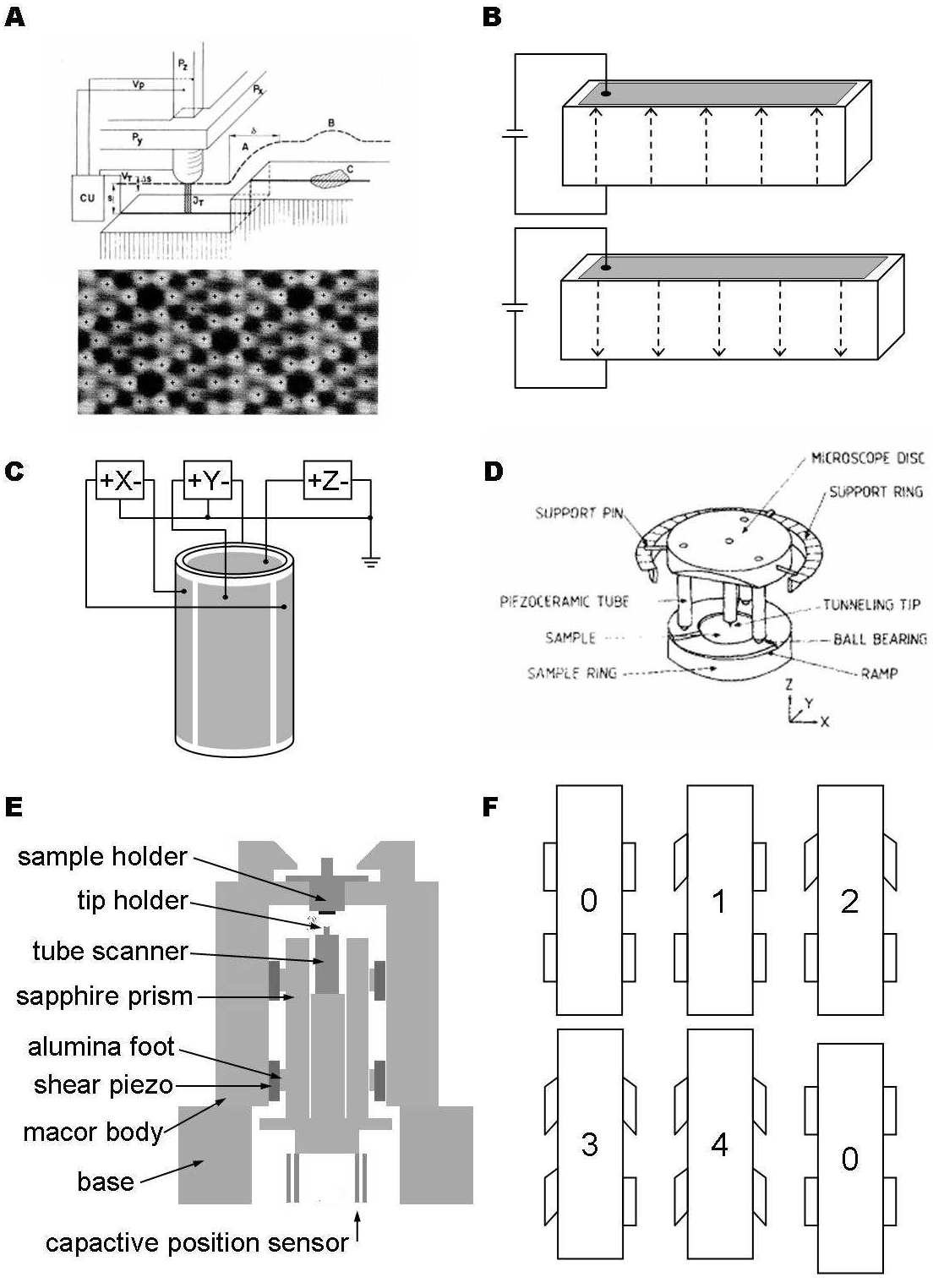

Figure 2.3: STM scanner and walker principles. A. Scheme of Binnig and Rohrer's first STM, with image of Si(111)-7×7 reconstructed surface [24, 30]. B. Principle of matchstick-type piezo element. C. Principle of tube scanner. D. Besocke-type STM design [31]. E. Pan-type STM design. F. Principle of Pan-type walker.

average of voltages applied to the outer electrodes, controls the Z (axial) extension and contraction of the tube. Bending in the X and Y directions is induced by differences in the extension/contraction of opposite sides of the tube. Thus the application of differential voltages to opposing pairs of outer electrodes controls the XY motion. By referencing all voltages to a common level, e.g. ground, the X, Y, and Z motions are controlled separately, with only five wires.

Another critical area of development was the coarse approach mechanism. Tunneling currents can normally be detected only when the tip is within $\sim$1 nm of a sample surface, and the tip has to approach this close from a starting distance of typically several mm, or what can reasonably be arranged by hand and eye. Moreover, the Z range of piezoelectric scanners is typically $\sim 1\,\mu$m. The coarse approach problem is to bring the tip-sample gap to within this distance. The size of steps taken during the approach should be smaller than about half the scan range. The procedure can then be to take a coarse step forward, and with a small tip-sample voltage applied, ramp the scanner to its full extension while monitoring for any sign of tunnel current. If there is none, relax the scanner and take another coarse step forward, repeating until the tip-sample gap is within range and a tunnel current is detected. If it is known that some hundreds of steps have to be taken before there is any risk of making contact, this can be done without ramping the scan piezo each time. However, a tip-sample crash will usually ruin a tip or at least require its reconditioning by field emission.

The overall geometry of an STM can be considered as constituting a "figure G", which represents the tip suspended over the horizontal sample surface and connected

to it by the "backbone" loop of the "G." The size and rigidity of this loop determines the ability of the STM to control the position of the tip relative to the sample with a precision of 10–100 pm. A key weakness is the coarse approach mechanism which must be included within this loop. It is generally less rigid than the other components of the loop (the scanner, tip and sample holders). Finding a good, dimensionally stable and rigid mechanism, which repeatably and reliably moves in steps of the right size, has been a process of trial, error and ingenuity.

The "louse" coarse approach mechanism of the original STM used a piezoelectric plate with three "feet" to "walk" horizontally [29]. The "feet" were metallic and rested on high-dielectric constant insulators with ground plates underneath. By applying high voltage to the "feet" they could be selectively clamped and unclamped to the insulators by electrostatic force, and by a cycle of clamping, expanding, unclamping, contracting, etc., the "louse" could be walked around in steps of 10–1000 nm.

Other early coarse approach mechanisms included mechanical screws and screw-driven mechanisms [34, 35] using mechanical leverage and differential bending of springs to reduce the scale of motion. These crude methods were generally unsatisfactory, both because of static friction leading to too-coarse motion, and the need to turn the screws by hand, often disturbing the tip-sample gap enough to cause a crash. However, Guha *et al.* [36] describe a method using a motor-driven screw with a 20:1 mechanical lever reduction, combined with a piezoelectric array similar to the Pan design (below). The piezoelectric elements are used not to move the tip but rather to create vibrations which break static friction. They also provide a rigid

grip when inactive.

A simple and ingenious design by Besocke [37, 31] (Fig. 2.3 D), uses a triangle of three scan tubes to both scan the tip and, for coarse approach, walk up and down a spiral of ramps. The tubes are mounted on a disk with the tip hanging from the center, and rest on metal balls which contact the ramp surfaces. Sudden motion of the tubes causes the balls to slip on the ramps, while with slow motion the balls stick and the disk moves. The same stick-slip motion can also be used to coarse position the tip in the XY plane. A variation on this design is to use the Besocke mechanism for coarse approach only, and use a separate tube scanner for the fine scanning [38].

Many other designs have made use of the intertial stick-slip mechanism, usually in linear configurations, both for coarse Z and also XY positioning [39, 40, 41, 42]. Such mechanisms are more successful when used for horizontal XY positioning than for sample approach, particularly when the latter is done vertically. It is difficult to precisely counterbalance a vertical Z positioner so that there is no net force of gravity which otherwise interferes with reliable operation of an inertial stick-slip positioner. Also, it is difficult to calibrate the balance of inertial and frictional forces in order to ensure a uniform and reliable step size, particularly over the entire working range of a stage mechanism. A speck of dirt, smear of oil, or minute surface irregularity can cause sticking or erratic behavior of these mechanisms. Changes in temperature can also throw them out of adjustment. While inconsistent stepping is a nuisance for XY positioning, for the Z approach it can be disastrous.

The Pan design [43, 44] (Fig. 2.3 E) provides a highly rigid and reliable, non-

inertial stick-slip mechanism, in which the sticking is controlled by the static friction of 5 out of 6 sliding contacts and the step size is reliably controlled by the range of piezoelectric motion, rather than by inertial sliding. The tip and tube scanner are mounted on a triangular sapphire prism which is used to provide a very hard, low-wear surface for stick-slip motion. The prism is held by 6 alumina "feet", two on each face of the prism, which are attached to shear piezos. Figure 2.3 F illustrates the walking cycle, with only 4 piezos represented instead of 6. First, each shear piezo, one at a time, is suddenly energized to shear. Because the other piezos are stationary and making static frictional contact with the prism, the one that is suddenly sheared slips (or, its alumina "foot" slips) along the prism. After all 6 (or 4 in the illustration) are sheared, the prism still hasn't moved. The piezos are then more slowly relaxed, all together, and the prism moves forward a step.

The Pan design is dimensionally stable for very low temperature operation, since all structural materials are insulators with negligible thermal expansion coefficients at very low temperatures. Because the amount of friction in the stick-slip mechanism is controlled by a single metallic spring, and because the step size is controlled by the extent of shear of the piezos rather than by a balance of inertia and friction, the walker is also reliable over a range of temperatures, although step size will be smaller at low temperatures due to the lower piezoelectric response. The design also allows for sample exchange by a transfer rod mechanism, without needing to warm up the STM and open the cryostat. Tip exchange is also possible with removable tip holders.

Chapter 3

MilliKelvin technology

3.1 Thermal conductivity of materials

In the construction of low-temperature experiments, one usually wants either to maximize or to minimize thermal contact between any two objects, for example, to cool a sample efficiently by mechanical contact with the cold plate of a dilution refrigerator, while not heating it too much by thermal conduction along wires from the warm environment, and shielding it from radiation and other heat leaks from nearby, warmer components. One therefore selects materials either to maximize or minimize thermal conductivity, together with whatever other properties are required.

Although one way to cool an experiment is to bathe it in liquid or superfluid He, the highest thermal conductivity solid materials that we use are pure metals, primarily Cu, although Ag is sometimes used. Au plating is used for the best thermal and electrical contact, and for low emissivity. The lowest thermal conductivity material considered here is powdered insulator, followed by crystalline and amorphous insulators. Low thermal conduction with zero electrical resistance can be provided by superconducting wire. Electrical insulators with high thermal conductivity are hard to come by, but AgSi, SiC, sapphire and BeO are used. Insulating layers can also be made thin to reduce their thermal resistance.

Thermal conductivity of materials can be modeled as a sum of parallel channels each of which is subject to a sum of serial resistances. The channels are the different types of heat carriers, principally phonons and electrons (plus holes, in semiconductors), and the resistances are different scattering mechanisms.

For a gas of particles (electrons, phonons) of number density n, average velocity v, and mean free path $\ell = v\tau$, where τ is the mean time between collisions, with a heat capacity per particle $\hat{c}$ and a temperature gradient $\dfrac{\mathrm{d}T}{\mathrm{d}x}$, the heat flux per unit area in the x direction will be [45, 46]

$$-\dot{q} = n\, v_x\, \ell_x\, \hat{c}\, \frac{\mathrm{d}T}{\mathrm{d}x} = \frac{1}{3}\, nv\ell\, \hat{c}\, \frac{\mathrm{d}T}{\mathrm{d}x}\,, \tag{3.1}$$

where v_x is the average velocity in the x direction and ℓ_x the average distance traveled in the x direction before equilibration at the new temperature, and the result uses $v_x\, \ell_x \;=\; v_x \cdot v_x\tau \;=\; v_x^2\, \dfrac{\ell}{v} \;=\; \frac{1}{3}\, v^2\, \dfrac{\ell}{v}$. From the definition of thermal conductivity, $\kappa \equiv -\dot{q} \Big/ \dfrac{\mathrm{d}T}{\mathrm{d}x}$ we have then

$$\kappa = \frac{1}{3} n\hat{c} v\ell = \frac{1}{3} c_v v\ell\,, \tag{3.2}$$

where c_v is the constant-volume heat capacity per unit volume of the gas.

For a material with several types of heat carriers subject to several scattering mechanisms, we can write $\kappa = \Sigma_i\, \kappa_i$ where κ is the total thermal conductivity and κ_i is the contribution from carrier type i. The inverse mean free path ℓ^{-1} is just the effective mean spatial frequency of scatterers along a trajectory, an additive quantity when centers are sparse and noninterfering. Thus, for each carrier type i we have $\ell_i^{-1} = \Sigma_j\, \ell_{ij}^{-1}$, where ℓ_{ij} is the mean free path for scattering of carrier type i by mechanism j [47], and κ_i can be calculated from ℓ_i using Eq. 3.2.

Thermal conductivities of most materials at mK temperatures can usually be approximated over some temperature range by a power law in temperature, and experimental values are often reported in terms of an exponent b and constant of proportionality a, meaning that the thermal conductivity of the material is given by $\kappa = a(T/\mathrm{K})^b$, at least approximately, within some range of temperatures. Extrapolation can sometimes be justified on theoretical grounds, but it is risky to extrapolate an empirical power law across orders of magnitude in temperature beyond the range of supporting data.

3.1.1 Normal metals

For normal metals, the Wiedemann-Franz-Lorenz (WFL) law relates electrical and thermal conductivity:

$$\frac{\kappa}{T\sigma} \;=\; K\,T^{-1}R \;=\; \frac{1}{3}\Big(\frac{\pi k_B}{e}\Big)^2 \;\equiv\; L_0 \;\simeq\; 2.45{\times}10^{-8}\,\mathrm{W\Omega K^{-2}} \tag{3.3}$$

where κ is the thermal and σ the electrical conductivity of a normal metal, or equivalently, K is the thermal conductance and R the electrical resistance of some piece of normal metal, such as a wire, e is the electronic charge and k_B is Boltzmann's constant, and the resultant L_0 is known as the Lorenz number. The experimental value of the Lorenz number may deviate from the theoretical value quoted here, and can be a function of temperature.

Equation 3.3 can be understood in terms of the fact that for normal metals electrons are the most important thermal carriers as well as charge carriers. This equation therefore assumes that the phonon contribution to thermal conduction can

be neglected. The average thermal energy carried by an electron (or hole) is $\frac{3}{2}k_BT$, while the charge carried is always e, which explains the appearance of T in the denominator of the constant ratio.

The fact that thermal conduction by electrons is sometimes impeded enough for phonons to make a relatively significant contribution is one reason for deviations from Eq. 3.3. Another is, the scattering processes that affect electrical conduction and thermal conduction by electrons are not exactly the same. A thermal gradient means that electrons moving in one direction are hotter, because they are coming from a hotter place, than those moving in the opposite direction. However, the hot and cold flows balance numerically (neglecting possible thermoelectric effects) and there is no net motion of the electrons. In contrast, an electric field induces net motion of electrons, and thus charge transport. This is impeded primarily by elastic scattering processes which reverse the momentum of charge carriers, a large momentum change given the high Fermi energy. Thermal transport, however, can be affected by "small angle" scattering involving phonons of energy k_BT, just enough to take "hot" to "cold" [48]. This is significant at intermediate temperatures, often cited as $0.1 \lesssim T/\Theta_D \lesssim 1$ [49], where Θ_D is the Debye temperature of the material. In this temperature range, inelastic scattering depresses electronic thermal conductivity but has little effect on electrical conductivity.

Deviations from Eq. 3.3 are also observed for alloys at temperatures of 1-10 K, for which the electronic contribution to thermal conductivity is suppressed relative to the lattice contribution because long-wavelength phonons are less efficiently scattered by point defects than are electrons [50]. Even in very pure Ag and Al,

thermal conductivity has been reported as depressed by factors of up to 3 for Al and up to 20 for Ag at temperatures as low as a few K [51].

Pure Cu is a case of particular importance, for which Eq. 3.3, with $L_0 = 2.3\times10^{-8}\,\mathrm{W\Omega K^{-2}}$ [51], is obeyed within a few percent in Cu at temperatures below 8 K down to a few mK [51, 52]. This makes the thermal conductivity of Cu at low temperatures dependent on its residual resistivity ratio (RRR), the ratio of its electrical resistivity at room temperature to that at 4.2 K, a temperature low enough that there is little further change in ρ below this temperature. For Cu at 4.2 K and below, phonons are insignificant not only as heat carriers but also as scatterers of electrons; therefore the "residual resistivity" is due to scattering by impurities, lattice defects, and (for sufficiently small samples) boundaries [49]. RRR is thus a measure of purity. Annealed high-purity (99.999% or "5N") Cu can have RRR in the range of a few times 10^2–10^3 [51, 4] whereas the more common oxygen-free high conductivity (OFHC) Cu may be expected to have RRR of $\sim10^2$, and electrolytic tough pitch (ETP) Cu, the most common type used as Cu wire, has RRR around 50 [4]. All grades of pure Cu have room temperature conductivity of about 17 nΩm.

Applying Eq. 3.3, we can calculate κ for Cu at low temperatures:

$$\frac{\kappa}{\mathrm{RRR}} = \frac{L_0 T}{\rho_{RT}} = \frac{2.3\times10^{-8}\,\mathrm{W\Omega K^{-2}}\cdot T}{1.7\times10^{-8}\,\Omega\mathrm{m}} = 1.4\,\frac{T}{\mathrm{K}}\,\frac{\mathrm{W}}{\mathrm{m\cdot K}}\,.$$

At the lowest temperatures, even in highly disordered normal metal alloys, lattice conductivity is suppressed by the T^3 dependence of phonon density, while the electronic contribution is governed by the width of the Fermi edge and is therefore proportional to T. Therefore Eq. 3.3 should be more generally correct at mK

temperatures.

In pure metals and very dilute alloys the major contribution to both thermal and electrical resistance at high temperatures is electron-phonon scattering, and due to the T^3 dependence of the phonon density accounts for the high RRRs observed in such metals. In contrast, alloys of more than one major constituent tend to be disordered at the atomic scale, and this disorder accounts for most of the electron scattering. Consequently, the RRR is often close to unity, i.e. the electrical conductivity is nearly independent of temperature.

Equation 3.3 defines a tradeoff between low electrical resistance and low thermal conductivity for normal metal wires running between the stages of a fridge. For metals in the superconducting state, the superconducting energy gap prevents substantial electronic thermal ecitation, hence the thermal conductivity is comparable to that of an insulator. Superconducting wire, usually Nb or NbTi, can thus be used to provide zero dc resistance with very low thermal conductivity. However, due to the difficulty of making connections to superconducting materials, superconducting wires are usually embedded in resistive matrix such as CuNi. The ratio of CuNi to superconductor, by volume, is often 1.5:1. The lengthwise thermal conduction is then comparable to that of CuNi wire, but with zero dc resistance.

3.1.2 Insulators

In insulating materials, i.e. those in which the electrons are not mobile, phonons are the only thermal energy carriers. Thus even at high temperatures

Material	Temp. range [K]	a [$\mathrm{W\,m^{-1}K^{-1}}$]	n	Reference
Cu	8–0.005	1.4 RRR	1	Gloos 1990 [51]
Cu	0.15–0.03	1.4 RRR	1	Risegari 2004 [52]
CuNi 70/30	4–0.3	0.093	1.23	Anderson 1963 [53]
CuNi 70/30	0.2–0.05	0.064	1	Greywall 1984 [54]
CuNi 70/30	3–0.1	0.065	1.1	Olson 1993 [55]
CuNi 70/30	4–0.3	0.080	1.1	Kushino 2005 [56]
SS 304	4–0.3	0.040	1.1	Kushino 2005 [56]

Table 3.1: Thermal conductivity data for selected normal metals. The thermal conductivity is given approximately by $\kappa = a(T/\mathrm{K})^n$ for the indicated temperature ranges.

the thermal conductivity of most insulators is lower than that of most metals. At low temperatures, since the phonon density scales as T^3 [46], the difference between the thermal conductivity of insulators and that of normal metals increases dramatically. For most crystalline insulators, at sufficiently low temperatures, thermal conductivity scales as T^3, i.e. is simply proportional to the density of thermal carriers.

Amorphous materials, including insulators such as glasses, alumina, metal surface oxides, epoxies, greases, hydrocarbon and fluorocarbon polymers, are characterized by molecular length scale disorder but uniform average chemical composition and hence uniformity at larger length scales. The combination makes such materials phonon "low pass filters" [57]. For phonon wavelengths $\gtrsim$30 nm, corresponding to temperatures around 1 K and below, the mean free path ℓ is roughly proportional to wavelength, while shorter-wavelength phonons are strongly scattered by the disorder and hence have a very short mean free path. As a result, while for crystalline insu-

lators the thermal conductivity $\kappa \propto T^3$ at low temperature, for disorderd insulators typically $\kappa \propto T^2$ in the milliKelvin range. Compared with crystalline materials, the difference is greater scattering in the disordered case, but the difference decreases for temperatures below 1 K, and at very low temperatures some disordered materials may have relatively high thermal conductivities compared with crystalline insulators.

Amorphous materials are also characterized by "anomalously high" heat capacities at low temperatures, as compared with the Debye model prediction of $C \propto T^3$ as $T \to 0$. The excess heat capacity can be attributed to the many different ways a disordered solid can rearrange and relax to a lower energy state as it cools. A law of the form $C \propto T^m$ with $m \gtrsim 1$ is found for many disordered materials at low temperature. Additionally, plastics, epoxies, and other materials containing hydrogen may exhibit intramolecular ortho-para conversion as a long-lived internal heat source. The high heat capacity, combined with low thermal conductivity at low temperatures, means that amorphous solids may not fully cool over experimental timescales at temperatures of 30 mK and below.

Thermal conductivity data for a few amorphous materials of interest in this work are shown in Table 3.2. The disagreement in measurements by various authors (particularly in the case of GE/IMI 7031 varnish) is a testament to the difficulty of measuring very low thermal conductivities at low temperature, as well as likely differences in the way the materials were prepared, and the presence of substantial boundary resistances, which not all authors seem to have paid attention to.

Material	Temp. range [K]	a [mW m^{-1}K^{-1}]	n	Reference
PTFE Teflon	0.7–0.3	3.8	2.4	Anderson 1963 [53]
PTFE Teflon	0.7–0.3	4.2	2.5	Reese 1965 [58]
PTFE Teflon	1.0–0.2	2.5	2.0	Scott 1972 [59]
PTFE Teflon	4.5–0.4	2.0	1.9	Kushino 2005 [56]
2850FT epoxy (Cat 11)	10–2	5.3	1.8	Tsai 1978 [60]
2850FT epoxy (Cat 9)	8–4	9.5	1.2	Rondeaux 2001 [61]
2850FT epoxy	2–0.065	9.2	2.65	Olson 1993 [55]
1266 epoxy	10–2	3.3	1.9	Olson 1993 [55]
Nylon	0.5–0.2	3.4	1.8	Reese 1965 [58]
GE/IMI 7031 varnish	4.2	60	-	McTaggart 1969 [62]
GE/IMI 7031 varnish	0.3–0.04	3.5	2	Anderson 1970 [63]
GE/IMI 7031 varnish	2–0.05	54	1.87	Stephens 1973 [64]

Table 3.2: Thermal conductivity data for selected amorphous insulators. The thermal conductivity is given approximately by $\kappa = a(T/\mathrm{K})^n$ for the indicated temperature ranges.

3.2 Thermal contact

When differing materials, or even two pieces of the same solid material, are in mechanical contact, in addition to the internal thermal resistances of the materials there will generally exist an extra thermal resistance interposed between them. This *thermal contact resistance* R_c increases at low temperature and can often be significant for the design of low-temperature experiments, apparatus and devices operating at mK temperatures. It determines the heat flow $\dot{Q}$ between two contacting systems at different temperatures T_1 and T_2 according to

$$\dot{Q} \;=\; \frac{T_1 - T_2}{R_c}\,. \tag{3.4}$$

If the contact is uniform over the area A, the area-independent contact resistivity[1] may be defined as $\tilde{R}_c \equiv R_c A$. Eq. 3.4 can also be written in terms of the heat per unit area $\dot{q} \equiv \dot{Q}/A$.

Note that this definition of $\tilde{R}_c$ implies that it could be a function of both temperatures, and on theoretical grounds (see below) we should expect that this will be the case. However, we usually linearize and write

$$\dot{q} = \Delta T \,/\, \tilde{R}_c(T)\,, \tag{3.5}$$

where $\Delta T \equiv T_1 - T_2$, and T can be defined as the average of T_1 and T_2, on the assumption that $\Delta T \ll T$.

The contact resistivity $\tilde{R}_c$ can considered a macroscopic quantity, and, as a matter of convenience, can be defined equally well for contacts of any type, including "sandwiches" filled with (defined amounts of) glue, solder, grease, dirt or other materials. In these cases, $\tilde{R}_c$ will generally include a component from the volume thermal resistance of the filling material. I will distinguish between $\tilde{R}_c$ and the intrinsic thermal boundary (Kapitza) resistivity $\tilde{R}_K$ of an interface between dissimilar materials. The latter is a microscopic quantity which gives rise to a *discontinuous* temperature profile across a perfectly clean and gap-free boundary. It is completely distinct from the volume thermal resistance of either material.

The Kapitza resistance R_K is of theoretical interest but is less closely related

[1]In much of the literature, the symbol R_K (or R_B) is defined as an area-independent property of a given type of interface, but this leads to confusion in its use. I hew to the more general convention that a resistance is the inverse of a conductance, and incorporates all geometrical factors. Hence, where the distinction matters, I will write the area-independent contact resitivity as $\tilde{R}_c$, and my R_c is a resistance, $R_c = \tilde{R}_c/A$. I use the same convention for the Kapitza component of R_c, $R_K = \tilde{R}_K/A$

to R_c than one would like. Although a complicated and often obscure subject, which is susceptible to possibly endless refinement, simple models for R_K do yield qualititatively and, less often, quantitatively accurate results in some, well-controlled cases. However, using these models to predict R_c in situations of practical interest is often impractical or impossible, because of variables such as surface condition, contaminants, and the area of actual contact between rough surfaces. Thus, in practice, empirical data is the best guide to estimating R_c, and even this is often unreliable (or unavailable).

Historically, the temperature discontinuity that arises across the boundary between two media when heat flows across was first observed at interfaces between metals and liquid helium (LHe) in the superfluid state [65], and measurements for superfluid LHe-bronze were reported by Kapitza in 1941 [5]. The term "Kapitza resistance" may refer specifically to the large R_K between solids and (normal or superfluid) LHe, but is also often applied to R_K between different solids.

The Kapitza resistance is a particular problem in the design of helium liquefiers and LHe-based refrigerators. The solution there is to provide a large contacting surface between metal parts and LHe that is to cool, or be cooled by, the metal, usually using porous sintered Cu or Ag powder. This is generally not needed at 4 K, but becomes necessary below 1 K. Thus, for example, a block of sintered Cu immersed in the ^{4}He/^{3}He mix at the bottom of the mixing chamber provides the thermal link to the cold plate in our dilution fridge, and sintered Ag is used in some of the heat exchangers.

3.2.1 Kapitza resistance: Theory

Khalatnikov in 1952 provided an explanation for the Kapitza resistance in terms of an acoustic mismatch between the different media [66]. This acoustic mismatch model (AMM) was developed independently by Mazo and Onsager [67], and extended to solid-solid interfaces by Little [68]. It predicts a T^{-3} dependence for R_K when only phonons are involved, which is generally observed experimentally, but with strong deviations. Poor quantitative agreement between the AMM and experimental data, particularly for Kapitza (solid-LHe) boundaries, led many researchers to attempt improvement of the AMM by considering the role of phonon absorbtion by electrons, and scattering by various mechanisms at or near the boundary (which in most cases will reduce R_K by providing a parallel channel for transport across the boundary) [69, 70, 5]. The mixed and inconsistent results, obtained from fairly detailed calculations, led Swartz in 1989 [70] to propose a simple alternative, the diffuse mismatch model (DMM). According to the DMM, all phonons are strongly scattered at the boundary, making acoustic mismatch irrelevant.

Despite its independent reasoning, the DMM agrees remarkably well with the AMM for metal-dielectric interfaces. For clean and well-characterized interfaces, the measured R_K usually lies between the values predicted by the AMM and DMM. The two models can can be considered as two limiting cases [70]. Alternatively, phonon transmission with and without scattering can be considered parallel channels. For Kapitza boundaries, in the absence of scattering, acoustic mismatch severely restricts transmission. The presence of scattering therefore opens up a larger channel.

In this case, the DMM predicts an R_K close to experimentally observed values, while the AMM prediction is up to two orders of magnitude too high.

Boundary resistance measurements are in general difficult and poorly reproducible, and unfortunately no simple model provides an adequate basis for quantitative prediction in the cases of greatest interest here: metal-metal and metal-dielectric interfaces with unknown effects of surface roughness, disorder and damage, and oxides and other contaminants.

For the benefit of understanding, adapting the treatments of Little [68], Peterson [69], and Swartz [70], I sketch the acoustic mismatch and diffuse mismatch models in their simplest forms, taking account of longitudinal phonons only. The extension to take account of transverse modes in solids is straightforward, but complicates the notation and would tend to obscure the theory.

Consider the boundary between media M_1 and M_2 at temperatures T_1 and T_2. Phonons from each medium collide with the boundary and are either reflected back or transmitted into the other medium, creating thermal currents $\dot{q}_1$ from M_1 to M_2 and $\dot{q}_2$ from M_2 to M_1, per unit area of the boundary. The net heat transfer is then

$$\dot{q} = \dot{q}_1 - \dot{q}_2 \,. \tag{3.6}$$

Thermodynamics requires that $\dot{q} = 0$ when $T_1 = T_2$.

According to Snell's law[2], for phonons from M_1 which are incident on the boundary at an angle θ_1 relative to normal, and which propagate into M_2 at θ_2, we have $v_1 \sin\theta_2 = v_2 \sin\theta_1$, where v_j is the phonon (group) velocity in M_j. Further-

[2]Actually, the law of refraction was described correctly by ibn Sahl of Baghdad circa 984 [71].

more, the fraction α_1 of such phonons which are transmitted is derived in classical wave theory (acoustic Fresnel equations) by matching pressures and normal components of velocity on each side of the boundary [72]. The result [68] is

$$\alpha_1(\theta_1) \;=\; 4\,\frac{\rho_2 v_2}{\rho_1 v_1}\cdot\frac{\cos\theta_2}{\cos\theta_1}\cdot\left(\frac{\rho_2 v_2}{\rho_1 v_1}+\frac{\cos\theta_2}{\cos\theta_1}\right)^{-2}, \tag{3.7}$$

where ρ_j is the mass density of M_j. Note that this form is invariant on exchange of indices, since $a^{-1}b^{-1}(a^{-1}+b^{-1})^{-2} = ab\,(a+b)^{-2}$. Thus $\alpha_1(\theta_1) = \alpha_2(\theta_2)$, as required by the principle of microscopic reversibility.

If the density of longitudinal phonons in M_1 is $N_1(\omega, T_1)$, where ω is the phonon angular frequency, then the total rate at which these phonons are delivered to a unit area of the boundary will be

$$\int_0^\infty \mathrm{d}\omega \int_0^{\pi/2} 2\pi \sin\theta_1\,\mathrm{d}\theta_1\,\left\{\frac{1}{4\pi}\;v_1\cos\theta_1\,N_1(\omega,T_1)\right\}, \tag{3.8}$$

where the factor $\dfrac{1}{4\pi}$ normalizes for the sphere of phonon propagation directions, $v_1\cos\theta_1$ is the normal component of the phonon velocity, and $2\pi\sin\theta_1\,\mathrm{d}\theta_1$ is the differential solid angle. Inserting the transmission probability $\alpha_1(\theta_1)$ and the phonon energy $\hbar\omega$ gives the expression for $\dot{q}_1$, which can be written as:

$$\dot{q}_1 = \int_0^\infty \hbar\omega\,N_1(\omega)\,\mathrm{d}\omega\cdot\frac{v_1}{2}\cdot\int_0^{\pi/2}\alpha_1(\theta_1)\cos\theta_1\sin\theta_1\,\mathrm{d}\theta_1\,. \tag{3.9}$$

Using the Debye approximation (for a single mode)

$$N_1(\omega,T_1) \;=\; \frac{\omega^2}{2\pi^2 v_1^3}\cdot\frac{1}{e^{\hbar\omega/k_B T_1}-1}\,, \tag{3.10}$$

in the low-temperature limit [46], the first integral becomes

$$\int_0^\infty \frac{\hbar\omega}{2\pi^2 v_1^3}\cdot\frac{\omega^2\,\mathrm{d}\omega}{e^{\hbar\omega/k_BT}-1} = \frac{\hbar}{2\pi^2 v_1^3}\cdot\Big(\frac{k_BT_1}{\hbar}\Big)^4\int_0^\infty\frac{z^3\,\mathrm{d}z}{e^z-1} = \frac{k_B^4\,T_1^4}{2\pi^2\hbar^3 v_1^3}\cdot\frac{\pi^4}{15}\,. \tag{3.11}$$

The second integral in Eq. 3.9

$$\Gamma_1\Big(\frac{v_1}{v_2},\frac{\rho_1}{\rho_2}\Big) \equiv \int_0^{\pi/2}\alpha_1(\theta_1)\cos\theta_1\sin\theta_1\,\mathrm{d}\theta_1 \tag{3.12}$$

is a complicated function of the indicated ratios, and is the transmission rate in the sense that $\dfrac{v_1}{2}\cdot\Gamma_1$ is the effective velocity of flow of the phonon gas of M_1 across the boundary into M_2. The maximum value of $\Gamma_1 = \frac{1}{2}$ is always obtained with $v_1 = v_2$ and $\rho_1 = \rho_2$, but matching of the acoustic impedance, $v_1\rho_1 = v_2\rho_2$, does not maximize Γ_1, nor $\dot{q}\propto\Gamma_1/v_1^2$, when $v_2 > v_1$. Thus, the acoustic mismatch is not precisely an "impedance mismatch."

As previously noted, if $T_1 = T_2$ we must have $\dot{q}_1 = \dot{q}_2$. Given that $\dot{q}_1$ is a function of T_1 but not of T_2, and vice versa, this implies that $\dot{q}_2(T) = \dot{q}_1(T)$ for any temperature T. Thus, from Eqs. 3.6 and 3.9–3.12,

$$\dot{q} = \frac{\pi^2 k_B^4}{60\hbar^3}\cdot\frac{\Gamma_1}{v_1^2}\cdot(T_1^4 - T_2^4)\,. \tag{3.13}$$

It may seem puzzling that this result appears to be asymmetrical with regard to M_1 and M_2, but Γ_1 contains information about both media. With Γ_2 defined as in Eq. 3.12 with the exchange of all indices, the symmetry is that $\Gamma_2/v_2^2 = \Gamma_1/v_1^2$.

To put the result into the form of Eq. 3.5, we assume that $\Delta T \ll T_1,\, T_2$. This is a risky assumption at low temperatures, but can only lead to an underestimate

for $\dot{q}$, hence an overestimate for R_K. We then rewrite Eq. 3.13 as

$$\dot{q}(T,\,\Delta T) \;=\; \frac{\pi^2\,k_B^4}{15\,\hbar^3}\,\cdot\,v_1^{-2}\,\Gamma_1\Big(\frac{v_1}{v_2},\frac{\rho_1}{\rho_2}\Big)\,\cdot\,T^3\,\Delta T\,. \tag{3.14}$$

Since temperature has entered only through $N(\omega, T)$, the prediction that $R_K^{-1} \propto T^3$ is actually independent of the acoustic mismatch model, whose physics is contained in the transmission probability Γ_1.

Further insight into Γ_1 can be had by considering the critical angle for total internal reflection, given by $\sin\theta_{c1} = v_1/v_2$. Phonons which are incident on the boundary at any $\theta_1 > \theta_{c1}$ will always be reflected. If M_1 is liquid ^{4}He and M_2 is Cu, we have $v_1/v_2 \approx 1/20$. In this case we must have $\Gamma_1 < 1/800$, and this would be the case even if (counterfactually) $v_1\rho_1 = v_2\rho_2$.

Using this estimate for Γ_1, with $v_1 = 238\,\mathrm{m/s}$ and $T = 2\,\mathrm{K}$, I calculate

$$\begin{aligned} \dot{q} \;&\approx\; 2.04{\times}10^{10}\,\frac{\mathrm{J\,K^4}}{s^3}\cdot 3.5{\times}10^{-8}\,\frac{\mathrm{s^2}}{\mathrm{m^2}}\cdot 8\,\mathrm{K^3}\cdot\Delta T \\ \Longrightarrow\;\; \tilde{R}_K \;&\equiv\; \frac{\Delta T}{\dot{q}} \;\approx\; 1.7{\times}10^{-4}\,\frac{\mathrm{m^2\,K}}{\mathrm{W}}\,. \end{aligned}$$

Apart from the casual estimate for Γ_1, the above treatment of the AMM is actually sufficient for this case, since LHe does not support transverse phonons, and other excitations (rotons, maxons) are insignificant at $T \lesssim 1\,\mathrm{K}$ [73, 74]. However, comparison with experiment shows that the predicted Kapitza resistance is a factor of 50 too large at 2 K, and still a factor of 10 too large at 0.1 K [75].

In general, for many boundaries, agreement with the AMM is better at temperatures in the range of about 20–100 mK [5], presumably because longer-wavelength phonons are less affected by most of the scattering mechanisms present at the boundaries. At still lower temperatures, other mechanisms, such as spin coupling between

^{3}He and metals or paramagnetic salts, and the formation of solid He surface layers, may intervene to reduce R_K [66, 49].

The AMM can be considered a limiting case in which no phonon scattering occurs at the boundary. Because scattering does in general play an important role, Swartz proposed, as an alternative limiting case, the diffuse mismatch model, in which all phonons are strongly scattered at the boundary.

The DMM postulates that a phonon reaching the boundary "forgets where it came from" [70] and scatters into a final state, on either side of the boundary, which is uncorrelated with its initial state. This implies that

$$\alpha_1 + \alpha_2 = 1\,, \tag{3.15}$$

since α_1, the probability that a phonon from M_1 ends up in M_2, must be the same as $(1-\alpha_2)$, the probability that a phonon from M_2 ends up in M_2.

Since α_j is independent of θ_j, the θ integral (Eq. 3.12) collapses to $\Gamma_j = \alpha_j/2$ and, setting $\dot{q} = 0$ for $T_1 = T_2 = T$, and using Eq. 3.15, Eq. 3.6 reduces to

$$\frac{\alpha_1}{v_1^2} = \frac{1-\alpha_1}{v_2^2}\,, \tag{3.16}$$

whence

$$\alpha_1 = \frac{v_1^2}{v_1^2 + v_2^2}\,. \tag{3.17}$$

By invoking detailed balance instead of just thermal balance, α can be calculated as a function of ω, if the phonon velocities are functions of ω.

Replacing Γ_1 in Eqs. 3.13 and 3.14 with $\alpha_1/2$ yields the equivalent expressions for the DMM:

$$\dot{q} = \frac{\pi^2 k_B^4}{120\hbar^3} \cdot \frac{1}{v_1^2 + v_2^2} \cdot (T_1^4 - T_2^4)\,, \tag{3.18}$$

and assuming ΔT is small,

$$\dot{q} \;\simeq\; \frac{\pi^2\, k_B^4}{30\,\hbar^3} \cdot \frac{1}{v_1^2 + v_2^2} \;\cdot\; T^3\, \Delta T\,. \tag{3.19}$$

Comparison with Eqs. 3.13 and 3.14 shows that in the limiting case of a perfect match, e.g. an imaginary boundary within a homogeneous medium, the DMM predicts an R_K twice that predicted by the AMM. It may seem paradoxical that either model would predict a nonzero R_K for this case, but both models assume a nonzero difference between two well-defined temperatures, accompanied by a nonzero heat flux, with R_K defined as their ratio (Eq. 3.5). In the case of a homogeneous medium, this assumption is satisfied by a system consisting of two large volumes with a narrow aperture between them, the temperatures being measured well inside one large volume and the other. In this case, there is no scattering in the area of the "boundary," and the AMM prediction is (trivially) correct, reducing to the "phonon radiation limit" analogous to the Stefan-Boltzmann law (Sec. 3.3.2) [70].

Unfortunately, the above treatment of the DMM is inadequate even for the Kapitza case, since the DMM requires that *all* available modes on *both* sides of the boundary be taken account of. This leads [70] to replacing Γ_1/v_1^2 in Eqs. 3.13 and 3.14 (note that Eq. 3.17 can be rewritten as $\alpha_1 = v_2^{-2}/(v_1^{-2} + v_2^{-2})$) with

$$\sum_j v_{1,j}^{-2}\,\Gamma_{1,j} \;=\; \frac{1}{2}\,\frac{\left[\sum_j v_{1,j}^{-2}\right] \times \left[\sum_j v_{2,j}^{-2}\right]}{\left[\sum_j v_{1,j}^{-2}\right] + \left[\sum_j v_{2,j}^{-2}\right]}\,, \tag{3.20}$$

where the first subscript refers to the medium, and the second to the modes (longitudinal, transverse, and sometimes rotational) in that medium.

For the Kapitza case, with M_1 liquid and M_2 solid, Eq. 3.19 becomes

$$\dot{q} \;=\; \frac{\pi^2\, k_B^4}{30\,\hbar^3} \cdot \frac{v_{1,L}^{-2} \cdot (v_{2,L}^{-2} + v_{2,T}^{-2})}{v_{1,L}^{-2} + v_{2,L}^{-2} + v_{2,T}^{-2}} \;\cdot\; T^3\,\Delta T\,, \tag{3.21}$$

where the subscripts L and T denote the longitudinal and transverse modes. Setting $T = 2\,\mathrm{K}$, and inserting values for ^{4}He ($v_{1,L} = 238\,\mathrm{m/s}$) and Cu ($v_{2,L} = 4910\,\mathrm{m/s}$ and $v_{2,T} = 2500\,\mathrm{m/s}$), we have

$$\begin{aligned} \dot{q} \;&=\; 1.02{\times}10^{10}\,\frac{\mathrm{J\,K^4}}{s^3} \cdot 2.03{\times}10^3\,\frac{\mathrm{s^2}}{\mathrm{m^2}} \cdot 8\,\mathrm{K^3} \cdot \Delta T \\ \Longrightarrow\; \tilde{R}_K \;&\equiv\; \frac{\Delta T}{\dot{q}} \;\approx\; 6{\times}10^{-5}\,\frac{\mathrm{m^2\,K}}{\mathrm{W}}\,, \end{aligned}$$

within a factor of ∼1.5 (higher than) the values measured by Synder [76] using high purity, polished, ion cleaned and vacuum annealed Cu, "probably the most carefully controlled R_K surfaces ever studied [as of 1976]" [75].

3.2.2 Thermal contact resistance: Reality

As noted above, the T^3 dependence of R_K^{-1} predicted by the acoustic mismatch and diffuse mismatch models is just the temperature dependence of the phonon density. This is generally observed for clean metal-dielectric and normal metal-superconductor interfaces at mK temperatures [70, 4], usually transitioning to lower exponents at higher temperatures, particularly for disordered dielectrics.

In normal metal-metal contacts, since at low temperatures electrons are the primary thermal carriers and their density is generally proportional to T [46], one might expect $R_K^{-1} \propto T$, but in practice exponents covering the range 1–1.7 are observed [77, 78, 79, 4], indicating that a mixture of effects is present. For dirty or

deliberately greased metal-metal contacts, thermal conductivity across the boundary may be limited by the presence of disordered, electrically insulating or semiconducting material, for which the expected temperature exponent at temperatures near 1 K would be about 2. For sufficiently thick layers of insulating material sandwiched between metals, e.g. very dirty, glued or heavily greased joints, R_K for the two metal-insulator boundaries may be dominated by the volume thermal resistance of the insulator.

The magnitude of R_c^{-1} in metal-metal contacts is not reliably predicted by the Wiedemann-Franz-Lorenz law (Eq. 3.3), but can be up to 10^5 times greater [4], consistent with the presence of electrically insulating oxides and other contaminants, and the possible role of electrons not only as direct thermal carriers but also as mediators of phonon scattering and absorbtion. However, Didschuns *et al.* [79] measured thermal conductivity for bolted contacts between Au surfaces plated on Cu in the temperature range 90–400 mK, and observed roughly linear temperature dependence. Although they did not measure the electrical resistances of their junctions, they argued that the results were of the correct magnitude to be consistent with the WFL law, as might be expected for clean metal-metal junctions.

Whenever preformed solid surfaces (metal-metal or metal-dielectric) are pressed together, due to surface roughness the area of actual contact is initially (at low pressure) a small fraction of the gross surface area. The fraction is often quoted as of order 10^{-6} for metal-metal contacts [49, 4, 5], but the basis for this number is obscure, and a recent review quotes "1–2 %" [80]. In reality, the fraction is strongly pressure-dependent.

Solid materials can generally be characterized by a pressure Y (hardness, or yield strength) above which, when the pressure is locally applied to a region of the surface, the material will yield and break or deform. This can be thought of as analogous to a taut balloon whose internal pressure (repulsive force) is balanced against the tension of its skin (cohesive force). When external pressure applied locally to the skin of the balloon exceeds the internal pressure, the balloon yields.

For rough surfaces in contact, this means that under an applied *force* F the asperities of one surface will blunt or dig into the other, depending on relative hardnesses and microscopic details. As as result, regardless of the gross area A of the surfaces, the area S of actual contact is expected to increase until

$$F \;=\; Y\,S\,. \tag{3.22}$$

Hence, assuming that $R_c \propto S^{-1}$, we may expect $R_c \propto F^{-1}$, and thus be *independent of the gross area of the contacting surfaces.*

Berman and Mate [77] found that $\dot{Q}$ for Cu-Cu contacts varied as $F^{0.88}$ at 4.2 K and as $F^{0.58}$ at 18 K, with F ranging from about 10 to 10^3 N. They suggested that the deviation from $\dot{Q} \propto F$ might be attributable to differences between plastic deformation upon compression and elastic relaxation upon decompression, but this hypothesis was inconsistent with the lack of appreciable differences between the data taken with force increasing and decreasing. In contrast, Colwell [78] observed $\dot{Q}/F$ constant for (superconducting) In-Cu contacts, with F ranging from 20–80 N and T ranging from 0.3–2 K.

However, because the "balloon" analogy ignores the effects of crystalline or

other microscopic structure, and possible dependences on the scale and shape of surface roughness, Y must be considered an effective parameter which could at best be only roughly estimated from tabulated values of hardness or yield strength (as determined by macroscopic measurements, according to any of several operational definitions). In addition, the linearity of Eq. 3.22 cannot continue to hold as $F \longrightarrow YA$, since the gross area A (times some factor of order unity) will set an upper bound on S.

For sufficiently soft materials, e.g. In, PTFE and certainly grease pressed against or between metals or other hard materials, a limit may be approached in which R_c is nearly independent of F.

However, even in these cases, trapped gases, oxides and other contaminants will still affect the reproducibility of R_c. In addition, this discussion has ignored the effects of damage to due to fracture or plastic deformation under pressure, which may either increase or decrease both the microscopic R_K and the macroscopic R_c [5]. There may also be effects dependent on the microscopic size of the contacting areas [77].

Given all these complexities, in practice metal-metal and metal-insulator thermal contact resistances are not predictable from theory, even when the materials are well-bonded, much less when pressed together. Instead, empirical data must be consulted when it is available, and used with caution given uncertainties about the condition of surfaces. Gmelin *et al.* [80] provide the most complete review of solid-solid contact resistances I have found, covering general principles and data for a wide range of materials.

If a reference value is known, extrapolation is possible within a limited range, based on observed or predicted dependences on temperature and pressure. However, one should remember that, for example, a phenomenon that is governed by a sum of quadratic and cubic terms may fit, over a limited range, to a power law with an exponent between two and three. The fact that a good fit is obtained within some given range does not imply that the phenomenon does not deviate from the reported power law immediately outside the reported range; it may imply the opposite.

3.2.3 Estimation of thermal boundary resistance: Empirical data

Anderson and Peterson [63] measured contact resistances R_c at temperatures of 0.3–0.04 K for several materials commonly used as low-temperature thermal bonding agents, including Apiezon N grease, RTV silicone, Epibond 121 epoxy, and superconducting In solder. They sought to separate the boundary resistances from the volume resistances of the bonding agents by fitting their data to assumed T^{-3} terms for the boundary resistances, plus T^{-n} terms for the volume resistances, with $n = 2$ usually assumed for amorphous materials. Their "most striking result" was that $\tilde{R}_K \simeq 0.75\,(T/\mathrm{K})^{-3}\,\mathrm{m^2\,K\,W^{-1}}$ "for all materials within ±20%."

In contrast, Colin [81] measured R_c for In solder and epoxy bonds with and without silver fill. The In bonds exhibited $R_c^{-1} \propto T^3$ over $T = 4 - 0.3\,\mathrm{K}$ whereas the epoxy bonds exhibited close to $R_c^{-1} \propto T^2$ over the same range. Below 1 K, the epoxy bonds had lower resistance than the indium bonds, and silver-filled epoxy lower resistance than unfilled. It is not clear whether this is due to the "contact

Materials	Temp. [K]	$\tilde{R}_K\,(T/\mathrm{K})^3$ [$\mathrm{m^2\,K\,W^{-1}}$]	Ref.
Cu–7031 Varnish	0.3–0.04	8.5×10^{-4}	Anderson 1970 [63]
Cu–Epibond 121 epoxy	0.3–0.04	6.2×10^{-4}	Anderson 1970 [63]

Table 3.3: Some thermal boundary resistivity data for deposited contacts.

Materials	T [K]	F [N]	R_c [K/W]	t	f	Ref.
Cu–Cu	1.6–20	445	$730\,T^{-t}$	1.31	-	[77]
Cu–Cu	4.2	18–770	$8.8\times10^{4}\,F^{-f}$	-	0.88	[77]
Cu–Cu	18	4–1200	$740\,F^{-f}$	-	0.58	[77]
Cu/Au–Au/Cu	2.8–4.2	445	$17.3\,T^{-t}$	1.0	-	[77]
Cu/Au–Au/Cu	0.09–0.4	$\gtrsim 10^3$	$11.6\,T^{-t}$	0.94	-	[79]
Cu–diamond	1.4–4.1	445	$22.4\,T^{-t}$	2.4	-	[77]
Cu–Apiezon N–Cu	1.6–6	100	$0.067\,T^{-t}$	1.57	-	[82]
Cu–0.13 mm In–Cu	1.6–6	448	$0.36\,T^{-t}$	2.2	-	[82]
Cu–PTFE–Cu	4.2	220-1100	$2.3\times10^{5}\,F^{-f}$	-	1.3	[83]

Table 3.4: Selected thermal boundary resistance data for pressed contacts.

resistance" being dominated by the body resistances of the materials. However, the results clearly indicate that Ag-filled epoxy is superior to solder for thermal contact at mK temperatures, particularly for the joining of wires where both electrical and thermal contact are desired.

3.2.4 Comparison of contact and volume thermal resistance

In the design of low-temperature apparatus, contact thermal resistance and the volume thermal resistance of components will in general be additive terms. One may be much greater than the other, so that the lesser term may be neglected, or the two may be comparable. Which is the case will depend on geometry and temperature, as well as the materials involved.

Consider the case of a cube with sides of length ℓ made of some material with volume thermal conductivity κ. Its volume thermal resistance R_V will be given by $R_V = \kappa^{-1}\ell^{-1}$. If it contacts another object on one face, through a contact resistivity $\tilde{R}_c$, the contact resistance will be $R_c = \tilde{R}_c\,\ell^{-2}$. Thus, $R_c/R_V = \ell^{-1}\,\kappa\,\tilde{R}_c$, and we see that the relative importance of contact resistance will decrease for larger objects with proportionately larger contact areas.

A useful measure of comparison is the thickness $\ell^*(T) \equiv \kappa\tilde{R}_c$ of a layer of material, contacting another material, whose volume thermal resistance perpendicular to the plane of contact is equal to the contact thermal resistance.

Pressed Cu-Cu: A case of interest here is Cu components bolted to the Au-plated Cu cold plates of our dilution fridge. I will consider first Cu-Cu junctions in the same geometry. Oxford provides M3 bolt holes in a 15 mm square lattice, i.e. one bolt hole per $2.25{\times}10^{-4}\,\mathrm{m}^2$ of area. The maximum load that stainless steel M3 bolts will support is about 1.6 kN [4], which should be derated to about 1 kN to avoid the risk of breaking.

Berman and Mate [77] measured R_c for Cu-Cu contacts under forces in the range of 10^1–10^3 N and over temperatures in the range of 1.6–20 K. Presumably their samples were as clean as could reasonably be achieved, but they did not report any special cleaning measures, and did report that they believed oxides were present (as they necessarily would be, given that the samples were prepared in air). For $F = 445$ N (100 lbf), they obtained $R_c = 730\,(T/\mathrm{K})^{-1.3}\,\mathrm{K/W}$. Whether this can be extrapolated an order of magnitude lower in temperature is questionable, but the

power law fit was good over the more than one order of magnitude range of their measurements.

While the total force F applied to the junction, rather than the pressure, determines R_c, to compute ℓ^* we need $\tilde{R}_c$, and thus we must specify the area over which the force is applied. To match Berman and Mate's $F = 445\,\mathrm{N}$, the area of the junction can be set at $1\times10^{-4}\,\mathrm{m}^2$, yielding $\tilde{R}_c = 0.073\,(T/\mathrm{K})^{-1.3}\,\mathrm{m}^2\mathrm{K/W}$.

From these data, using $\kappa = L_0\,T/\rho = 140\,(T/\mathrm{K})\,\mathrm{W\,m^{-1}K^{-1}}$ for OFHC Cu with RRR=100 (Table 3.1) we calculate $\ell^* = \kappa\,\tilde{R}_c \simeq 10\,(T/\mathrm{K})^{-0.3}\,\mathrm{m}$. This means that, under the stated assumptions, *contact thermal resistance dominates volume thermal resistance* when OFHC Cu is broken by a pressed Cu-Cu contact at LHe or mK temperatures. An example would be a $(15\ \mathrm{mm})^2$ square Cu bar bolted at one end to a Cu cold plate with a single M3 bolt; only if the bar were 10 m long would the volume resistance compare with the contact resistance at $T \lesssim 1\,\mathrm{K}$.

Au plated Cu: As mentioned above, the cold plates of our dilution fridge are Au-plated Cu. Some parts that are bolted to the cold plates are Cu only, and others are Au-plated Cu. Berman and Mate [77] found $R_c = 17(T/\mathrm{K})^{-1}\,\mathrm{K/W}$ for Cu/Au–Au/Cu contacts under 445 N force at $T = 2.8 - 4.2\,\mathrm{K}$, which agrees reasonably well with Didschuns *et al.* [79], who found $R_c = 12(T/\mathrm{K})^{-0.94}\,\mathrm{K/W}$ over $T = 90-400\,\mathrm{mK}$ under somewhat greater force. Note that any boundary resistance between the Au plating and the bulk Cu has been taken into account by the data and is expected to be small, since electrons will be the dominant thermal carriers.

Using Berman and Mate's result, we predict for Cu/Au–Au/Cu at low tem-

peratures $\ell^* \simeq 20\,\mathrm{cm}$. Thus, the effect of Au plating is to lower R_c by a factor of up to ∼40 at 1 K, ∼80 at 0.1 K, and ∼120 at 30 mK. In the latter case, we will have ℓ^* the order of 1 mm, so the volume resistivity of OFHC Cu will generally dominate the contact resistance for Au-plated Cu at the base temperature of our dilution fridge.

When only one of the Cu surfaces is plated, we may expect that R_c for the Cu/Au–Cu contact will be roughly half of R_c for a Cu–Cu contact under the same force, assuming that the contact resistance is mostly due to the presence of oxides, contaminants and gaps between the asperities of the (usually harder) Cu. Thus in most cases it will make little sense to plate only one surface.

Cu-Apiezon N-Cu: Where higher R_c can be tolerated or Au plating is unavailable, Cu–Cu contacts are often greased. Apiezon N$^{\mathrm{TM}}$ is a popular type of thin-spreading, low-viscosity grease used especially for thermal contact. The ideal amount of grease would be just enough to fill the voids between contacting asperities, thus providing additional thermal contact without reducing metal-metal contact. In practice it is impossible to control the amount of grease so precisely, but if excess grease is expelled from the junction under pressure, its viscosity will roughly determine a limiting thickness. One then obtains a Cu–grease–Cu sandwich, with an R_c that is not strongly dependent on the applied force [82].

Anderson and Peterson [63] measured R_c for a Cu-Apiezon N-Cu sandwich with grease thickness $\ell = 6.4\,\mu\mathrm{m}$, over the temperature range 40–500 mK. They fit this data to the form $\tilde{R}_c = aT^{-3} + b\ell T^{-2}$, under the assumption that these terms would represent the boundary and volume resistances respectively, finding that

$\tilde{R}_K = aT^{-3} = 6.5\times10^{-4}\,T^{-3}\mathrm{K}^4\mathrm{m}^2\mathrm{W}^{-1}$ and $\tilde{R}_V = \ell bT^{-2} = 1.0\times10^{3}\,T^{-2}\,\mathrm{K}^3\mathrm{m}^2\,\mathrm{W}^{-1}$.

Salerno *et al.* [82] measured R_c for a Cu-Apiezon N-Cu sandwich of unknown grease thickness but under pressure of 0.27–8.2 MPa over the temperature range 1.6–6 K. They found that R_c was insensitive to pressure in this range at the lowest temperatures. Fitting their data to a single power law, they found $\tilde{R}_c = 5.5\times10^{-3}\,(T/\mathrm{K})^{-1.55}$. Extrapolating their results down, and Anderson and Peterson's up, to $T = 1\,\mathrm{K}$, the two can be reconciled by assuming that $\ell \simeq 5.4\mu\mathrm{m}$ for Salerno *et al.*, which is close to Anderson and Peterson's $6.4\,\mu\mathrm{m}$, although the latter was determined by the thickness of a mylar spacer.

Assuming, then, that a layer of Apiezon N grease is likely to be about $6.4\,\mu\mathrm{m}$ thick, and relying on Anderson and Peterson's data for the millikelvin range, we expect that the volume resistance of the grease will be the dominant contribution to R_c above about 0.2 K, and the boundary resistance will dominate at lower temperatures.

More significantly, we can calculate ℓ^* for Cu sitting on top of a Cu-Apiezon N-Cu sandwich. This is the thickness of a Cu layer whose volume resistance is equal to the contact resistance of the sandwich. Using Anderson and Peterson's $\tilde{R}_c = [6.5\times10^{-4}(T/\mathrm{K})^{-3} + 6.4\times10^{-3}(T/\mathrm{K})^{-2}]\,\mathrm{K\,m^2W^{-1}}$, and using $\kappa = 10^2\,(T/\mathrm{K})\,\mathrm{W\,m^{-1}K^{-1}}$ for OFHC Cu (see above), we have $\ell^* = \tilde{R}_c\kappa_{Cu} = [0.065(T/\mathrm{K})^{-2} + 0.64(T/\mathrm{K})^{-1}]\,\mathrm{m}$. Thus, even at 1 K, $\tilde{R}_c$ is equivalent to about half a meter of Cu, increasing to about 10 m at 100 mK.

Cu-7031 varnish: GE/IMI 7031 varnish is used, among other purposes, as an

electrically insulating thermal bonding agent to assist the thermal anchoring of fine wires, typically wrapped around Cu, or Au-plated Cu, heatsink posts. In this application, the varnish joins the surface of the post to pre-existing insulation bonded to the wire, but the insulation will usually be similar in characteristics to the varnish; thus its boundary resistance to the wire will be comparable to that of the varnish to the post, and the boundary between the varnish and insulation can be ignored. The interesting question is how the Cu-varnish boundary resistance compares with the volume thermal resistance of the varnish. Therefore the ℓ^* to be computed is the thickness of varnish for which the volume thermal resistance of the varnish exceeds twice the boundary resistance of the Cu-varnish boundary.

Anderson and Peterson [63] measured R_c for a $1\,\mathrm{cm}^2$ Cu-7031-Cu sandwich with 7031 thickness $\ell = 6.4\,\mu$m over the temperature range 40–300 mK. They fit this data to the form $\tilde{R}_c = 2aT^{-3} + b\ell T^{-2}$, under the assumption that these terms would represent the boundary and volume resistances respectively, finding that $a = 8.5\,\mathrm{K}^4\mathrm{W}^{-1}$ and $b = 2.86\times10^6\mathrm{K}^3\ \mathrm{W}^{-1}\mathrm{m}^{-1}$. Equating these terms, we find that $\ell^* = T^{-1}/, 2a/b = 6\,\mu\mathrm{m}(T/\mathrm{K})^{-1}$. Thus, R_V will in most cases dominate R_K at 1 K, but at 30 mK, $\ell* = 0.2$ mm, indicating that boundary resistance is *not* negligible for the case of fine wires ($\sim$0.1 mm diam.) varnished to heat sink posts at mK temperatures.

Cu-Soft Solder: Common Pb-Sn soft solder is generally not used where good thermal contact is desired at mK temperatures, because it will be superconducting below about 7 K [84]. Steyert [85] measured contact resistance for 10 μm thick Cu-

SnPb-Cu junctions using 50/50 SnPb, finding $\tilde{R}_c = 2.13\times10^{-4}\,(T/\mathrm{K})^{-2.74}\,\mathrm{m^2K/W}$. He measured thermal conductivity for the superconducting SnPb separately, finding $\kappa = 0.10\,(T/\mathrm{K})^{-2.31}\mathrm{W\,m^{-1}K^{-1}}$. From $R_c = 2R_K + R_V$ and $\tilde{R}_V = \ell/\kappa$, with $\ell = 10^{-5}\,\mathrm{m}$, we have $\tilde{R}_V = 1\times10^{-4}\,(T/\mathrm{K})^{-2.74}\,\mathrm{m^2K/W}$, i.e. $2R_K \approx R_V$ at 1 K. The ratio R_K/R_V is expected to increase at lower temperatures as roughly $T^{-\frac{1}{2}}$.

3.3 Heat leaks

The inner vacuum can (IVC) of our dilution refrigerator is immersed in LHe at 4.22 K and encloses components at much lower temperatures. The mixing chamber and cold experiment are normally shielded from the 4 K radiation by a shield anchored to the cold plate at a nominal 50 mK. Heat leaks in and around the experiment, other than conduction through solid materials, include thermal radiation and molecular gas conduction across the vacuum space. A pathological case is superfluid He film conduction, but there shouldn't normally be enough ^{4}He in the can to form a troublesome film. In addition, unwanted heating can be caused by eddy currents induced by a time-varying magnetic field, or by vibration through a magnetic field, and by electrical heating due both to currents through the wiring as required by the experiment, and due to unwanted electrical noise. A final type of "heat leak" is just the heat capacity of materials as compared with diminishing thermal conductivity at low temperature. Particular contributions to the heat capacity at low temperature, such as relaxation of spins in a high magnetic field, and ortho-para conversion of hydrogen, may need to be considered when trying to work in the low

mK temperature range.

3.3.1 Gas conduction

Conduction of heat by gases at low pressure generally divides into two regimes according to whether the mean free path ℓ is shorter or longer than the characteristic distance d between hot and cold surfaces.

For $\ell \ll d$, the high pressure, hydrodynamic regime, gas thermal conduction (absent convection) is diffusive and characterized by a conductivity κ like that of solids. The heat flux $\dot{q}$ per unit area due to conduction by a gas with mean thermal conductivity $\bar{\kappa}$ between parallel plates at separation d and temperature difference ΔT is thus

$$\dot{q} = \bar{\kappa}\,\frac{\Delta T}{d}\,. \tag{3.23}$$

The diffusive thermal conductivity of a gas was derived in Sec. 3.1 as $\kappa = \frac{1}{3}\,\ell v n \hat{c}$, where n is molecular number density, v is the average velocity, and $\hat{c}$ is the heat capacity per molecule. κ is thus temperature-dependent through both v and $\hat{c}$, but relatively independent of pressure since $\ell \propto n^{-1}$. Since $\eta = \frac{1}{3}\ell v n m$ is the viscosity[3], with m the molecular mass, we have $\kappa = \eta\,\dfrac{\hat{c}}{m}$. Experiment and more sophisticated theory find that $\kappa = b\,\eta\,\dfrac{\hat{c}}{m}$, where b ranges between 1.5–2.5 [86].

The second regime, $\ell \gg d$, is free molecular conduction, and is the normal case in mK-STM. Already at 4K, only helium has an appreciable vapor pressure, and all other gases are frozen. When the fridge is cold, the mixing chamber and

[3]This follows from replacing the energy $\hat{c}T$ with momentum mv in the derivation of Eq. 3.1, and defining viscosity as the diffusive momentum transport coefficient of velocity.

other components at millikelvin temperatures will pump any He down to the vapor pressure for the coldest surface temperatures present. One symptom of a He leak into the IVC is periodic spikes in temperature at the mixing chamber. He condenses on the cold parts, forming droplets and dripping down onto the warmer shield or the 4 K IVC. Each drop becomes a sudden burst of warm gas which condenses again on the cold parts. Whether this occurs is controlled by the total amount of helium left in the IVC. We use ^{3}He as exchange gas, which needs to be pumped out at 4 K. The vapor pressure of ^{3}He is about 3 times higher than that (1 bar) of ^{4}He at 4.22 K, yet it still takes many hours to pump down to pressures compatible with fridge operation.

Table 3.5 shows the approximate vapor pressures of ^{4}He and ^{3}He at 4 K and lower temperatures. Also shown are values for ℓ calculated using [4]

$$\ell = 28.7\,\mu\text{m}\left(\frac{T}{1\,\text{K}}\right)^{1.147}\left(\frac{p}{1\,\text{Pa}}\right)^{-1}, \tag{3.24}$$

where p is pressure, and assuming $T = 1$ K (although the coldest components limit p, the gas temperature in the vicinity of warmer components may be higher). For comparison, the relevant dimension d for a mK-STM cryostat ranges from 1 mm to 10 cm.

Once the mixing chamber reaches 0.1 K or lower, the pressure of ^{3}He can't be greater than 10^{-8} Pa [3], from which we calculate $\ell \approx 3$ km, i.e. well in the free molecular regime. However, if the mixing chamber is as warm as 0.2 K, we find $p \approx 10^{-2}$ Pa, and then $\ell \approx 3$mm, crossing into the diffusive regime. Of course, if we raise the temperature in a dilution fridge this high, using a heater, we are probably

T [K]	^{4}He p [Pa]	^{3}He p [Pa]	^{4}He ℓ	^{3}He ℓ
4.2	1×10^5	3×10^5		
2	3×10^3	2×10^4		
1	2×10^1	1×10^3	1.4 μm	
0.5	2	3×10^2	14 μm	0.1μm
0.3	10^{-1}	10	0.3 mm	3μm
0.2	10^{-4}	10^{-2}	0.3 m	3 mm
0.1	10^{-10}	10^{-8}	300 km	3 km

Table 3.5: Vapor pressure and mean free path of ^{4}He and ^{3}He. Data from [1, 2, 3, 4, 5]

not concerned about the heat leak.

The theory of free molecular heat conduction developed by Knudsen is described in [45]. For parallel surfaces **1** and **2** at temperatures T_1 and T_2, assuming a steady state, we can consider the molecules as shuttling back and forth between the two surfaces. The gas stream thus emanating from surface **1** is incident on **2** at $T_1{}'$, and that emanating from **2** is incident on **1** at $T_2{}'$. Gas temperatures $T_1{}'$ and $T_2{}'$ are not necessarily equal to surface temperatures T_1 and T_2. The central idea of the Knudsen theory is that only partial equilibration occurs at each encounter of a gas stream with a surface. One possibility is that a fraction a of the molecules are adsorbed and equilibrate to the surface temperature before desorbing, while a fraction $(1-a)$ are reflected elastically (and specularly, although surface roughness may hide this). This is expressed in terms of *accomodation coefficients* a_1 and a_2 for surfaces **1** and **2** such that

$$T_1{}' \;=\; a_1\,T_1 + (1-a_1)T_2{}' \;\text{ and }\; T_2{}' \;=\; a_2\,T_2 + (1-a_2)T_1{}'. \tag{3.25}$$

Solving these equations, we find that

$$T_1{}' \;=\; \frac{a_1 T_1 + a_2(1-a_1)T_2}{a_1 + a_2 - a_1 a_2}\,, \quad T_2{}' \;=\; \frac{a_2 T_2 + a_1(1-a_2)T_1}{a_1 + a_2 - a_1 a_2}\,, \tag{3.26}$$

$$\begin{aligned} \text{and}\;\; T_1{}' - T_2{}' \;&=\; \frac{a_1\, a_2}{a_1 + a_2 - a_1 a_2}\,(T_2 - T_1) \\ &\equiv\; G \cdot (T_1 - T_2)\,. \end{aligned} \tag{3.27}$$

The heat flux from surface **1** to **2** per unit area is then given by [45, 86]

$$\dot{q} = \frac{1}{4}\, G\, \frac{\gamma+1}{\gamma-1} \sqrt{\frac{2R}{\pi M}}\, p\, \frac{T_1 - T_2}{\sqrt{T}} \tag{3.28}$$

where γ is the heat capacity ratio C_p/C_v, which has the value $\frac{5}{3}$ for He, R is the molar gas constant 8.3 $\mathrm{J\,K^{-1}mol^{-1}}$, M is the molar mass (3 or 4 $\times 10^{-3}\,\mathrm{kg\,mol^{-1}}$ for He), p is pressure, and T is an effective gas temperature such that (for parallel surfaces)

$$\frac{1}{\sqrt{T}} = \frac{1}{2}\Big(\frac{1}{\sqrt{T_1{}'}} + \frac{1}{\sqrt{T_2{}'}}\Big). \tag{3.29}$$

For nested surfaces of substantially differing areas, T will be weighted toward the temperature of the outer surface. The factor $G = a_1 a_2/(a_1 + a_2 - a_1 a_2)$ can also be modified for such geometries (see below).

Unfortunately, accomodation coefficients a are not well characterized for many surfaces, gases and temperatures. For He on very clean metal surfaces, a can be as low as $\sim 10^{-2}$, but for most cases $a > 0.2$ [45, 87]. For estimation purposes, one can use $a \approx \frac{1}{2}$ and simplify Eq. 3.28 to

$$\dot{q} = b \cdot \frac{p}{1\,\mathrm{Pa}} \cdot \frac{(T_2 - T_1)}{\sqrt{T \cdot 1\,\mathrm{K}}} \cdot \frac{\mathrm{W}}{\mathrm{m}^2}\,, \tag{3.30}$$

where the constant b takes the approximate values 14 for ^{3}He and 12 for ^{4}He.

3.3.2 Radiation

The heat of thermal electromagnetic radiation from a surface is given by the Stefan-Boltzmann equation,

$$\dot{q} = \epsilon \, \sigma \, T^4, \tag{3.31}$$

where $\dot{q}$ is the radiated power per unit area, $\sigma = 5.67 \times 10^{-8} \, \dfrac{\mathrm{W}}{\mathrm{m^2 K^4}}$ is the Stefan-Boltzmann constant, and emissivity ϵ is a property of the surface whose value can range between close to unity for a "black body" and as low as about 10^{-2} for highly polished metal surfaces [86]. Emissivity is related to reflectivity R by $\epsilon = (1 - R)$. Since R, defined as the ratio of reflected to incident power, is a function of wavelength, ϵ as defined by Eq. 3.31 is necessarily a function of temperature.

For the simplest case, two parallel surfaces of equal emissivity ϵ, at temperatures T_1 and $T_2 \leq T_1$, the net heat flux per unit area is

$$\dot{q} = \sigma G \, (T_1^4 - T_2^4) \tag{3.32}$$

where G is the geometric factor (Sec. 3.3.3) which in this case is $G = \dfrac{\epsilon}{2 - \epsilon}$.

Classical theory and some books [4] predict that emissivity scales as the square root of resistivity ρ according to $\epsilon = 0.365 \sqrt{\dfrac{\rho}{\lambda \cdot 1 \, \Omega}}$, but for pure metals with low residual resistivity, at low temperature the reflectivity is limited by the anomalous skin effect [88, 86], and ϵ for even highly polished cold metal surfaces is typically not smaller than $\sim 10^{-2}$.

The spectrum of black body radiation has a peak in wavelength at

$$\lambda_{max} = 2.9 \, \mathrm{mm} \cdot \frac{1 \, \mathrm{K}}{T}, \tag{3.33}$$

known as Wien's law [86]. For most materials at most temperatures, this gives a useful estimate of wavelength for most of the radiated power. Thus, for example, at 50 mK, the nominal temperature of the radiation shield surrounding the mixing chamber plate and experimental volume of our dilution fridge, $\lambda_{max} \simeq 6\,\mathrm{cm}$. The wavelength is long enough to interact with the geometry of parts and affect radiative heat transfer at this temperature.

Wien's law is typically quoted for the wavelength domain. However, since $\mathrm{d}\lambda = -\frac{c}{f^2}\,\mathrm{d}f$, the power spectral density in the frequency (or energy) domain peaks at a slightly different value, with $f_{max} \approx 59\,T\,\mathrm{GHz/K}$. Thus at 50 mK, $f_{max} \approx 3\,\mathrm{GHz}$.

3.3.3 Geometrical factors

Heat leaks between exposed surfaces in the vacuum space of a cryostat are due to two mechanisms, radiation and gas conduction in the free molecular regime. Both involve the random emission and reflection, or absorption and re-emission, of energy carriers. Accomodation coefficients and emissivities are analogous in that they quantify the fractional equilibration of the energy stream in each encounter with a surface. This leads to similar geometric factors.

The easiest cases to model are those in which one surface completely encloses the other. In a cryostat typically an enclosed surface **2** will be colder than surface **1** enclosing it. For geometries such as concentric cylinders or spheres, the probability that a photon emitted from the enclosing surface **1** hits the enclosed surface **2** is estimated by the area ratio $A = \frac{A_2}{A_1}$ where A_2 and A_1 are the areas of the two

surfaces. The fraction of the flux emitted by **1** that is absorbed by **2** is then $A\epsilon_2$ and the fraction that returns to **1** is $1 - A\epsilon_2$. Only a fraction ϵ_1 of the returning flux is absorbed while $1 - \epsilon_1$ of it is reflected, and $A\epsilon_2$ of *that* is absorbed by **1**, etc.

Therefore if $\sigma\, A_1\, \epsilon_1\, T_1^4$ is the total flux emitted by the enclosing surface **1**, and if we define $x \equiv (1-A\epsilon_2)(1-\epsilon_1)$ as the factor by which the reflection of the reflection is diminished, we have the total power absorbed by the enclosed surface **2** as

$$\dot{Q}_1 \;=\; A\epsilon_2 \times \sigma A_1\, \epsilon_1\, T_1^4 \times [1 + x + x^2 + ...] \;=\; \sigma A_2\, T_1^4\, \epsilon_1 \epsilon_2\, \frac{1}{1-x}. \tag{3.34}$$

Similarly, the total flux emitted by **2** is $\sigma A_2 \epsilon_2 T_2^4$, and that absorbed by **1** is $\sigma A_2 \epsilon_2 T_2^4 \dfrac{1}{1-x}\, \epsilon_1$. Hence the net heat transferred from **1** to **2** is

$$\dot{Q} \;=\; \sigma\, A_2\, G\, (T_1^4 - T_2^4), \tag{3.35}$$

where we have defined

$$G \;\equiv\; \frac{\epsilon_1 \epsilon_2}{1-x} = \frac{\epsilon_1 \epsilon_2}{1-(1-A\epsilon_1)(1-\epsilon_2)} = \frac{\epsilon_1 \epsilon_2}{\epsilon_2 + A\epsilon_1(1-\epsilon_2)} \tag{3.36}$$

By replacing emissivities ϵ_i with accomodation coefficients a_i in Eq. 3.36, we have the geometrical factor for molecular gas conduction.

This formula for G was derived under the assumption of no correlation between the direction of reflected radiation and its source, i.e. that each "bounce" is independent and the probability of hitting the inner surface is subject to the same area factor each time. This is true for diffuse reflection or for desorbtion of molecules. It is not true for specular reflection with a geometry, such as concentric surfaces, such that a ray that has transited between two surfaces is likely aligned to

continue bouncing between the two. In this case, the area ratio A can be taken out of the formula for G.

These calculations can in general provide only rough estimates of heat, particularly for mK temperatures. The geometries are idealized, and the formulas ignore such factors as the dependence of ϵ on temperature and wavelength, or the effect of electromagnetics and geometry when thermal peak wavelengths are the size of cryostat parts.

3.3.4 Shields

Another important geometry is that of n "floating" parallel planar shields interposed between parallel surfaces S_0 and S_{n+1} at temperatures T_0 and $T_{n+1} < T_0$. Here "floating" means that the heat fluxes in and out of an area element via vacuum heat leaks are large in comparison to any solid-solid thermal contact. Such shields are typically metallic, but need not be.

Assume that there is no significant leakage into, out of, or across ("short-circuiting") the system of shields. Further, assume that the temperature on both sides of one shield is the same. For each pair of facing surfaces assume that the net heat transfer is the sum of fluxes in each direction, each of which is the same function of the temperature of the emitting surface only (taking into account emissivities and multiple reflections). This would be the case, for example, if all the surfaces are similar.

If $\dot{Q}_k$ is the heat flux from a surface at temperature T_k, and $T_1 \ldots T_n$ are

the temperatures of the shields, then energy conservation requires in the steady state that $\dot{Q}_{k-1} - \dot{Q}_k = \dot{Q}_k - \dot{Q}_{k+1}$ for $1 \leq k \leq n$. It follows directly that $\dot{Q}_{n+1} - \dot{Q}_0 = n(\dot{Q}_k - \dot{Q}_{k-1})$, i.e. the net heat flux through the system of shields is $\frac{1}{n}$ of what it would be without them.

Although many books derive this principle by invoking the Stefan-Boltzmann law [89], as seen here the result is more general and should be valid not only for radiation but also approximately for molecular conduction. For radiation, the condition $\Delta T^4 = const.$ for the temperature steps leads to $T^3 \Delta T \approx const.$, so that the largest steps in absolute temperature occur between the lowest temperatures. When molecular conduction is important, the steps will be closer to $\Delta T = const.$.

Interposing "floating" shields will not be effective in the case of diffusive conduction, but *thermally anchored* shields may still be useful to intercept the vacuum heat leaks and create a cold environment.

3.3.5 Example calculation: Heat transfer to 50 mK shield

As an example, we can consider the vacuum heat leaks to the radiation shield surrounding the mixing chamber and experimental volume of our dilution refrigerator. This shield is thermally anchored to a point along the heat exchanger line between the still and mixing chamber which is expected to be at ∼50 mK. It consists of a copper cylinder 159 mm in diameter and 211 mm long with a cylindrical tailpiece 67 mm in diameter and 457 mm long. It fits snugly inside the stainless steel IVC with a 3–5 mm gap. Although the geometry is nested cylinders, they are close

enough in radius to use the parallel surface approximation with an area equal to that of the shield, which is (including end disks) $0.24\,\mathrm{m}^2$.

For molecular conduction, accomodation coefficients for He on clean metal surfaces can be as low as $\approx .02$ [45], but the surfaces here are not very clean and so I estimate $a = 0.2$, or $G = 0.11$. Then, using Eq. 3.30 with $p = 10^{-8}\,\mathrm{Pa}$, $T = 2.1\,\mathrm{K}$, $T_2 = 4.2\,\mathrm{K}$,

$$\dot{Q}_{mol} = \frac{A}{\mathrm{m}^2}\,3\,b\,G\frac{p}{\mathrm{Pa}}\frac{\Delta T/\mathrm{K}}{\sqrt{T/\mathrm{K}}}\mathrm{W} = 0.24 \times 42 \times 0.11 \times 10^{-8} \times \frac{4.1}{\sqrt{2.1}}\mathrm{W}$$

$$= 32\,\mathrm{nW},$$

where I used the value of b quoted in Section 3.3.1 for ^{3}He, which had incorporated $G = \frac{1}{3}$. Given the uncertainty in a, I estimate $\dot{Q}_{mol} = 10 - 100\,\mathrm{nW}$.

For radiation, typical values of ϵ for clean surfaces are 0.02 for Cu and 0.07 for stainless steel [4]. Although the surfaces in the cryostat are actually not very clean or highly polished, at $4.2\,\mathrm{K}$, $\lambda_{max} = 0.7\,\mathrm{mm}$. The surface oxides are much thinner than this, so the surfaces should be effectively clean at this wavelength. Using these values of ϵ, then, $G = 0.016$. Using Eq. 3.32,

$$W_{rad} = A\sigma G(T_2^4 - T_1^4) = 0.22\,\mathrm{m}^2 \times 5.7 \times 10^{-8}\,\mathrm{W\,m^{-2}\,K^{-4}} \times 0.016 \times (4.2\,K)^4$$

$$= 69\,\mathrm{nW}.$$

Given the uncertainty in ϵ, I estimate $W_{rad} = 20 - 200\,\mathrm{nW}$.

Is this amount of heat significant? Recalculating $W_\Sigma = W_{mol} + W_{rad}$ using the worst case $G = 1$ gives $W_\Sigma \approx 5\,\mu\mathrm{W}$. From the dimensions of the shield, with room temperature resistivity for Cu $17\,\mathrm{n\Omega\,m}$, and assuming a modest RRR of 50, I get

$R = 0.6\mu\Omega$ for the end-end electrical resistance of the cold shield. Using Eq. 3.3, I get for the thermal conductance

$$K = \frac{L_0\,T}{R} = \frac{2.44\times10^{-8}\,\mathrm{V^2\,K^{-2}} \times 0.05\,\mathrm{K}}{6\times10^{-7}\,\mathrm{V\,A^{-1}}} = 0.002\,\mathrm{W/K}.$$

As a loose upper bound, if a $5\,\mu$W heat load were applied across this conductance, the temperature rise would be $\frac{5\,\mu\mathrm{W}}{0.002\,\mathrm{W/K}} = 2.5\,\mathrm{mK}$. It seems unlikely that the heat load on the shield will cause a significant temperature increase.

3.3.6 Eddy current heating

When experiments at mK temperatures require high magnetic fields ($\sim$1 T and above), significant heating can be caused by eddy currents induced in copper and other low-resistivity metal components as the magnetic field is changed or as parts move or vibrate in the field. The latter mechanism could be beneficial if it dissipates vibrational energy in support structures, reducing motion transferred to the experiment. However, when copper is used extensively as a structural material, field sweeps of the order of 1 T can result in significant heating, and should be carried out slowly or may require additional cooldown time afterward.

The effect can be reduced by design techniques such as the incorporation of slits in bulk copper structures to interrupt the current. Unfortunately, this is not always practical, as for example with electromagnetic shielding which must be continuous.

A particular case is the electrical isolation can enclosing the STM in our design. This consists of a cylinder of OFHC Cu, 178 mm long by 58 mm diam., with 1.2 mm wall thickness, coaxial with the field and placed in its strongest region. A field

ramp of $\dot{B} = 1\,\mathrm{mT/s}$ will induce an emf around the circumference of the shield equal to $V = \dot{B}A = 2.6\,\mu\mathrm{V}$. The loop resistance, using $\rho = 0.34\,\mathrm{n\Omega\,m}$ for Cu at low temperature with RRR = 50, will be $290\,\mathrm{n\Omega}$. Power dissipated in the shield will then be $P = V^2/R = 23\,\mu\mathrm{W}$. This is a substantial load on the mixing chamber. Using the specific heat of Cu $c_p \approx 0.013\,\dfrac{T}{1\,\mathrm{K}}\,\mathrm{J\,kg^{-1}\,K^{-1}}$, for $T \approx 1\,\mathrm{K}$ [66], with the mass of the shield $m = 0.035\,\mathrm{kg}$, we have

$$\mathrm{d}T = \frac{P}{m\,c_p}\,\mathrm{d}t \quad\Longrightarrow\quad \frac{T}{1\,\mathrm{K}}\,\mathrm{d}T = \frac{23\,\mu\mathrm{W}}{0.035\,\mathrm{kg}\times 0.013\,\mathrm{J\,K^{-1}}}\,\mathrm{d}t$$
$$\Longrightarrow\quad T^2 = T_0^2 + 2\,t\times 0.051\,\mathrm{K^2\,s^{-1}},$$

where t is time and T_0 is the starting temperature. Thus, with no cooling, the 23 mJ deposited in the shield during a 1000 s field sweep at 1 mT/s would raise its temperature to around 10 K. Note that for a given field change, the total heat pulse is inversely proportional to the time taken, while for a long constant field ramp, with a constant cooling rate, the steady state temperature rise should be proportional to the square of the ramp rate, which is one reason for sweeping slowly.

3.4 Electrical noise and filtering

An ideal low-pass filter would pass all frequencies below some cutoff, and block all frequencies above. At least, we want attenuation to only increase with frequency. However, in mK-STM we generally use only low-frequency signals, so that our signal wires need to pass only up to ∼20 kHz. At the same time, 300 K radiation peaks at ∼18 THz. In order to prevent heating and noise effects, our "low pass" filter must therefore block frequencies up to nine decades above its passband.

Lumped-element filters are useful for frequencies up to a few GHz, but fail at higher frequencies due to parasitic capacitive, inductive and radiative coupling. For example, a 1 kΩ metal film resistor with 1 pF of parallel capacitance will have a capacitive reactance at 1 GHz of only 159 Ω. A surface mount component might have ten times lower capacitance, but that would be just as bad at 10 GHz.

In order to achieve high attenuation at high frequencies, it is necessary to screen the output of a filter from its input. For example, if a low-pass filter is built on a circuit board and mounted inside a metal box a few inches on a side, with wires to the board from rf connectors mounted on the box, at 10 GHz (3 cm) the box will act as a lossy cavity and couple the input and output ports regardless of the circuit. The general solution is elongate the attenuating elements, which therefore take the form of a lossy transmission line between physically separated input and output terminals. The need for dc insulation means that shielding around feedthrus and components can never be perfect. However, a conducting shell that is sufficiently close around the signal conductors will form a waveguide with a cutoff frequency f_c

which can be set fairly high. For example, given a cylindrical coaxial geometry with $r_{inner}/r_{outer} = 0.5$, the cutoff wavelength for the lowest mode is $\lambda_c \approx 2\, r_{inner}$ [90], so we have

$$f_c = \frac{c}{2\, r_{inner}\sqrt{\epsilon}}, \tag{3.37}$$

with c the speed of light and ϵ the dielectric constant of the insulator. Thus for $r_{inner} = 0.1\,\text{mm}$ and $\epsilon = 10$ we find $f_c \approx 500\,\text{GHz}$. A waveguide cutoff above 100 GHz is generally good enough since higher frequencies will be absorbed, reemitted and thermalized along the length.

Lossy transmission lines can be based on dissipation in conductors or dielectrics. Distributed RC filters use the capacitance of a shielded transmission line with resistive conductors. Dissipative dielectrics include metals powders and ferromagnetic materials. These high-frequency loss mechanisms may be combined with lumped-element RLC filtering to define the low-frequency cutoff, which may involve separate filters built out of lumped-element components, or may take advantage of the integral RLC characteristics of the lossy transmission line.

3.4.1 Dissipative dielectric filters

The metal powder filter, invented by Martinis, *et al.* [91], may be generalized as a lossy transmission line in which the loss is due to electromagnetic interaction with a medium which is dissipative at high frequencies and which fills the cavity space between the conductor and the outer body. The conductor can be chosen for low (or zero) dc resistance. Martinis used copper powder as a dissipative medium,

leading to this type of filter being commonly known as a "copper powder filter." However, other investigators [92, 93, 94, 95] have found alloys such as bronze and stainless steel powders to be more effective at low temperatures. Recently, several groups [96, 97] have reported the use of magnetic materials such as ferrite powders in polymer matrix. The coupling is far stronger and provides far higher attenuation per unit length, enabling long coiled wires to be replaced with short, impedance-matched striplines.

In Martinis-style metal powder filters, the metal grains are typically 10-100 μm in size. The native oxide layer at the surface of each grain insulates to low voltages, and microwave energy can penetrate into the metal powder matrix because it is insulating on the scale of a wavelength. Within each metal grain, just below the oxide layer, eddy currents are excited which act to cancel the electromagnetic field and thus exclude it from the interior of the metal. These currents decay exponentially into the bulk metal with a length scale δ called the skin depth. The total surface current required to cancel the field is determined by the field intensity, therefore applying $W = I^2R$, the formula for power dissipation in a resistance R carrying a current I, we expect that the power dissipation will be proportional to the ratio of resistivity to skin depth,

$$w \propto \frac{\rho}{\delta} \equiv R_s \tag{3.38}$$

which defines the surface resistance R_s, where ρ the resistivity of the metal, and

$$\delta = \sqrt{\frac{\rho}{\pi f \mu}} \tag{3.39}$$

is the skin depth[4] at frequency f for a metal with magnetic permeability μ. For Cu at room temperature, $\delta = 6.6\,\mu$m at 100 MHz [99].

An explicit calculation of power loss per unit area of a plane metal surface subject to a tangential magnetic field $H_0 e^{-2\pi i f t}$ [100, 99] finds

$$w = \frac{1}{2} H_0^2 \sqrt{\pi f \mu \rho} = \frac{1}{2} J_s^2 R_s \tag{3.40}$$

in agreement with this argument. Here J_s is the surface current and is equal in magnitude to H_0, the magnetic field intensity tangential to the surface. Since H_0 is locally varying over the surface of each grain as well as dependent on its location and the overall geometry of a filter, it would be hard to use Eq. 3.40 to directly calculate the total attenuation of a filter (also, the plane approximation would be invalid at low frequencies). However, since we know that $H_0^2 \propto P_{in}$, where P_{in} is power input to a filter, Eq. 3.40 tells us how power loss in the metal grains depends on frequency, resistivity and permeability, assuming the skin depth is less than the particle radius.

If we consider a filter as divided into n equally-constituted sections, taking the limit as $n \to \infty$, the power lost in each section is

$$W_k = P_k \frac{\alpha R_s}{n} \tag{3.41}$$

for some unknown coupling constant $\alpha \ll R_s^{-1}$, where P_k is the power input to section k from section $k-1$. By energy conservation, neglecting the possibility of

[4]The anomalous skin effect [98], which occurs at low temperatures when the mean free path of electrons exceeds the classical skin depth, is not relevant here since powder filters typically use low-purity or alloy metals.

reflection,

$$P_{k+1} = P_k - W_k = P_k\left(1 - \frac{\alpha R_s}{n}\right). \tag{3.42}$$

Taking the limit, and defining $\beta \equiv \alpha\sqrt{\pi}/\ell$, we obtain

$$\frac{P_{out}}{P_{in}} \;=\; \lim_{n\to\infty}\left(1 - \frac{\alpha R_s}{n}\right)^n \;=\; \exp(-\alpha R_s) \;\equiv\; \exp(-\beta\ell\sqrt{f\mu\rho}\,) \tag{3.43}$$

as the functional form of the high-frequency attenuation for a filter of length ℓ. Note that the definition of β serves to eliminate $\sqrt{\pi}$ and introduce ℓ, and the purpose of Eq. 3.43 is just to show some of the dependence of the attenuation on some variables. However, β will depend on details of the filter geomtery, particle size and density, and other factors, possibly including some of the variables appearing in Eq. 3.43. In the latter case, Eq. 3.43 will only approximate the dependence on these variables.

Equation 3.43 does not appear to have been reported in the literature on metal powder filters. Usually such filters are made to have such high attenuation that they hit the noise floor of typical network analyzers above about 1 GHz, making it hard to measure the attenuation at high frequency. Also, the filters are subject to resonances which can affect the attenuation curve where it is measurable.

Milliken *et al.* [94] observed apparent exponential behavior for their 50 Ω straight-wire powder filters, or $P_{out}/P_{in} \propto \exp(-f/f_c)$. Their data are shown in Fig. 3.1. In contrast, measurements of a coiled-wire powder filter made in our lab (Fig. 5.4, Chapter 5) are consistent with $P_{out}/P_{in} \propto \exp(-(f/f_c)^\gamma)$ with $\gamma \approx 0.63$. Both filters used similar (perhaps not identical) spherical, -325 mesh, 70/30 Cu/Sn bronze powder, which Milliken *et al.* found to provide the best attenuation out of several types they tested. Figure 3.1(A) shows an SEM image of the material, taken

in our lab. I do not have resistivity data for this particular bronze, but estimating $\rho \approx 40\,\mathrm{n\Omega\,m}$ based on data for similar materials [101], I find $\delta \approx 3\,\mu\mathrm{m}$ at 1 GHz. This is about the diameter of the smaller particles seen in Figure 3.1(A), suggesting that, in addition to geometrical resonances of the filter assembly, the particle size distribution may well affect the attenuation for $f \lessapprox 1\,\mathrm{GHz}$. Eq. 3.43 should then be better obeyed at higher frequencies, but verifying this would require further study, including the preparation of short (leaky) filters so that their high-frequency attenuation could be measured.

As seen in Fig. 3.1(B), Milliken *et al.* found that the bronze powder (BZ) provides better attenuation than Cu powder even at 300 K, while at 4 K the difference is even more pronounced. This is presumably due to the Cu having lower resistivity to begin with, and even lower residual resistivity at low temperature (the higher resistivity of alloys is primarily due to disorder, and does not vary much with temperature). Other groups [92, 95] have reported better results using stainless steel powders.

Martinis *et al.* [91] originally used "copper powder with a grain size of about $30\,\mu$m." They reported potting the filters with Stycast 2850 epoxy after filling with Cu powder "to ensure good thermal contact." Later authors have reported mixing the epoxy with the metal powder before injecting the mixture into the filter assembly. The epoxy fills the voids between metal grains and provides better cooling of the wire, at the expense of some attenuation since the density of metal particles is slightly reduced. Milliken *et al.* found that attenuation depends strongly on mixing as much metal as possible into the epoxy, limited ultimately by the stiffness of the

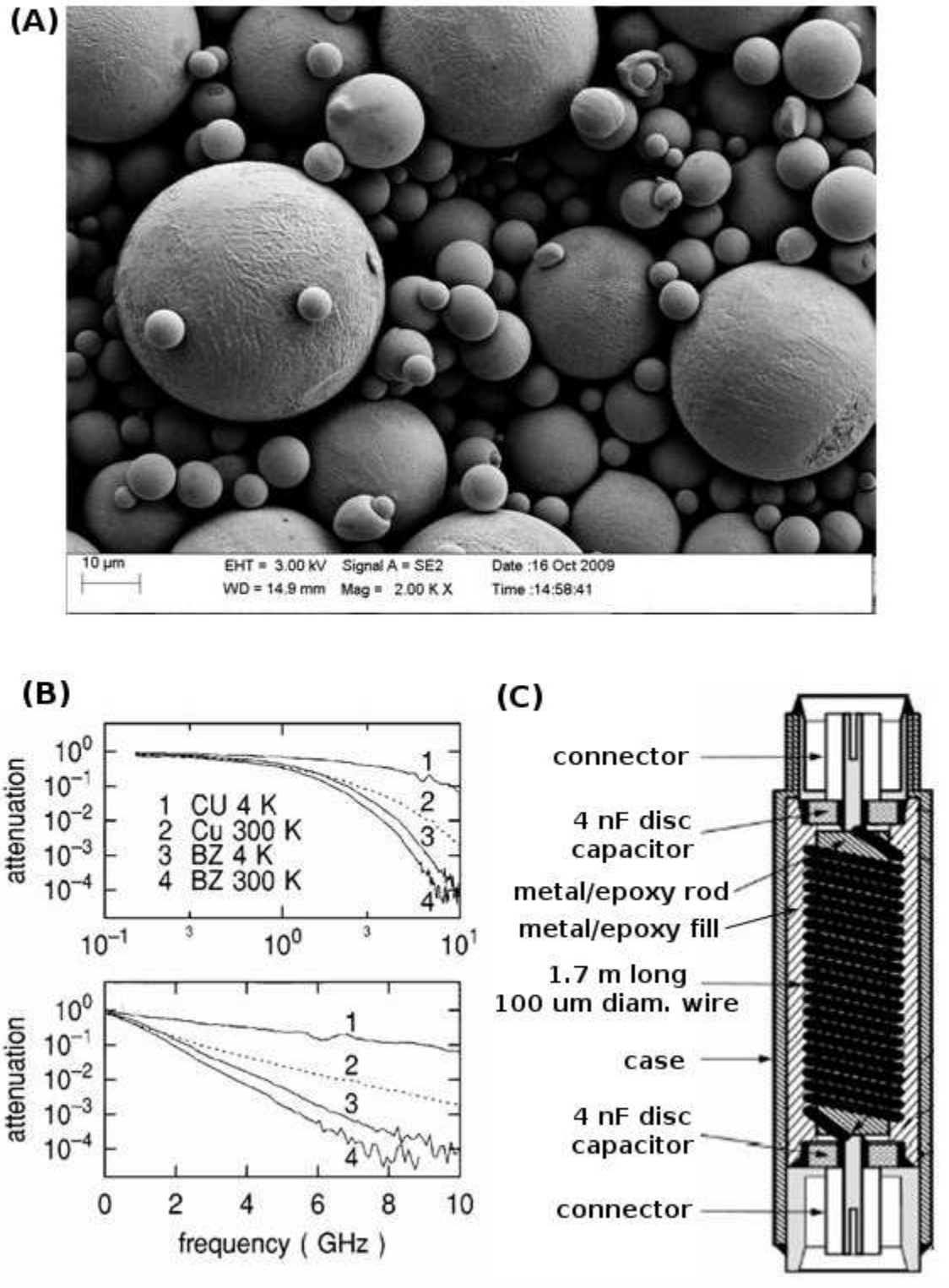

Figure 3.1: A. SEM image of a 30/70 Sn/Cu bronze powder. B. Attenuation performance of the same type bronze powder at 300 K and 4 K, compared with Cu powder, from [94]. The Cu powder's RRR means loss of attenuation at low temperature. C. A recent high-performance pi/powder filter design [95].

resulting paste [94].

Stycast 2850FT is an epoxy filled with grains of an unreported but hard, crystalline material. Its thermal conductivity in the mK range is not particularly high: $9.2 \times \left(\frac{T}{1\,\mathrm{K}}\right)^{2.65} \frac{\mathrm{mW}}{\mathrm{m{\cdot}K}}$ [60, 55], four times lower at 1 K than the unfilled Stycast 1266, (which also exhibits a lower exponent, as expected for disordered polymers). Popular legend claims the thermal contraction of 2850FT is matched to Cu, but in fact its thermal contraction integral from 300 to 4 K, $\frac{\Delta\ell}{\ell} = 0.44\%$, is higher than that of Cu (0.324%) or of most metals, but much lower than pure epoxies ($\gtrsim 1\,\%$). This lower thermal contraction is the principal advantage of mixing the metal powder with 2850FT instead of an unfilled epoxy. Otherwise, stresses developed during thermal cycling can crack the metal/epoxy, potentially breaking the wire.

The relatively weak eddy current coupling of Martinis-style filters means that typically 1–4 m of wire needs to pass through the metal powder to provide adequate attenuation. The only practical way to do this in a filter of reasonable dimensions is with tightly coiled fine wire. Copper wire is often used, or Cu-clad NbTi. Some people fashion freestanding coils and then fill them with powder or metal/epoxy, but this results in poor control of the geometry and characteristics. It is better to wind the coils on pre-cast rods of metal/epoxy. Lukashenko and Ustinov [95] have reported very reproducible, compact ($\sim$1 in. length), high performance filters using 0.1 mm diameter Cu wire wound on pre-cast rods with no space between turns (Fig. 3.1). They add capacitors at either end, exploiting the inductance of the coil to place an LC pi-filter effectively in series with the inductively-coupled microwave dissipation.

Coiled-wire filters have large inductances and usually exhibit unwanted resonances as well as creating a severe impedance mismatch. Milliken *et al.* developed coaxial straight-wire filters with 50 Ω impedance, useful for wideband time-domain measurements, but with 6 in. length these filters achieved only 20 dB of attenuation at 2 GHz [94]. Martinis-style filters are mostly used for dc or low frequency wiring, or for transmitting rf signals when multiple reflections and attenuation are not problematic.

Another approach to filter construction is to start with a Minicircuits LC barrel filter assembly [102]. These are available with a range of cutoff frequencies up to around 1 GHz, and are engineered for 50 Ω impedance within their passband, with a steep rolloff. Their attenuation drops at higher frequencies due to parasitic capacitances and transmission via the cavity space around components and conductors. To reduce the latter, the barrel can be filled with metal/epoxy through holes drilled in its side. About -70 dB of attenuation from 2-40 GHz has been achieved this way using Cu powder mixed 50 % by weight with Stycast 1266 [103].

A recent development, at least in low-temperature physics, is the use of ferromagnetic or ferrimagnetic microwave absorbing materials, such as Eccosorb [104] silicones and epoxies loaded with carbonyl iron or ferrite [96, 97]. These materials are much stronger microwave absorbers than nonmagnetic metal powders, and can provide adequate attenuation in filters constructed as short, impedance-matched striplines. Eddy current losses are expected to be higher given the higher resistivity and permeability of these materials, and hysteresis losses may play a role also. Carbonyl iron appears to be the better absorber above about 10 GHz, while ferrites

work better in the 1-10 GHz range [105]. The two can be mixed to achieve optimum overall performance.

Whereas the 50 Ω coaxial metal powder filters reported by Milliken *et al.* achieved about 5.9 dB of attenuation, at 10 GHz, per cm of length, a ferromagnetic stripline filter, designed for 50 Ω impedance at low frequencies, achieved > 30 dB/cm [96]. This means that very compact, impedance-matched filters can be made quite easily. However, the behavior of these filters at frequencies above 40 GHz has not been reported, and will depend on the loss characteristics of the absorbing materials at higher frequencies, which in the case of Eccosorb are also not reported by the manufacturer.

3.4.2 Dissipative conductor (distributed RC) filters

Perhaps the simplest type of low-pass filter is the lumped-element RC network with resistance R and capacitance C (Fig. 3.2(A)), for which, with $\omega \equiv 2\pi f$

$$\frac{V_{out}}{V_{in}} = \frac{(i\omega C)^{-1}}{R + (i\omega C)^{-1}} = \frac{1}{1 + i\omega RC} \tag{3.44}$$

provided $|Z_{load}| \gg (\omega C)^{-1}$. The filter is not impedance matched, but if $Z_{out} = Z_{in}$ and is fixed, then the power gain ratio is just

$$\frac{P_{out}}{P_{in}} = \frac{1}{1 + (\omega RC)^2}. \tag{3.45}$$

Due to waveguide coupling and parasitic capacitance across the resistor, such a circuit becomes ineffective at high frequencies, but can be replaced by a lossy transmission line in the form of a distributed RC circuit (Fig. 3.2(B)). For such a

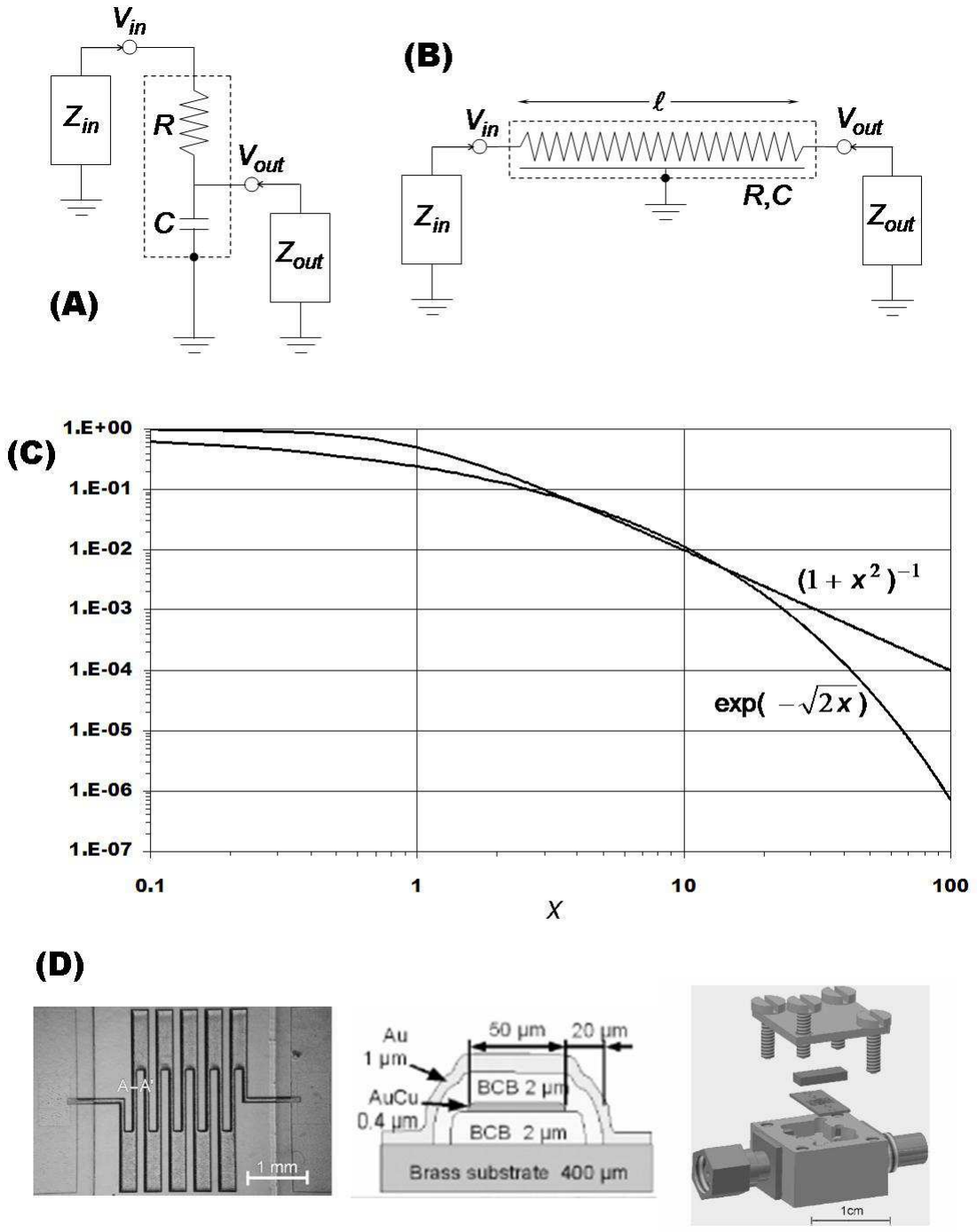

Figure 3.2: (A) Simple RC filter circuit; (B) Distributed RC filter circuit. C. Frequency dependence of P_{out}/P_{in} for RC filter ($(1+x^2)^{-1}$, where $x \equiv \omega RC$) and distributed RC filter ($\exp(-\sqrt{2x})$). D. Details of le Sueur's [106] design for microfabricated DRC filters, showing the chip layout, meander cross section, and housing.

line, neglecting inductance (which is not generally valid), the complex propagation constant γ is [99]

$$\gamma = \sqrt{i\omega RC/\ell^2} \tag{3.46}$$

where R and C are the total resistance and capacitance, and ℓ the total length. The voltage attenuation constant per unit length is $\alpha = \mathrm{Re}(\gamma)$ [99], i.e.

$$\frac{P_{out}}{P_{in}} = \exp(-2\alpha\ell) = \exp(-\sqrt{2\omega RC}). \tag{3.47}$$

Comparing Eqs. 3.45 and 3.47 (Fig. 3.2) shows that, in the high-frequency limit, the distributed RC is more effective than the lumped RC circuit of the same total resistance and capacitance, even without considering parasitic reactances and stray coupling.

One of the attractions of distributed RC filters is that, provided the shielding is tight enough to prevent leakage or propagation down its length (up to some waveguide cutoff which in general can be set quite high), this type of filter does not suffer from the resonances at low frequencies and loss of attenuation at very high frequencies ($\gtrsim 100\,\mathrm{GHz}$) that affect metal powder filters. Attenuation is only expected to increase with frequency, since the loss mechanism is just the resistance of the conductors combined with the capacitance between them. The surface resistance of the conductors only increases with frequency due to the skin effect, not accounted for in Eq. 3.47), while the dielectric constant ϵ, and hence the capacitance, may vary with frequency, but is bounded below by $\epsilon \geq 1$.

Vion *et al.* [107] introduced distributed RC filters to the literature on single electron devices, in the form of a resistive meander line microfabricated on a chip.

They used an oxidized Si chip as substrate, deposited an Au ground plane, Si_3N_4 insulating layer, and AuCu meander with 1.5 kΩ total resistance and 20 pF total capacitance to ground. They topped this with another Si_3N_4 insulating layer, and mounted the chip in a close-fitting housing with SMA connectors. An indium seal across the top of the insulated meander line served to reduce stray coupling of the input and output terminals. However, successive folds of the meander line were not shielded from each other. Courtois *et al.* [108] described similar filters, using CuNi meander and straight lines deposited directly on a Cu block with a spun-on PPQ (polyphenylquinoxaline) resist layer as insulator.

Le Sueur and Joyez [106, 109] developed an improved method for microfabricated RC filter construction (Fig. 3.2), depositing AuCu on a brass substrate with BCB (benzocyclobutene) photoresist as a dielectric. They insulated the top of the meander with BCB and stripped the dielectric between folds so that an Au layer, deposited on top of the insulator, contacted the brass substrate between folds to form a shield all the way around the meander line, shielding each fold from the next and ensuring a very high waveguide cutoff. Alternating narrow and wide sections of the meander also served to increase reflection at high frequencies, a technique known as stepped-impedance filtering [110].

The resulting filters are compact ($\sim$1 cm^3), have total resistance 77 Ω and capacitance 80 pF. Two were used in each line of le Sueur's mK-STS system, one at 4 K and one at 30 mK. 25-line filter banks, and pair filters with triaxial connectors for twisted-pair wiring, were also made. An important advantage of these microfabricated RC filters is that, due to the thinness of the dielectric, and the use of

AuCu, a normal metal with low thermal contact resistance, the filters provide good thermal grounding for the wires.

Another popular form of distributed RC filter, introduced by Zorin [90], is based on Thermocoax [111], a resistive coaxial cable normally intended for use as a high-temperature heating element.

Although these cables are available in a range of sizes with different materials, for this purpose the best choice is the smallest diameter, 0.5 mm, with 304L stainless steel shield. The center conductor is 80/20 NiCr, and the dielectric is tightly packed, powdered MgO. The capacitance is high, 490 pF/m, and the dc resistance of the inner conductor is 50 Ω/m. At high frequencies the resistance is enhanced by the skin effect. To account for this, R in Eq. 3.47 can be replaced by

$$R_{effective} = \frac{\ell}{2\pi r_1} R_s = \frac{\ell}{2\pi r_1} \sqrt{\pi f \mu \rho}\,, \tag{3.48}$$

where r_1 is the radius of the inner conductor. By Zorin's estimate, cutoff for the lowest waveguide mode is above 0.5 THz. Higher frequencies are still strongly attenuated by the resistive conductors and will thermalize along the length of the cable. Thus, Thermocoax filters exhibit a smooth rolloff and reliable high frequency attenuation.

Drawbacks of Thermocoax include the difficulty of cutting the shield to expose the inner conductor without breaking it, and of soldering NiCr and SS304, which requires the use of acid flux which can cause corrosion and electrical leakage. The MgO powder is hygroscopic and develops significant leakage at room temperature when it has aborbed moisture (let alone acid). The leakage current is noisy (Sec. 5.2.6) and

progressively worsens when leakage currents are allowed to flow at high voltage, so that if Thermocoax is used with high-voltage lines, room temperature testing may lead to a permanent failure. Therefore it is necessary to keep the Thermocoax dry during assembly and to seal finished cables in order to keep water out.

Another issue is thermalization of Thermocoax cable at low temperature. Mineral powders (dry and in vacuum) have sometimes been used for cryostat (thermal) insulation [89]. As shown in Sec. 3.5.4, the radial thermal conductance k_r of the insulation of 0.5 mm diameter Thermocoax at low temperature may be estimated as $k_r \lesssim 2.3\times10^{-3}\,(T/\mathrm{K})^3\,\mathrm{W\,m^{-1}K^{-1}}$. For Thermocoax with its shield anchored at 30 mK, this implies a 10 mK temperature rise for $P \lesssim 6\times10^{-10}\,\mathrm{W/m}$ of Joule heating, or a current of $I = \sqrt{P/49\,\Omega\mathrm{m}^{-1}} \lesssim 3.6\,\mu\mathrm{A}$. Thus, at the lowest temperatures, even small currents can cause significant heating of Thermocoax filters.

However, as also shown in Sec. 3.5.4, the length of Thermocoax that is required to be anchored at low temperature in order for the inner conductor to thermalize is not necessarily long. I estimate that two 1/e thermalization lengths at 30 mK would be $\sim$3 cm.

Finally, a relatively new type of distributed RC filter uses twisted pairs of normal or superconducting wire inside a close-fitting shield. Cu foil tape is used for the shield, and by pressing many parallel twisted pairs between pieces of the tape, multi-pair ribbons can be prepared. This type of filter offers the advantages of integrating the filter function into the length of the wiring and of not requiring that the inductive pickup immunity of twisted pairs be sacrificed in order to run the conductors through separate filters.

Spietz *et al* [112] reported using 100 μm diameter manganin wire pairs with Cu adhesive tape folded in thirds over up to "10s" of the pairs at once. After folding the tape over the pairs, they used a "rolling pin" (presumably rubber) to press it into a form-fitting cover over the pairs, ensuring good shielding and relatively high capacitance, 200 pF/m to the shield and 51 pF/m between the conductors. Together with the inductance and resistance of the wire pairs, they achieved in the neighborhood of 60 dB/m of attenuation at 1–40 GHz.

Bluhm *et al* [113] improved on this concept with the use of custom wire consisting of 200 μm OD CuNi with a 50 μm diameter NbTi core. At microwave frequencies the skin effect forces the current into the resistive outer shell of CuNi, providing high attenuation with zero dc resistance.

3.5 Thermalization of wiring

3.5.1 Thermalization of a coaxial cable

At millikelvin temperatures the thermal conductivity of most insulators is orders of magnitude lower than that of even highly resistive normal metals. Thus the outer shield of a coaxial cable coming from a higher temperature may need to be in contact with a thermal anchor for a considerable length at a lower temperature in order for the inner wire to thermalize.

Heat flow in the coax can be modeled (Fig. 3.3) by axial heat conductances K_w and K_s for the wire and shield, and a radial heat conductance through the dielectric k_d per unit length of the coax. I assume that the temperatures T_w and T_s of the wire

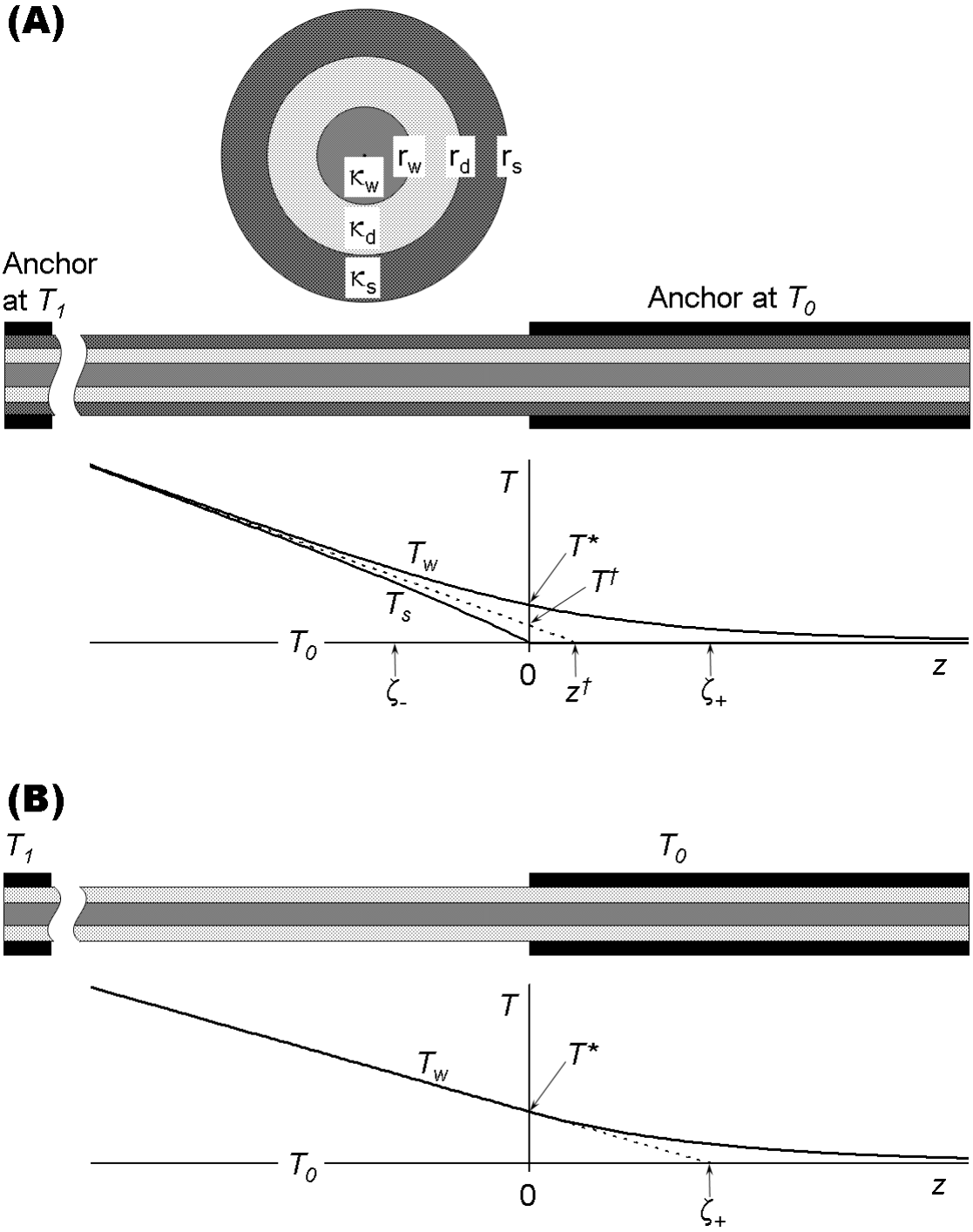

Figure 3.3: (A) Thermalization of a coaxial cable. The cable, with cross section as shown, is anchored at temperature T_1 for some $z \ll 0$ and at T_0 for $z \geq 0$. The temperatures T_w and T_s of the wire and shield are plotted; the dashed line is $T_{-\infty}$ (see text). (B) The simpler case of an unshielded, insulated wire.

and shield are functions of the axial dimension z only, whereas the temperature of the dielectric T_d is a function of both z and radius r. Also, I neglect the dependence of thermal conductivity on temperature, and assume constant conductivities which are the values at some mean temperature within the range of z in which the model operates; the results will clarify the conditions under which this approximation is valid.

The heats conducted axially by the wire and shield, $\dot{Q}_w$ and $\dot{Q}_s$ are given by

$$\dot{Q}_w = -K_w \frac{\mathrm{d}T_w}{\mathrm{d}z}\,, \quad \text{and} \quad \dot{Q}_s = -K_s \frac{\mathrm{d}T_s}{\mathrm{d}z}\,. \tag{3.49}$$

With $r_w,\ r_d$, and r_s the outer radii and $\kappa_w,\ \kappa_d$ and κ_s the thermal conductivities of the wire, dielectric, and shield materials,

$$K_w = \pi\, r_w^2\, \kappa_w\,, \quad \text{and} \quad K_s = \pi(r_s^2 - r_d^2)\, \kappa_s\,. \tag{3.50}$$

If $\dot{q}_r$ is the total radial heat per unit length, we can write

$$\frac{\partial T_d}{\partial r} \;=\; \frac{\dot{q}_r}{2\pi r \kappa_d} \quad \Longrightarrow \quad T_d(r,z) \;=\; \frac{\dot{q}_r}{2\pi\kappa_d}\ln(r) \;+\; C\,. \tag{3.51}$$

If thermal contact resistance (Sec. 3.2) is a significant factor, there will be a jump in temperature at the inner and outer surfaces of the dielectric, given by $\Delta T \;=\; \dot{q}_r \tilde{R}_c (2\pi r)^{-1}$, where $\tilde{R}_c$ is the area-independent thermal contact resistivity. In principle, $\tilde{R}_c$ could be different for the wire-dielectric and shield-dielectric interfaces, so using $\tilde{R}_c^{wd}$ and $\tilde{R}_c^{sd}$ to distinguish these cases, we have

$$\begin{aligned} T_s \;&=\; T_w + \dot{q}_r \cdot k_r\,, \text{ where} \\ k_r \;&\equiv\; \left[R_c^{wd} + R_d + R_c^{sd}\right]^{-1} \;\equiv\; \left[\frac{\tilde{R}_c^{wd}}{2\pi r_w} \;+\; \frac{\ln(r_d/r_w)}{2\pi\kappa_d} \;+\; \frac{\tilde{R}_c^{sd}}{2\pi r_d}\right]^{-1}. \end{aligned} \tag{3.52}$$

To construct a simple model predicting $T_w(z)$ and $T_s(z)$, I assume (Fig. 3.3) that the shield is in contact with the anchor at temperature T_0 for $z \geq 0$. Thus, for all $z \geq 0$, $T_s = T_0$. I define $T^* \equiv T_w(0) > T_0$, while for $z \to +\infty$, $T_w \to T_0$. Energy conservation demands that, for $z > 0$,

$$\frac{\mathrm{d}\dot{Q}_w}{\mathrm{d}z} \;=\; -\dot{q}_r \,, \tag{3.53}$$

whence, applying Eqs. 3.49 and 3.52,

$$K_w \, \frac{\mathrm{d}^2 T_w}{\mathrm{d}z^2} \;=\; (T_w - T_0)\, k_r \,, \tag{3.54}$$

whence

$$\frac{\mathrm{d}^2 T_w}{\mathrm{d}z^2} \;=\; \frac{T_w - T_0}{\zeta_+^2} \,, \quad \text{where} \quad \zeta_+ \;\equiv\; \sqrt{\frac{K_w}{k_r}}. \tag{3.55}$$

Solving, for $z \geq 0$,

$$T_w \;=\; T_0 \;+\; (T^* - T_0) \exp(-z/\zeta_+). \tag{3.56}$$

For $z \to -\infty$, $T_w \to T_{-\infty}$ and $T_s \to T_{-\infty}$, where

$$T_{-\infty}(z) \;\equiv\; T^\dagger \;+\; \tau \, |z| \,. \tag{3.57}$$

Here $T^\dagger$ is a (so far) unknown temperature between T_0 and T^*, and $\tau \equiv \lim\limits_{z \to -\infty} \left| \dfrac{\mathrm{d}T_s}{\mathrm{d}z} \right|$ is the temperature gradient for $z \ll 0$. Note that $\dot{Q} \equiv \tau \, (K_w + K_s)$ is the total heat conducted along the coax from the higher to the lower temperature stage. Energy conservation demands that, for all $z < 0$, $\dot{Q} = \dot{Q}_w + \dot{Q}_s$, and that

$$\frac{\mathrm{d}\dot{Q}_w}{\mathrm{d}z} \;=\; -\dot{q}_r \;=\; -\frac{\mathrm{d}\dot{Q}_s}{\mathrm{d}z} \,. \tag{3.58}$$

Applying Eqs. 3.49 and 3.52,

$$K_w \, \frac{\mathrm{d}^2 T_w}{\mathrm{d}z^2} \;=\; k_r \, (T_w - T_s) \;=\; -K_s \, \frac{\mathrm{d}^2 T_s}{\mathrm{d}z^2}, \tag{3.59}$$

and combining terms,

$$\frac{\mathrm{d}^2(T_w - T_s)}{\mathrm{d}z^2} \;=\; \frac{T_w - T_s}{\zeta_-^2}\,, \tag{3.60}$$

where, defining $\eta \equiv \dfrac{K_w}{K_s}$,

$$\zeta_- \;\equiv\; \sqrt{\frac{K_w\,K_s}{k_r(K_w + K_s)}} \;=\; \zeta_+(1+\eta)^{-\frac{1}{2}}\,. \tag{3.61}$$

Solving, for $z \le 0$,

$$T_w \;-\; T_s \;=\; (T^* - T_0)\,\exp(-|z|/\zeta_-)\,. \tag{3.62}$$

Noting that the second derivative of $T_{-\infty}$ (Eq. 3.57) is zero, and applying Eq. 3.59, I infer that, for $z \le 0$,

$$\begin{aligned} T_w \;&=\; T^\dagger \;+\; \tau\,|z| \;+\; \frac{1}{1+\eta}\,(T^* - T_0)\,\exp(-|z|/\zeta_-) \\ T_s \;&=\; T^\dagger \;+\; \tau\,|z| \;-\; \frac{\eta}{1+\eta}\,(T^* - T_0)\,\exp(-|z|/\zeta_-)\,. \end{aligned} \tag{3.63}$$

To find T^*, I apply the continuity of $\dfrac{\mathrm{d}T_w}{\mathrm{d}z}$ (energy conservation) at $z = 0$:

$$\begin{aligned} \left.\frac{\mathrm{d}T_w}{\mathrm{d}z}\right|_{z=0-} \;&=\; -\tau \;+\; \frac{1}{1+\eta}\,\frac{T^* - T_0}{\zeta_-} \;=\; -\tau \;+\; \frac{T^* - T_0}{\zeta_+\sqrt{1+\eta}} \\ =\; \left.\frac{\mathrm{d}T_w}{\mathrm{d}z}\right|_{z=0+} \;&=\; -\frac{T^* - T_0}{\zeta_+}\,; \end{aligned} \tag{3.64}$$

whence

$$T^* - T_0 \;=\; \frac{\tau}{\dfrac{1}{\zeta_+} + \dfrac{1}{1+\eta}\cdot\dfrac{1}{\zeta_-}} \;=\; \frac{\tau\,\zeta_+}{1 + (1+\eta)^{-\frac{1}{2}}}\,. \tag{3.65}$$

To find $T^\dagger$, in Eq. 3.63 I set $z = 0$ and $T_s(0) = T_0$, obtaining

$$T^\dagger - T_0 \;=\; (T^* - T_0)\,\frac{\eta}{1+\eta}\,, \tag{3.66}$$

and applying Eq. 3.65,

$$T^\dagger - T_0 \;=\; \frac{\tau\,\zeta_+}{1+(1+\eta)^{-\frac{1}{2}}}\cdot\frac{\eta}{1+\eta} \;=\; \frac{\tau\,\zeta_+}{1+\eta+\sqrt{1+\eta}}$$
$$=\; \tau\,\zeta_+\left[1-(1+\eta)^{-\frac{1}{2}}\right] \;=\; \tau\,[\zeta_+ - \zeta_-] \tag{3.67}$$

Finally, τ is generally not known directly, but rather, a section of coax of length ℓ stretches between the anchor at T_0 and another anchor at temperature $T_1 > T_0$. If $\ell \gg \zeta_-$, a condition for the validity of this model, then

$$\tau \;=\; \frac{T_1 - T_0}{\ell + z^\dagger}\,, \tag{3.68}$$

where $z^\dagger$ is the T_0 intercept of the $T_{-\infty}$ line (Fig. 3.3). Clearly,

$$z^\dagger \;=\; \frac{T^\dagger - T_0}{\tau}\,, \tag{3.69}$$

and using Eqs. 3.66 and 3.65,

$$T^\dagger - T_0 \;=\; (T^* - T_0)\,\frac{\eta}{1+\eta} \;=\; \frac{\tau\,\zeta_+}{1+(1+\eta)^{-\frac{1}{2}}}\cdot\frac{\eta}{1+\eta}\,. \tag{3.70}$$

Therefore,

$$z^\dagger \;=\; \frac{\zeta_+\,\eta}{1+\eta+\sqrt{1+\eta}} \;=\; \zeta_+\left[1-(1+\eta)^{-\frac{1}{2}}\right] \;=\; \zeta_+ \,-\, \zeta_-. \tag{3.71}$$

Collecting and rewriting the results, defining $\alpha \equiv \sqrt{1+\eta} = \sqrt{1+\,K_w/K_s}$, and $\zeta \equiv \zeta_+ = \sqrt{K_w/k_r}$, for $z \le 0$,

$$T_w \;=\; T_0 \,+\, \tau\left[|z| \,+\, \zeta\left\{1 - \frac{1}{\alpha} \,+\, \frac{1}{\alpha(1+\alpha)}\,\exp\Big(-\alpha\,\frac{|z|}{\zeta}\Big)\right\}\right]$$
$$T_s \;=\; T_0 \,+\, \tau\left[|z| \,+\, \zeta\left\{1 \,-\, \frac{1}{\alpha} \,-\, \Big(1-\frac{1}{\alpha}\Big)\exp\Big(-\alpha\,\frac{|z|}{\zeta}\Big)\right\}\right], \tag{3.72}$$

and for $z \geq 0$,

$$\begin{aligned} T_w &= T_0 + \tau \frac{\zeta}{1+\alpha^{-1}} \exp\Big(-\frac{z}{\zeta}\Big) \\ T_s &= T_0 \,. \end{aligned} \tag{3.73}$$

For practical purposes, the most useful of these results is the thermalization length ζ. One might have written this down directly, but working out the model provides clarity and confidence.

A further elaboration of these calculations would be to include the effect of temperature on the thermal conductivities of the materials. One might work out the cases for every combination of normal metal conductors with $\kappa \propto T$, superconductors with $\kappa \propto T^3$, polymer dielectrics with $\kappa \propto T^2$, and powdered mineral dielectrics with $\kappa \propto T^3$. However, assuming that one is only interested in ensuring adequate thermalization, the use of the simpler model with mean values for the conductivities is good enough provided the model self-consistently predicts $\dfrac{\mathrm{d}\kappa}{\mathrm{d}z} \lessapprox \dfrac{\kappa}{\zeta}$ for $|z| \lessapprox \zeta$.

3.5.2 Thermalization of an unshielded wire

The results of the previous section can be applied to the case of an unshielded, insulated wire by considering this as the limit $K_s \to 0$. In this case $\zeta_- \to 0$, and while this may seem to make Eq. 3.62 invalid, this just means that any difference in temperature between the wire and "shield" (outer surface of the insulation) vanishes

for $z < 0$. Also, $z^\dagger = \zeta_+$, and $T^\dagger = T^*$. Collecting and simplifying the results,[5]

$$\begin{aligned} T^* &= T_0 + T'_{-\infty}\,\zeta \\ T'_{-\infty} &= -\frac{T_1 - T_0}{\ell + \zeta} \\ z < 0: \qquad T_w &= T_0 + (z - \zeta)\,T'_{-\infty} \\ z \geq 0: \qquad T_w &= T_0 + (-T'_{-\infty}\,\zeta)\exp(-z/\zeta) \end{aligned} \tag{3.74}$$

where the surviving symbols have the same meanings as in Sec. 3.5.1.

3.5.3 Thermalization of CuNi and Cu microcoax

Kushino *et al.* [56] measured the lengthwise thermal conductivity of 0.33 mm diam. coaxial cable supplied by Coax Co. Ltd. of Japan [115], made of 70/30 CuNi inner and outer conductor with PTFE dielectric. Since I use similar coax from the same supplier but 0.4 mm diam. (type SC-040/50-CN-CN), I would like to use Kushino's and other data to estimate K_w, K_s, k_r, and ζ for the 0.4 mm CuNi coax. I would also like to estimate the same quantities for all-Cu microcoax which I used for the coldest wiring.

Unfortunately, the thermal contact resistance between the CuNi and PTFE is a substantial unknown. I will assume it may be similar to that between Cu and PTFE. Berman [83] measured R_c at 4.2 K for a 305 μm-thick, 1 cm diam. PTFE disk sandwiched bewteen Cu rods, under force of 220-1100 N, or pressures from 2.8–14 MPa. Subtracting the volume thermal resistance of the Teflon, Berman found that R_K^{-1} was roughly linear in the force (Table 3.4). Even in the highest-pressure

[5]Equivalent results, for the unshielded wire only, were obtained by Hust [114].

measurement, the contact resistance was 14% of the volume resistance. Assuming a T^{-3} dependence for R_K, and T^{-2} for R_v, the contact resistance would be expected to dominate the volume resistance at any temperature below ∼600 mK.

I have no way to determine the pressure under which the PTFE dielectric has been packed, much less the pressure remaining at low temperature. A reasonable guess might be that the manufacturer packs the PTFE to a good fraction of its yield strength, which various sources give as in the range of 15–25 MPa. However, the Young's modulus of PTFE, which gives a crude estimate of its compression under this pressure, is about 600 MPa [116] at RT. If I assume a packing pressure of 12 MPa, I predict about 2% compression. However, the thermal contraction of PTFE from RT to 4.2 K is a bit more than 2%, and that of Cu or CuNi about an order of magnitude lower. Therefore, it is impossible to know, on the basis of this information, whether the PTFE will still be under any pressure at all at low temperature.

Since the CuNi coax is made especially for cryogenic use, it is possible that the manufacturer has compressed the PTFE enough to ensure that some pressure and thermal contact remains at low temperature. However, the numbers seem to indicate that the pressure at low temperature will be at best a small fraction of the PTFE yield strength.

Even if the outer diameter of the cold PTFE has shrunk to less than the inner diameter of the shield, the two will be in contact at many points, particularly where the coax bends or has been pinched. The PTFE will have shrunk around the wire, so R_K^{wd} should be $\ll R_K^{sd}$ although the area of the wire-dielectric boundary is only $\frac{1}{3}$

that of the shield-dielectric boundary.

Berman's lowest-force measured value of R_c for one Cu-PTFE interface was 100 K/W at 4.2 K, with 50 lbf applied to a 1 cm diam. disk, or 2.9 MPa over an area of 7.8×10^{-5} m^2. This is about 10%–20% of the yield strength of PTFE and represents an optimistic estimate of pressure that might remain on the dielectric when cold. Using X_a to denote an unknown multiplier of this measured value of $\tilde{R}_c$, I have

$$R_c^{ds} \;=\; X_a \cdot 100\,\frac{\mathrm{K}}{\mathrm{W}} \cdot \left(\frac{T}{4.2\,\mathrm{K}}\right)^{-3} \cdot \frac{7.8\times10^{-5}\,\mathrm{m}^2}{2\pi\cdot 130\,\mu\mathrm{m}} \;=\; 700\,X_a \left(\frac{T}{\mathrm{K}}\right)^{-3} \frac{\mathrm{K\cdot m}}{W}\,.$$

A realistic range of possible values for X_a might be 0.3–300. The former value would imply that the PTFE when cold remains under pressure around half of that at RT, which seems unlikely. The latter would imply that overall effective contact would be as poor as if under a uniform pressure of 1 N/cm^2, which seems a worst case.

The volume thermal resistance of the dielectric R_d is given by (Sec. 3.5.1)

$$R_d \;=\; \frac{\ln(r_d/r_w)}{2\pi\kappa_d} \;=\; \frac{\ln(130\,\mu\mathrm{m}/40\,\mu\mathrm{m})}{2\pi\cdot 2.5\times10^{-3}\,(T/\mathrm{K})^2\,\mathrm{W\,K^{-1}m^{-1}}} \;=\; 75\left(\frac{T}{\mathrm{K}}\right)^{-2}\frac{\mathrm{K\cdot m}}{\mathrm{W}}\,.$$

Thus, even if the unknown factor X_a were as low as 0.1, meaning that the PTFE remained under high pressure even at low temperature, R_c^{ds} would be expected to dominate R_d at temperatures below 1 K. It seems more likely that factor X_a is large, e.g. in the range of 1–100. This would make contact resistance the only significant contribution to k_r^{-1} at low temperature.

The wire conductance is given by

$$K_w = \pi r_w^2 \kappa_w = \pi(40\mu\mathrm{m})^2 \cdot 0.073 \left(\frac{T}{\mathrm{K}}\right)^{1.1} \frac{\mathrm{W}}{\mathrm{m}\cdot\mathrm{K}}$$
$$= 3.7\times10^{-10} \left(\frac{T}{\mathrm{K}}\right)^{1.1} \frac{\mathrm{W}\cdot\mathrm{m}}{\mathrm{K}},$$

where the value used for κ_w interpolates between those found by Kushino [56] and Scott [59] (Table 3.1) for 70/30 CuNi.

For the thermalization length, if $X_a \gtrsim 1$ we have $k_r^{-1} \approx R_c^{ds}$, and

$$\zeta = \sqrt{\frac{K_w}{k_r}} = \sqrt{3.7\times10^{-10} \left(\frac{T}{\mathrm{K}}\right)^{1.1} \frac{\mathrm{W}\cdot\mathrm{m}}{\mathrm{K}} \cdot 700\, X_a \left(\frac{T}{\mathrm{K}}\right)^{-3} \frac{\mathrm{K}\cdot\mathrm{m}}{W}}$$
$$\approx 0.5\,\mathrm{mm}\,\sqrt{X_a} \left(\frac{T}{\mathrm{K}}\right)^{-1}.$$

At $T = 30\,\mathrm{mK}$, the thermalization length will be a problem if $X_a \gtrsim 10$, meaning $\zeta \gtrsim 5\,\mathrm{cm}$. At temperatures above 1 K, even with $X_a = 100$ we should obtain good thermal anchoring with a few cm of the coax clamped. However, clamping the coax sufficiently to deform it by a few percent may be sufficient to ensure that X_a is not too large. Therefore, it is not impossible that a few cm of clamping will be sufficient to achieve good thermal anchoring even at 30 mK.

For the all-Cu microcoax, Micro-Coax Inc. type UT-047C [117], the Cu is specified by the manufacturer as "cryogenic-grade" and probably has an RRR of around 100. At low temperature its thermal conductivity is thus expected to be about $140\,(T/\mathrm{K})\,\mathrm{WK}^{-1}\mathrm{m}^{-1}$. Thus, we expect

$$K_w = \pi r_w^2 \kappa_w = \pi\,(143\,\mu\mathrm{m})^2 \cdot 140\,\frac{T}{\mathrm{K}}\,\frac{\mathrm{W}}{\mathrm{m}\cdot\mathrm{K}} = 9\times10^{-6}\,\frac{T}{\mathrm{K}}\,\frac{\mathrm{W}\,\mathrm{m}}{\mathrm{K}},$$
$$K_s = \pi(r_s^2 - r_d^2)\kappa_w = \pi\,[(597\,\mu\mathrm{m})^2 - (470\,\mu\mathrm{m})^2] \cdot 140\,\frac{T}{\mathrm{K}}\,\frac{\mathrm{W}}{\mathrm{m}\cdot\mathrm{K}}$$
$$= 6\times10^{-5}\,\frac{T}{\mathrm{K}}\,\frac{\mathrm{W}\,\mathrm{m}}{\mathrm{K}},$$

and, making use of the same data, with an unknown factor X_b not necessarily of the same value as X_a for the CuNi coax, but falling in the same range,

$$R_c^{ds} \;=\; X_b \cdot 100\,\frac{\mathrm{K}}{\mathrm{W}} \cdot \left(\frac{T}{4.2\,\mathrm{K}}\right)^{-3} \cdot \frac{7.8{\times}10^{-5}\,\mathrm{m}^2}{2\pi \cdot 4.7{\times}10^{-4}\,\mathrm{m}} \;=\; 200\,X_b \left(\frac{T}{\mathrm{K}}\right)^{-3} \frac{\mathrm{K}{\cdot}\mathrm{m}}{W}\,.$$

There are two thermalization lengths,

$$\begin{aligned}\zeta \;&=\; \sqrt{\frac{K_w}{k_r}} \;=\; \sqrt{9{\times}10^{-6}\,\frac{T}{\mathrm{K}}\,\frac{\mathrm{W}{\cdot}\mathrm{m}}{\mathrm{K}} \cdot 200\,X_b \left(\frac{T}{\mathrm{K}}\right)^{-3} \frac{\mathrm{K}{\cdot}\mathrm{m}}{W}} \\ &\approx\; 4.2\,\mathrm{cm}\,\sqrt{X_b}\left(\frac{T}{\mathrm{K}}\right)^{-1},\end{aligned}$$

and

$$\zeta_- \;=\; \zeta\left(1+\frac{K_w}{K_s}\right)^{-\frac{1}{2}} \;=\; \zeta\left(1+\frac{9{\times}10^{-6}}{6{\times}10^{-5}}\right)^{-\frac{1}{2}} \;\approx\; \zeta\,.$$

Of course ζ_- turns out to be almost equal to ζ. It tells us the maximum distance between thermal anchoring points of the shield in order for the anchoring to be about as effective as continuous anchoring of the shield. As described in Section 5.2.4, I use the all-Cu coax only in the span from the filters mounted on the mixing chamber cold plate down to the STM itself. The Cu coax is well-anchored at 6 points along a length of about 45 cm, but it would be impractical to try to anchor it continually along the full length. The fact that ζ_- is long compared with the distance between anchoring points reassures me that continuous anchoring would be superfluous.

As this calculation shows, even if the unknown factor $X_b = 1$, which is optimistic (3 MPa pressure on the cold PTFE), at 30 mK $\zeta = 140$ cm. However, the objective here is not to cool the wire within the span which is thermally anchored before it continues to a lower temperature stage. Rather, we want to cool the wire in order to cool the heat source (the STM) at one end of it. The Cu coax is intended

to serve as the primary heat sink for the tip, sample, and piezo wires of the STM. Since ζ is long compared with the total length of the coax, it can be expected that the heat will be sunk along the full length.

However, it is unclear whether this method of heatsinking the STM will be adequate. For example, at 1 V bias with a tunnel gap resistance of 1 GΩ, we will have at least $P = 1\,\mathrm{nW}$ of dissipation, most of it in whichever electrode (tip or sample) is biased positive. To estimate the temperature rise ΔT, from a base temperature $T = 30\,\mathrm{mK}$, I assume that the heat is sunk over the full 45 cm of the Cu coax. The total thermal resistance of this heat sink should then be about the resistance of the length of the wire plus the full resistance between the wire and shield, the latter including R_c^{ds}. At 30 mK, for 45 cm of the Cu coax, these are:

$$\begin{aligned}
\tfrac{1}{2}\,K_w^{-1} \times 45\,\mathrm{cm} &= 5.6{\times}10^4\,(0.03)^{-1}\,\frac{\mathrm{K}}{\mathrm{W\,m}} \cdot 0.45\,\mathrm{m} = 8.3{\times}10^5\,\frac{\mathrm{K}}{\mathrm{W}} \\
R_c^{ds} \div 45\,\mathrm{cm} &= 200\,X_b\,(0.03)^{-3}\,\frac{\mathrm{K{\cdot}m}}{\mathrm{W}} \div 0.45\,\mathrm{m} = 1.6{\times}10^7\,X_b\,\frac{\mathrm{K}}{\mathrm{W}}\,, \\
R_d \div 45\,\mathrm{cm} &= \frac{\ln(470\,\mu\mathrm{m}/143\,\mu\mathrm{m})}{2\pi \cdot 2.5{\times}10^{-3}\,(0.03)^2\,\mathrm{W\,K^{-1}m^{-1}}} \div 0.45\,\mathrm{m} = 1.9{\times}10^5\,\frac{\mathrm{K}}{\mathrm{W}}\,.
\end{aligned}$$

Note that the thermal resistance of the wire is greater than that of the dielectric, but both are much smaller than the contact resistance even in the optimistic case $X_b = 1$. Since the thermal resistance of the dielectric is insensitive to the radius of the coax (depending only on the logarithm of r_d/r_w), if heatsinking is to be provided by coax it would be better to use thicker coax with a thicker wire. However, it remains that thermal contact between the dielectric and the shield is likely the major problem.

These results are not very encouraging, and suggest that some redesign may be needed in order to obtain better heat sinking of the STM. In fact, it is likely

that the STM body, which I did not work on, may need to be redesigned to provide lower-resistance thermal links to the coaxes, since the current design relies on thin Cu wires bonded with Ag-loaded epoxy. Ignoring that issue for now, with 1 nW dissipation, the temperature rise just in the Cu coax, if it is to serve as the heat sink, would be given by

$$\Delta T \;\approx\; 1\times10^{-9}\,\mathrm{W}\cdot[1\times10^{6}+1.6\times10^{7}\,X_b]\,\frac{\mathrm{K}}{\mathrm{W}} \;=\; (1+16\,X_b)\,\mathrm{mK}\,.$$

Evidently, a great deal will depend on the unknown factors X_a and X_b. These are unknown in that I have no way of predicting them in advance, but they are not entirely uncontrollable. It may be that some measures such as deliberately flattening the jackets of the coaxes, as well as bends, will significantly enhance thermal contact to the PTFE dielectric. This remains to be determined.

3.5.4 Thermalization of Thermocoax

Thermal conductivity for 80/20 NiCr, the center conductor material of Thermocoax, is poorly reported at low temperatures. As a high-concentration alloy, its electrical conductivity is almost independent of temperature [90]. Data published by Lakeshore Cryotronics Inc. [118] report κ about 6 times greater than predicted by the WFL law (Eq. 3.3) at 80 K and 20 K, but at 10 K and 4 K it trends back to within a factor of 3 of the predicted value. It may be expected that at lower temperatures the phonon contribution to κ, which scales as T^3, will vanish compared with the electronic contribution ($\propto T$), so WFL should be obeyed more closely. I take this as the best available prediction of κ for NiCr below 1 K. Thus, based on

$R = 49\Omega/\mathrm{m}$ [90], using Eq. 3.3, we have directly the thermal conductance K_w of the wire:

$$K_w \;=\; \frac{L_0 T}{R} \;=\; \frac{2.45\times10^{-8}\,\mathrm{W\Omega K^{-2}}}{49\,\Omega\mathrm{m}^{-1}}\,T \;=\; 5\times10^{-10}\,\frac{T}{\mathrm{K}}\,\mathrm{W\cdot m\cdot K^{-1}}\,. \tag{3.75}$$

Estimating the thermal conductivity of the dielectric is more difficult. As a pure crystalline electrical insulator, the thermal conductivity κ_s of solid crystalline MgO varies as T^3 at low temperature [119]. Its value at 1 K as "recommended" by Touloukian [7], based on extrapolation from Slack's [120] measurements on two samples at temperatures as low as 2.4 K, is $1.2\,(T/\mathrm{K})^3\,\mathrm{W\,m^{-1}K^{-1}}$. However, extrapolation from the two lowest-temperature points of what would appear to be the better-quality sample, which showed higher conductivity also at much higher temperatures, leads to $\kappa_s = 2.6\,(T/\mathrm{K})^3\,\mathrm{W\,m^{-1}K^{-1}}$, a number which is closer to Slack's prediction [120] from boundary and isotope scattering, and which agrees with the later measurements of Gardner and Anderson [119].

The MgO in Thermocoax consists of irregular grains which appear under microscopy to be about $1\,\mu$m in size (Fig. 3.4), packed to a volume fraction of 60% [111]. The thermal conductivity κ_p for the powder will certainly be lower than that of the solid, κ_s. At very low temperatures, particularly for small grains, boundary scattering will dominate, and the mean free path for the bulk within grains will be just the grain size. Since this is a constant, the temperature dependence of κ_p will be controlled by the phonon density, which is $\propto T^3$. The contact resistance between MgO grains should also be $\propto T^{-3}$ at low temperature [49, 66].

Figure 3.4: Electron micrograph of MgO powder in Thermocoax. A broad dispersion of particle sizes is evident. Small black box at left is 1 μm square.

From first principles, we expect [49]

$$\kappa_s = \frac{1}{3} C\, v\, \ell \tag{3.76}$$

where C here is the heat capacity per unit volume, v the phonon velocity and ℓ the phonon mean free path. The velocity of sound, measured warm, is 7.0 km/s [120]. Gardner and Anderson [119] measured C for single crystal MgO, at $T = 0.2$–10 K, and found $C \approx 0.37\,(T/\mathrm{K})^3\,\mathrm{Jm^{-3}K^{-1}}$. For the same crystal, with minimum dimension 3 mm, they found $\kappa = 2.6\,(T/\mathrm{K})^3\,\mathrm{W\,m^{-1}K^{-1}}$ over the range of $T = 0.06$–2 K, in agreement with Eqs. 3.76 for $\ell = 3$mm:

$$\kappa_s \;\approx\; \frac{0.37}{3}\left(\frac{T}{\mathrm{K}}\right)^3 \frac{\mathrm{J}}{\mathrm{m^3K}} \cdot 7\,\frac{\mathrm{km}}{\mathrm{s}} \cdot 3\,\mathrm{mm} \;=\; 2.6\left(\frac{T}{\mathrm{K}}\right)^3 \frac{\mathrm{W}}{\mathrm{m^{-1}K^{-1}}}\,.$$

This implies that for the bulk material, $\ell \geq 3$ mm. Therefore, for grains much smaller than this, κ_s is certainly controlled by boundary scattering and the effective ℓ is just the geometric size.

To estimate κ_p for the powdered MgO in Thermocoax at low temperature, I replace $\ell = 3\,\mathrm{mm}$ in the above calculation with $\ell = 1\,\mu\mathrm{m}$, the apparent grain size, and multiply by the volume fraction (0.6). The result is $\kappa_p = 5{\times}10^{-4}\,(T/\mathrm{K})^3\,\mathrm{W\,m^{-1}K^{-1}}$. This would appear to set an upper bound on κ_p, but is perhaps not too far above the true value, since an independent method of estimation (see Appendix, Sec. 3.5.5) yields a somewhat greater value.

Applying this as an estimate for κ_d of the Thermocoax dielectric, we have for the radial thermal conductance per unit length (Sec. 3.5.1), using Eq. 3.52 but neglecting any contact resistance between the metal and dielectric,

$$\begin{aligned} k_r &= \frac{2\pi\kappa_d}{\ln(r_d/r_w)} = 2\pi\cdot 5{\times}10^{-4}\left(\frac{T}{\mathrm{K}}\right)^3 \frac{\mathrm{W}}{\mathrm{m{\cdot}K}}\cdot\ln\left(\frac{175\mu\mathrm{m}}{85\mu\mathrm{m}}\right) \\ &= 2.3{\times}10^{-3}\left(\frac{T}{\mathrm{K}}\right)^3\frac{\mathrm{W}}{\mathrm{m{\cdot}K}} \end{aligned}$$

I have here ignored contact resistance because the thermal resistance of the powdered MgO is so large and is primarily due to many contacts between grains of the material. Also, unlike the case with PTFE, thermal contraction of MgO is quite small, about 0.12% [121], less than half that of the stainless steel jacket [4]. Therefore the tightly-packed MgO should not loosen on cooling.

The thermalization length is then (Eq. 3.55)

$$\zeta = \sqrt{\frac{K_w}{k_r}} = \sqrt{\frac{5{\times}10^{-10}\,(T/\mathrm{K})\,\mathrm{W\,m{\cdot}K^{-1}}}{2.3{\times}10^{-3}\,(T/\mathrm{K})^3\,\mathrm{W\,m^{-1}K^{-1}}}} = 0.5\left(\frac{T}{\mathrm{K}}\right)^{-1}\mathrm{mm}\,.$$

The result is a reassuringly short thermalization length, although it is as long as 5 cm at 10 mK. Without having done this calculation, we would not have known it was not much longer.

3.5.5 Appendix to Sec. 3.5.4: Another method of estimating κ_p for MgO

I have not found thermal conductivity data for powdered MgO at low temperature. High-temperature data (300–1300 K) [7], taken in the presence of air or inert gases, show thermal conductivity for powdered MgO which is strongly dependent on factors including volume fraction, particle size, gas pressure and composition, and which is 1–2 orders of magnitude lower than that of the solid crystal. The ratio κ_s/κ_p is also not independent of temperature; in fact κ_p tends to increase by factors of 2–3 over this temperature range, while κ_s decreases by almost an order of magnitude. This suggests a large role for gas conduction and radiative coupling between grains in the conditions under which these values were measured (high temperature and gas pressure).

Shapiro *et al.* [6] measured the thermal conductivity of powder and bead beds of five ceramic and glassy materials, with particle sizes ranging from 50 μm–3 mm, at temperatures of $\sim$55 C, under 19 kPa of mechanical pressure, and gas pressures of 10–10^7 Pa. Their data show that gas conduction plays a dominant role at any gas pressure above $\sim$0.1 Pa [6]. They also estimated that radiation would contribute negligbly at these (and lower) temperatures.

Their data reveal a curious phenomenon: for sufficiently low gas pressure, all of the powder bed samples tested had $\kappa_p \approx 0.1$–$0.2\,\mathrm{W\,m^{-1}\,K^{-1}}$ despite κ_s for the solid materials varying over an order of magnitude (0.74–8.4 $\mathrm{W\,m^{-1}\,K^{-1}}$). These results are displayed in Table 3.5.5, along with representative values for the Vickers

Material	Hardness [GPa]	Particle size [μm]	Volume fraction	κ_s [W/mK]	κ_p [W/mK]	ratio κ_s/κ_p	pred. ratio
Metco	[2.2]	50	0.53	2.0	0.14	14.3	[14.3]
Al_2O_3	26	60	0.49	8.4	0.12	70	68.8
ZrO_2	12	128	$\sim$0.5	1.8	0.12	15	21.5
Rimax	8	700	0.68	1.72	0.10	17.2	8.5
Rimax	8	2700	0.68	1.72	0.24	7.2	7.3
Glass	6	1000	0.62	0.74	0.12	6.2	8.2
MgO	9.1	1	0.6	5.5	?	?	1270

Table 3.6: Thermal conductivities at $T = 50$–$60\,\mathrm{C}$ of glass and ceramic solids compared with those of gas-free powder and bead beds made of the same materials. Data from [6, 7, 8, 9, 10, 11, 12, 13]. Values given with $\sim$ are estimated. "Hardness" is the Vickers number, which is about twice the indentation pressure. "Metco" is a powder used for plasma-spray coating of metals. "Rimax" is a grinding bead made of primarily SiO_2 and ZrO_2. "MgO" is the Thermocoax powdered magnesium oxide insulation. Also shown is a predicted value for the ratio κ_s/κ_p based on a best fit to Eq. 3.77. "Metco" was effectively removed from this fit by making its unknown hardness a free parameter, yielding the values shown in brackets. It puts no pressure on the results, but is included as a sanity check on the procedure.

hardness of the solids, obtained from various sources. One might expect κ_s/κ_p to correlate with material hardness, since for the same mechanical pressure and particle size, softer materials will have larger particle-particle contact areas. The data in Table 3.5.5 bear this out to some extent, and the "Rimax" data are also consistent with κ being an increasing function of particle size.

Shapiro *et al.* presented a three-parameter model which gave a reasonable fit to their data for particle beds with helium, argon and air at pressures of $10^{-2} - 10^4\,\mathrm{Pa}$. Fitting the data across the six decades of gas pressure variation always reproduced the low-pressure limit. It is not clear that this is not just the result of providing enough adjustable parameters, but the motivation for their model is instructive. They consider the total thermal resistance of a column of the particle bed as a

sum of particle resistances and contact resistances, or equivalently total thermal resistivity of the bed, considered as a bulk medium, as the sum of volume and contact resistvity terms, ρ_v and ρ_c.

One may reasonably expect that, for a network of particles, and contacts between them, that can be scaled by a single parameter d which we call the particle size (which may be a peak in the distribution of linear dimensions of the particles), ρ_v, the total thermal resistivity *due to the bulk material*, will be independent of d. However, ρ_v may be expected to scale inversely to the average cross-sectional area, or $\rho_v \propto f^{-2/3}$, where f is the volume packing fraction.

In addition, there will be a geometric factor due to heat flow through the network being convoluted rather than simply parallel to the overall heat flow. This factor is hard to estimate, but it will be of order unity, and will tend to increase κ_s/κ_p. The geometric factor may reasonably be expected to be independent of the particle size parameter.

Smaller particle size d will, on the other hand, mean proportionally more interpositions of the contact resistance, hence one can write $\rho_c \propto d^{-1}$. Also, ρ_c should be inversely proportional to the total area of each layer of contacts, or proportional to hardness H divided by mechanical pressure p_m, which is the inverse of the dimensionless fraction of cross-sectional area in contact per interfacial layer.

Summarizing, we can write

$$\begin{aligned}
\rho_v &= \alpha_v \, \kappa_s^{-1} f^{-2/3} \\
\rho_c &= \alpha_c \, \kappa_s^{-1} d^{-1} H \, p_m^{-1} \\
\kappa_p &= \frac{1}{\rho_v + \rho_c} = \frac{\kappa_s}{\dfrac{\alpha_v}{f^{2/3}} + \dfrac{\alpha_c}{d}\dfrac{H}{p_m}} ,
\end{aligned} \tag{3.77}$$

where the free parameters α_v and α_c incorporate the unknown shape factors and relationship of interfacial resistances to solid resistivity.

Equation 3.77 can be considered a simplification of the Shapiro model in the gas-free limit. It provides a basis for predicting κ_s/κ_p by comparison with other materials. Shapiro *et al.* presented a somewhat more complicated form for the dependence of ρ_c on contact area and hence on H and p_m. However, the data shown here does not provide an adequate basis for distinguishing which form provides a better fit, so I use the simpler form.

By optimizing the parameters in Eq.3.77 to minimize squared residuals of the predicted κ_s/κ_p for five of the Shapiro samples (Table 3.5.5), I calculated a prediction of $\kappa_s/\kappa_p = 1300$ for 1 μm MgO. Using $\kappa_s = 2.6\,(T/\mathrm{K})^3\,\mathrm{W\,m^{-1}K^{-1}}$, we find $\kappa_p = 2\times10^{-3}\,(T/\mathrm{K})^3\,\mathrm{W\,m^{-1}K^{-1}}$.

The prediction for 1 μm MgO is clearly an extrapolation outside the range (in particle size) of the sample materials. It is encouraging that this result is within an order of magnitude of that obtained by the method presented in the main text. However, it is *larger* than that result. Since the method presented in the main text is based on what seems a necessary assumption–that the mean free path for phonons is limited by the grain size–I think the result by that method must be closer to reality.

3.5.6 Thermalization of unshielded wiring

The application of Eqs. 3.74 requires knowing the thermal conductances K_w and k_r. The former can be calculated for a wire directly from the thermal conductivity if it is known. The latter is the sum of boundary resistances as well as volume thermal conductivity of the insulator.

To ensure low thermal conductance between refrigeration stages, very fine resistive or superconducting wire is used. The need for a substantial number of wires leads to the use of multiwire cables and looms. The use of twisted pair wiring and the weave of wiring looms mean that each wire will be directly exposed to a thermal anchoring surface only at a fraction of its length. Pressure cannot be applied without risk of damaging the wire or insulation. Inevitably the use of some type of potting material is the best one can do. This is generally a disordered polymer which is expected to have thermal conductivity roughly $\propto T^2$. The choice of a particular material apparently makes little difference at mK temperatures [63, 122]. GE/IMI 7031 varnish is often used for convenience.

Thermalization of fine wires in cryogenic apparatus was modeled by Hust [114], who calculated thermalization lengths based on mean thermal conductivities of copper and constantan, bonded to a thermal anchor through a bridge of varnish. Hust's calculations showed that for constantan wire of about 100 μm diameter bonded with 7031 varnish, only a few mm of contact are needed at 4 K. Similar results obtain for other resistive wires such as manganin, stainless steel and phosphor bronze [4]. In the case of Cu, however, the required thermalization lengths, for the

same thickness of wire, are more than an order of magnitude greater. This follows from the fact that for Cu with RRR of 50, at low temperature $\rho \approx 3\times10^{-10}\Omega$m, whereas for constantan $\rho \approx 5\times10^{-7}\Omega$m. Applying Eqs. 3.3 and 3.55, we have $\zeta_{\rm Cu}/\zeta_{\rm constantan} = \sqrt{5\times10^{-7}/3\times10^{-10}} = 41$.

Whereas at 4 K the thermalization lengths for varnish-bonded wire can be estimated on the basis of the volume thermal conductivity of the varnish, at mK temperatures the volume resistance increases as the square of temperature and is overtaken by boundary resistance, which increases as T^3. For a 50 μm radius wire with a 13μm thick layer of insulation resting on a Cu surface and varnished to it, I estimate, based on a rough numerical integration, that the varnish bridge plus the insulation on the wire is equivalent to a 100 μm wide strip of varnish that is 18μm thick. The boundary resistance should be roughly equal to $1+2/\pi \approx 1.6$ times that due to a 100 μm wide strip of Cu–varnish boundary.

Available data for the thermal conductivity of GE/IMI 7031 varnish near and below 1 K disagree by more than an order of magnitude (Tables 3.2. The lowest value for the volume thermal conductivity was reported by Anderson and Peterson [63], in a measurement which separated the volume term from the Kapitza term by assuming that the volume conductivity was $\propto T^2$ while the Kapitza resistance was $\propto T^{-3}$. These measurements were taken in the mK range (to 40 mK), and while it is possible that they assigned too large a share of the total thermal resistance to the volume component, the effective thickness I am assuming for the varnish film is only a factor of 3 greater than the thickness in Anderson and Peterson's study, which is comparable and would only bias my use of their results in a conservative direction.

Therefore I use Anderson and Peterson's data for both the volume and boundary terms in preference to Stephens [64] who found much higher volume conductivity (also in the mK range) but did not separate out the boundary term.

Thus, in the notation of Eq. 3.55, the thermal conductance k_r from the wire to the Cu anchor per unit length of the wire is found as:

$$\begin{aligned} k_r &= (R_K + R_v)^{-1} = \left[1.6 \frac{\tilde{R}_K}{10^{-4}\,\mathrm{m^2/m}} + \left(\kappa_v \frac{100\,\mu\mathrm{m}}{18\,\mu\mathrm{m}} \right)^{-1} \right]^{-1} \\ &= \left[1.6 \frac{8.5\times10^{-4}(T/\mathrm{K})^{-3}\,\mathrm{m^2K\,W^{-1}}}{10^{-4}\,\mathrm{m}} + \left(3.5\times10^{-3}(T/\mathrm{K})^2\,\mathrm{W\,m^{-1}K^{-1}} \frac{100}{18} \right)^{-1} \right]^{-1} \\ &= \left[13.6 \left(\frac{T}{\mathrm{K}} \right)^{-3} + 51 \left(\frac{T}{\mathrm{K}} \right)^{-2} \right]^{-1} \frac{\mathrm{W}}{\mathrm{m\cdot K}}\,. \end{aligned}$$

Note that while the boundary resistance term R_K can safely be ignored at 4 K, it is already significant at 1 K and becomes the dominant term below 0.3 K. Note also that this result is based on the data of Anderson and Peterson, who reported a relatively high value for the volume resistance. The calculations of Hust [114] and values given by Ekin [4] for thermalization at 4.2 K ignore the boundary resistance.

The thermal conductance of the wire K_w, for 110 μm constantan wire can be calculated using the WFL law (Eq. 3.3) from the wire's specified resistance R_w:

$$K_w = T\frac{L_0}{R} = T\frac{2.45\times10^{-8}\,\mathrm{W\Omega K^{-2}}}{66\,\Omega/\mathrm{m}} = \frac{T}{\mathrm{K}}\cdot 3.7\times10^{-10}\,\frac{\mathrm{W\,m}}{\mathrm{K}}\,.$$

For NbTi:CuNi wire with CuNi cross sectional area $3.1\times10^{-9}\,\mathrm{m^2}$, using the data of Kushino [56] for 4.2–0.6 K, and of Greywall [54] for 100–10 mK (Table 3.1), K_w is given by

$$\begin{aligned} K_w &= \left(\frac{T}{\mathrm{K}} \right)^{1.1} 2.5\times10^{-10}\,\frac{\mathrm{W\,m}}{\mathrm{K}}\,, \quad 4.2 - 0.6\,\mathrm{K}, \text{ and} \\ K_w &= \frac{T}{\mathrm{K}}\,2.0\times10^{-10}\,\frac{\mathrm{W\,m}}{\mathrm{K}}\,, \quad 0.1 - 0.01\,\mathrm{K}. \end{aligned}$$

Temperature [K]	4.2	1.4	0.6	0.1	0.03	0.01
ζ Constantan [mm]	0.07	0.13	0.21	0.83	2.5	7.2
ζ NbTi:CuNi [mm]	0.06	0.11	0.17	0.61	1.8	5.3

Table 3.7: Estimated thermalization lengths ζ for unshielded wire varnished to Cu posts. "Constantan" = 0.10 mm diameter constantan, 0.01 mm polyester. "NbTi:CuNi" = 0.05 mm diameter NbTi, 0.08 mm diameter CuNi, 0.01 mm polyester.

Using these results, with (Eq. 3.55) $\zeta = \sqrt{K_w/k_r}$, I calculate the results shown in Table 3.7. The calculated thermalization lengths are reassuringly short, but note that ζ is the $1/e$ length for $T_w - T_0$ and several times ζ should be allowed for good thermal anchoring. In the case of twisted pair wiring, ζ should be multiplied by a factor of 2 and for the twisted pair looms, where the pairs are alternately exposed and covered (Fig5.3), a factor of 4, at least, seems justified.

Chapter 4

Installation of cryostat, dilution refrigerator, pumps and plumbing

4.1 Basic facilities

A number of major design choices for the LPS mK-STM system were made before I arrived at the lab in February 2006. The dilution refrigerator was chosen to be an Oxford Kelvinox 400HA system [123] rated at 300 μW cooling power at 100 mK, with a guaranteed base temperature <10 mK at installation, although the operating temperature would certainly be somewhat higher. A superinsulated LHe cryostat [124] was purchased from Kadel Engineering for initial use, and a second cryostat with an integrated 13.5 T vertical solenoid magnet [125] was ordered from American Magnetics for experiments requiring a high field.

The STM and UHV chamber system was designed by Barry Barker and Michael Dreyer based on the 4 K STM system at LPS and similar systems built at Berkeley, Hamburg and elsewhere [126]. The STM body is to be mounted below the cold plate of the fridge, with a vertical transfer rod mechanism on the cryostat central axis used to ferry samples and replacement tips up and down between the STM body and a UHV chamber located directly above on top of the cryostat. A second, horizontal transfer rod and associated piping allows transport of samples between the transfer chamber, a load lock chamber, and two auxiliary UHV chambers for sample and tip preparation, characterization and storage.

Ion getter and Ti sublimation pumps are attached to the chambers to reach 10^{-8} Pa typical base pressure. Although the time to deposit a monolayer at this pressure is measured in hours, experience with the LPS 4 K STM system shows that sample preparation and transfer past numerous small leaks or contamination sources can scatter contaminants across freshly-cleaved or cleaned samples.

The system is mounted on a 59×96 inch optical table with a pneumatically damped air suspension system from Technical Manufacturing Corporation [127]. Isolation efficiency for the table system, was specified as up to 97% at 5 Hz and 99% at 10 Hz, in the vertical mode, with resonance frequency 0.8-1.7 Hz. For the horizontal mode, isolation is specified as up to 90% at 5 Hz and 95% at 10 Hz, with resonance frequency 1-1.9 Hz. The pneumatic isolators rest on the floor of an electromagnetically shielded room, with no other measures to isolate the table from vibrations. The shielded room walls and floor are constructed of 3/4 inch wood particle board sandwiched between layers of galvanized steel. The floor rests on Masonite shims which sit on the linoleum floor tiles glued to the concrete floor slab of the building, which in turn rests on underlying gravel and soil. The building is built on a hillside set back from heavily-trafficked roads, and is a single storey in the part of the building where the lab room is located.

The shielded room [128] provides some reduction of low-frequency magnetic fields, and its RF electromagnetic attenuation is specified as better than 100 dB from 1 kHz–10 GHz, although its performance could be expected to degrade with time and abuse. The room has a 12×14 ft. floor with 8 ft. ceiling height, and was built into the rear-left corner of a lab space 19 ft. wide $\times$ 25 ft. deep. A 13 ft. deep,

3.5×7.5 ft. concrete-lined pit was constructed through the slab and into the ground beneath to accommodate the dewars. The shielding extends down the walls and floor of the pit, and the room is also equipped with a 2×2 ft. $\times 6$ ft. high "top hat" extension to accommodate a vertical transfer rod above the STM.

Not including the experimental chambers and instruments, and the building itself, these facilities represented an investment of well over half a million dollars, more than half of that for the dilution fridge.

I was involved in setting up the lab space external to the shielded room, including the layout of workbenches, drawers, cabinets and desks. I constructed shelving on the outside and inside of the shielded room, and a ladder for access to storage space atop the shielded room, using primarily surplus material. One possible problem, though, is that it may be necessary to airgap the shielded room wall from external disturbances, such as people working at desks or accessing shelved materials, while taking data.

4.2 Pit scaffolding

When I arrived at LPS, the shielded room had just been installed, and my first task was to build a scaffolding and platform in the pit to support work on the fridge and STM when the dewar was lowered.

The heights of the fridge and STM body were already determined by the basic design as described above. From prior experience working on dilution fridges, I knew that turning the bolts at the top of the inner vacuum can (IVC) of the fridge,

making or breaking the indium seal, and lifting to install or remove the IVC, can be clumsy yet must be done with care to avoid damage to the system; therefore the top of the IVC should not be high above one's head. At the same time, installing an STM tip or making adjustments to the STM can be delicate and tedious, and one would not want to have to do this while crouching in an uncomfortable position. In order to ensure convenient access to all levels where work might need to be done, I decided to build a platform that could be easily set to either of two heights, differing by 16 inches (Fig 4.1).

The platform was built in five sections which are easily removable with attached handles. One large square section sits at the front of the pit and only at the upper height, and normally is not meant to be moved. Four smaller sections are light enough to be easily removed in order to raise or lower the dewar, and can be placed at the lower height for close work on the STM. The platform sections are made of 3/4 inch thick wood composite with attached 2×4 lumber reinforcements.

The scaffolding is made of 2×4 and 2×6 lumber with flat sides against the walls of the pit to minimize constriction of the pit space. I used notch construction, as well as screws and adhesive to ensure the safety and stability of the scaffolding. Ladder rungs were built into two sides, and I scalloped out the faces against the walls to allow room for one's fingers. I pre-assembled each of four frames of the scaffolding before lowering them into the pit. The two end frames press the two side frames against the walls of the pit, and after screwing them together I added shims to make a tighter fit. If it is ever necessary to remove this scaffolding without destroying it, the screws that tie the frames together can be removed or cut.

Figure 4.1: View into dewar pit showing construction of platform. Three panels of the platform floor have been removed, and stand on the panel in the back. Cross-beams of the platform panels fit into the notches in the scaffolding, at either of two heights. The dewar is stored below the platform. The ladder to the bottom of the pit (4 m depth) is visible on one side. A stepladder leads to the top of the pit.

4.3 Table installation

The next task was installation and testing of the optical table and its air suspension. The table had been built to order with a 30 inch hole for the fridge and two 12 inch holes for pumps mounted underneath the UHV chambers. By dropping a plumb line, I placed the table so that the large hole lay centered under the shielded room's "top hat." However, I later found it necessary to lift the table and move it about an inch forward to make room for the plumbing vibration isolation box. Viewing the table from the front of the pit, the back edge is 20 in and the left edge is 25 in from the respective walls, both within $\pm\frac{3}{16}$ inch. I located the air suspension "legs" near the corners of the table.

Each "leg" has four adjustable "feet" which I located to rest on the linoleum tile rather than on the steel strips that join sections of the shielded room floor. I later had to move the left-rear leg an inch forward of the symmetrical position to accommodate the vibration isolation bellows box. Using a spirit level, I adjusted the foot bolts to make the columns as nearly as possible vertical, equal in height, and with roughly equal pressure on each foot (as gauged by the resistance to turning). Then I lowered the table onto the columns and into the position in which it will remain, since the plumbing connections do not permit moving the table.

I connected the air suspension system to a supply of pressurized gas, floated the table, and adjusted the regulators to set the float height to $\frac{3}{8}$ inch as per the manufacturer's instructions. The pneumatic pistons in each leg support metal disks on which the table directly sits. It was necessary to move these disks by tapping on

them gently with a screwdriver and hammer, until the pistons were centered and sitting level.

The 30 inch diameter hole in the table is covered by a 1 inch thick circular aluminum top plate. This the smaller top flange of the fridge sits on this plate, and the dewar hangs from the plate by a bolt circle. It has cutouts for gas, cryogen, and electrical connections to both the non-magnet and magnet dewars. The plate was designed by Dan Sullivan.

4.4 Force on magnet dewar

When testing the table air suspension I noticed that the float is "soft" (as required for mechanical isolation) and slight force applied to an edge of the tabletop results in an intial substantial tilting. After a few seconds the regulators readjust the pressure in each cylinder to restore their heights to their setpoints and re-level the table. This led me to consider what forces might unbalance the table under experimental conditions.

I was concerned when I realized that there could be considerable horizontal force on the high-field magnet due to its being located towards the rear of the steel-lined pit, rather than in its center. It did not seem practical to relocate the table in order to place the dewar more in the center of the pit, given the location of the top hat and the need for access to the pit. Worse than the torque applied to the table, the sideways force might cause internal misalignment or damage to the magnet dewar.

While it initially appeared that calculating the magnitude of this force would require a nontrivial finite-element computation, the permeability of the steel lining is very high, meaning that the field is close to zero past the wall. Also, the pit is deep, and the magnet, a solenoid of 25 cm length, sits about 75 cm deep in the pit, while the distance to the three near walls of the pit is about 50 cm. These numbers suggest that modeling the magnet as a dipole and the pit as an infinite rectangular tube of infinite permeability is not a bad first approximation, and in any case gives an upper bound on the force.

The interaction between the magnet and the wall can then be modeled as that between the magnet and its image dipoles behind the walls (Fig. 4.2 A). The boundary conditions would be matched by an infinite 2D array of dipoles. These dipoles are coplanar and aligned normal to the plane. The attractive (repulsive) force F between any two antiparallel (parallel) dipoles of moment m separated by a distance r in their common equatorial plane is

$$F = \frac{3\mu_0}{4\pi}\frac{\mathsf{m}^2}{r^4}. \tag{4.1}$$

Given the r^{-4} dependence of the force, and given that the magnet is centered in the left-right dimension of the pit and is off center in the front-rear dimension by a ratio of $\sim$7:2, only the three nearest images behind the rear wall need to be considered. Referring to Fig. 4.2 B, if w is the width of the pit, the distance of the solenoid to its nearest images (1 and 3) is $r_1 = w$. The distance to the next nearest neighbors (images 2) is $r_2 = r_1\sqrt{2}$. Therefore, if F_1 is the magnitude of the force due to image 1, the magnitude of forces due to images 2 is $F_2 = F_1 \times 2^{-4/2} = F_1/4$.

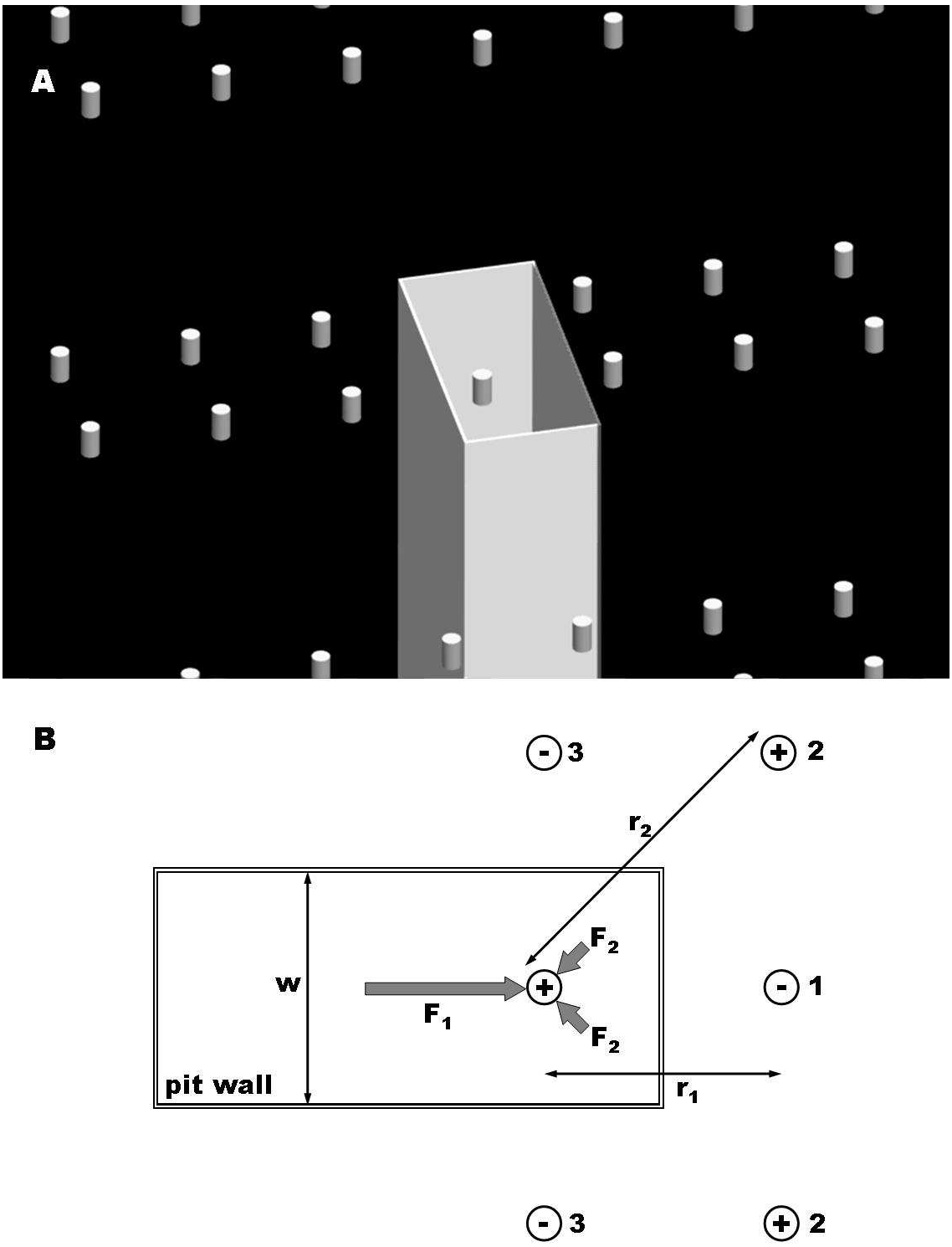

Figure 4.2: Method of estimating force on superconducting solenoid in magnet dewar due to interaction with pit walls. A. Representation of solenoid, pit walls, and image solenoids. B. Only nearest images contribute significant force. The image in position 1 makes the largest contribution (F_1). It is partly offset by positions 2 (F_2). The two images in positions 3 cancel, but create an instability (see text).

The vector sum of all three will then have the magnitude

$$F \;=\; F_1 - 2\,\frac{F_2}{\sqrt{2}} \;=\; F_1\left(1 - \frac{1}{2\sqrt{2}}\right) \;\approx\; 0.65\,F_1\,.$$

To calculate the maximum value of m for the solenoid, I have the following data from the manufacturer:

$$B_{max} = 13.5\,\mathrm{T} \;\text{ for }\; i_{max} = 100\,\mathrm{A}; \quad L = 45\,\mathrm{H}.$$

I use the formulas for the field intensity B and inductance L of a "long" solenoid of length ℓ and area A, consisting of N turns carrying current i, to calculate an effective value for the product NA:

$$B = \mu_0 \frac{Ni}{\ell}, \qquad L = \mu_0 \frac{N^2 A}{\ell} \quad\Longrightarrow\quad NA = \frac{Li}{B}.$$

Since $r_1 \gg \ell$, I can also use $\mathsf{m} = NA\,i$ (i.e. treat the "long" solenoid as a dipole). Thus, using $r_1 = 1.07\,\mathrm{m}$

$$\mathsf{m}_{max} \;=\; \frac{45\,\mathrm{H}(100\,\mathrm{A})^2}{13.5\,\mathrm{T}} \;=\; 3.33{\times}10^4\mathrm{Am}^2$$

$$F_{max} \;\simeq\; 0.65\,\frac{3\mu_0}{4\pi}\frac{\mathsf{m}_{max}^2}{r^4} \;=\; 0.65 \times 3{\times}10^{-7}\,\mathrm{H\,m^{-1}} \times \frac{(3.33{\times}10^4\,\mathrm{A\,m^2})^2}{(1.07\,\mathrm{m})^4} \;\simeq\; 165\,\mathrm{N}.$$

While it seems unlikely that this amount of horizontal force (up to ∼37 lbf) on the magnet would cause structural damage to the magnet or the dewar, it might have some negative effects.

This has not been tested yet, but in case the horizontal force turns out to be a problem, one possible solution would be to balance the attraction to the rear wall of the pit with a removable square steel sheet roughly the width of the rear wall and held at roughly the same distance in front of the dewar. This would not have to be

as heavy as it sounds, since the sheet could be thin and supported by a lightweight frame. The balance could be fine-tuned by mounting a laser or stick pointer to reveal any deflection of the floating table, and ramping the magnet current to detect an unbalanced condition by observing the deflection. Once the correct distance for the removable sheet is found, brackets to hold it can be fixed in position, and further adjustment should not be necessary.

Unfortunately, such a balance will be unstable, since the residual horizontal force will be linear in small displacements of the magnet from the balanced position. This is a potential issue not just for the proposed front-rear balancing scheme, but for the existing unstable right-left balance. Differentiating (4.1) gives:

$$\left|\frac{\mathrm{d}F}{\mathrm{d}r}\right| \;=\; \frac{3\mu_0}{\pi}\frac{\mathsf{m}^2}{r^5}.$$

and the resultant sideways force in the direction of a small displacement left or right from the center position (and front or back if the balancing scheme is used) will be four times this since the two image dipoles will each move closer and further by twice the displacement. Thus for the parameters here,

$$\frac{f_{max}}{\delta} \;=\; \frac{4F_{max}}{1.07\,\mathrm{m}} \;=\; 4.8\,\frac{\mathrm{N}}{\mathrm{cm}}\,,$$

where f_{max} is the force resulting in the direction of a small displacement δ for the magnet at maximum current. This seems a large enough response ($4.5\,\mathrm{N} \approx 1\,\mathrm{lbf}$) to worry about its potentially causing some instability.

Actually, if the center of mass of the entire system (table, fridge, dewar and UHV chambers) lies above the plane of the air suspension pistons, the system is already top-heavy and would be unstable if, for example, the air cylinders were

simply connected together, thus equalizing pressure in the cylinders, instead of using the height regulators. With the regulators and internal damping, the air suspension system is normally able to stabilize a top-heavy mass distribution, as when the table is bare, or has heavy equipment mounted only on the top side.

An unstable balance of magnetic forces will add to any mechanical instability resulting from a top-heavy system. The interaction of the magnetic field with the steel may also be nonconservative, dissipating energy from the magnet. Combined with the dynamic response of the table and its height regulators, one has to be concerned about the possibility of oscillations under some conditions. Given the complexity of the entire system, it may be easier to test whether this occurs than to try to predict it. If problems do arise, it might be possible to stabilize the system by adding weights to the dewar or to other structures pendant from the bottom of the table.[1]

In any case, I would be especially careful when testing the magnet in place for the first time, starting with low field and watching for any signs of instability as the field is increased. This should include deliberately perturbing the system to gauge its response, bearing in mind that the magnet stores up to 2.2 MJ at high field and that if oscillations occur they might grow out of control before the field could be ramped back down.

[1] Another possibility would be to add a magnetic pole piece centered below the dewar, to create a restoring force when the axis of the magnet was off-center. However, for such a geometry the restoring force would be quadratic in small displacements, whereas the destabilizing force is linear.

4.5 Raising and lowering the dewar

My next task was to design and build a system for raising and lowering the dewar between its storage position at the bottom of the pit, and its operating position pendant from the table. For this purpose, the dewar is suspended from its two lifting eyes via cables. The cables hang over two idler pulleys mounted on the top plate. Therefore the dewar can be raised vertically by pulling the cables horizontally, using a winch.

Based on my previous experience with a large dilution refrigerator, I felt it would be worthwhile to use a variable-speed electric winch rather than a hand-cranked one. The Golo winch [129] operates very smoothly, and with the use of a variac can be made to go at very low speed when the dewar is passing delicate parts of the fridge, or quite fast for covering the distance up and down into the pit. A single operator can raise or lower the dewar by remote-controlling the winch, but must pay close attention and must guide the dewar by hand to avoid collisions with the helium siphon, cold trap, level meter, and baffles. Such "hangups" can cause severe damage to the fridge if not noticed in time.

It was important that the cables wind neatly in a single layer on the winch drum, so that the dewar would remain level as it was lifted and not suddenly jump or tilt, possibly damaging the fridge. After some experimentation, I settled on the arrangement shown in Fig. 4.3. Each successive turn winds neatly next to the previous one because it is pulled to the center by the small angle ϕ. The full depth of the table is used to provide a long enough baseline that ϕ does not become large

enough to pull the next turn over the previous one.

In practice, I have found that when first lifting the dewar from the bottom of the pit, ϕ is too small to ensure winding without gaps, so it is sometimes necessary to guide the cable by hand. This can be safely done by touching the cable *at some distance away from the drum.* However, this problem occurs in the part of the lift where the dewar is clear of the fridge, so there is no danger of damage due to a hangup. When the dewar reaches the height where one's attention needs to be focused on avoiding collisions, ϕ is large enough that the cable winds itself neatly.

I find it useful to gently shake the dewar with one hand as it is being raised past potential hangup points. The dewar will then find its way past hangup points, or shake free of them, and one can feel if the dewar is free or if it is caught on something. It is helpful that, pulling at low speed, the winch slows noticeably or stalls if a hangup occurs, and the operator can quickly release the remote control to stop the motor.

It was important for safety reasons that a single cable be strong enough to support the entire weight of the dewar, and that the cable not be subject to corrosion. I used 304 stainless steel wire rope, $\frac{5}{32}$ inch diameter, the largest that would wind in a single layer for the required length of travel, with a many-stranded configuration for flexibility. I used self-tightening "strong grip" [130] end fittings, since the more common U-clamps tend to come loose over time.

When the dewar is fully raised, the bolts that hang it from the top plate can be inserted. It is best to leave the dewar hanging a bit loose so that it can be rotated slightly for the first bolt to find its hole. When all bolts are threaded, they can be

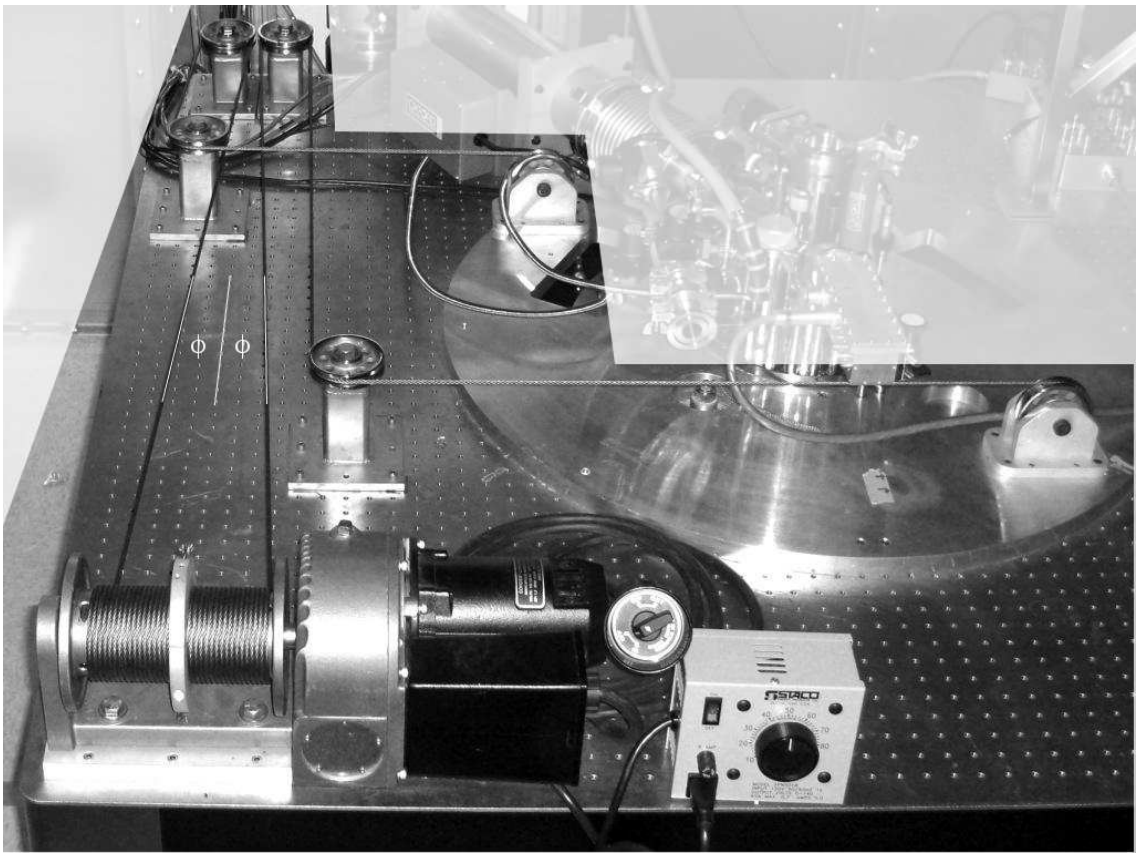

Figure 4.3: Configuration of the winch and lifting cables.

tightened to fasten the dewar and compress its O-ring seal to the top plate.

Turnbuckles are included to permit adjustment of the cables for leveling the dewar when it is hanging. I have found that the best way to adjust these is with the dewar bolted to the top plate, tensing the cables with the winch and then equalizing tension in the two cables with the turnbuckles.

Before the fridge could be tested, it was necessary to get the non-magnet dewar down into the pit. The dewar was brought into the shielded room by using a hand forklift, and could be moved into a position at the front of the pit by tipping it slightly and rolling it on edge in small steps. The design of the shielded room

included a steel I-beam over the pit to support lifting, but unfortunately this was not centered over the part of the pit that is not covered by the table. I thought, however, that lifting could be done at an angle if combined with a few strong men pushing the dewar sideways. This method worked, but I would not recommend it. A better method would be to use a bridge-type crane, at least one of which is available at the LPS.

4.6 Initial testing of dilution refrigerator

Once the table was set up, it was possible to install the dilution fridge on the table, set up pumps and plumbing lines temporarily and do an initial cooldown run. This was done with the help of Mark Jackson of Oxford Instruments.

Examining a drawing of our non-magnet dewar, Mr. Jackson noticed a problem: it appeared the internal filling tube would interfere with the IVC of the fridge. We could not reach deep into the dewar to bend the tube, and if we had been able to, the tube would not have been long enough to reach the bottom of the dewar. However, I was able to propose a repair: we could reach the tube near the top, where it comes out into the wide belly of the dewar's liquid helium space. We cut it off there, leaving a stub of an inch or so, bent the tube into the desired shape, and reinstalled it using a section of black Neoprene rubber hose to join the tube where it was cut and to make up the lost length. The hose needed to be tightly clamped since rubber expands on cooling. The repair remains in place to this day.

The pumps for the fridge were set up in the main lab room outside the shielded

room. The electrical supply and relay box for the pump system were installed in the pump room. In order to connect the pumps and the system control panel to the relay box, we broke a small hole in the wall with a sledgehammer, through which the cables could pass. Plumbing connections to the fridge were made through a removable access panel in the shielded room wall, and flexible stainless steel bellows were used for the plumbing lines, including a fairly monstrous 10 ft. long, 4 inch diameter bellows for the still pumping line. Initial cooldown and checkout procedures were conducted by Mr. Jackson, and after cooldown, nuclear orientation thermometry (NOT) was used to verify a base temperature of 6-7 mK. The cooling power was also tested by applying 400 μW of heat to the mixing chamber, with 40 mW of heat to the still, and measuring the mixing chamber temperature as 101.8 mK with the RuO_2 resistance thermometer supplied with the fridge.

4.7 The Vibration Problem

Following initial testing of the fridge, I undertook the permanent reinstallation of the pumps and plumbing lines. The problem was to identify and incorporate the best feasible measures of isolation to prevent vibrations from the pumps and other sources from being transmitted to the tabletop through the plumbing. A balance needed to be struck between the effectiveness of various proposed measures and the time and expense of developing and installing them. Although in principle a straightforward engineering problem, given the resources and knowledge I had available, this became largely a matter of intuition, aided by analysis of the physics

involved and simple calculations to estimate optimal or preferable parameter choices.

Members of the group felt that the following elements should be incorporated for vibration isolation:

1. The plumbing lines should be concreted into the cinderblock wall between the pump room and the main lab room.

2. The lines should pass through a sand-filled box.

3. Highly flexible bellows should be used for the final link to the table.

A fourth possible measure was to mount the pumps on a concrete inertia block in order to isolate the pumps from the floor slab, so that excessive vibration would not be transmitted through the floor. This had been done for an identical Kelvinox 400 system installed in the adjacent lab 1220. While this seemed like a good idea, it was preferred to avoid the cost and delay of getting a similar concrete block installed for the lab 1224 pumps.

The overall architecture that emerged is illustrated schematically in Fig. 4.4. The combination of concreting pipes into the masonry wall and passing them through the sandbox reduces any vibration transmitted through the pipes from the pumps to a very low level. Unfortunately, the pipes must then pass through the relatively noisy shielded room wall. The final stage of isolation of the plumbing lines is the T-bellows, inside the shielded room, connecting the plumbing to the table. Some vibration is transmitted from the pumps, and from other sources in the building, through the floor slab, to the shielded room floor and walls, which in addition may be excited by ambient sound.

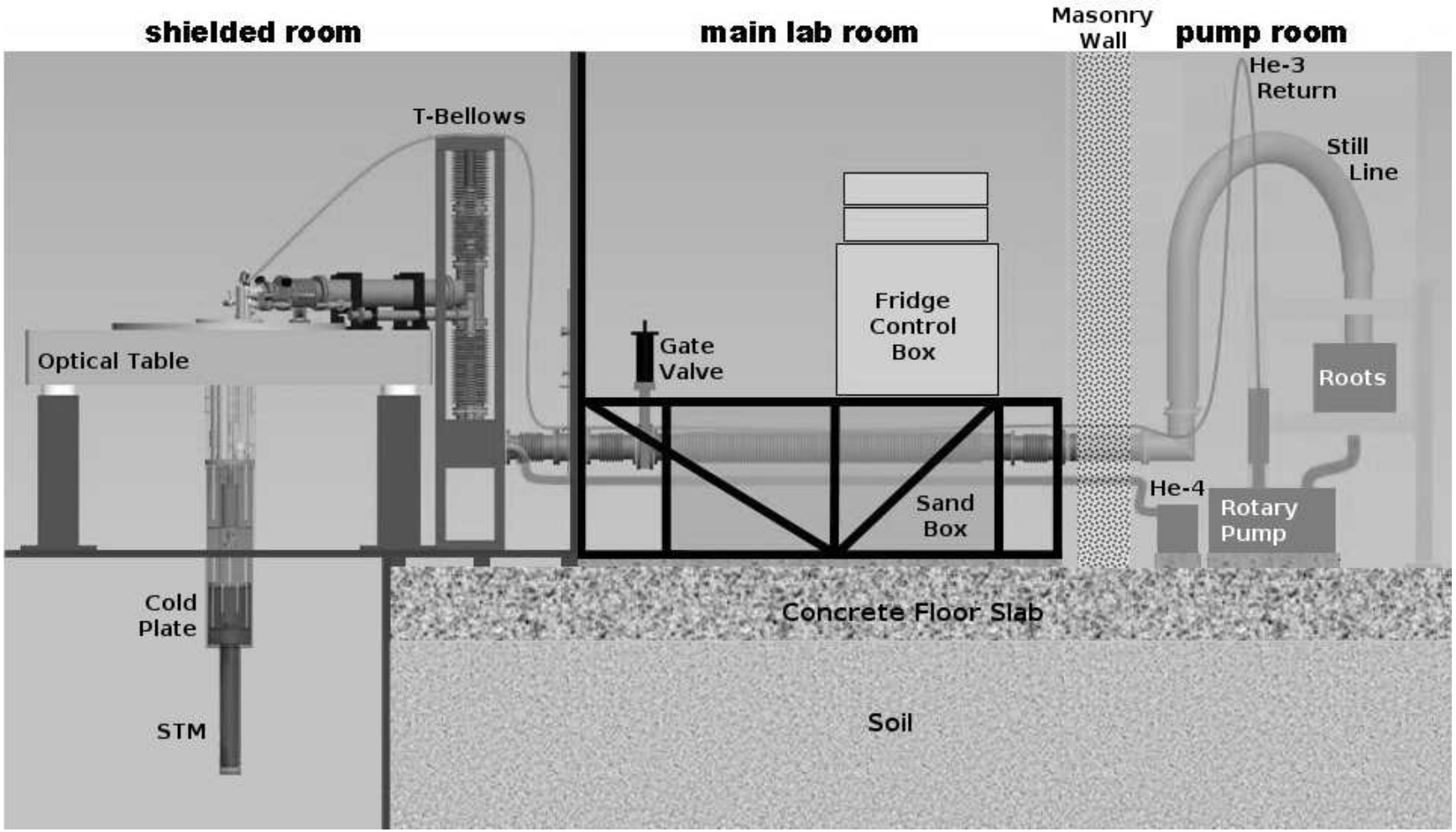

Figure 4.4: Plan of plumbing and vibration suppression. The shielded room rests on the floor slab through Masonite shims. The sandbox and pumps rest on the floor slab through rubber pads. The pipes are set into the masonry wall with concrete sand mix. Plumbing connections to the control box are not shown, but do interrupt the ^{3}He return line, the ^{4}He pumping line, and the line between the rotary pump and Roots blower.

Figure 4.5 presents the vibration spectrum from 1-1200 Hz measured at the tabletop on the top plate near the fridge/STM axis after reinstallation, with the pumps running and the table floated; I introduce it here to show the range of vibrations that are problematic and that needed to be minimized. These vibration measurements were made with a velocity-sensitive geophone [131] consisting of a fixed coil and moving spring-suspended permanent magnet which serves as the proof mass. This sensor is usable at frequencies above ∼1 Hz and has a very flat frequency response above ∼12 Hz, but I found that the coil picks up electromagnetic noise at frequencies above ∼1.2 kHz.

Although the output voltage of the sensor is proportional to velocity, I have chosen to display acceleration in Fig. 4.5 since, if, as expected, the resonant frequency of the STM "figure G" is at least a few kHz, the tip-sample vibration amplitude in response to vibration below 1 kHz should be proportional to the force experienced, i.e. acceleration. In fact, if the STM tip is modeled as a mass on a spring, of resonant frequency f_{ts}, driven by motion of the tabletop at frequency f with amplitude A_{table}, the resulting amplitude of tip sample motion A_{ts} is given by [132]

$$T_{rel} \equiv \frac{A_{ts}}{A_{table}} = \frac{F^2}{\sqrt{(1-F)^2 + (2HF)^2}}\,; \tag{4.2}$$

where $F \equiv \frac{f}{f_{ts}}$ and $H \equiv \frac{\eta}{\eta_c}$ is the damping coefficient relative to critical damping. Clearly, for $F \ll 1$ and $H < 1$ we have $A_{ts} \approx F^2 A_{table}$, i.e. tip-sample amplitude is proportional to table acceleration.

The upper panel of Fig. 4.5 plots the rms acceleration per $\sqrt{\text{Hz}}$ on a logarithmic

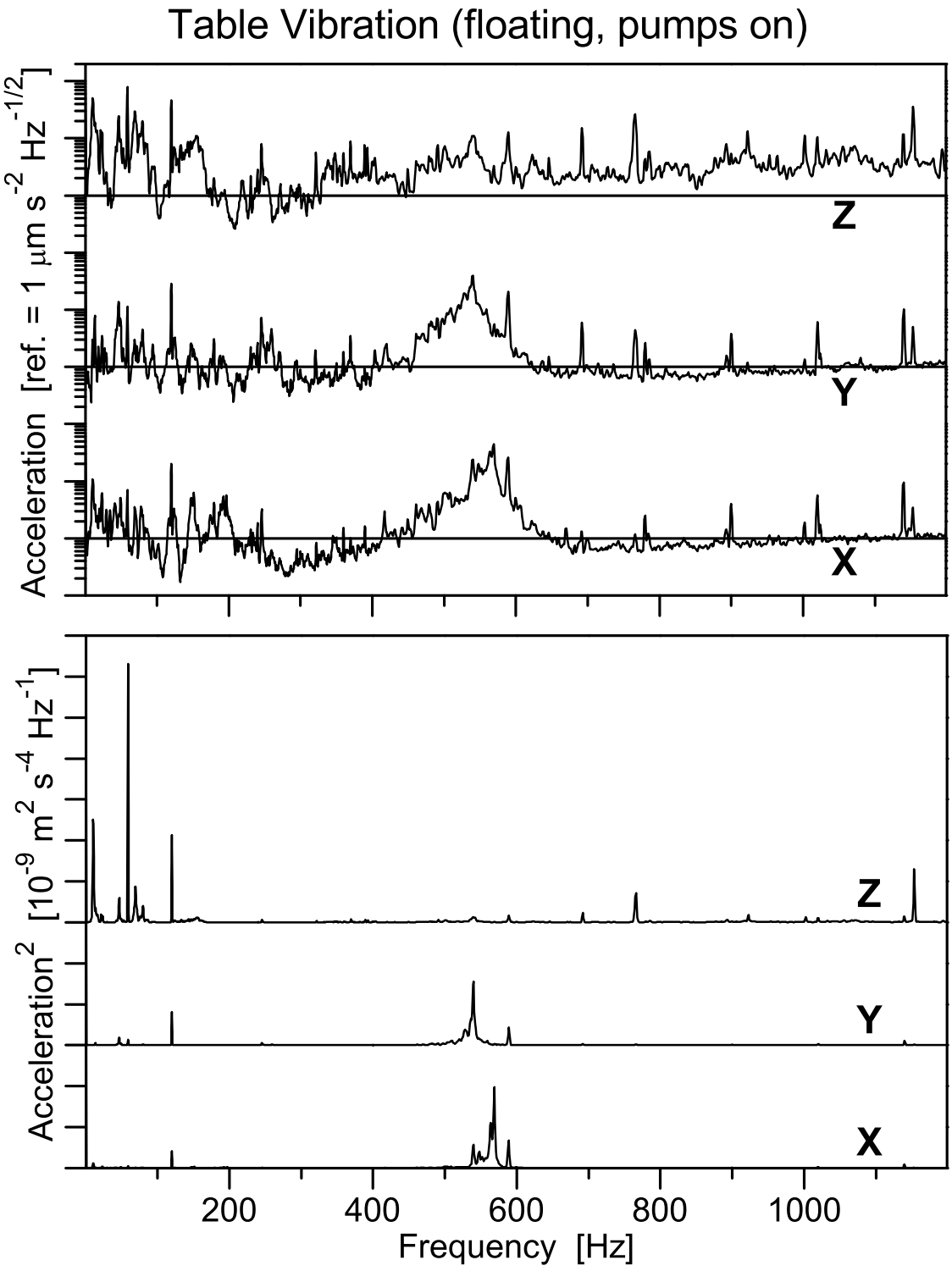

Figure 4.5: Vibration measured at the tabletop, with no plumbing connected, the pumps running, and the table floating. **Upper panel:** X, Y, and Z components of acceleration on a logarithmic scale. The reference line for each trace is equal to $1\,\mu\mathrm{m\,s^{-2}Hz^{-1/2}}$. **Lower panel:** The same data plotted as squared acceleration on a linear scale. The apparent baseline for each trace is equal to zero. Equal areas under the peaks make equal contributions to the rms acceleration.

scale, to show all portions of the spectrum. I checked the intrument noise floor with an equivalent resistor and it was at well below the sensor output from 1-1200 Hz. Note that the acceleration noise floor approaches 1 μm/s^2 Hz$^{1/2}$ at the upper end of the frequency range for the horizontal axes, and about a factor of 4 higher for Z. The acceleration in the Z axis is generally higher, except for a hump around 500-600 Hz in X and Y, which may represent a torsional resonance of the top plate with the fridge and dewar bolted on.

However, since the response of the STM is expected to be flat in this low frequency range, what matters is the square-integrated acceleration. The lower panel of Fig. 4.5 shows the same spectrum plotted as (acceleration)^2 per Hz; equal areas under this curve make equal contributions to the square-integrated acceleration. It is apparent that only a few frequency bands are significant. The peaks below 200 Hz correspond to noise from the pumps and other sources transmitted through the floor and plumbing; higher frequencies are primarily transmitted to the table by airborne sound.

4.8 Pump Room setup

4.8.1 Design

It was planned that the pumps would be installed in the adjacent pump room, roughly 4 m from the nearest corner of the table. With a cinderblock wall intervening, plus the shielded room wall, and with the possibility of adding sound-absorbing materials as needed, we were not concerned with airborne sound from the pumps, but only with low-frequency (< 200 Hz) vibration transmitted through the floor slab,

as well as any vibration transmitted through the plumbing lines.

There are three pumps: A small rotary vane pump for evacuating the ^{4}He pot, a larger rotary vane pump for circulating ^{3}He, and a Roots blower for boosting ^{3}He circulation and lowering pressure in the still line. Each pump is a source of vibration. However, although the Roots makes more audible noise, by far the strongest source of low-frequency vibration that can be transmitted through the floor slab is the ^{3}He rotary circulation pump.

The data presented in Fig. 4.6 shows (top) the squared acceleration when the pumps are on minus that when they are off, and (bottom) the squared acceleration when only the main pump is on minus that when all pumps are off. The peaks in these differences between 500-600 Hz for X and Y are attributable to changes in the background sound exciting the "hump" that is observed at these frequencies in Fig. 4.5, but are not consistent with attributing the "hump" to noise from the pumps. Note that negative peaks in these traces would indicate that the table was *quieter* with the pumps on, which only makes sense if the excitation comes from other sources.

The difference peaks in Fig. 4.6 which are reproducible and attributable to pump vibrations are at 59 Hz in Z only, and at 120 Hz in X, Y and Z. The largest component of acceleration which can be attributed to the pumps is the one at 59 Hz. It is about equally large in both the upper and lower panels, indicationg that it is almost entirely accounted for by the ^{3}He rotary pump alone. It appears that at least some of the 120 Hz can be attributed to the other two pumps, or to other sources. 120 Hz vibration is common due to the interaction between magnetic fields from

60 Hz coils and nearby high-susceptibility parts, where frequency doubling results from the fact that the force is attractive regardless of polarity.

The ^{3}He rotary is a 2-vane pump (Fig. 4.10 A), with a nominal rotation speed of 1640 rpm, or 27.3 Hz. It runs a little faster under high vacuum (if the motor were under zero load, it would run at 30 Hz). However, the main component of the vibration is at 59 Hz, double the rotation rate. This is probably due to the pair of sliding vanes. Their center of mass lies on the pump axis when they are horizontal, and below it when they are vertical, which occurs twice per cycle.

For each pump, the generation of oscillatory momentum, up to frequencies comparable to any mechanical resonances of the pump case itself, can be modeled as a periodic motion of some internal mass m relative to the mass M of the rigid case, motor and remainder of the pump. In the simplest example, which approximates the sliding vane pump, the motion can be described as an oscillation $A\cos(2\pi ft)$ in the vertical position of the center of m relative to M, along a line which passes through the center of M. By momentum conservation, neglecting any forces transmitted through the plumbing, wiring, or air, if the pump were floating in a zero gravity environment, the case would simply vibrate with amplitude $-A(m/M)$, so that the center of mass of the entire pump remained stationary. However, if the case were prevented from vibrating by being rigidly bolted to the floor, all of the oscillatory momentum would necessarily be transmitted to the floor.

From the point of view of containing vibration, then, it would be best to allow the pump to vibrate freely. This is approximately the situation if the pump is supported by a sufficiently soft spring. However, the main pump weighs about

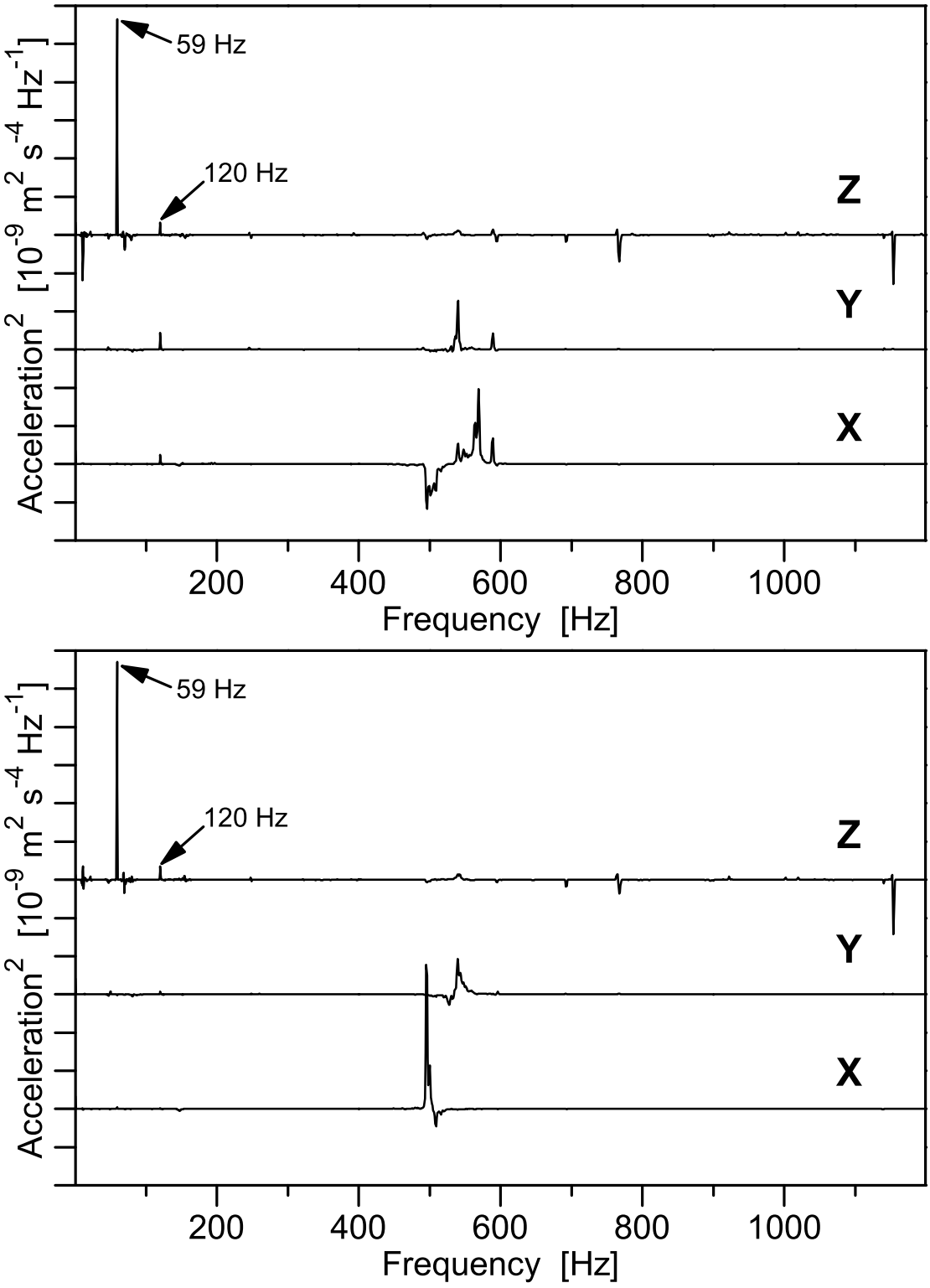

Figure 4.6: Vibration of tabletop due to pumps. Refer to Fig. 4.5 (lower) for explanation of vertical scale. **Upper panel:** Difference in squared acceleration with pumps on and off. **Lower panel:** Difference with only the ^{3}He rotary pump on vs. off. The main difference peak that is reproducible and can clearly be attributed to the pumps is at 59 Hz, and it is almost entirely due to the ^{3}He rotary pump.

80 kg, and the Roots about 74 kg. If the pumps are mounted on damped spring isolators, the springs must be stiff enough to support the weight of the pumps and to prevent their dislocation.

In reality, the floor slab is not completely immobile, but carries away the transferred momentum as very small amplitude traveling waves, which dissipate into the soil and building materials. However, the amplitude of floor vibration will be much smaller than that of the pump provided that the floor's effective mass m_f (roughly the mass of concrete contained within a quarter-wavelength radius of the pump, or about 90 m at 100 Hz) is large compared with the mass m_p of the pump, and that the isolation spring is reasonably soft.

The momentum transmission coefficient to the floor slab is given by [132]

$$T = \frac{m_f}{m_p + m_f} \sqrt{\frac{1 + (2HF)^2}{(1 - F^2)^2 + (2HF)^2}}, \tag{4.3}$$

where $H \equiv \frac{\eta}{\eta_c}$ and $F \equiv \frac{f}{f_n}$. Assuming $H < 1$, this function peaks at resonance ($F = 1$) and declines rapidly for $F > 1$. For example, for $H = 0.1$ and $F = 3$, $T = 0.145$, meaning better than 85% isolation. Thus, to achieve high isolation of a pump that vibrates at a dominant frequency f_p, what is required of the pump mass-spring system is $H \ll 1$ and $f_p \gg f_s = \sqrt{k_s/(m + M)}$, where k_s is the spring constant of the support/isolator.

An inertia block can be used to increase isolation of the pumps, after choosing a suitable damped spring isolation mount, by adding a second damped mass-spring isolation stage, so that the transmission of vibration from the pumps to the floor would be roughly the product of the transmission coefficients for each stage of isola-

tion. However, in order for this to be effective, the resonant frequency of the inertia block should be lower than the vibration frequency by a factor of 3 or more.

The inertia block that was installed for lab 1220 measures 24 inch × 60 inch × 18 inch high, weighs about 1 ton, and rests on rubber/cork pads which sit on the floor. Data published by a supplier of the type of rubber/cork pad used [133] indicates deflection of 0.2 inch at 50 psi, from which I calculate $f_s \approx 40$ Hz. However, the dominant frequency of vibration of the rotary pump is about 28 Hz, suggesting that this block may not be as effective as it might have been with the use either of a softer material or 4-8 stacked layers of the same material to support the block.

In any case, we chose not to use an inertia block, but I designed the installation of the pumps so that such a block could be added later. Since only the main ^{3}He pump adds measurably to the low-frequency vibration at the tabletop, and since the total mass of the block is less important than its resonant frequency, it might make sense to use a smaller block fitted for the main pump alone, perhaps a block of steel or lead rather than concrete, plus a soft enough support to ensure that its resonant frequency is below 10-20 Hz.

4.8.2 Realization

Figure 4.7 shows the arrangement of pumps as installed. All of the plumbing lines entering and exiting the pump room pass through pipe sections which I cemented into the cinderblock wall with masonry sand mix. As I was careful to ensure that these pipe sections were completely embedded in cement which completely filled the voids in the cinderblock, the lines are very well anchored to the wall. To

minimize the transmission of vibration to the wall, all connections to the pumps are made through flexible stainless steel bellows.

The 4 in. diameter still pumping line passes through the wall at a height of 16.5 in., which is about as low as possible in order for the pipe on the lab side to run horizontally through a sandbox and just above the bottom of the windowframe into the shielded room (Fig. 4.4).

I had the 4 in. diameter bellows supplied by Oxford for the still line cut up into several pieces and welded to ISO-100 flanged straight sections. One such section loops in an 18 in. radius semicircle to connect the Roots blower to a section of pipe passing through the wall (Fig. 4.7). Just where the bellows is welded to the straight section that runs down along the wall, the straight section is clamped in place with a soft wood yoke which is bolted to a frame that is anchored to the wall. The looping bellows provides vibration isolation of the Roots from the wall, and the yoke provides some damping. The bolts that hold the yoke are adjustable to center it on the straight section. The flange clamps that connect the straight section to the elbow, and the elbow to the pipe that is cemented into the wall, should be tightened before adjusting and tightening the yoke bolts, to ensure that the yoke applies no static force.

The Roots blower is mounted via isolating springs on its own frame, which has four feet that rest on the floor slab through rubber pads which are honeycombed to soften them and improve isolation. I used cardboard shims to level the frame and equalize pressure on the foot pads. To ensure that the Roots does not walk or get pushed in a way that could damage the bellows, I drilled holes in the floor and glued

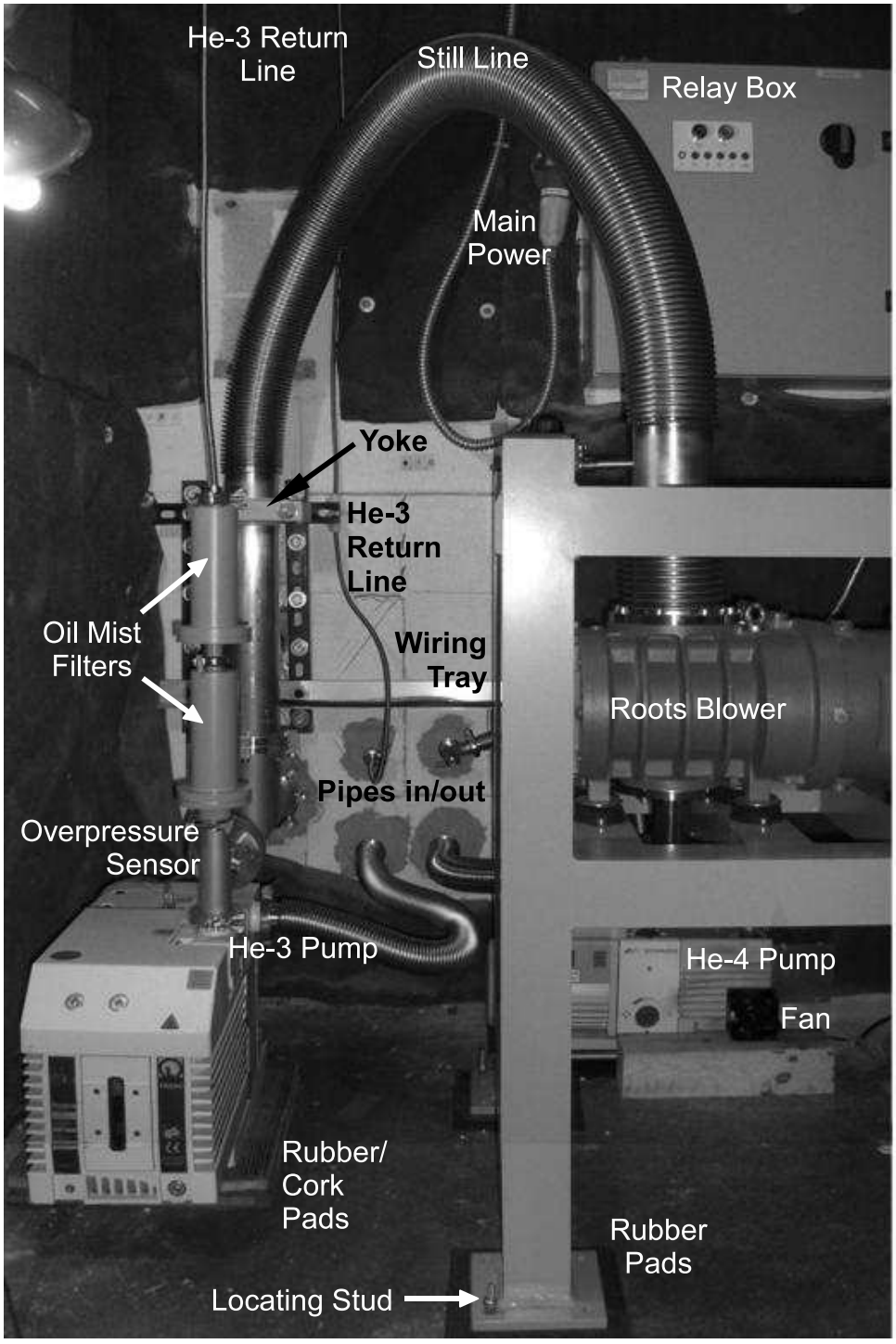

Figure 4.7: Installation of pumps in pump room.

locating studs into the holes for the feet of the Roots frame (Fig. 4.7). Vibration from the Roots does not appear to be a problem, but should it turn out to be one, isolation can be increased by adding more pad layers, or by using high-quality spring isolators, without a need for any modification of the plumbing. Should an inertia block need to be added under the Roots, an additional flanged section of 4 in. pipe can be added in order to raise the still line.

Oxford's gas handling system design requires that the ^{3}He pumping line, after compression by the Roots blower, passes back to the control panel, which we located in the lab room. It returns to the pump room as the foreline of the ^{3}He rotary pump (Fig. 4.7). After compression by the pump, the ^{3}He passes by an overpressure sensor, through two oil mist filters and into the 0.25 in. I.D. return line. I used an extra-long section for the return line and ran it vertically upward after the mist filters before looping it back down to pass through the wall, in the hope that this would trap and drip-return some of the oil that inevitably gets past the filters.

The ^{3}He rotary pump rests on a double layer of 1 in. thick rubber/cork padding laid directly on the floor slab (Fig. 4.7). The level of isolation provided by these pads is such that vibration from ^{3}He rotary pump is a strong signal but not a dominant contribution to the total low-frequency vibration measured at the STM tabletop. If in the future it is desired to improve the isolation of this pump, it can easily be raised so that additional padding and/or an inertia block can be placed beneath it. The foreline should easily accomodate raising the pump by up to 18 in., or the line can be extended if needed.

The ^{4}He rotary pump sits on the floor behind the Roots frame (Fig. 4.7). The

^{4}He is discharged directly into the (well-ventilated) pump room, and the pump sits in a stainless steel pan to catch oil that escapes from the discharge filter. This small pump is not a major source of vibration. A single layer rubber honeycomb pad is placed under the oil pan. Additional padding would provide better isolation, if needed. Because the ^{4}He rotary pump was observed to run quite hot, a small fan was placed next to it.

The relay box that controls power to the pumps is mounted on the wall behind the Roots blower (Fig. 4.7). The front panel has reset buttons for the overpressure and power fail (mains fail) conditions, and inside the box are a number of fuses and manually operable relays which need to be accessed from time to time. I took care to allow room for access to the box, and ran all wires neatly and tied down to a wiring tray or suspended from above so that they would not interfere with access–or be tripped over.

4.9 Sandbox and Dilution Refrigerator Control Panel

4.9.1 Design

As described previously, the group had planned to incorporate a sand-filled box with flexible bellows passing through it as a measure to decouple the STM optical table from the pumps. Since there was little space for such a construction inside the shielded room, it was decided to include this in the main lab room where the lines pass from the pump room to the shielded room (Fig. ref:sandbox1).

Since the pumping lines are cast in concrete and thus well-anchored to the masonry wall that separates the pump room from the lab, the level of low-frequency

vibration carried by the pipes at that point is quite low. Furthermore, the lines must then pass through the shielded room wall. As compared with the masonry wall, the shielded room wall is quite soft and makes a good transducer for sound, as well as being subject to mechanical disturbance by people (unless strict rules are observed to avoid touching the room, which may be necessary when taking data). Furthermore, the pipe sections passing through the shielded room wall will inevitably be somewhat misaligned with the pipes passing through the masonry wall, requiring the use of bellows sections which will further decouple them.

These considerations cast doubt on whether the sandbox, as inserted in the main lab room, is an effective or necessary measure. What might have been more effective would be to construct a sandbox right against the shielded room where the lines pass through, thus using the shielded room wall, and the window plate, with the pipes welded into it, as one wall of the box. With the sand in contact with the window plate, its mass and internal friction would serve to deaden vibrations of the wall. This should have been more effective than deadening the pipes with the sandbox and then re-exciting them with the noisy shielded room wall.

As a second-best solution, I decided to use the sandbox as a vibrationally quiet mass coupled to the shielded room wall by being bolted strongly to the steel channel supports on either side of the window plate. The frame of the sandbox is made of steel channel in two welded sections with a "V" construction to ensure rigidity at the upper points where it is bolted to the shielded room frame. This I thought should at least reduce vibration of the wall and window plate where the lines pass through.

4.9.2 Realization

The sandbox is constructed of a double layer of $\frac{3}{4}$ in. plywood, glued and screwed together at many points, to ensure rigidity of its walls and to prevent sand leakage. The outer layer of plywood is polyethylene-laminated, and the steel frame is made of c-channel, used normally for electrical construction; both were surplus on-hand materials. The outer layer of the box is screwed into the frame at many points to ensure vibrational coupling of the frame to the box walls. Crossbars connecting the front and rear sections of the frame are bolted with heavy ($\frac{1}{2}$ in.) bolts. The bottom of the box sits on top of three c-channel crossbars, and the entire frame is resting on rubber pads to decouple it from the floor (Fig. 4.8). I poured about 614 kg of sand into the box.

The still line, ^{4}He pumping line, and ^{3}He return line all pass through the box, entering and exiting through holes drilled in the end walls (Fig.4.9), which I closed around the pipes with wood split-collars and sealed with caulk. The still line and ^{4}He line incorporate sections of flexible bellows, which are welded-in between straight sections of pipe passing through the right and left end walls. Thus, the sandbox serves to deaden any vibration carried by the pumping lines after the masonry wall.

An additional function of the sandbox, one which I think makes a greater contribution to reducing vibration at the tabletop, is to provide a large, quiet mass attached to the shielded room wall surrounding the window where the lines pass through. To this end, the steel frame of the sandbox is strongly bolted to the steel frame of the shielded room (Fig. 4.9).

The top of the sandbox provides a convenient location for the fridge control box, which incorporates a number of electrically-operated valves, pressure gauges, and electronics for thermometry and heaters, including a PID controller for maintaining a constant temperature at the mixing chamber. These components are also readable and controllable by a remote computer, which can be used to program and maintain a time record of the state of the fridge.

Figure 4.4 shows a simplified version of the plumbing circuit. In reality, the still line does not pass directly from the Roots blower to the ^{3}He rotary pump, but rather through the wall to the control box. Figure 4.8 shows the connections in and out of the control box. The still line passes through an electric throttling valve in the control box, and is tapped for a pressure gauge and an option to evacuate the line ahead of the rotary pump, before passing back through the wall to the rotary pump. This somewhat clumsy arrangement could have been eliminated by removing the valve and gauge from the control box and installing them in the pump room. The ^{3}He return and ^{4}He pumping lines also pass through the control box.

The ^{4}He line has high (convection) and low (Pirani) pressure gauges and can be switched within the control box so that the pump evacuates the ^{3}He loop. There is an additional valve and port provided on the control box for using the ^{4}He rotary to pump the Dewar space or outer vacuum can (OVC). I capped this off, and instead provided valves on the STM tabletop for this purpose, in order to eliminate one more pumping line to the tabletop which would have needed to be vibration-isolated.

The ^{3}He return line is normally routed through one of two LN_2 cold traps via electrically operated valves in the control box. The Dewar for the cold traps is

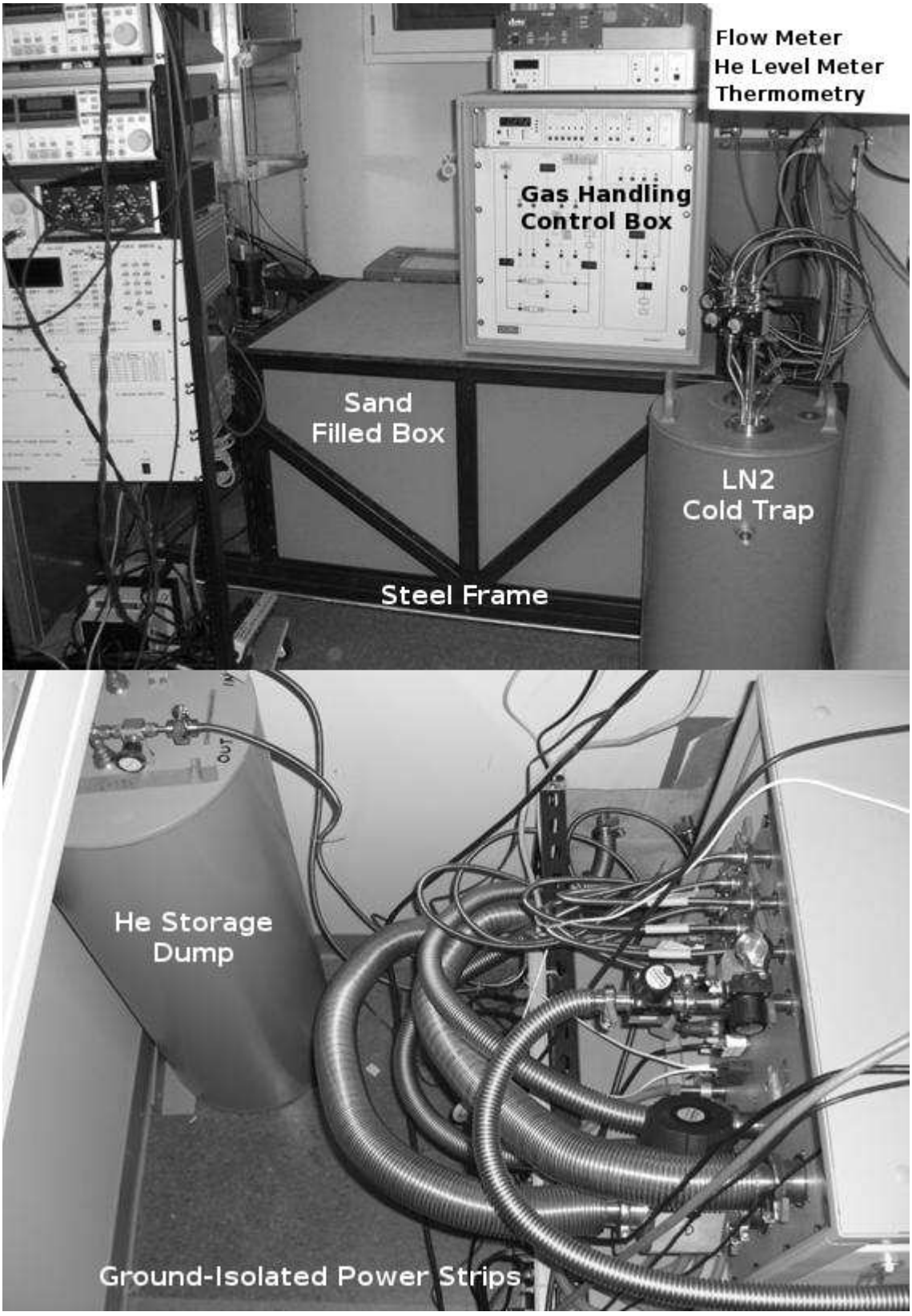

Figure 4.8: Top: The gas handling control panel sits on top of the sand box. Bottom: Plumbing connections at the rear of the control panel.

located directly in front of the control box (Fig. 4.8). When the fridge is warmed, the ^{4}He in the mixture comes out with the ^{3}He and is stored in the dump, a 100 liter tank located behind the sandbox. The dump also provides a place for the mixture to go in case of blockage of the ^{3}He line at any point after the rotary pump, or in case the fridge warms up when unattended, e.g. after a power failure. The pressure relief valves leading into the dump for this purpose begin to open at around 200 mbar (which is a bit low). For this reason, the manual valve on the inlet side of the dump (mounted atop the dump) *must remain open* at all times when operating the fridge.

I added manual valves directly on both sides of the cold traps for several reasons. The electrically operated valves in the control box do not allow throttling to control the flow rate. One of the valves is supposed to provide a variable impedance, but in reality it gives very little control, going quickly from closed to wide open. In addition, this valve leaks a bit when closed.

Another reason for the manual valves, and for having them on both the inlet and outlet sides of each of the LN_2 cold traps, is so that the traps can be detached from the system, warmed to not greater than 100^{o}C, and vacuum pumped in order to remove water and other contaminants. Having valves attached directly to the cold traps allows them to be kept under vacuum after cleaning. The lines can be evacuated through the control box vent after reattaching them to the cold trap valves (it is preferable not to pump the traps through the box while heating them).

Figure 4.9 shows the plumbing connections at each end of the sandbox. A mass flow sensor is inserted in the ^{3}He return line just before it enters the shielded room. In operating the fridge, I have found it important to limit the flow below

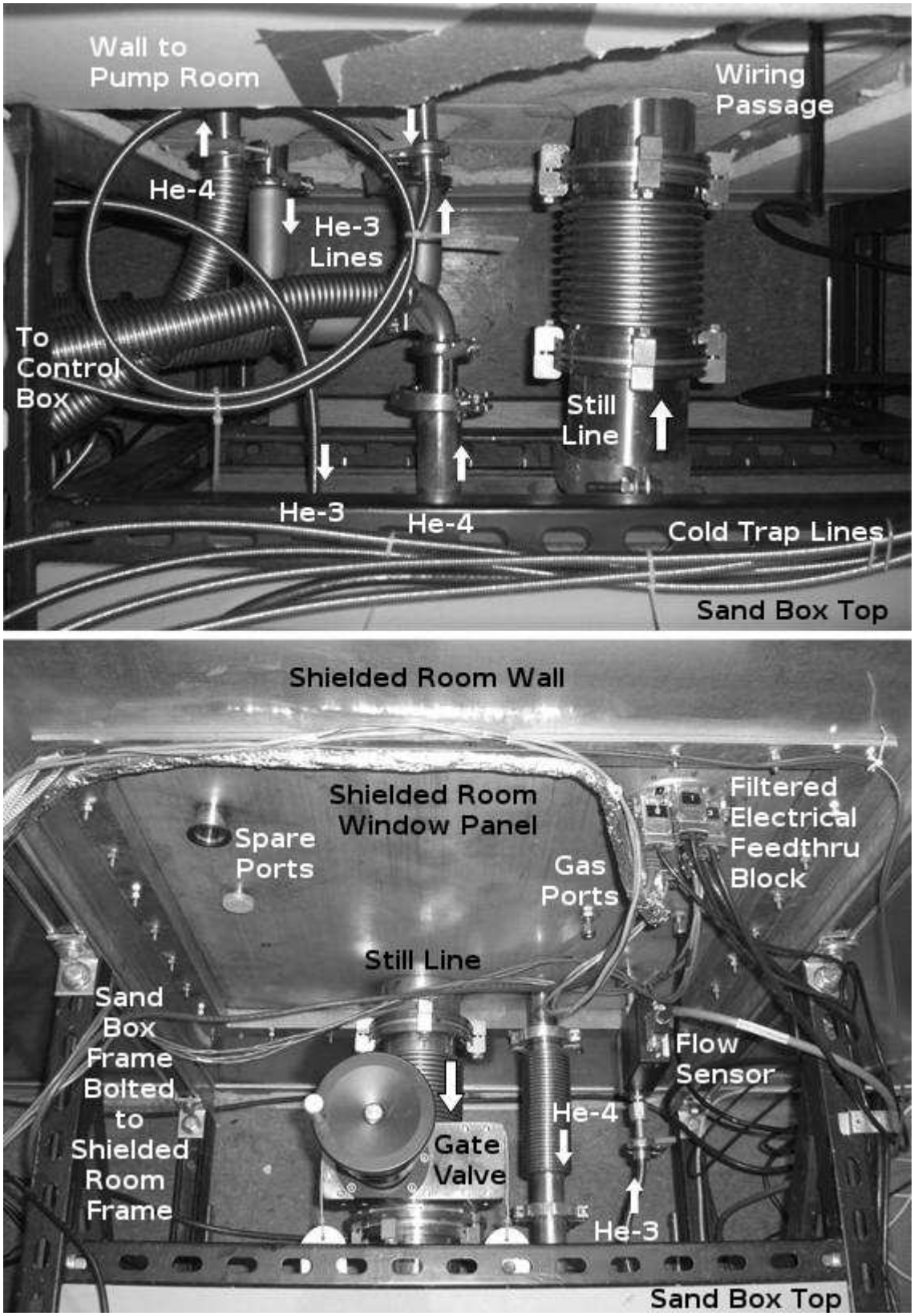

Figure 4.9: Top: Connections from the pump room to the control box and sand box. Bottom: Connections from the sand box into the shielded room.

200 sccm (standard cubic centimeter per minute) under all conditions. Higher flow rates seem to lead to blockage of the LHe cold trap, probably by water or hydrogen ice. Special care must be taken while condensing the mixture on cooldown, as the flow rate into the fridge can initially be much higher. The flow rate can be limited by throttling the manual valve coming out of the LN_2 cold trap while watching the flow rate meter.

A gate valve was also added to the still line just after it exits the shielded room. Another manual valve was added to the still line where it enters the control box after passing through the Roots blower. These valves are occasionally useful for isolating the large volumes of the still line for leak checking or breaking vacuum. They should otherwise be left open.

The window panel for the plumbing to the shielded room, actually a stainless steel plate with pipes and fittings welded into it, also provides two spare vacuum ports with NW-25 and NW-16 flanges, and two $\frac{1}{4}$ in. pressurized gas lines, one of which is normally used to supply N_2 into the room for levitating the table. An electrical feedthru block provides 8 D-subminiature 15-pin connector feedthrus with integral pi filters rated for 70 dB of attenuation at 1 GHz [134]. These lines are used for fridge thermometry, heaters, the LHe level meter, and the electrically operated needle valve for the 1 K pot, plus spare wires into the cryostat which can be used for additional experimental or instrumentation purposes.

4.10 Vibration-Isolated Plumbing to Tabletop

4.10.1 Design

Plumbing connections to the tabletop present the most critical vibration isolation problem, in order not to spoil the ability of the pneumatic supports to isolate the table from the vibration of the shielded room floor. In fact, the vibration level of the plumbing lines as they pass through the shielded room wall is higher than that of the floor, even after the measures described above. Unfortunately, the wall is not very stiff, and it makes a large diaphragm for transducing sound.

A vibration-isolated vacuum line is constructed out of flexible bellows, which may be described as a pipe which is a soft rather than a very stiff spring. The 4 in. diameter still line is particularly hard to isolate, since the spring constant of bellows of any given type must scale as the square, at least, of its diameter. Two types of bellows suitable for vacuum are available. Hydroformed bellows are essentially thin-walled stainless steel tubing with circumferential ridges pressed in. Edge-welded bellows are made of preformed concave washers welded together alternately at inner and outer edges. The latter are more expensive but have lower spring constants, and are needed to achieve good isolation.

The simplest way to use highly flexible edge-welded bellows would be to insert a section of it into a line connecting to the table. By making this section sufficiently long, the overall spring constant for static displacements could be made arbitrarily low. However, the bellows has mass, hence for any given frequency its oscillatory displacements will have a finite wavelength, and the length of the bellows that

is compressed by oscillatory force applied at one end will be limited to one-half wavelength.

For example, I located a source [135] for stainless steel edge-welded bellows having 102 mm (4 in.) ID, 145 mm OD, with longitudinal spring constant k specified as 2.45 N/mm for one segment, mass $m = 0.225\,\mathrm{kg}$ per segment, and nominal segment free length $\ell = 37.1\,\mathrm{mm}$ per segment. I calculate the longitudinal wave velocity v as

$$v \;=\; \sqrt{\frac{k\ell}{m/\ell}} \;=\; 0.0371\,\mathrm{m} \cdot \sqrt{\frac{2450\,\mathrm{kg\,m\,s^{-2}/m}}{0.225\,\mathrm{kg}}} \;=\; 3.9\,\frac{\mathrm{m}}{\mathrm{s}} \tag{4.4}$$

which shows that for frequencies as low as 10 Hz, the effective spring constant cannot be softened by increasing the length of this bellows beyond about $3.9\,\mathrm{m}/20 = 19\,\mathrm{cm}$.

On the other hand, since the mass of the table is much greater than that of the bellows, the induced motion of the table will be much smaller than the motion of the bellows. High-frequency displacements will be reflected at each end, and the bellows will have resonant modes for $f = (n + \frac{1}{2})\,\frac{v}{\ell}$, where ℓ is now the total length of the bellows.

The impulse delivered to the table will be proportional to the amplitude of motion of the bellows. Therefore it is desirable that the half-wave resonant frequency of the bellows (10 Hz for 19 cm in the case above) lie as low as possible below the frequency range of concern. Damping will also affect the response of the bellows to external vibration, particularly on resonance.

If the bellows is held vertically, and one end is subject to a small horizontal displacement, the restoring force due to the bellows spring is quadratic, not linear,

in the horizontal displacement, since if the length of the bellows, when perfectly vertical, is ℓ_0, the extended length of the bellows when displaced horizontally by x is $\ell = \sqrt{\ell_0^2 + x^2}$, whence

$$\frac{d\ell}{dx} = \frac{1}{2}\frac{2x}{\sqrt{\ell_0^2 + x^2}} \quad \Longrightarrow \quad \left.\frac{\mathrm{d}\ell}{\mathrm{d}x}\right|_{x \ll \ell_0} = \frac{x}{\ell_0}. \tag{4.5}$$

Thus if the spring constant of the bellows for extension of ℓ is k, the spring constant for static horizontal displacement is $k\,\dfrac{x}{\ell_0}$. For dynamic displacements at a given frequency, ℓ_0 will have some effective value less than the geometric length, but the stiffness k will still be small for small amplitude displacements.

However, if the bellows is evacuated, extension of the bellows by $\mathrm{d}\ell$ will require work $\mathrm{d}W = A\,\mathrm{d}\ell \times 1\,\mathrm{atm.}$, where A is the average cross-sectional area. If the extension is due to a small static horizontal displacement $\mathrm{d}x$, we can equate this to the formula $\mathrm{d}W = kx\,\mathrm{d}x$ for extension of a spring of constant k:

$$\mathrm{d}W = A\,\mathrm{d}\ell \times 1\,\mathrm{atm.} = \frac{A}{\ell_0}\,x\,\mathrm{d}x \times 1\,\mathrm{atm.} \equiv kx\,\mathrm{d}x \tag{4.6}$$

and thus find an effective spring constant $k \equiv \dfrac{A}{\ell_0} \times 1\,\mathrm{atm.}$

This effective spring constant for lateral displacement of an evacuated bellows has been interpreted by some authors [136, 137] as "tension" in the bellows, but this is a bit confusing since, if the bellows is held at both ends, the atmospheric pressure on its cross-sectional area is borne by whatever is holding the ends. Pressure around outer edges of each convolution of the bellows causes a local deformation equivalent to compression, and the pressure around inner edges causes a local deformation equivalent to extension, but the compression and extension alternate between inner and outer edges. Thus there is no average deformation equivalent to an overall

tension, other than that due to the normal spring if the bellows is stretched past its free length. To put this another way, the force is external pressure on the ends of the bellows, not an internal tension of the bellows.

However, as regards the restoring force given small horizontal displacements, the effect of atmospheric pressure on the evacuated bellows acts as if it were a tension. One easily sees that $\frac{x}{\ell_0}$, in the case of a static displacement x, is just the tangent of the angle, and the same factor obtains for the case of a dynamic displacement, where ℓ is an effective length. From this one can derive the equation of a vibrating string, as if $A \times 1\,\mathrm{atm.}$ were the string tension.

For the 102 mm bellows, with $\ell = 19\,\mathrm{cm}$, $A = 0.0121\,\mathrm{m}^2$ [135] and one obtains $k = 6.4\,\mathrm{N/mm}$, which is 2.6 times stiffer than the longitudinal spring constant. It follows that the lateral resonant modes will be $\sqrt{2.6} = 1.6$ times higher than the longitudinal modes, or equivalently, that the bellows should be 1.6 times longer in order to obtain the same resonant frequencies.

I conclude that it is desirable to use as long as possible a length of highly flexible edge-welded bellows, and add damping to suppress resonance and transmission of vibrational energy through the bellows. Since we want to suppress vibration that may be transmitted through the floor, it does not seem appropriate to use a damping mechanism, such as magnetic damping, which requires an external support. A cloth or rubber shroud could be wrapped around the exterior of the bellows to increase damping. Attaching air vanes would be another possibility.

References [136] and [137] discuss various geometries for bellows isolators, but the discussion is based on static displacements and does not consider that, for ex-

ample, the 102 mm diameter × 185 mm long bellows discussed here has an internal resonance as low as 10 Hz. Thus I believe the actual dynamics of the "crossed bellows" and "double gimbals" designs discussed are more complicated than suggested by the analyses given, and therefore that the results obtained may depend on serendipitously tuned avoidance of resonance with pumps or other strong local sources, or other aspects of construction which are not accounted for.

I considered several possible geometries for bellows isolators. One was a two-stage isolator in the form of an inverted "T" (Fig. 4.10 C) using two 185 mm long horizontal sections of bellows and one 300 mm vertical section, with a mass of Pb bricks hanging from the vertex. The two horizontal sections would balance each other, but atmospheric pressure unbalanced in the vertical direction would support most of the weight of the Pb bricks when the bellows were evacuated. A tire tube would support a small fraction of the weight for stability, without trasmitting much vibrational energy to the mass, and would catch the entire weight when vacuum was broken.

Based on this design, I placed an order for both the 102 mm diameter bellows for the still line and 25 mm diameter bellows for the ^{4}He pumping line. Since this was a custom order, it could not be readily recalled once I realized that there might be a problem with my design.

The problem was that the pressure at the top end of the vertical section was uncompensated. Although the table's pneumatic suspension could easily compensate the 823 N due to static pressure, the 102 mm diameter cross section of the vertical pipe would create a diaphragm transducing any internal pressure variations

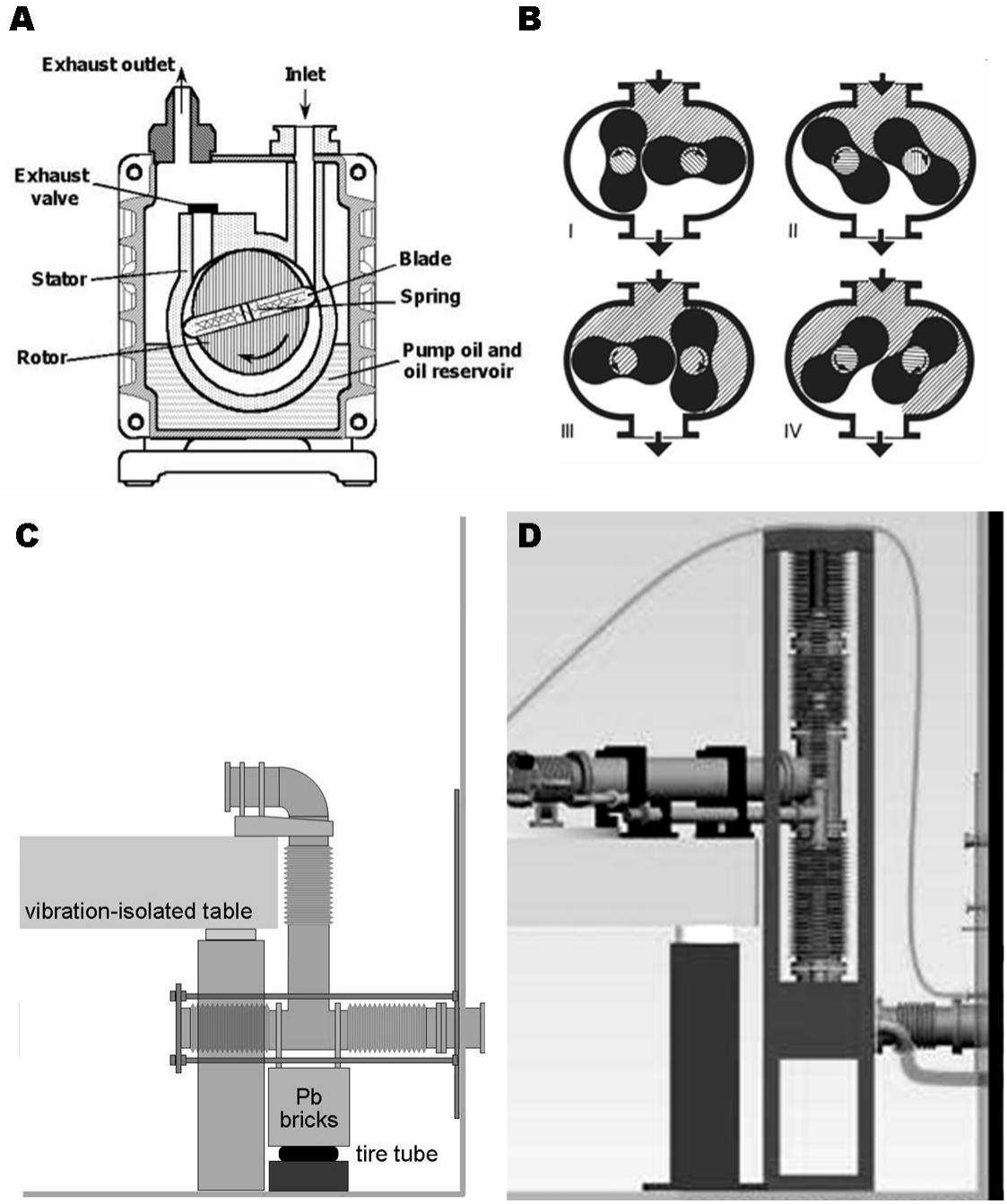

Figure 4.10: Principles of pumps and plumbing vibration isolation schemes. A. Principle of rotary pump. Spring-loaded sliding vanes maintain contact with outer cylinder as inner cylinder rotates. Center of mass of vanes, and hence of pump, oscillates vertically, generating vibratory momentum at twice rotation rate. B. Principle of Roots pump. Less vibration is generated than by rotary pump, but strong pressure oscillations are generated at inlet. C. My early 'inverted T" concept for isolation of plumbing lines to tabletop. Mechanical performance would probably have been good, but pressure variations in still line would have transduced to tabletop in vertical direction. D. "Sideways T" design avoids coupling pressure variations to table in any direction.

to table vibration. Average pressure inside the still line at the table is expected to be ∼30 Pa. The line is being pumped by the Roots blower (Fig. 4.10 B), which does not operate like a continuous turbine but rather takes 240 scoops of gas per second. The two lobes rotate at high speed and kick gas backward in part of each cycle as well as drawing it forward. The 240 Hz pressure variation at the inlet of the Roots is thus likely comparable to ±100% of the average pressure. While this pressure variation is likely to be highly attenuated at the other end of the still line, the force transmitted through the spring constant of the 102 mm bellows is $\sim 3 \times 10^{-4}$ N for a 1 μm motion, whereas a 0.1 Pa pressure variation would transduce to 8×10^{-4} N force on the table.

In order to avoid this potential problem, I decided to use a geometry (Fig. 4.10 D) which would not transduce any pressure variation in the pumping lines to table motion. In this "sideways T" design, the vertex of the "T" is held by rigid pipe which is clamped firmly to the table. Atmospheric pressure on the upper and lower ends of the bellows is held by the frame and there is no net force on the table. I was able to use the bellows as ordered, but the result is a bit strange-looking. In order to make the bellows as long as possible, I used the longer sections for the lower bellows, and clamped the two shorter sections together for the upper bellows.

4.10.2 Realization

I built the box to support the T-bellows (Figs. 4.11 and 4.12 using primarily surplus material. The frame is made of Al channel and is strongly bolted together. A heavy Al yoke holds the elbows at the lower ends, while the upper end of the still

line bellows is o-ring sealed directly to a plate that is bolted to the frame. Three sides of the box are covered with Al-laminated Masonite panel, bolted at many points to the frame, which provides both stiffening and damping. The open front side is stiffened with diagonal crossbraces. By tapping on the box, one can tell that it is quite vibrationally "dead."

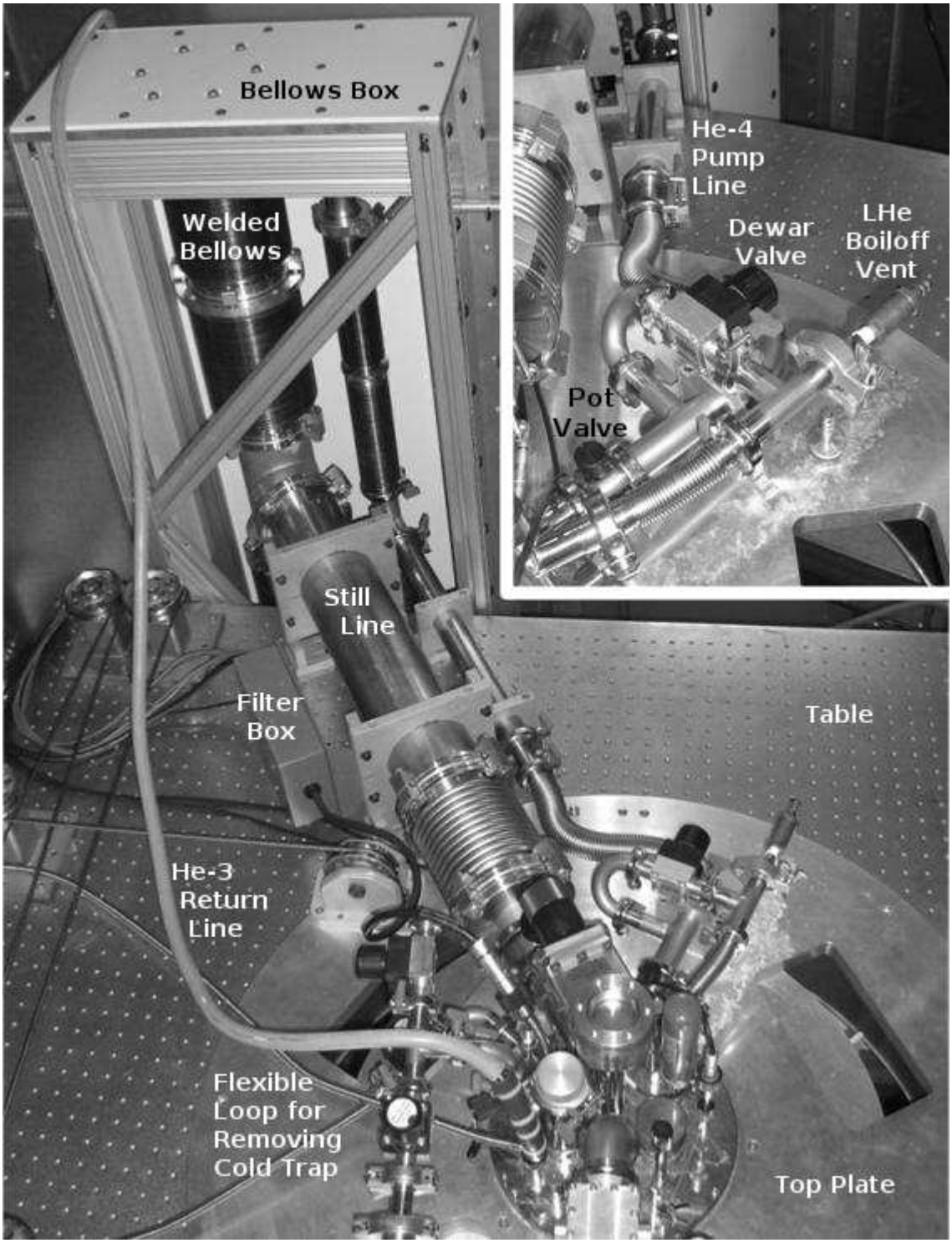

Figure 4.11: Top view of T-bellows box and routing of plumbing lines on tabletop. Inset: The He-4 pumping line serves alternately to evacuate the dewar LHe space and pump the He-4 pot.

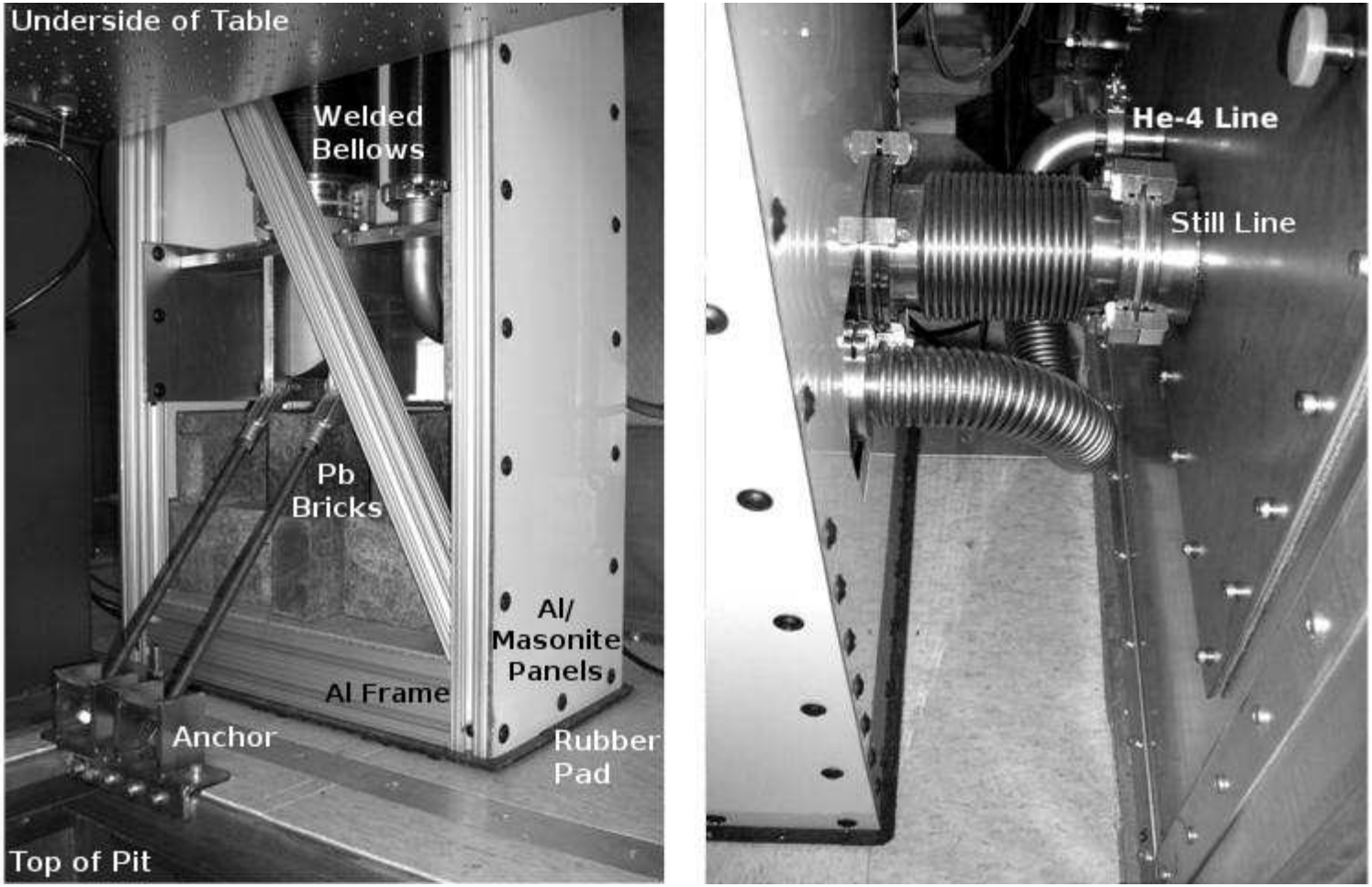

Figure 4.12: Front and rear views of the lower half of the T-bellows box. Left: Front view from the pit. The box rests on a rubber pad. It is weighted with 200 lbs. of Pb bricks to lower its response to vibration. The anchor and rods pull against the atmospheric force on the evacuated lines. Right: Rear view showing hydroformed bellows connecting to the shielded room wall.

The bellows box rests on a rubber pad and is weighted with 113 kg. of Pb brick for further isolation from the floor. It is airgapped from the table by $\frac{1}{2}$ in.. Since atmospheric pressure on the elbows applies about 943 N horizontally toward the back of the box, this force is borne by two rods in front which are anchored to the upper rim of the pit.

For best performance of the T-bellows isolators, the rigid "T" fitting joining the two bellows sections should be tightly aligned with the bellows in their equilibrium positions. To ensure this, after fully installing the box in its final location, I removed the sections of hydroformed bellows in the still and pumping lines on top of the table (Fig. 4.11) and replaced them with blank flanges to cap the lines. I then floated the table and evacuated the bellows, and loosened the clamps holding the pipes and the bolts holding the clamps to the table. The bellows automatically drew the "T" into the correct position and rotation. I then tightened the clamps and replaced the tabletop lines. This procedure might need to be repeated in case there is any disturbance of the bellows box, table, or piping on the tabletop.

The ^{4}He pumping line is routed on the tabletop through a butterfly valve to the 1 K pot and through a bellows valve to the Dewar LHe space (Fig. 4.11, inset). The Dewar space is also normally vented for liquid boiloff through a check valve. This can be removed and replaced by a nipple inlet for pressurizing the dewar, e.g. with He gas to blow out LN_2. Finding a compact and convenient arrangement of available components for this tabletop plumbing took a number of trials.

The ^{3}He return line is a floppy, flexible, $\frac{1}{4}$ in. diameter stainless steel bellows, and I did not think it required any additional vibration isolation. To improve

damping of vibrations transmitted along its length, I slit a piece of rubber tubing to fit over it. I also added a piece of heavy rubber hose to reinforce the line at the point where it attaches to the LHe cold trap, to prevent repeated flexure at that point leading to failure of the line.

4.11 Overall performance

The final performance assessment of the measures taken for vibration isolation will be the quality of images and spectra obtained when the system is used for mK-STM. Vibration issues not addressed in this chapter include the rigidity of the fridge and support structures for the STM body and of the STM figure "G" itself, as well as noise generated by the 1 K pot [138, 139, 140]. However, these issues have nothing to do with the installation of the pumps and plumbing. To assess how well I did with the latter, I took a series of careful vibration measurements at the tabletop.

Figure 4.13 shows the ratios of vibration amplitudes for the X, Y, and Z axes and for frequencies between 1 and 400 Hz. Two conditions are compared: table floated and all plumbing disconnected, and table down, i.e. isolators deflated and table resting rigidly through its legs on the shielded room floor. This gives a measure of the performance of the table isolators alone. As can be seen, the isolation is most effective at frequencies between 10-100 Hz, with some effectiveness up to a few hundred Hz. For 1-7 Hz, the Z component is actually higher with the table floating.

Unfortunately, the level of vibration obtained with this table in this setting is far from the best that has been achieved, at higher cost, in other labs. For example, Fig. 4.14 compares our (Z-component) vibration levels with data reported by J. C.

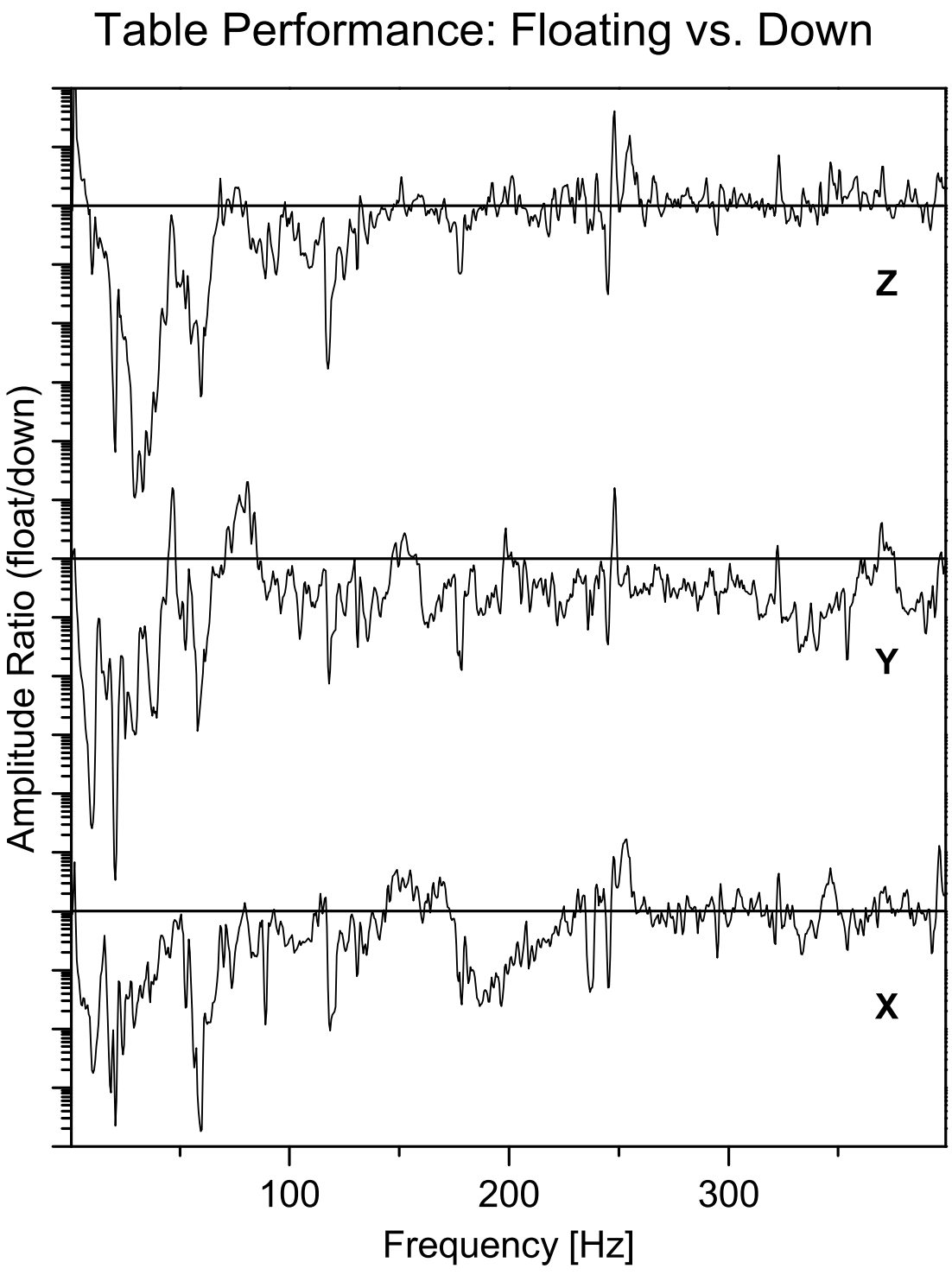

Figure 4.13: Vibration isolation performance of the table alone, without the plumbing. The vertical axis is the ratio of the amplitude of vibrational noise with the table floating to that with the table down; the scale is logarithmic and marked in decades. For each mode, the horizontal line represents unity, i.e. no difference between table up and table down. Values above this line represent resonant enhancement of the ambient noise, values below represent effective isolation.

Davis for a mK-STM installation at Cornell. That lab uses a homemade table in a triangular shape with three pneumatic isolators. The table itself and the legs supporting its isolators are Pb weighted (3 Tons total). They are placed within an acoustically quiet room which is mounted on a 30 Ton concrete block, which itself is supported by 6 air springs and enclosed within an outer acoustic room. The pumps are located in separate chamber, and the entire setup is located in a quiet basement. As seen in Fig. 4.14, the vibration level they report, measured by acceleration, is 100–1000 times lower than ours between 2–400 Hz.

Although Davis's state-of-the-art installation provides a useful comparison, it would have been impossible to equal his level of vibration performance with the basic setup that I started with.

In hindsight, some improvement could likely have been made by better isolating the table legs from the shielded room walls and floor. One way this could have been done would have been to cut holes in the floor for the table legs. To maintain electromagnetic shielding, the legs themselves, or a metal plate interposed between them and the lab floor, could be joined to the shielded room floor with flexible metal screen. I have done a similar installation in another lab. Additionally, passage of the plumbing lines through the shielded room wall could have been done through a sandbox constructed as suggested in Section 4.9. Another possibility would have been to deaden the shielded room floor by resting it on a bed of sand, but this would need to have been done when the shielded room was installed, and would have created problems for the contractor.

Some form of external friction or aerodynamic damping should yet be added

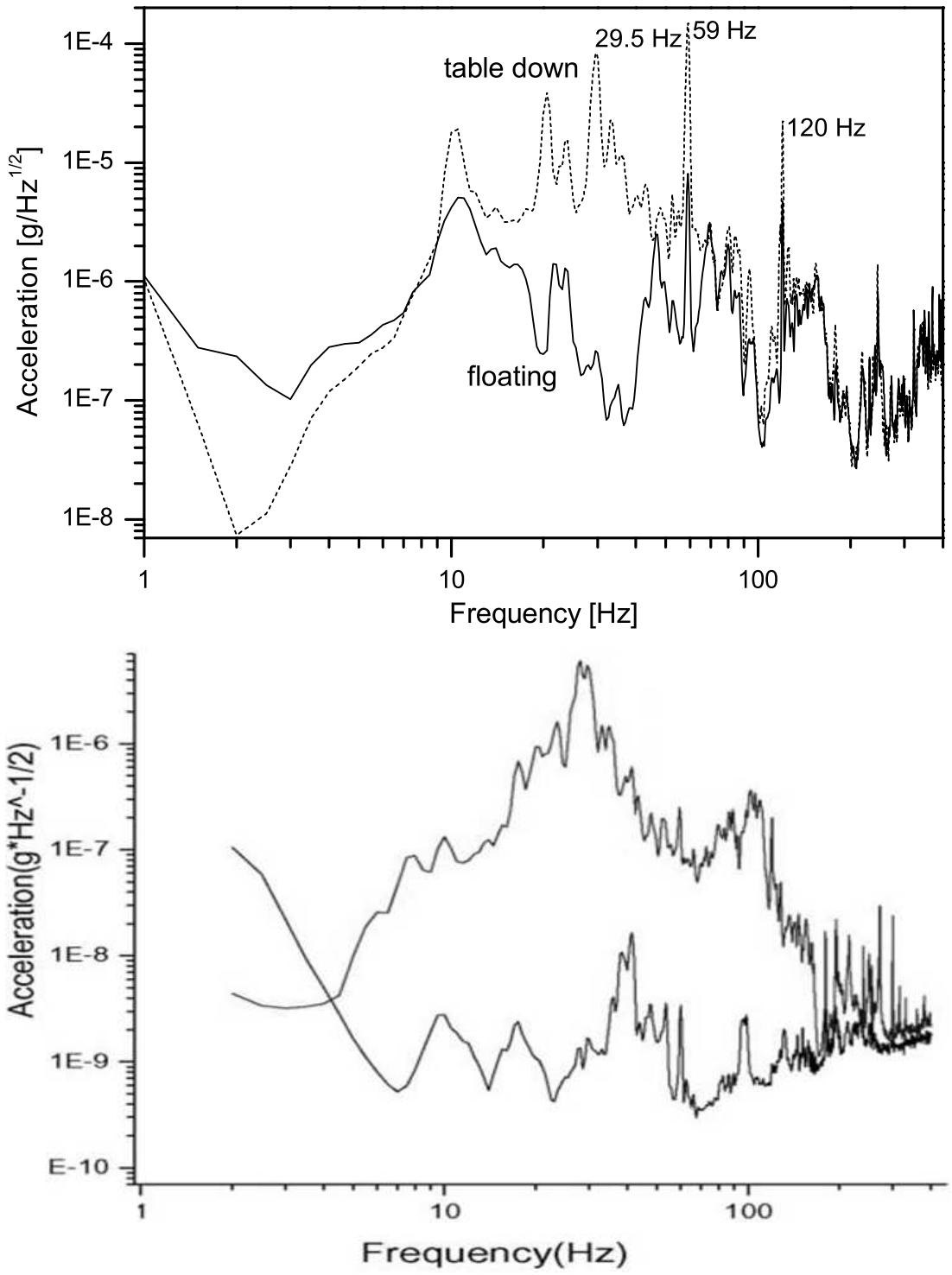

Figure 4.14: Top: Vibration levels measured at our tabletop under operating conditions with the table down and floating. Bottom: Comparable measurements reported by J. C. Davis [141] for a mK STM housed in a state-of-the-art low vibration lab with double pneumatic isolation, showing the vibration levels with isolators down and floating.

to the T-bellows isolators. It also is likely that the tabletop will be quieter at frequencies of a few hundred Hz when the shielded room has been lined with sound-absorbing materials. Applying such materials to the outside of the room might also help.

A final, overall assessment of the vibration-isolation measures described in this chapter is presented in Table 4.1, which compares the quadrature-summed (square root of sum of squares) totals for X, Y, and Z acceleration between 2-100, 2-200, and 2-1200 Hz. under various conditions. I chose these overlapping ranges because the cumulative totals are the relevant measure, but most of the weight is contributed from low frequencies.

Looking at the numbers, one sees that the acceleration totals are about an order of magnitude lower when the table is floating. The pumps apparently contribute at most about 10% to the totals when they are running. The contribution from the pumps for room 1220 is about half as large, even though these pumps are not connected through plumbing lines to our table, are located almost twice as far away from our table, and are isolated from the floor slab by an additional concrete inertia block. Finally, the difference between the levels with the plumbing to the tabletop connected and disconnected is at most a few percent.

4.12 Conclusions

I believe the vibration isolation measures taken in the plumbing installation are adequate and well-matched to the basic facilities. The most important measures

Plumbing connected						x	x	x
Table floating				x	x	x	x	x
1224 Pumps running			x		x		x	
1220 Pumps running								x
Mode	Freq. range	μm/s^2	μm/s^2	μm/s^2	μm/s^2	μm/s^2	μm/s^2	μm/s^2
Z	2-100 Hz	1869	1935	126	146	130	142	131
	2-200 Hz	1883	1949	141	160	144	156	146
	2-1200 Hz	1886	1953	194	212	205	208	202
Y	2-100 Hz	414	483	46	52	35	30	-
	2-200 Hz	429	497	54	59	41	44	-
	2-1200 Hz	445	513	116	118	116	143	-
X	2-100 Hz	502	589	25	26	25	27	-
	2-200 Hz	519	604	39	39	35	40	-
	2-1200 Hz	541	626	119	115	133	157	-

Table 4.1: Summary of vibration measurements taken at the tabletop, near the axis of the fridge and STM, under various conditions as indicated by the matrix at top. Each measured value is the quadrature sum of acceleration components measured within the indicated (cumulative) frequency ranges. It is seen that the vertical component (Z mode) is a factor of four larger than the horizontal components when the table is not floated, and a factor of 2-3 larger in other cases. Floating the table reduces the acceleration in the range 2-100 Hz by an order of magnitude, roughly as promised by the manufacturer. Connecting the plumbing lines has only a small effect on the totals, and even seeems to decrease the Y component at low frequencies, while increasing the X and Y components at higher frequencies. Similarly, the effect of turning the pumps on is small, and there is not much difference between the cases where the pumps for lab 1224 are running and when the 1220 pumps are running. Thus, the level of isolation achieved for the pumps and pumping lines is adequate from the perspective that their contribution to the totals is much less than the vibration level of the table itself as installed in the lab.

were the use of rubber pads to reduce transmission of vibration from the pumps to the floor slab, the concreting of pipes into the masonry wall of the pump room, and the T-bellows isolation of the plumbing lines to the tabletop. More elaborate measures to isolate the pumps and plumbing lines might have reduced their contribution to the tabletop vibration level, but this contribution is less than 10% of square-integrated acceleration in the frequency range 2–1200 Hz. The tabletop vibration level appears to have been determined primarily by the effectiveness of the pneumatic isolation system of the optical table system itself, and by the level of ambient vibration of the shielded room floor and walls. The sandbox was probably unnecessary, but would have been more effective if built right against the shielded room wall.

Chapter 5

Mounting the STM and Wiring the Cryostat

In this chapter I describe the design and construction of the STM mount, which extends downward from the cold plate of the dilution refrigerator and places the STM in the center of the high-field magnet. I then describe the cryostat wiring which enters the vacuum space at the top of the cryostat and connects to the STM, thermally anchored and filtered at the various stages of cooling along the way. I describe the design and construction of two kinds of filters against radio frequency (rf) energy which are used at the coldest stage. I also describe a magnetically shielded sample mount which was used for experiments toward the development of Josephson phase STM [142].

5.1 STM mount

The STMs that have been used in the LPS 4 K STM lab [126] are derived from designs developed at Berkeley by Seamus Davis and Shu-Heng Pan [44]. A principal modification from the Pan–Davis design is that the STM is suspended from a metal flange at its top, rather than resting on a cold plate.

The STM body is made of Macor, a machinable ceramic. An advantage of using a ceramic material for the STM body is that its thermal expansion coefficient, particularly at low temperature, is very small, as are those of the lead zirconium ti-

tanate (PZT) scanner tube and of the sapphire prism used in the walker mechanism. These components comprise the figure "G" loop of the STM, and their differential expansion and contraction due to temperature drift would be disastrous, particularly for the ability to hold the tip at constant height without feedback during spectroscopic measurements. A disadvantage of Macor, relative to metallic materials, is its very low thermal conductivity, implying a long cooldown time before stabilization, and a need for the tip, sample and piezos to be cooled through the wiring.

The STM mount was designed to accomodate a single-tip STM which is a legacy from the LPS 4 K STM, and to also accomdate a new dual-tip design intended for use either in Josephson phase STM [142] or for independent dual-tip operation of the STM. The body of the dual-tip STM is longer and wider in order to accomodate two stacked, independent, Pan-type walker mechanisms [43] and two concentric piezo scanner tubes.

The overall configuration of the STM mount is shown in Figure 5.1. The Macor STM body is bolted to a Cu flange, with bolt patterns provided for both the single and dual-tip STM designs. The STM mounting flange is suspended inside a Cu can for electrical shielding. The can is 7 in. long × 2.3 in. OD, and is designed to fit inside the tailpiece of the 100 mK radiation shield without touching. Three 2.5 in. long × $\frac{1}{4}$ in. square Cu rods suspend the STM mounting flange from the Cu top flange of the STM shielding can. The shielding can top flange is in turn suspended by three 11.7 in. long × $\frac{1}{4}$ in. × $\frac{1}{2}$ in. rectangular Cu bars, which are bolted to the mixing chamber cold plate.

All these main Cu parts of the STM mount are Au-plated to promote thermal

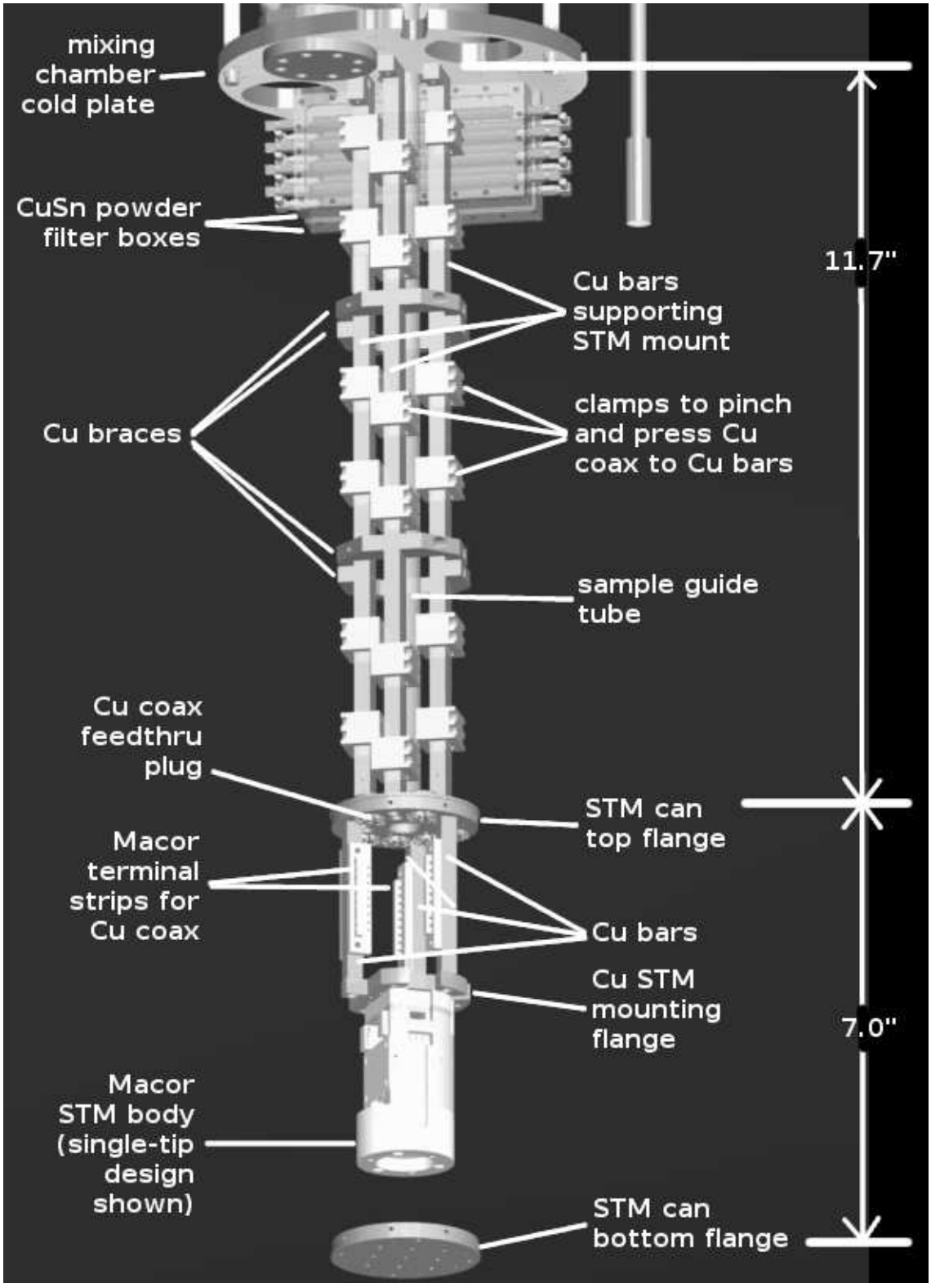

Figure 5.1: Computer rendering of the STM mount, bolted to the undeside of the mixing chamber cold plate. Behind it are two boxes containing 4 bronze powder filters each. The wiring is not shown, but would run along the bars and under the clamps. Also not shown is the Cu can for electrical shielding of the STM.

contact to each other and to the Au-plated Cu cold plate of the fridge. The 11.7 in. long upper bars are bolted to the cold plate by two M3 cap screws each, and their top ends are extended in an "L" shape to facilitate this, since the bolt holes on the cold plate are spaced 0.59 in. (15 mm) apart. At the lower end of the bars, they are bolted to the top flange of the can by two UNC 4-40 cap screws. The three shorter bars suspending the STM mounting flange inside the can are attached with single 4-40 cap screws threaded into their ends.

The three 11.7 in. long bars could not be arranged in an equilateral triangle due to space constraints imposed by the design of the fridge. Instead, two bars are approximately coplanar with the axis, on opposite sides of it, with the third bar in front (as viewed in Fig. 5.1). This geometry is inherently less stiff in the front-back direction than in the right-left. Making the bars rectangular in cross-section, with the long side running front-back, compensates for this weakness. In addition, two sets of Cu braces are bolted between the three bars, pinning their lowest internal vibrational modes and stiffening the assembly.

A $\frac{1}{2}$ in. OD Cu tube is soft-soldered into the top flange of the STM can, on its axis, and runs up to the mixing chamber cold plate where it is to be sealed by an rf-tight shutter (not yet developed). This tube provides access to the STM for sample and tip exchange, and guides the exchange rod. It is thermally anchored at the mixing chamber cold plate via a Cu clamp which is bolted to the plate, although the cooling of this tube is not critical.

As discussed in Sec. 3.2, the bolts should be as tight as possible for good thermal contact. We had originally specified the use of Ti bolts on the STM mount

in order to avoid magnetic materials, due to our interest in Josephson phase STM. However, Ti has quite small thermal contraction, $\Delta\ell/\ell = 0.151\%$ between RT and 4 K, compared with 0.324% for Cu [4]. This 0.15% difference is 6× greater than when using stainless steel bolts [4].

The maximum recommended load on a 4-40 stainless steel bolt into Al is 0.8 kN [4], and the shear strength of Cu is about the same as Al. Ti is stronger than stainless steel, but my experience is that an overtightened stainless steel screw into Cu will strip the Cu threads before breaking the screw. Therefore I assume a similar rating for a 4-40 Ti bolt into Cu. The cross sectional area of the bolt is $\sim$4 mm^2, and the Young's modulus of Ti alloys is $\sim$110 GPa. Based on these numbers, we expect stretching of up to about 0.18% when the Ti bolts are tightened at RT. Comparing this with the 0.15% differential thermal contraction, we see that the Ti bolts would loosen substantially or completely when cold.

For this reason, it is probably better to use ZnCu brass bolts, which have $\Delta\ell/\ell = 0.38\%$, slightly greater than that of Cu. Although Ti is as much as 5 times stronger than ZnCu, the factor limiting tightness of the bolts is more likely the Cu threads. Since the brass bolts will tighten slightly on cooling, they should not be overtightened.

5.2 Cryostat wiring

5.2.1 General requirements

STM and STS at millikelvin temperatures normally require only low-frequency (dc to about 20 kHz) electrical connections between the STM inside the cryostat and the external instrumentation at room temperature. However, the wiring must satisfy a number of demanding and sometimes conflicting criteria. Lengthwise thermal conduction must not impose an excessive heat load on the refrigeration, but reasonably low-resistance electrical connections must be provided from room temperature down to the STM. Thermal anchoring must be provided at each stage of cooling in order not to impose excessive heat loads on the colder stages, but electrical insulation must be maintained.

Since tunneling resistances are typically up to 1 GΩ and might be as high as 300 GΩ, the tip and sample wires must be very well insulated. The insulation must be able to withstand up to ∼200 V which is periodically applied to clean the tip by field emission. Capacitance must also be limited to minimize the noise current due to noise voltage present on the input of the transimpedance preamplifier.

Since the STM body is generally made of an insulating material (Macor in our case), the wires must carry away and sink the bulk of any heat dissipated due to the tunneling current or due to the operation of the piezos.

Achieving the lowest physical temperatures at the tip-sample junction, and the lowest effective temperatures in spectroscopy, requires shielding and filtering to exclude ambient rf signals and noise generated by the instrumentation and wiring at

Function	Wire	Signal type	BW f_{max} [KHz]	Max V [V]	How many
STM	tip, sample	low noise	20	200	2×2
STM V_{sense}	tip, sample	shielded pair	20	200	2×2
position sensor	high, low	low noise	20	low	2×2
scanner	X±, Y±, Z	HV, triangle wave	1	300	2×5
walker	1-6, Gnd	HV, fast rise	10	300	2×7
thermometry	3 pairs	low f, low V	1	10	6
spares		each type			1:2

Table 5.1: Wires needed for the dual mK-STM system.

temperatures above that of the STM. Filtering of the wires for the walker must not excessively slow the rising edges of the waveforms that drive the walker's stick-slip mechanism, taking into account the inherent capacitance ($\sim$1–3 nF) and resistance ($\sim$100 Ω) of the wires and piezos. These wires must also be insulated to withstand several hundred volts, the normal operating voltages of the piezos.

Table 5.1 summarizes the wiring required by the millikelvin STM system, taking into account that the system was designed to accommodate a double-tip STM with two walkers and two scanners. The required wires divide into two broad categories: (1) signal wires, which connect to the tip and sample, plus the capacitive position sensor for the walker, and (2) all others, including wiring to the piezo scan tube, the walker piezos, and resistance thermometers. In addition, spare wires of both types need to be provided both to replace inevitable failures, and to provide for possible uses not thought of in advance.

5.2.2 Signal wires

The signal wires are those particularly in need of shielding and low, stable capacitance, and include the STM tip and sample wires, and the capacitive tip position sensor wires. All of these wires are driven by low-impedance instruments at the warm end, and their cold end terminations are usually high-impedance. The tunneling current is very small, and as a result its measurement will be very sensitive to charge induced by electric coupling from noise sources.

For normal STM with two independent tips, a minimal wiring scheme would require three signal wires (Fig. 5.2 A): one for the sample, plus one for each tip. The sample wire would conventionally carry the bias voltage, and each tip wire would conventionally drain into a transimpedance amplifier (current-voltage converter). Each transimpedance amplifier acts as a virtual ground, i.e. an active device that supplies current as needed in order to maintain its input at some set potential, which might be the environmental ground potential, or might be a different setpoint. In some experiments, each tip might be set at a different potential.

Somewhat more complicated wiring schemes may provide better performance. Züger *et al.* [143] used separate twisted pairs to carry differential tip and sample signals referenced to a common local ground at the STM body (Fig. 5.2 B). This arrangement may be expected to reduce any noise from potential differences between the instrumentation and the local (cold) environment, which might couple unequally to the tip and sample.

le Sueur and Joyez [144, 109] demonstrated a dramatic reduction in voltage

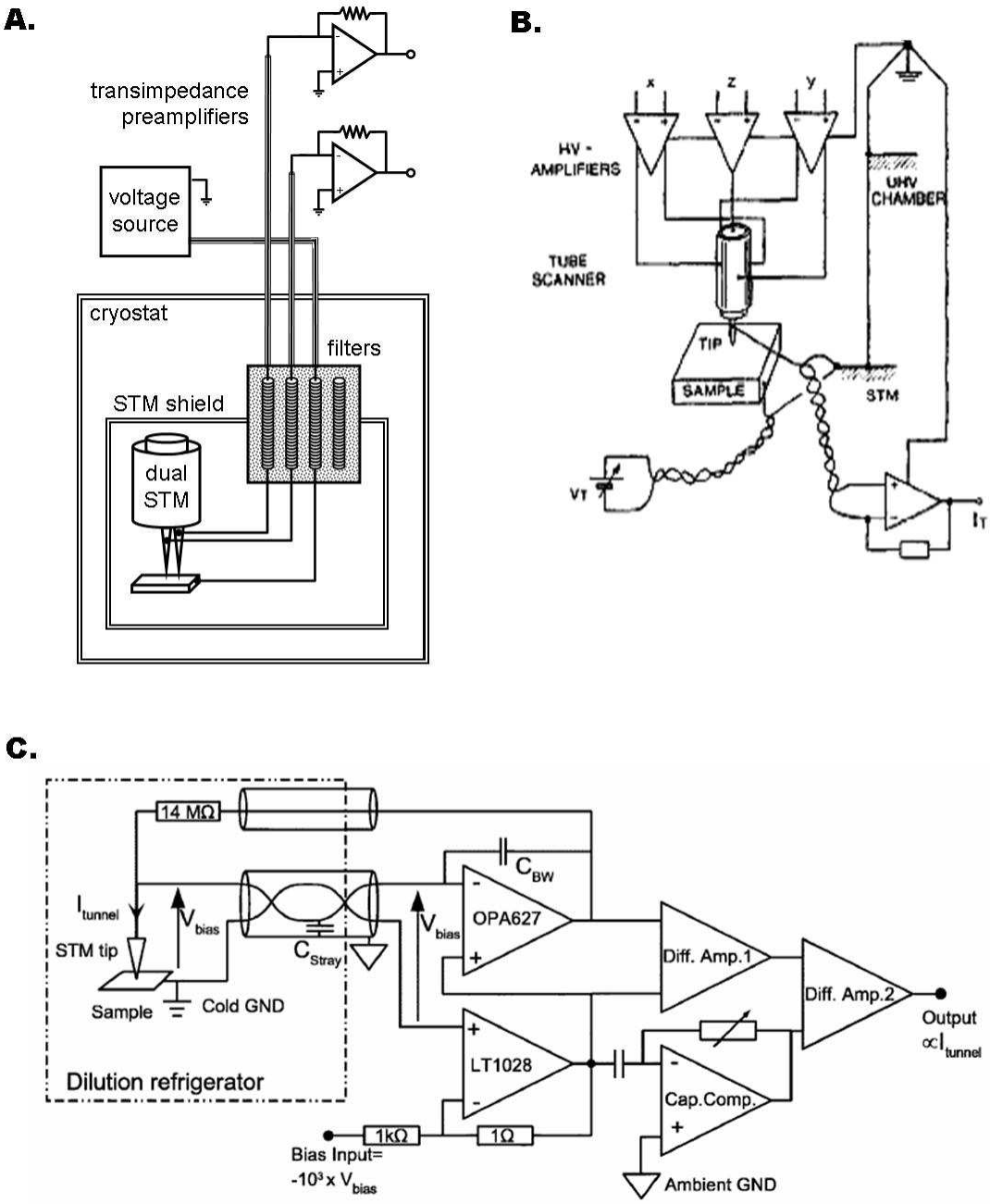

Figure 5.2: Basic schemes for STM signal wires. A. Simple circuit used in LPS 4 K STM as adapted for mK dual STM. B. The scheme used by Züger *et al.* [143] (with scanner wiring shown), essentially the same as A. except that twisted pairs are used instead of coax. C. Scheme used by le Sueur *et al.* [144]. Shielded twisted pair is used to sense the tip-sample voltage independently of the tunneling current, which is supplied through a separate coax and the cold 14 MΩ resistor. The LT1028 sets the bias voltage and is selected for ultra-low voltage noise. Ac voltage present at its output measures noise coupled through the stray capacitance in the shielded twisted pair, which is offset in final output via "Cap. Comp.".

noise, and hence improved spectroscopic resolution, by using a twisted pair in parallel with the tunneling current wires to sense the voltage between tip and sample (Fig. 5.2 C). Additionally, the transimpedance feedback resistor, through which the tunneling current flows, was mounted on the cold STM to reduce Johnson noise in the resistor, while keeping the active devices of the preamp at room temperature. They claimed that this cold resistor–warm amplifier arrangement provided most of the benefits of a cold transimpedance preamp, while avoiding the difficulties of the latter, and that the result was a spectroscopic effective temperature of $\sim$45 mK, very close to their sample temperature, and much better than previous efforts using conventional electronics and wiring.

At least one commercial supplier [145] provides CuNi braid-shielded twisted pair wiring, including superconducting NbTi and, for connection to RT, brass conductor versions. In combination with CuNi or stainless steel tubing to provide better shielding after low temperature filtering, this might be a good option for providing voltage-sense pairs or other situations where elimination of magnetically coupled noise is critical.

For the proposed Josephson phase STM [142], two superconducting tips would be joined by a flexible superconducting wire, which with tunneling to a superconducting sample would form a SQUID. In this approach, there would be only one tip-sample voltage. In the originally-proposed scheme, a two-wire measurement would be adequate, but another possible approach would likely benefit from four-wire measurement to reduce noise. Phase STM may also require additional signal wires. In particular, it would probably need at least one pair for a magnetic feed-

back coil. This would be a low-impedance circuit, carrying a relatively high current (μA), but it would probably need to be well-shielded from noise sources.

To provide for these possible configurations, and in order to have spare wires available in case of failures, I chose to route 12 wires as signal wires. The number should be sufficient for the schemes considered here, but a somewhat larger number of spares might be desirable.

We do not need to worry about impedance matching and rf propagation in these wires. Actually, we want to block rf as much as possible, and reflection caused by impedance mismatch is one mechanism which can contribute to this [110]. Reflections will not appreciably degrade the signal quality at 20 kHz, since the path length from the STM to the preamplifier is at most a few meters.

However, the STM signal wires need to be well-shielded to exclude rf as well as low-frequency electrical noise. Another possible noise source is magnetic pickup due to 60 Hz fields and, when the high-field magnet is used, vibration of the wire or of nearby magnetic parts through the field.

Experience has shown [146] that one of the most troublesome noise sources in low temperature STM is microphonic pickup of ambient sound by coaxial cables used for the STM signal wires. The measured quantity is usually current (and its derivatives) in the range of 10^{-11}–10^{-7} A. Since 2 m of 50 Ω coaxial cable will typically have about 200 pF of capacitance, if it is charged to 1 V and if the capacitance changes by a factor of $1+10^{-4}$, the charge dislodged will be equivalent to 200 pA for 0.1 ms, for example. Motion of the cables may also release charge through piezoelectric or triboelectric effects.

Whatever the mechanism, the braid-shielded teflon coax used in the 4 K STM at LPS is apparently quite sensitive to sound. Semi-rigid coax (continuous metal shield) is much stiffer and should be less microphonic. Semi-rigid coax is also far better shielded against rf pickup, which is particularly important for the cable between the STM and the cold filters. It can be joined with rf connectors which are also quite rf-tight.

For these reasons, I used semi-rigid coax for all signal wires inside the vacuum space of the cryostat. To minimize the thermal load, and to provide some rf attenuation, I used resistive coax made of CuNi (375nΩm @ RT[115]) inner and outer conductor and PTFE dielectric [115]. The 0.4 mm diam. micro-coax has shield inner diameter 0.26 mm and wire (inner conductor) diameter 0.08 mm, for a total cross-section of CuNi $A = 8 \times 10^{-8}\,\mathrm{m}^2$. Using the data of Olson [55] (Table 3.1), the heat leak through a length ℓ of the CuNi coax connecting a thermal anchor at temperature T_1 to the next higher anchor at temperature T_2 is given by

$$\begin{aligned} \dot{Q} &= \frac{A}{\ell}\int_{T_1}^{T_2} \kappa(T)\,\mathrm{d}T = \frac{A}{\ell}\int_{T_1}^{T_2} 0.065\left(\frac{T}{\mathrm{K}}\right)^{1.1}\frac{\mathrm{W}}{\mathrm{m}}\,\mathrm{d}\left(\frac{T}{\mathrm{K}}\right) \\ &= \frac{A}{\ell}\cdot 0.031\cdot\left[\left(\frac{T_2}{\mathrm{K}}\right)^{2.1} - \left(\frac{T_1}{\mathrm{K}}\right)^{2.1}\right]\frac{\mathrm{W}}{\mathrm{m}}\,. \end{aligned} \tag{5.1}$$

We are most interested in knowing the heat leak to the mixing chamber cold plate. The next higher anchor is at the radiation shield cold plate, which is nominally at 50 mK. However, there is no cooling power at this stage; the radiation shield is cooled below the still temperature by the mixing chamber. Therefore it is appropriate to compute the total heat leak from the still, at $T_2 = 0.7\,\mathrm{K}$, to the mixing chamber at

$T_1 \approx 0$. With $\ell = 0.25\,\mathrm{m}$ of cable running between them, we have

$$\dot{Q} \;=\; \frac{8\times10^{-8}\mathrm{m}^2}{0.25\mathrm{m}} \cdot 0.031 \cdot 0.7^{2.1}\,\frac{\mathrm{W}}{\mathrm{m}} \;=\; 5\,\mathrm{nW}. \tag{5.2}$$

A dozen of these will thus create a heat leak to the mixing chamber of about 0.06 μW, which should not be significant.

The $\sim$2 m of this coax, 1 m from RT to 4 K and 1 m from 4 K to the MXC, inserts about -39 dB at 1 GHz and -120 dB at 10 GHz [117]. Additional rf filtering is provided by homemade bronze/epoxy powder filters, described below, which provide high frequency attenuation without significant added capacitance.

5.2.3 Piezo and thermometry wires

The piezo wires do not carry very low-level signals that require shielding inside the IVC. The thermometry wires do carry low-voltage signals, but resistance thermometry measurements can be averaged over considerable lengths of time to reduce noise. We do not want these wires to serve as strong rf sources inside the otherwise well-shielded IVC. To prevent this, the walker wires can be grounded when not in use, and thermometers turned off for scanning. The scanner wires will, however, need to be "live." These wires should be filtered on entry to the shielded room and perhaps on entry to the cryostat as well.

I used woven "loom" wiring [147], the same type used by Oxford Instruments, for convenience and a low heat load. These wiring ribbons have 12 twisted pairs of $\sim$100 μm diameter wire per ribbon, woven with Nomex thread in a pattern that alternately covers and exposes the wire (Fig. 5.3). The standard method of thermal

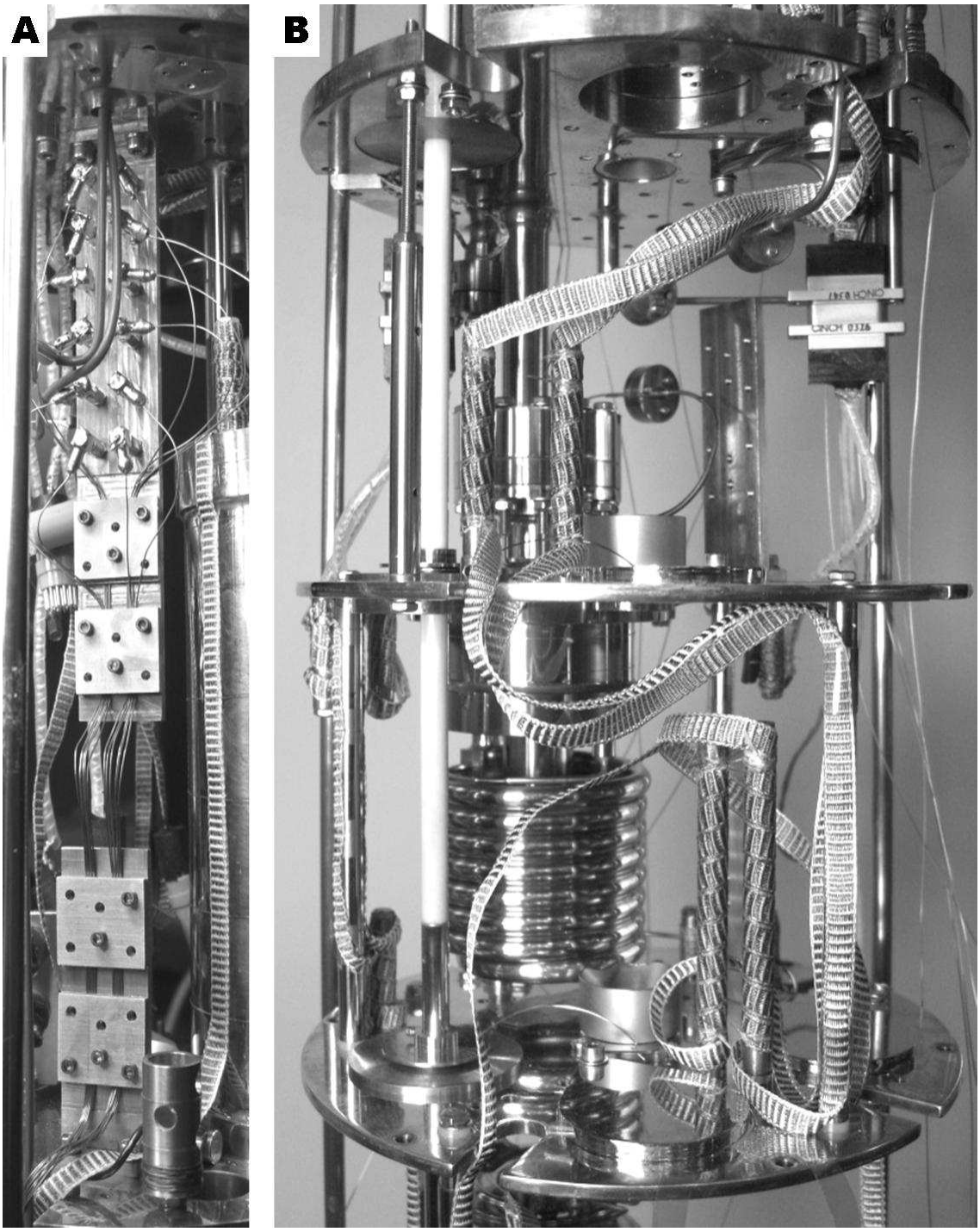

Figure 5.3: Wiring and thermal anchoring methods used for the signal and piezo wires inside the IVC. A. CuNi microcoaxes used as signal wires at with SSMC connectors and thermal anchors at 4 K flange (hanging from top) and thermal anchors at 1 K plate (bottom). 0.4 mm OD microcoaxes are bunched beneath the square plates into 0.3 mm deep channels to compress them for thermal contact. B. NbTi loom wiring between 1 K plate and 50 mK plate. 1.5 in. long Cu thermal anchoring posts are used at the 600 mK still stage, and 3 in. long posts are used at the 50 mK shield stage.

anchoring of loom wiring, used by Oxford, is to wind them around $\frac{1}{4}$ in. OD Cu posts. When the ribbon is wrapped around a heatsinking post, exposed sections of the wires come into contact with the post, and thermal contact can be enhanced by using varnish as a bonding agent.

For the upper section running from 300 K down to the 1.4 K stage, I used 110 μm diameter Constantan wiring loom. This choice provides a low heat load at the cost of somewhat high electrical resistance, 66 Ω/m, with little variation of resistance (hence the name "Constantan") due to temperature changes as liquid helium is depleted or when refilling.

For the lower section running from 1.4 K down to the mixing chamber, I used CuNi-clad NbTi loom, 100 μm diameter, which has room temperature resistance 52 Ω/m but is superconducting below about 9 K. The CuNi cladding is mainly for solderability. Transmission of microwave energy is also suppressed by the resistive cladding due to the skin effect and capacitance between the twisted pairs, while dc resistance (when cold) is zero.

The heat leak to the mixing chamber due to the CuNi-clad NbTi wiring is almost entirely through the CuNi. Although the amount of the CuNi is not specified by the supplier, the wire diameter is specified as 100 μm, and similar wire made by Supercon, Inc. (type SW-M) [148] contains 62 μm of NbTi with the balance CuNi. Assuming this is the correct proportion (1.5:1 area proportion of matrix to superconductor appears to be standard), the area of CuNi for 48 wires is $2.3 \times 10^{-7}\mathrm{m}^2$. Comparison with the calculation done for the CuNi coax (above) shows an expected heat leak of 12 nW, which is insignificant.

Oxford Instruments conventionally wraps loom wiring around 25 mm long, 6 mm diameter Cu posts, which are hollow and are bolted to the cold plates with long stainless steel screws. They tie down the loom with thread and apply varnish to provide additional thermal contact to the post. While this method appears to be adequate for the upper stages of a dilution fridge, my experience has been that the wires are not adequately thermalized at the mixing chamber.

To ensure adequate thermal anchoring of the looms, I used extra-long heat sinking posts: 40 mm at the 4 K, 1 K, and 0.7 K stages, and 75 mm at the 50 mK shield stage and at the mixing chamber (Fig. 5.3). These posts were also threaded and screwed directly into the cold plates for better contact. Holes drilled horizontally into the posts allowed them to be tightened with a steel bar (actually, a small Allen wrench). Bending of the bar was used to gauge the tightening torque so that the posts could be put in as tightly as possible without breaking.

Although 48 total wires are brought down on two looms, 12 of these are treated as spares and left open at the mixing chamber. The 36 remaining wires are to be filtered at the mixing chamber, and shielded after filtering until they enter the STM can. I planned to use Thermocoax wound on spools to filter the piezo and thermometry wires. Due to difficulties with this type of filter, it may be desirable to use a different filtering element at this stage, but I describe the Thermocoax filter design below.

5.2.4 Cold end wiring

After filtering at the mixing chamber, all 48 wires (36 from the looms and 12 from the CuNi coaxes) continue to the STM can as 0.047 in. O.D. semirigid coax with Cu shielding, PTFE dielectric, and Ag-plated Cu inner conductor wires. This coax was chosen for its relatively high thermal conductivity, so that heat from the STM tip, sample and piezos would be conducted away from the STM by the wires, and be sunk through the dielectric to the shield as well as into the filters.

Unfortunately, as discussed in Sec. 3.5.3, it is unclear whether the Cu coax will be an effective thermal anchor for the STM, due to shrinkage of the PTFE at low temperature. Thermal contact resistance, rather than the bulk thermal conductvity of the PTFE, is the main problem at mK temperatures, and is strongly dependent on pressure applied to the PTFE-Cu boundary. The PTFE contracts about 2.1% as compared with about 0.3% for Cu, suggesting that there is likely to be little pressure or even a loss of contact between the PTFE and the Cu outer conductor at low temperature, at least for straight and undistorted sections.

In order to promote contact between the PTFE and Cu shield, and hopefully apply sufficient pressure to achieve some degree of heat sinking, Cu clamps are used to compress and flatten the Cu coaxes and press them against the Cu bars of the STM mount (Fig. 5.1). As currently realized, these clamps will flatten the 0.047 in. coax to 0.040 in. along a 0.5 in. length, with each coax compressed by 6 such clamps. This 15% distortion of the coax from round may not be sufficient to ensure the PTFE remains under pressure at low temperature, and could be increased by

milling the clamps. Since the diameter of the wire plus twice the thickness of the shield equals 0.021 in., the squeezing of the coax could probably be as drastic as 0.03 in. without causing an internal short. Thus it is reasonable to hope that, with the use of these clamps, effective thermal anchoring of the inner wires and of the STM may be achieved.

However, if this method fails, and if insufficient cooling of the STM is observed, it may be necessary to introduce a different type of thermal anchor close to the STM. The Fukuyama group at Tokyo University initially used sintered Ag heat exchangers in an epoxy cell filled with ^{3}He/^{4}He mix to provide an electrically insulating thermal link [149, 150] for their mK-STM, with Ag wires connecting the He cell to the sample and tip holders and to the MXC. However, they later abandoned the He cell and instead brought high-purity, annealed, Ag foils and wires from the MXC down to the STM tip and sample holders, where they were thermally linked through 25 μm thick Mylar (polyester) films [151]. A similar thin insulating film device could probably be integrated into the STM mount or into the STM body itself.

The STMs as currently designed do not provide the best possible thermal link between the STM tip, sample and piezos and the Cu coax wiring. Cu wire is used throughout, but with several Ag-filled epoxy connections in each pathway. The latter are superior to solder connections at mK temperatures, but still far from ideal [81]. It may be necessary to review the STM design with attention to thermal contact and conduction issues.

To ensure rf-tightness after filtering at the MXC, SSMC connectors are used to join the Cu coaxes to the filters. The coaxes are soft-soldered into brass plugs where

they enter the STM can (Fig. 5.1), and the plugs can be sealed with In. Inside the can, the wires are unshielded and exposed to each other. The coaxes are brought down to Macor terminal strips, where a loop of the wire is exposed for connection. Ag-filled epoxy is used for electrical and thermal bonding of the wires that connect to the STM.

5.2.5 Bronze powder filters

Some filtering is provided by the CuNi coax used for the signal wires, and additional filtering is provided by homemade bronze powder filters (Fig. 5.4). Each filter line consists of 5.0 m of 50 μm diameter Cu-clad NbTi wire per line embedded in a bronze/epoxy composite. Each wire is wound evenly on a pre-cast rod of the composite, in four sections of alternating helicity in order to reduce magnetic coupling. Four filters are housed together in one Cu box, and two such units provide a total of eight lines. A single 12-line unit was also designed and built.

These filters utilize the bronze powder/epoxy recipe of Milliken *et al.* [94]. The bronze is 70/30 CuSn spherical powder made by Kennametal [152] screened to -325 mesh (i.e. all particles had to pass through a 325 wires/in. screen), resulting in the particle size distribution seen in Fig. 3.1 A. The bronze powder is mixed with Stycast [104] epoxy resins and catalyst. The principal reason for the epoxy matrix is the increased thermal conductivity of the resulting composite as compared with bare metal powder. The following proportions, by weight, were used: 80% CuSn, 14.9% Stycast 2850FT, 3.7% Stycast 1266, 1.4% Catalyst 23LV. As described by

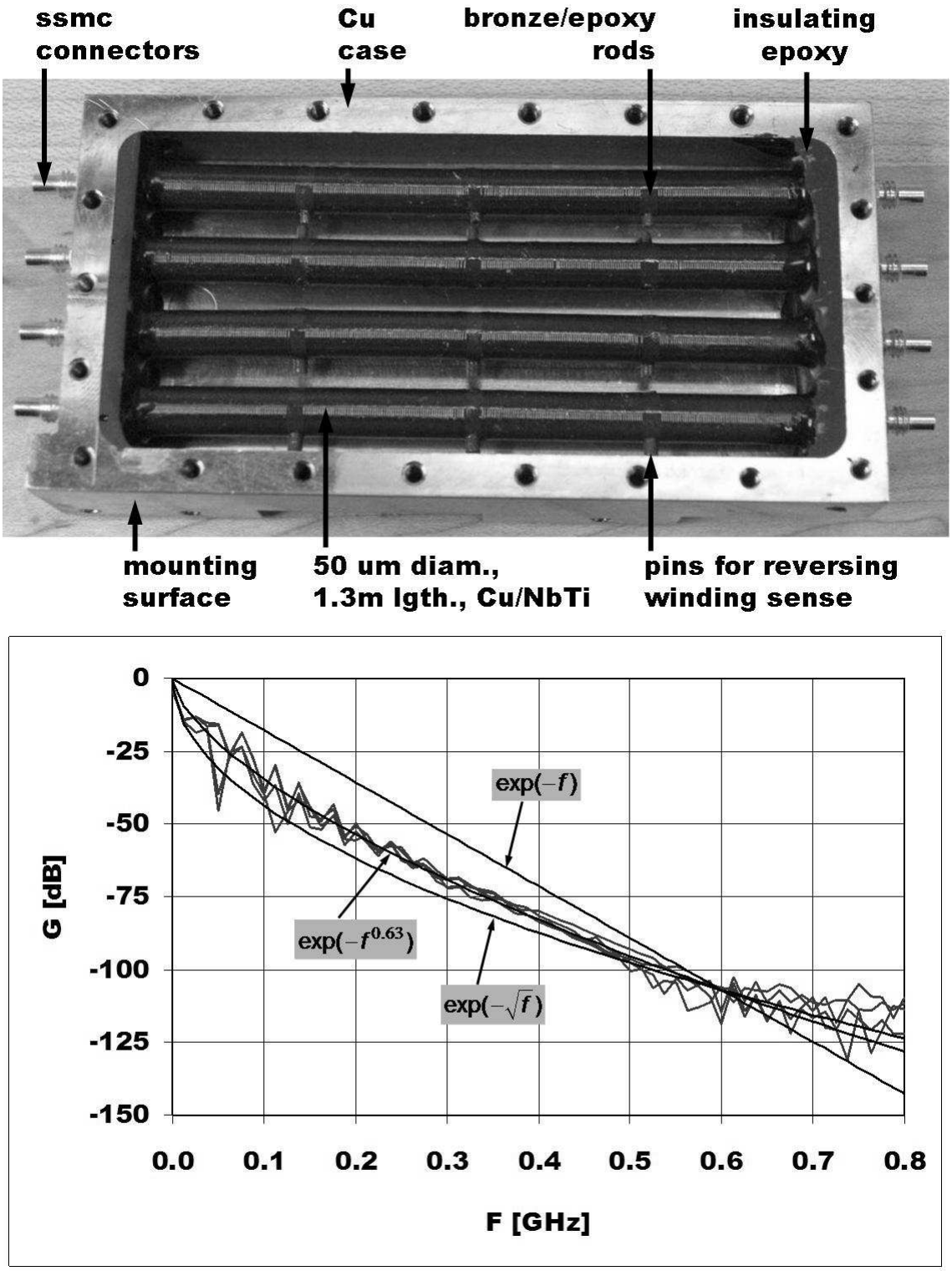

Figure 5.4: Metal powder filter with 4 lines. Top: the filter after installation of the coils and potting the ends in epoxy, but before filling the case with bronze-epoxy. Bottom: measured attenuation for the four lines appears to hit the noise floor at 600 MHz. See Section 3.4.1 for discussion of the fitting curves.

Milliken, the addition of unfilled Stycast 1266 to the ceramic-filled 2850FT helps to reduce cracking, and 23LV is the lowest viscosity catalyst available for use with these epoxies. The fraction of bronze that can be mixed into the epoxy is limited by the viscosity of the resulting paste; tests by Milliken *et al.* showed that attenuation was highest when the maximum fraction of the mixture was metal.

The epoxy must be mixed very thoroughly, which leaves the paste full of small air bubbles (Fig. 5.5 E). To remove most of these bubbles, the tray of paste can be put into a bell jar and pumped to low pressure, causing the air bubbles to expand and burst. Repeated evacuation and sudden venting of the jar "slaps" the paste and helps to burst the bubbles. A few cycles of this treatment is apparently enough to remove most of the air bubbles, which begin expanding immediately as the pressure was lowered. However, at very low pressure, the mixture seems to boil indefinitely, probably due to volatile components of the epoxy.

The rods for winding the wires into coils needed to be cast and machined. Drinking straws with an inner diameter of 5.5 mm were used as mold liners, and the rods are 79.25 mm long. Early attempts showed that it was necessary to make a mold, consisting of holes drilled into a block of Teflon, in order to enforce roundness. A Teflon block was used to cap the bottom end of the mold, but left loose to allow air to escape. After cutting the straws to length and inserting them in the mold (Fig. 5.5 A), I filled a 10 ml syringe with the bronze/epoxy paste by removing the plunger and spooning the paste into the back, taking care to avoid trapping air in the syringe. I then injected the paste into the straws from the top until it started to come out the bottom of the mold.

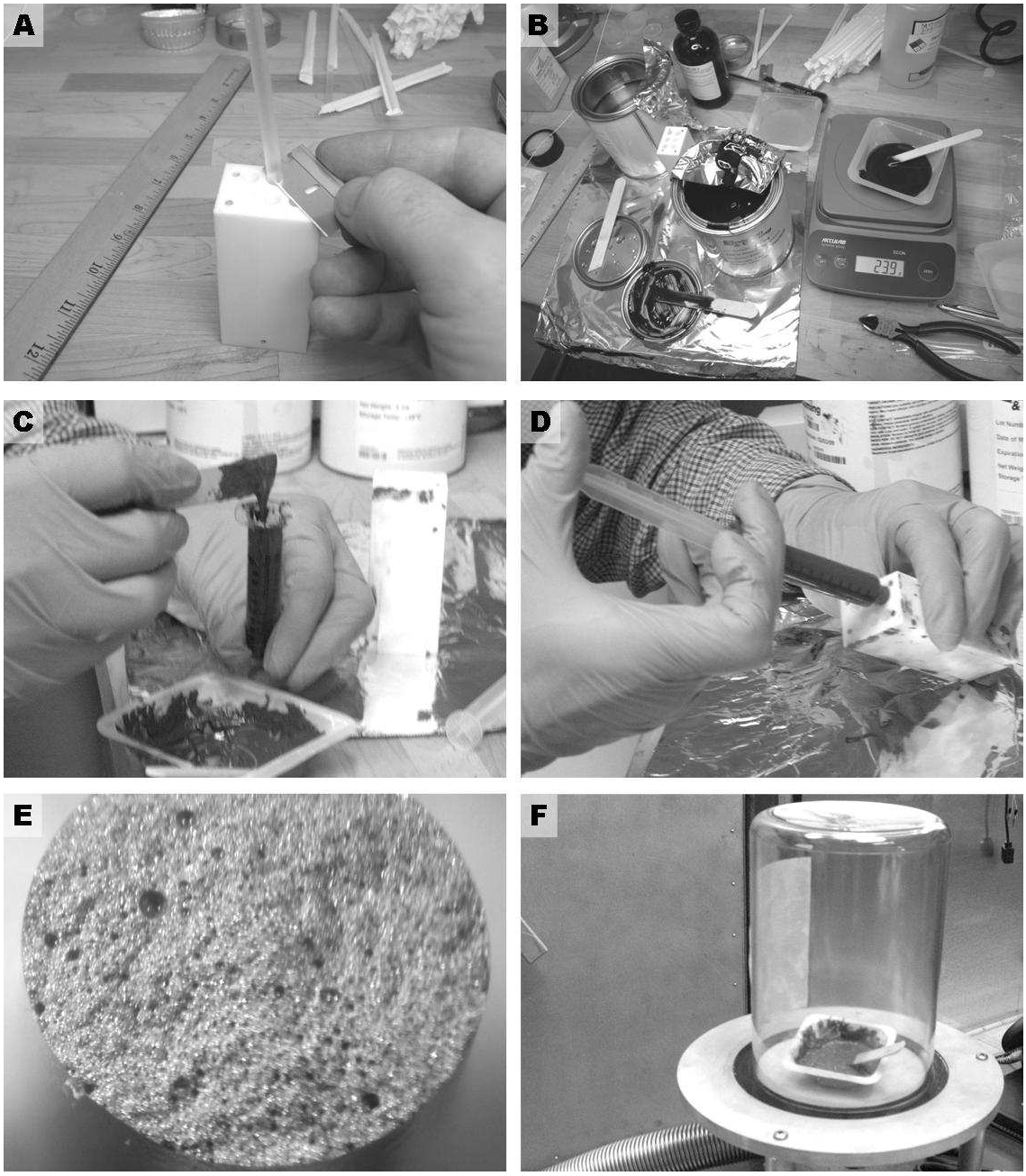

Figure 5.5: Some aspects of making powder filters. A. Drinking straws used as mold liners. B. Mixing the bronze/epoxy paste. C. Spooning the paste into a syringe. D. Injecting the paste. E. Bubbles in a test rod. F. Using vacuum to remove bubbles from the paste.

After allowing the mixture to cure for 24 hours, the bottom cap could be removed and excess material trimmed off with a razor blade. The rods could then be pushed out of the mold by using a drill press with a soft plastic rod. The straws could be scored lengthwise with a razor blade and peeled off. The rods needed to be cast extra long and then cut to length because of bubbles at the ends. After casting and cutting, the rods could be weighed and compared to detect any large hidden bubbles. I obtained a yield of about 2 out of 3 good rods.

I found that the bronze/epoxy composite is initially somewhat soft, and gradually hardens over a period of 1–2 weeks. The best time to machine it is a few days after casting, before it is fully hard and brittle. The rods have three 1.59 mm holes drilled across their diameter, dividing them lengthwise into four equal sections. The holes are used to insert short pegs around which the wire can be wrapped $\frac{1}{2}$ turn to reverse the winding sense. Because of the ceramic filler in Stycast 2850FT, the composite quickly abrades drill bits and other tools used to machine it.

Holes are also drilled into the ends of the rods for short brass sleeves that mate to pins connecting the wires to the outside (Fig. 5.5). For reasons of electrical insulation, as described below, I found it necessary to drill these holes wider and deeper than the brass sleeves, refill them with Stycast 2850FT (without the bronze) and, after curing, redrill the holes to the correct diameter and depth for the brass sleeves. The sleeves need to stick out of the ends of the rods by 1.25 mm, just enough to attach the wires using Ag-filled epoxy. The brass sleeves are also drilled to an internal diameter of 0.036 in., which makes a gentle press fit over the BeCu soldering pins of SSMC bulkhead jacks used for connection of the filters to the outside. Since

ZnCu brass has greater total thermal contraction (0.384%) than BeCu (0.316%) [4], contact is maintained at low temperature, and a bit of Ag-filled epoxy is also applied on the pins for good measure.

The wire was wound on the rods using a small coil winder equipped with a computer-controlled traverse (Fig. 5.6) used to regulate the spacing, in this case to 250 μm per turn. I fitted the traverse with V-grooved Teflon wheels to guide the fine wire, and used a small weight to regulate tension in the wire. I used plastic insulation sleeve glued into the rods with cyanoacrylate "super glue" to make pegs for reversing the winding sense. The wire would be started at one end of the rod with a drop of cyanoacrylate to attach it, leaving a "pigtail" for connection to the brass sleeve. Seventy-three turns would be wound in one sense, then the wire wrapped half a turn around the first peg and fixed in place with cyanocrylate. Then 73 turns in the opposite sense, and repeat for all four sections of the rod (for the final section, the rod needed to be removed from the winder and turned around so it could be wound to its end). Finally, the "pigtails" of the wires needed to be chemically stripped and wound around the protruding brass sleeves. Cyanoacrylate was used to hold the pigtail in place while the Ag-filled epoxy cured to complete the connection to the brass sleeves. Of course it was necessary to keep the connections free of the cyanoacrylate, and to manage to complete all these steps without breaking the 50 μm diameter wire! Although I developed the methods, I thank Anita Roychowdhury for her patience in finishing the work.

After winding the rods, they were coated with two layers of thinned GE/IMI 7031 varnish, and then installed into the filter boxes. To do this, the SSMC bulkhead

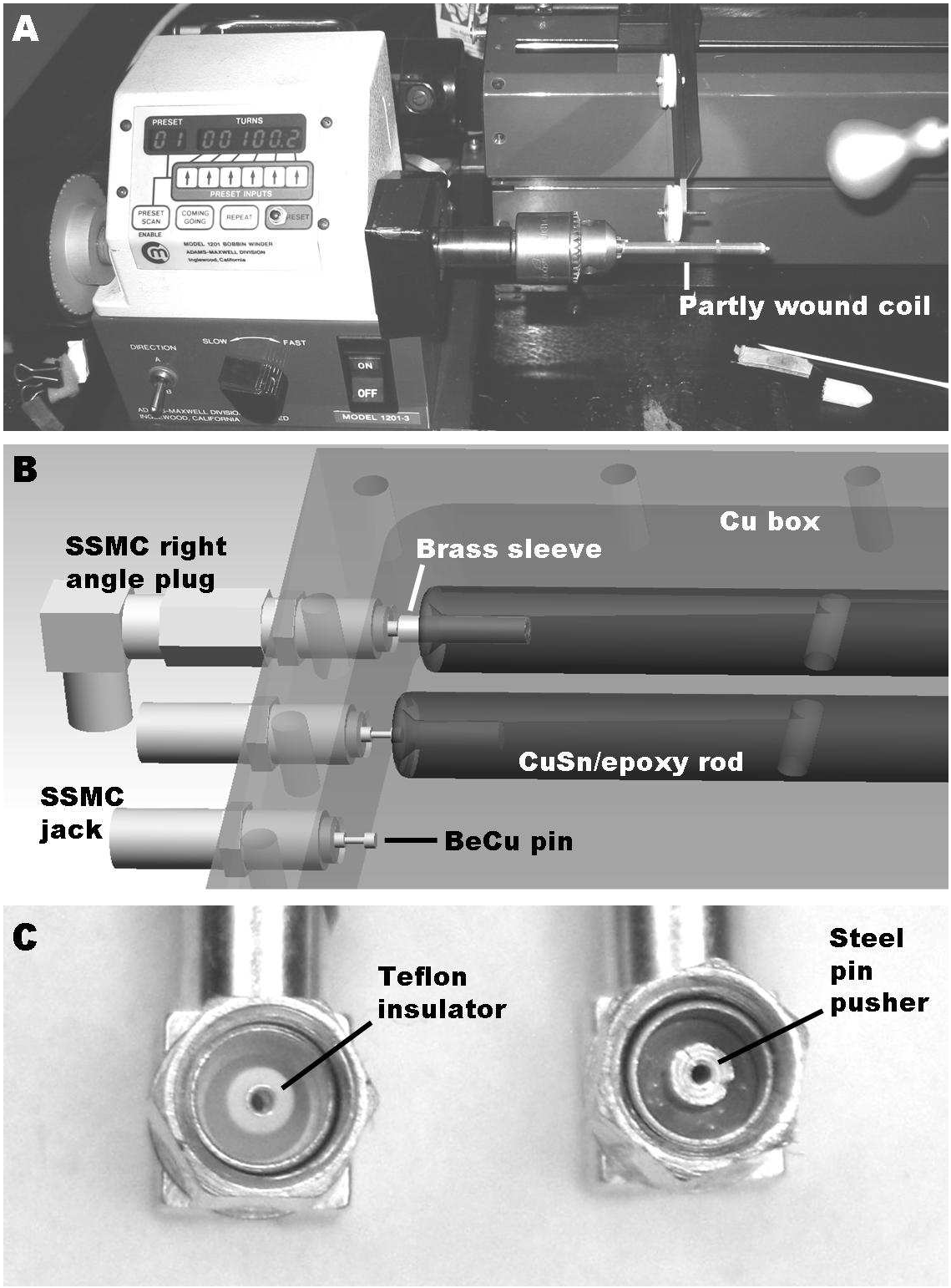

Figure 5.6: Winding and intalling powder filter coils A. Coil winder with computer controlled traverse. B. Detail of filter construction (CAD image), showing how contact is made to SSMC connectors. C. SSMC right angle plugs as supplied and as modified to hold pins of SSMC jacks in place during installation of the rods.

jack connectors (Fig. 5.5) were pre-installed part way in their threaded holes on both sides of a rod, then slowly tightened to push the pins into the brass sleeves, checking to ensure they inserted evenly on both ends. Unfortunately, due to the construction of the SSMC bulkhead jacks, I found that instead of inserting into the sleeves the pins would push out of the jacks as the latter were tightened down. To solve this problem, I modified two SSMC right angle plugs with machined stainless steel "pin pushers" (Fig. 5.6)

The metal particles have a native oxide layer which causes the powder to appear electrically insulating when tested at low voltage, e.g. by dipping the probes of an ohmmeter into the powder. The presence of such an oxide layer on the surface of metal objects is normally unnoticed because it is so easily scraped through by the touch of another piece of metal, such as an ohmmeter probe. In the case of the powder, the oxide would have to be scraped through on many contiguous particles, and not re-form in the ambient air, in order to form a percolation path between two solid conductors. Normally this does not occur mechanically when dipping probes into the powder.

The insulating property of the bronze powder is retained by the bronze/epoxy composite when cured, which allows microwave energy to penetrate into the composite and be dissipated by surface currents on the particles. However, the native oxide is very thin. Although many thin layers add up, in the presence of a moderate electric field, energy is available which a disordered system may act to concentrate here and there. Chains of contact, if roughly aligned with the field, will concentrate the field at their ends, furthering an avalanche breakdown process. This would also

create high-frequency components, which may assist the process as in the coherer-type detectors used in early radio.

Whatever the mechanism, I found that, if the composite is cast in contact with the bare conductors, the cured composite short-circuits the filters whenever voltages in excess of 30–100 V are applied. For this reason, it was necessary to varnish the coils after winding and to cast a few mm of Stycast 2850FT, without the bronze filler, at each end of the filter boxes in order to exclude the composite from the vicinity of the SSMC connectors and the brass sleeves (Fig.5.4). With these measures to ensure insulation, the filters were able to withstand at least 500 V.

After casting the insulating epoxy at the ends, the remaining volume of the the boxes needs to be filled with the bronze/epoxy composite. The major difficulty in this is to work the stiff paste past the coils (Fig.5.4) and into the space behind them. In order to avoid trapping large air bubbles, it is best to work the paste in from the center so that it pushes out toward toward the walls of the box from under the coils. Use of the vacuum bell jar to remove bubbles is also important; the paste expands when this is done and it is necessary to build a paper dam to prevent its spilling over the sides of the box.

I overfilled the composite and it cured in the form of a baked loaf; after curing, it needed to be milled to provide a flat surface for the cover, which was bolted on and sealed with H20 Ag/epoxy. This method of construction may not be the best for powder filters, since it leaves the cover in proximity but perhaps not actually in contact with the milled-flat surface of the composite. It is possible that this creates a surface-wave channel, bypassing the coils, which would not exist if the composite

had been cast in contact with all walls of the filter housing.

5.2.6 Thermocoax filters

For the piezo and thermometry wires, some filtering is provided by the distibuted resistance and capacitance of the constantan wires, the capacitance of the NbTi wires and, at microwave frequencies, the resistance of the CuNi cladding of the NbTi wires. However, at microwave frequencies, energy that enters or is thermally generated within the vacuum space can be conducted along structural members, plumbing and wiring to the vicinity of the mixing chamber, and coupled into the wires. Below the mixing chamber, the wiring is tightly shielded using Cu coax and SSMC connectors, but above that stage, unshielded twisted pair looms are used. Therefore there is a need for filtering the 36 piezo and thermometry wires at the mixing chamber.

Thermocoax filters (Sec. 3.4.2) seemed an attractive option for the piezo wires because they appeared, in comparison with metal powder filters, to be simple, compact, easy to make, and well-characterized electrically [90]. In principle, the filter is nothing but a length of coaxial cable with a 0.17 mm OD inner conductor of NiCr and 0.38 mm ID, 0.5 mm OD shield of SS304, with powdered MgO dielectric. The coax must be thermally anchored to the working temperature and connectorized or otherwise electromagnetically isolated, at least at the cold end. I planned to wind 1.5 m of Thermocoax around 11.7 mm diameter Cu spools (Fig. 5.9) and attach SSMC right angle plugs to both ends, creating interchageable filter elements.

The spools were designed to bolt horizontally onto a vertical rack so that 36 of them could be packed into the space above the mixing chamber cold plate (Fig. 5.7). The rack was machined from a single piece of OFHC Cu, the base of which was turned to form a round flange which fits over one of the large holes in the mixing chamber cold plate. The base flange is clamped to the cold plate with a bolt circle into a matching flange. The rack also provides space for SSMC connectors to join the filter units to the loom wiring coming down, and to the Cu coax going down.

In practice, making the filter units proved more difficult than it sounds. The main problem is to keep the Thermocoax dry and to seal the filter units so as to prevent water from entering after they are assembled. This is complicated by the difficulty of cutting and preparing the ends and of soldering NiCr and stainless steel, using acid flux, without wetting the MgO powder dielectric with acid.

The first step to making a filter was to cut the appropriate length of Thermocoax, strip a few mm of the jacket off from both ends and attach SSMC right angle plugs, sealing them so that the Thermocoax could be exposed to the environment and remain dry. While doing this, I worked in a closed room with a dehumidifier running, and removed pieces from a dessicator box only for short periods to work on them.

Because the jacket is only 0.5 mm diameter, and the coax is subjected to up to 300 V, sometimes in the presence of low-pressure gases, in order to minimize the likelihood of corona or arc-over it was important to cut the jacket as cleanly as possible (Fig. 5.8 D). Methods I had used before included cutting through the jacket

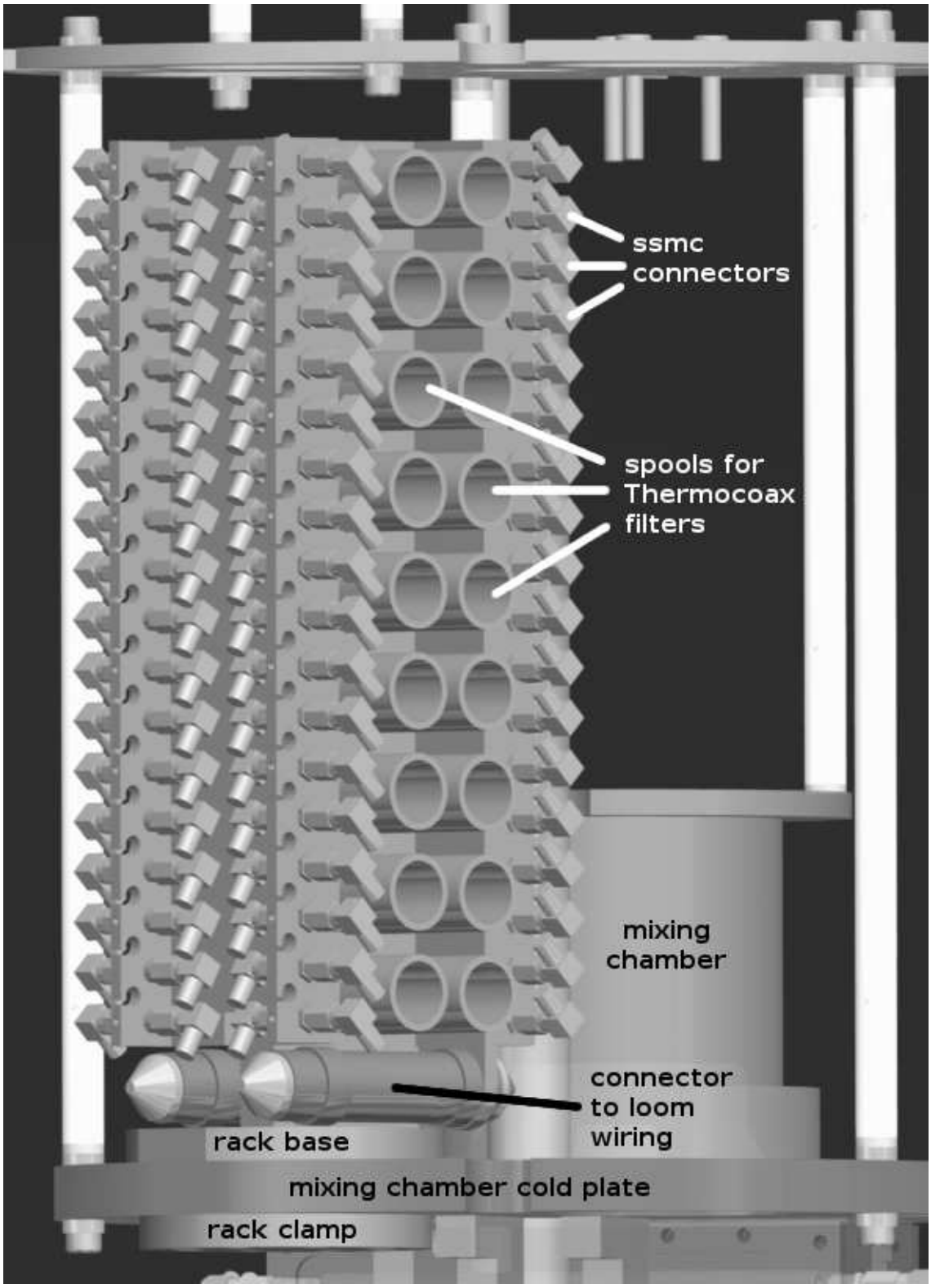

Figure 5.7: Thermocoax filter rack mounted on mixing chamber cold plate.

with an abrasive wheel or with cutting pliers. These methods tended to produce ragged and deformed ends when they worked at all. I therefore sought to develop a better method, and the first thing I tried was laser cutting. I thank Dr. Victor Yun of LPS for help in this. However, laser cutting did not work, because it was hard to keep the coax precisely centered while rotating it, and to terminate the cut after cutting through the jacket without cutting the wire, and because laser cutting produced a shower of carbonized steel which contaminated the dielectric.

However, in the attempt to use laser cutting I had set up a motorized jig (Fig. 5.8 B) to rotate the coax at 60 rpm while holding it in place at the laser focus. The coax passed through a rotating tube with a clamp at one end to hold the coax, and a plug at the other end of the tube with a hole from which the coax emerged to be cut. The key to making this work was not to attempt to ensure precise centering of the rotating hole, but rather to run the wire over into a stationary hole drilled into a brass block, and cut close to the block. Because the hole in the block was not moving, while the wire rotated, this solved the centering problem.

While the laser method didn't work, I found that by using the motorized jig with a razor blade (Fig. 5.8 C), pressing the blade against the brass block to keep it in place as the coax rotated, I could neatly score the jacket. Then with few gentle bends using pliers, I could obtain a clean break (Fig. 5.8 D). I wanted to break off about 2 mm of the jacket, and found it necessary to do this in two steps of about a mm each, because the MgO is packed so tightly that any greater length would break the inner conductor rather than pull free. The short lengths, once broken, could be wiggled to loosen the powder.

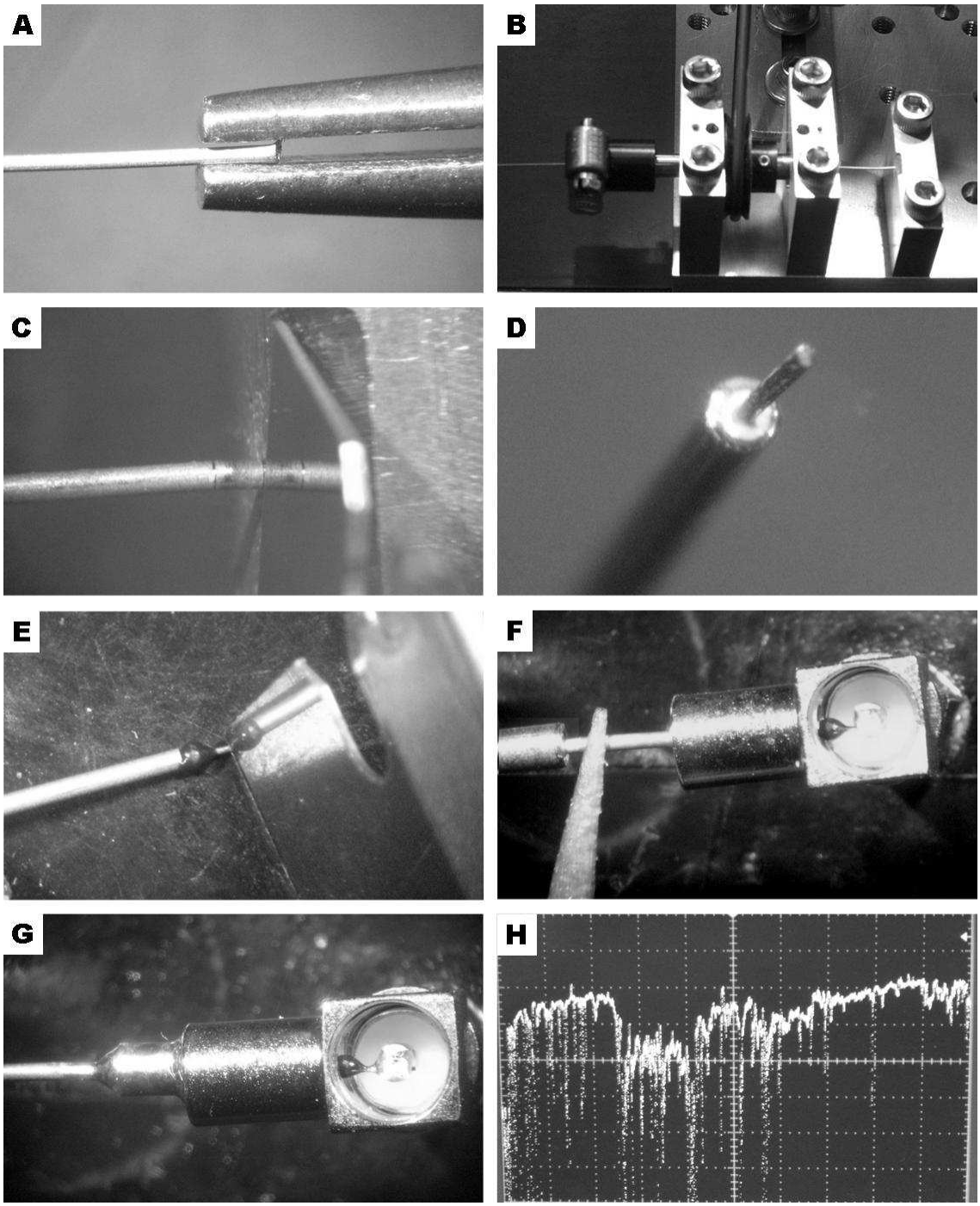

Figure 5.8: Steps in cutting Thermocoax and attaching connectors. A. Straightening and rounding end with needlenose pliers after cutting to length. B. Inserted into motorized cutting jig. C. Scoring with razor blade. D. Stripped end after breaking off two short sections. E. Scraping center conductor clean after end dipped in epoxy and cured. F. Applying acid flux to SS304 jacket, after center conductor has been soldered to pin. G. Jacket soldered with brass sleeve into connector. H. Noisy leakage current when HV applied, due to water or acid flux. Vertical scale, 100 nA/div., horizontal 2 s/div.

After stripping 2 mm from each end of the coax in this way, I used Stycast 2850FT epoxy to seal the ends. Sealing the ends of the coax was necessary because soldering the NiCr required the use of acid flux containing $ZnCl_2$, NH_4Cl, and HCl [153], which I applied in a thin layer with a sharpened wooden stick. The same flux was also used to solder the SS304 jacket (Fig. 5.8 F,G).

I found it convenient to simply to dip each end of the stripped coax into the epoxy, leaving a bead over the end of the jacket and also coating the wire. Two brass sleeves were also threaded onto the coax before dipping, to be used to match the 0.5 mm OD of the Thermocoax to the much larger (2.16 mm) ID of the SSMC connector. After curing the epoxy, I used a razor blade to scrape away the thin epoxy coating from the wire, and also to clean the surface of the NiCr wire which was oxidized and roughened by the packed MgO (Fig. 5.8 E), which I had found to be necessary in order to obtain a good solder bond to the NiCr, (so cleaning off the epoxy came at no extra cost).

After soldering the wire and jacket, the connectors were finished by filling their empty volumes with 2850FT, and after curing, soldering the covers on, hopefully keeping water and rf energy out, and any trapped gas in.

On testing the finished connectorized coaxes with high voltage and a sensitive current amplifier, in about a third of cases I observed leakage currents up to a few milliamps at a few hundred volts, whereas "good" coaxes exhibited insulation better than 500 GΩ at voltages up to 1 kV. Moreover, these leakage currents were noisy (Fig. 5.8 H) and unstable, tending to get worse over time with voltage applied. It is likely that in some cases small quantities of the acid flux did get past the epoxy

bead as it was heated during soldering, but moisture could also have been a source of trouble. I rejected any coaxes that showed leakage greater than 5 nA at 500 V.

The spools (Fig. 5.9 A) are machined from $\frac{1}{2}$ in. diameter OFHC Cu rods, and hollowed to reduce mass. The inner end of each spool is a solid Cu disk 3.8 mm thick, with a hole in the center for bolting it to the rack. An S-shaped groove is cut, using a CNC mill, into the surface that presses against the rack, and is used for reversing the sense of the winding.

To wind a spool (Fig. 5.10), I started with a length of Thermocoax pre-cut and with connectors attached. I found the midpoint of the length and pressed it into the S-shaped groove, and then bolted the spool to a mandrel chucked into an electric hand drill which I had strapped into a horizontal mounting. I used a Variac to control the speed of winding. Two turns of the coax would be wound per turn of the spool, in opposite sense relative to the overall direction of current, thus producing a magnetically canceled coil in a single layer. I attached weights to the connectors to tension the Thermocoax as it was wound. Finally, I soldered the coaxes to the outer end of the spool to tack them in place and hold them under tension, leaving a short pigtail on each end (Fig. 5.9 B).

When winding Thermocoax around Cu spools, the coax must be pre-strained to compensate for the greater thermal contraction of Cu compared with SS304; otherwise the windings would be loose when cold, and thermal anchoring would be poor. The weights I used to tension the Thermocoax as it was wound were custom-made and fitted to hang from the SSMC connectors soldered to the ends of the coax. The total contraction $\Delta\ell/\ell$ (RT to 4 K) of Cu is 2.8×10^{-4} greater than that of SS304

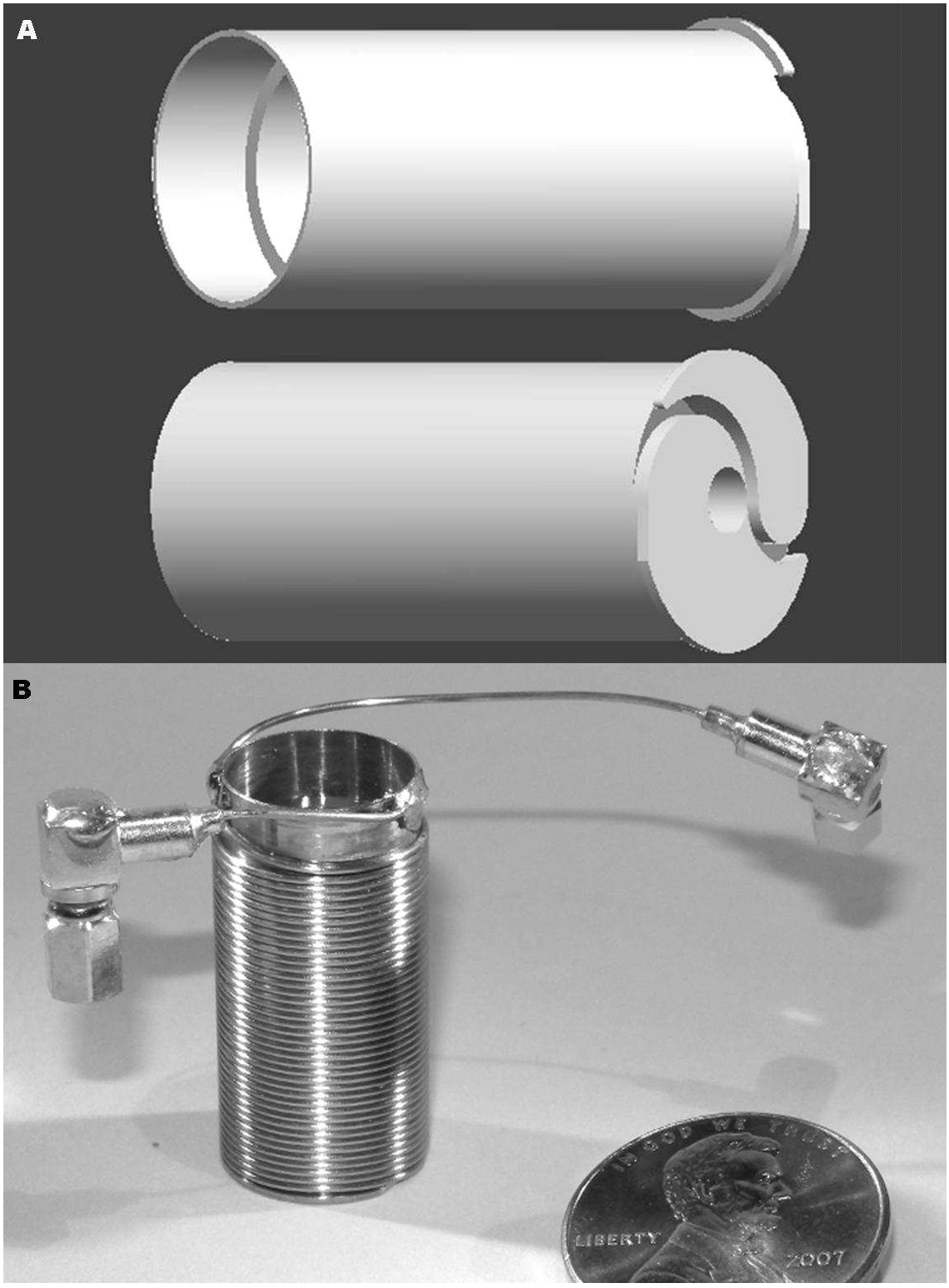

Figure 5.9: Thermocoax filter spools. A. Computer model of spools viewed from each end, showing S-shaped groove on inner end for reversing winding sense, and outer end thinned for soldering. B. Completed Thermocoax filter wound on spool with connectors attached.

[4], and the Young's moduli of SS304 and NiCr are both ∼200 GPa [4, 154]. To obtain pre-strain just greater than the predicted differential contraction would thus require a tensile stress of $3\times10^{-4} \times 200\,\mathrm{GPa} = 60\mathrm{MPa}$. I wanted to use more, so that the Thermocoax would make tight contact with the Cu when cold, but this purpose could be defeated by the SS304 undergoing the austenite (face centered cubic) to martensite (body centered cubic) phase transition, which can occur in SS304 at temperatures around 100 K as it is cooled, and is promoted by stress [155]. To prevent this, the stress should be kept well below 240 MPa, the 0.2% yield strength of SS304. I compromised at 120 MPa of tensile stress, twice the minimum required and half the yield strength. Given the $1.1\times10^{-7}\mathrm{m}^2$ total cross section of the wire and jacket, the required tension was provided by 1.3 kg weights.

5.3 Magnetically shielded sample stage for SQUID experiment

As a preliminary test of a possible principle for Josephson phase STM, we wanted to study the behavior of an extremely asymmetric superconducting quantum interference device (SQUID), consisting of two microfabricated Al-Al_2O_3-Al Josephson junctions, one with a critical current I_0 of ∼1 μA, the other with I_0 of ∼1 nA, joined in a loop of fairly large area, $\sim(0.4\,\mathrm{mm})^2$. Such a SQUID device was considered as a model for a device in which the ∼1 nA junction would be formed by a superconducting STM tip over a superconducting sample, with the ∼1 μA junction added to stabilize the gauge-invariant phase difference across the tip-sample junction, allowing changes in the loop gauge-invariant phase to be observed as the

Figure 5.10: Setup for winding Thermocoax filters on Cu spools. Spool is bolted to mandrel in drill with speed controlled by variac. Weights are hung from the SSMC plugs attached to the ends of Thermocoax. Winding starts from the center of the length of coax and inside end of the spool, so coils are fully counterwound.

tip is scanned across the sample [142].

The objective of the experiment [156] was to see if the escape current I_c histogram of such a highly asymmetric SQUID would exhibit periodic modulation in an applied magnetic field, despite I_0 for the small junction, or the tip-sample junction in phase STM, being in the fluctuation-dominated regime [157, 142]. The expected modulation would have a periodicity of one quantum $\Phi_0 \approx 2{\times}10^{-15}\mathrm{T\,m^2}$ of magnetic flux, or $1.25{\times}10^{-4}\,\mathrm{G}$ given the $1.6{\times}10^{-5}\,\mathrm{m^2}$ area of the SQUID. This very high magnetic sensistivity (familiar from other experiments involving large-area SQUIDS) implied the need for good shielding of the SQUID from ambient 60 Hz and other low-frequency magnetic field sources.

The simplest way to achieve high magnetic shielding in a low-temperature experiment is with superconducting shields. Almost the only geometry which will give very high attenuation of ambient dynamic fields, while still allowing penetrations such as wiring and a cold finger, is a long tube which is closed at one end, with the sample located inside near the closed end (Fig. 5.11). Ambient fields will attenuate roughly as $\exp(-\ell/d)$, where ℓ is the length and d the diameter of a cylindrical tube.

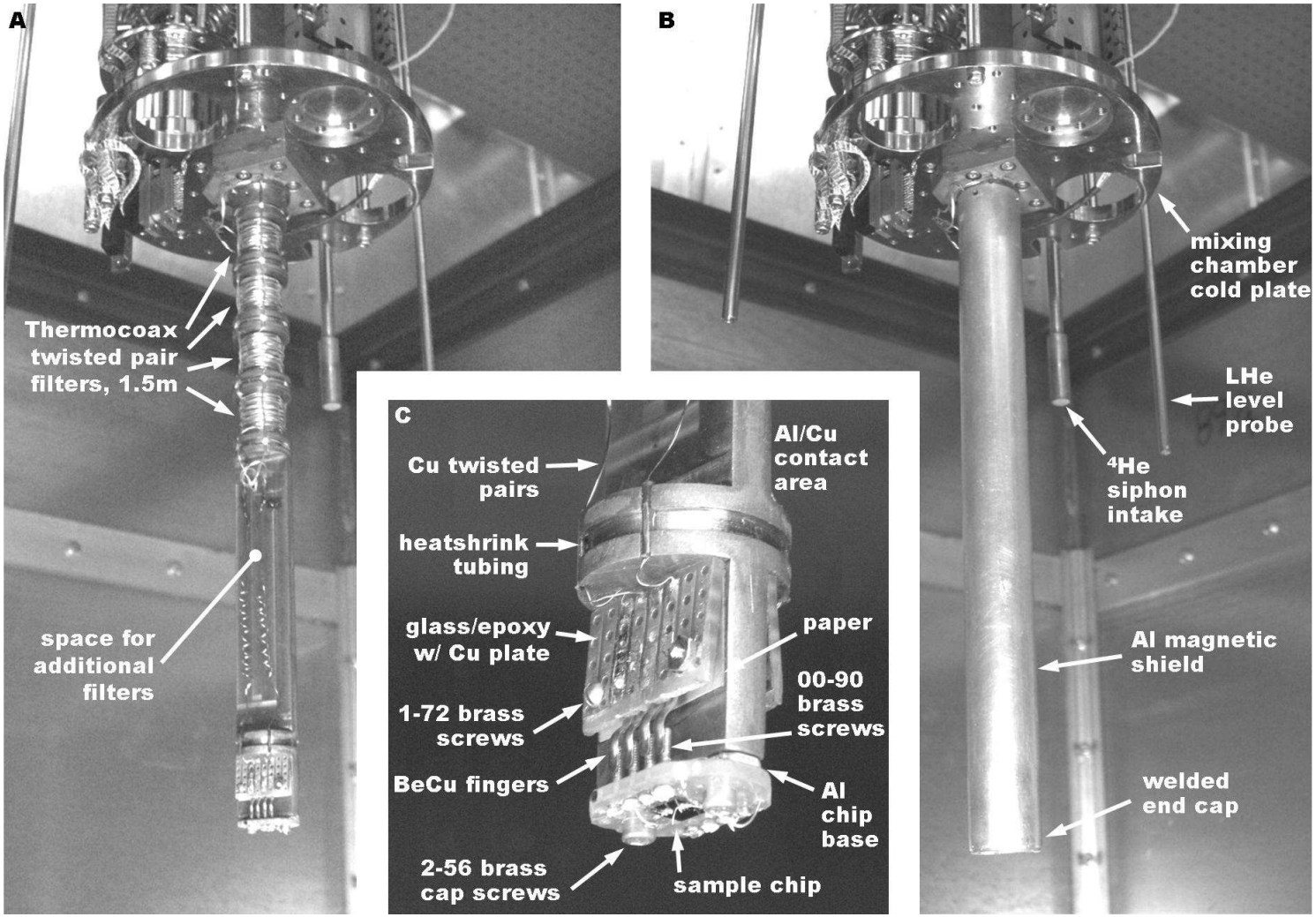

Figure 5.11: Sample stage for SQUID experiment, mounted on fridge. A. Cu cold finger with shield removed. B. Sample stage with Al shield in place. C. Detail of sample mounting at end of cold finger. The chip is mounted directly on a header made from a piece of glass-epoxy board with an attached Al block, which are held onto the cold finger by 2-56 brass cap screws. Wirebonding pins are made from 00-90 brass screws, and contacted by BeCu fingers soldered to a pair of glass-epoxy boards.

I designed for the highest reasonably achievable attenuation, as limited by the reach of available tooling; I used a 1 in. OD, 0.875 in. ID, 10 in. length Al tube, giving an internal aspect ratio of about 11. As a type II superconductor, Al below its critical temperature (∼1.1 K) will freeze in rather than exclude the ambient dc field, but will not allow it to change, which satisfies the requirements for the SQUID experiment. I had an Al end cap welded into one end of the tube; although the welded area would contain many defect sites, any flux trapped in the weld Al should be pinned at mK temperature.

The sample stage was designed to hang from the mixing chamber cold plate in the position to be later occupied by the STM mount. A Cu cold finger runs through from the open end to the closed end (Fig. 5.11 A). It is tightly clamped at the top end by a block which bolts into the cold plate. The cold finger was machined from a 1 in. diameter OFHC Cu rod, most of which was first turned to 0.875 in. diameter.

Due to the low thermal conductivity of Al in the superconducting state, and the high latent heat of the superconducting transition, I was warned that the long tube should not be cooled from just one end. Therefore the cold finger makes contact with the shield along its length. To achieve this, the shield was made from an Al tube with nominal ID 0.880 in., and I used a reaming tool to cut its interior surface to a smooth and uniform 0.875 in., so that it made a loose contact fit over the cold finger. On cooling, the differential contraction of Al relative to Cu is 0.091%, so that the Al tube contracts 0.0004 in. in radius relative to the Cu cold finger, enough to guarantee pressure on the contacting surfaces (Fig. 5.11 C).

Thermocoax filters were integrated into the sample stage, occupying the upper

half of the cold finger (Fig. 5.11 A). Four 0.7 in. long, 0.5 in. diameter spool sections were cut into the cold finger, and I wound 1.5 m of Thermocoax twisted pair around each spool section, for a total of eight lines. Between each spool section a double ring for contacting the shield was left at 0.875 in. diameter. I fed the Thermocoax past the contacting rings through grooves cut in the length of the cold finger, and used fine wire to tie it down.

Below the Thermocoax filters, I left a 4 in. section of the cold finger cut flat to create a volume for additional low-frequency filters, should they be needed, or for other experimental purposes. The cross-sectional area of the flat was equal to that of the 0.5 in. round spool sections. The wiring in this section converted from the Thermocoax to Cu twisted pairs which I coiled to make weak springs (Fig. 5.11 A). Although neither these coils nor the Thermocoax filter sections were counterwound, due to the Al shield any axial ac magnetic field should be extremely weak for the coiled Cu twisted pairs and effectively zero for the Thermocoax coils; in addition, any induced emf would be approximately the same for both wires of a pair. Therefore I did not consider counterwinding to be necessary in this case.

For the SQUID experiment, the samples were mounted on removable chip headers bolted onto the end of the cold finger, placing them in the best-shielded location and orientation, at the far end of the shield tube, with the SQUID area perpendicular to the axis. The chip headers conisted of machined Al blocks to which the chips were directly attached with vacuum grease, plus wirebonding posts mounted on a glass-epoxy skirts glued to the Al blocks (Fig. 5.11 C). I made the skirts from pieces of electronic prototyping board pre-drilled with a 0.1 in. square

array of holes. To make the wirebonding posts, I threaded eight 00-90 brass screws into the holes, soldered them to the metallization around the holes, and sanded the screw heads flat, as a group, to create bonding pads.

I made a half-dozen copies of this chip header design. The samples were made and mounted by Dan Sullivan, and as he preferred to solder the wires to the chip using In, after initial failures we found that pre-tinning the brass posts with In made this work.

Since the SQUID samples were delicate and had to be mounted and wire-bonded on the bench, then transferred to the sample stage, it was important that the chip headers be easily installable and that reliable electrical contact be easily made to the bonding posts. I found scraps of BeCu finger strip intended for making EMI gaskets, which I used to make fingers for contacting the posts. I used two more small pieces of prototyping board, which had metallization strips running in one direction, and soldered the BeCu fingers to the boards (underside of boards as seen in (Fig. 5.11 C).

The boards and attached BeCu fingers were then clamped over the brass posts with two bolts which could be loosened to release the chip headers. I varnished a piece of heavy paper to the Cu cold finger beneath each board for insulation.

The design of the removable chip headers and the method of mounting them on the cold finger proved reliable and easy to use in repeated trials of the experiment. The magnetic shielding was also adequate, and we were ultimately successful in demonstrating the observability of single flux quantum critical current modulation in a highly asymmetric SQUID despite the unobservability of a critical current in

one of the two junctions [156].

5.4 Conclusions

I have described and partly assessed a set of design choices for the STM mount, cryostat wiring and filtering, and an auxiliary sample mount for a SQUID experiment. The latter was proven in a successful demonstration of the asymmetric SQUID principle [156] intended for Josephson phase STM.

The design of the STM mount has been realized. It provides the possibility of achieving the best shielding of the STM from ambient and thermal electromagnetic noise. Mechanical rigidity and thermal conductance were given due consideration in compromise the the length and mass of the (inverted) "legs". Operational testing is needed.

I would note that this STM mount was designed to place the STM in the center of the high-field magnet for conventional mK-STM studies, whereas for the proposed Josephson phase STM there will be no use for the magnet, and therefore no need for the long pendant STM mount. Vibration of the STM, whether excited by external sources such as ambient sound and building vibrations or internal sources such as the 1 K pot, may turn out to be a major problem, particularly for the two-tip STM, which is likely to be more vibration-sensitive than the simpler single-tip STM. If this is the case, serious consideration should be given to redesigning the STM mount either to shorten its "legs" or eliminate them entirely in favor of a more rigid connection between the STM body and the mixing chamber cold plate.

Temp range	Wire type	Dimensions O.D. [mm]	Res. [Ω/m]	Cap. [pF/m]	10GHz Atten. [dB/m]	How many
300K-10 K 10 K-MXC	CuNi coax	CuNi 0.08 PTFE 0.26 CuNi 0.40	wire 75 shield 5.2	96.2	61	12
300 K-10 K 10 K-1.4 K	Constantan loom 12 tw. pairs	Constan. 0.10 polyester 0.12	66	∼50 (diff. mode)	∼100 (diff. mode)	48 wires 2 looms
1.4 K-MXC	CuNi-clad NbTi loom 12 tw. pairs	NbTi 0.05 CuNi 0.08 polyester 0.10	52	∼50 (diff. mode)	∼100 (diff. mode)	48 wires 2 looms
MXC-STM	Cu coax	Cu 0.29 PTFE 0.94 Cu 1.19	wire 0.26	96.1	3.7	48

Table 5.2: Wires provided for the dual mK-STM system. The CuNi coax lines are provided for STM signal wiring. The loom wires are provided for the piezos and thermometry. Both groups transition to the Cu coax at the mixing chamber (MXC). Attenuation for the loom wires is based on the quoted resistance and differential mode capacitance, but this high attenuation is not achieved in practice because of common mode transmission and rf coupling through the cavity.

My choices with regard to wiring are summarized in Table 5.2. After installation, a few of the wires have already been found to be broken, due to the sensitivity of fine wires and the difficulty of routing and installing them without damage. The CuNi coax has been particularly problematic and should these wires ultimately need to be replaced I would recommend using a stronger material such as stainless steel (despite the difficulty of soldering the latter). Enough spares were provided in the design, but evidently not an excessive number especially given that future requirements remain unknown.

A major unknown is how well the Cu coax will be able to sink heat generated in the STM and conducted away from it by the Cu wires in the STM body. The

problem is not the volume thermal conductance of the PTFE dielectric, which in the given coaxial geometry is adequate even at mK temperatures, but rather the boundary resistance. This would be greater than the volume resistance even if the interface were under high pressure, and obviously becomes extremely large if the pressure goes to zero, or no contact, when the PTFE contracts at low temperature. The latter effect is mitigated by the many bends in the Cu coax, as well as by the clamps which are designed to partially flatten sections of the coax ensuring maintenance of contact; however, the pressure that will remain on the interface between the Cu jacket and the PTFE is unknown.

It is possible that the scheme of using the Cu coax as a heat sink will prove to be inadequate, requiring a redesign to better ensure heat sinking close to the STM. In that case, however, it is also likely that the STM body needs some redesign since the wiring within the existing STM bodies provide only poor thermal linkage at several connection points.

A possible improvement on the wiring choices would be to provide a number of individually electrically shielded twisted pairs with good control of geometry and minimization of any enclosed area where the paired wires are separated, for possible use either as STM signal wires in a scheme like that of le Sueur *et al.* [144], or other experimental needs which may arise. This would necessitate also the development of a twisted-pair filter of some kind, but we have several options for this.

Realization of both Thermocoax and metal powder filters, in sufficiently compact form to accomodate the large number of lines into the shielded STM can, proved to be tedious and difficult, and there is considerable room for improvement

here, although the filters as realized will support initial experiments in mK-STM and our efforts to develop phase STM.

Based on considerations discussed in Sec. 3.4, I would now consider microfabricated distributed RC filters [106] or stripline filters using ferromagnetic aborbers [96, 97] as alternative filter technologies. The micro-RC filters add less capacitance, at the cost of somewhat higher resistance, for the same attenuation performance as Thermocoax, and provide the added benefit of good thermal anchoring. The stripline filters are compact and easy to make, and provide impedance matching with near zero capacitance. Another possibility for the signal wires, with built-in filtering, would be close-shielded twisted pair wiring [112, 113], but microphonic effects might be a problem, requiring careful attention to mechanical construction and installation.

Chapter 6

Conclusions and Further Work

6.1 Conclusions from the work done so far

To put an STM into a dilution refrigerator is not difficult; this was done by Hess, et al. as early as 1989 [158], but with the result that "The microscope was operated at 0.3±0.1 K," and the benefits of operation at lower temperatures were not obtained. Major problems in mK-STM include simultaneous vibration isolation and cooling of the STM tip, sample and piezos; low-noise preamplification and electrical filtering of the wires to prevent heating and smearing of spectra by ambient and thermal rf voltages; thermalization of the wires and sinking of both heat conducted down from warmer stages and heat generated by the STM head; elimination of noise generated by the 1 K pot; and the engineering of sample and tip exchange between RT and the mK environment.

Controlling all these problems simultaneously requires careful consideration of many details of mK science and technology which can be contrary to intuition developed from work at room temperature or even under milder cryogenic conditions. The heat capacities and thermal conductivities of various classes of materials, the contributions of radiation and gas conduction to thermal transport, and the importance of thermal contact resistance may all scale with different exponents of temperature, meaning that the balance of these phenomena is qualitatively differ-

ent at 4 K than it is at room temperature, and again qualitatively different at mK temperatures. Below 100 mK, radiation and gas conduction are negligible factors (Sec. 3.3.5), thermal contact resistance is often more important than bulk thermal resistance (Sec. 3.2.4), and residual contributions to heat capacity such as ortho-para conversion of hydrogen and the nuclear spin states of Cu need to be considered, as well as heat sources such as eddy currents and mechanical vibration (Sec. 3.3.6).

Success is also, inevitably, an iterative process building on knowldege gained from earlier attempts.

Although many commercial dilution refrigerators can reach base temperatures below 10 mK, experience has shown that when complex experimental apparatus are built in them, with many wires in and out and several levels of structure interposing interfaces and insulating layers between the critical element of the experiment (which one wants to keep cold) and the mixing chamber of the fridge, it is difficult to achieve effective temperatures below about 30 mK. For mK STMs the record is particularly bad, with early results reporting effective temperatures, as determined e.g. by the measurement of superconducting gap spectra, as high as 200–300 mK despite much lower temperatures measured at the mixing chamber or even at the STM sample holder. Progress has only slowly been made towards bringing spectroscopic effective temperatures in line with fridge temperatures.

In the present work, the installation and vibration isolation of the pumps and plumbing appears to have been done in a satisfactory manner as judged by the fact that low-frequency acceleration at the tabletop was increased by less than 10% as compared with the level observed with the pumps off and no plumbing connections

to the table (Sec. 4.11, Table 4.1). Marginal improvement might be possible by adding damping (e.g. cloth shrouds) to the T-bellows (Sec. 4.10), or by adding better isolation under the ^{3}He rotary pump (Sec. 4.8). The sandbox may have been superfluous, but would have been more effective if incorporated into the shielded room wall to better control vibrations of the wall (Sec. 4.9). Lining the shielded room with sound-absorbing material will most likely be important to reduce higher-frequency vibrations acoustically transmitted to the tabletop.

The electrical low-pass filtering described here could probably be improved but is good enough for a first attempt to record STM images and spectra at mK temperatures. Better filtering technologies have been reported in the last few years than were known when I began this work. In particular, the use of ferromagnetic/ferrimagnetic microwave absorbing materials is a considerable improvement over conventional metal powder filters and should make filter fabrication far less laborious. Microfabricated distributed RC filters are another compact, high-performing type which have the added benefit of providing good heat sinking.

The wiring, as installed, should provide adequate electrical performance, and should be adequately cooled with respect to heat conducted down from RT and from warmer to colder stages of the fridge. However, my use of Cu-PTFE-Cu coax as a heat sink for heat generated within the STM is dubious and may not provide sufficient cooling. If better cooling of the STM is required, it probably will be necessary to add specially designed heat sinks, such as metallized polyester film, close to the tip and sample holders, or perhaps in the space just above the STM body. In either case, some redesign of the STM body will probably be needed, either

to make space for heat sinking devices close to the heat sources or for better thermal links to carry heat away from the sources to heat sinks mounted outside the STM body.

6.2 Further work

In the immediate future, we intend to complete the installation of a dual-tip STM in the cryostat as wired, and of supporting electronics outside, cool down and begin testing the STM system.

Initial samples for characterization and debugging of the system may include graphite, Au, Si, and $NbSe_2$ or a conventional superconductor such as Nb or Al for assessment of effective temperature and spectroscopic resolution. We are also interested in the use of superconducting tips e.g. of Nb or Al, and we will want to test these against both normal and superconducting samples. However, there are many issues to be worked out regarding tip and sample preparation before this can be done effectively. The sample preparation vacuum chambers will need to be installed and the sample exchange mechanism will need to be operating reliably so that samples can be cleaned or cleaved under UHV, and techniques for Nb or Al tip preparation will need to be developed.

Ultimately we intend to use this system to study phenomena of interest in the development of quantum computing technologies, including Si-based and superconducting qubit technologies. This may include the study of isolated donor states in Si, as well as spectroscopic study of quasiparticle states in high-temperature su-

perconductors, exotic superconductors such as ruthenates and uranium compounds, and the pnictides. Even where the characteristic energy scales or critical temperatures for such phenomena are well above the mK range, ultralow temperatures, as well as the use of superconducting tips, provide the best spectroscopic resolution and aid in the discrimination of states with small energy differences. Another area of interest for superconducting quantum computing is the study of defects in Al_2O_3 and other materials used as insulators in superconducting qubits. It may be useful to study the dynamic behavior of such states at the temperatures at which qubit experiments are normally performed.

A further goal is the development of some technique for observing the guage-invariant phase of the superconducting order parameter in superconducting samples. This should be possible by using a two-tip STM with superconducting tips joined by a superconducting bridge to form a SQUID. However, this is complicated by the fact that it is normally only possible to observe a small fluctuation-dominated tunneling current in Josephson STM [157]. One possible solution to this problem is the asymmetric SQUID scheme proposed by Wellstood *et al* [142] and validated in our asymmetric SQUID experiment [156]. However, I would speculate that the fluctuation-dominated Josephson tunneling will also exhibit modulation in the enclosed gauge-invariant phase if two tips operating in this regime are configured together as a SQUID.

Bibliography

[1] Robert D. McCarty. Thermodynamic Properties of Helium 4 from 2 to 1500 K at Pressures to 10^8 Pa. *Journal of Physical and Chemical Reference Data*, 2, 923–1041, 1973.

[2] N. H. Balshaw. *Practical Cryogenics*. Oxford Instruments Superconductivity Limited, 1996.

[3] Y. H. Huang and G. B. Chen. A practical vapor pressure equation for helium-3 from 0.01 K to the critical point. *Cryogenics*, 46, 833–839, 2006.

[4] Jack W. Ekin. *Experimental Techniques for Low-Temperature Measurements: Cryostat Design, Material Properties, and Superconductor Critical-Current Testing*. Oxford University Press, 2006.

[5] Guglielmo Ventura and Lara Risegari. *The Art of Cryogenics: Low-Temperature Experimental Techniques*. Elsevier, 2008.

[6] Michael Shapiro, Vladislav Dudko, Victor Royzen, Yuri Krichevets, Samuel Lekhtmakher, Victor Grozubinsky, Moshe Shapira, and Moti Brill. Characterization of Powder Beds by Thermal Conductivity: Effect of Gas Pressure on the Thermal Resistance of Particle Contact Points. *Particle and Particle Systems Characterization*, 21, 268–275, 2004.

[7] Y. S. Touloukian, R. W. Powell, C. Y. Ho, and P. G. Klemens. *Thermal Conductivity: Nonmetallic Solids*, volume 2 of *Thermophysical Properties of Matter*. IFI/Plenum, 1970.

[8] Rami Ceramic Industries, Nazareth, Palestine; http://www.circonio.net/rimax.pdf (21 June 2010).

[9] James F. Shackelford and William Alexander, editors. *CRC Materials Science and Engineering Handbook, Third Edition*. Chemical Rubber Company.

[10] Australia Azom.com, New South Wales. Zirconia ZrO2 Grades, Mechanical, Thermal and Electrical Properties. http://www.azom.com/details.asp?ArticleID=3272 (21 June 2010).

[11] CALCE. Hardness of Materials.

[12] H. Carreon, A. Ruiz, J. Zarate, and G. Barrera. Ultrasonic Velocity Measurements in Alumina-Zirconia Ceramic Composite System.

[13] Structure Probe Inc. SPI Supplies Brand MgO Magnesium Oxide Single Crystal Substrates, Blocks, and Optical Components. http://www.2spi.com/catalog/submat/magnesium-oxide.shtml (August 2010).

[14] E. W. Müller. Elektronenmikroskopishe Beobachtungen von Feldkathoden. *Zeitschrift für Physik*, 106, 541–550, 1937.

[15] E. W. Müller. Weitere Beobachtungen mit dem Feldelektronenmikroskop. *Zeitschrift für Physik*, 108, 668–680, 1938.

[16] Erwin W. Müller. Study of Atomic Structure of Metal Surfaces in the Field Ion Microscope. *Journal of Applied Physics*, 28(1), 1–6, January 1957.

[17] R.F. Hochman, E.W. Müller, and B. Ralph, editors. *Applications of field-ion microscopy in physical metallurgy and corrosion.* Georgia Institute of Technology, 1969.

[18] Erwin W. Müller. Die Sichtbarmachung einzler Atome und Moleküle im Feldelektronenmikroskop. *Zeitschrift für Naturforschung*, 5a, 473–479, 1950.

[19] Michael K. Miller, Philippe J. Pareige, and Kaye F. Russell. Seeing and Catching Atoms: ORNL's Atom Probe Field Ion Microscope. *Oak Ridge National Laboratory Review*, 28, 1995. http://www.ornl.gov/info/ornlreview/rev28-4/text/atoms.htm (July 2010).

[20] A. V. Crewe, J. Wall, and J. Langmore. Visibility of Single Atoms. *Science*, 168(3937), 1338–1340, June 1970.

[21] R. M. Henkelman and F. P. Ottensmeyer. Visualization of Single Heavy Atoms by Dark Field Electron Microscopy. *Proc Nat. Acad. Sci. USA*, 68(12), 3000–3004, December 1971.

[22] L. Reimer and H. Kohl. *Transmission Electron Microscopy: Physics of Image Formation, 5th Edition.* Springer, 2008.

[23] Taylor Hobson Ltd, Leicester, UK. History. http://www.taylor-hobson.com/history.html (August 2010).

[24] G. Binnig, H. Rohrer, Ch. Gerber, and E. Weibel. Surface Studies by Scanning Tunneling Microscopy. *Physical Review Letters*, 49, 57–61, 1982.

[25] D. M. Eigler and E. K. Schweizer. Positioning single atoms with a scanning tunneling microscope. *Nature*, 344, 524–526, 1990.

[26] C. Julian Chen. *Introduction to Scanning Tunneling Microscopy.* Oxford University Press, 1993.

[27] Russell Young, John Ward, and Fredric Scire. The Topografiner: An Instrument for Measuring Surface Microtopography. *Review of Scientific Instruments*, 43(7), 999–1011, July 1972.

[28] G. Binnig, H. Rohrer, Ch. Gerber, and E. Weibel. Tunneling through a controllable vacuum gap. *Applied Physics Letters*, 40, 178–180, 1982.

[29] G. Binnig and H. Rohrer. Scanning Tunneling Microscopy. *Surface Science*, 126, 236–244, 1983.

[30] G. Binnig, H. Rohrer, Ch. Gerber, and E. Weibel. 7 x 7 Reconstruction on Si(111) Resolved in Real Space. *Physical Review Letters*, 50, 120–123, 1983.

[31] J. Frohn, J. F. Wolf, K. Besocke, and M. Teske. Coarse tip distance adjustment and positioner for a scanning tunneling microscope. *Review of Scientific Instruments*, 60, 1200–1201, 1989.

[32] G. Binnig and D. P. E. Smith. Single-tube three-dimensional scanner for scanning tunneling microscopy. *Review of Scientific Instruments*, 57, 1688–1689, 1986.

[33] C. Julian Chen. Electromechanical deflections of piezoelectric tubes with quartered electrodes. *Applied Physics Letters*, 60, 132–134, 1992.

[34] M. D. Kirk, T. R. Albrecht, and C. F. Quate. Low-temperature atomic force microscopy. *Review of Scientific Instruments*, 59, 833–835, 1988.

[35] Douglas P. E. Smith and Gerd Binnig. Ultrasmall scanning tunneling microscope for use in a liquid-helium storage Dewar. *Review of Scientific Instruments*, 57, 2630–2631, 1986.

[36] A. Guha, S. Kim, and A. L. de Lozanne. Novel frictionless approach mechanism for a scanning tunneling microscope. *Review of Scientific Instruments*, 74, 4384–4388, 2003.

[37] K. Besocke. An easily operable scanning tunneling microscope. *Surface Science*, 181, 145–153, 1987.

[38] R. R. Schulz and C. Rossel. Beetle-like scanning tunneling microscope for ultrahigh vacuum and low-temperature applications. *Review of Scientific Instruments*, 65, 1918–1922, 1994.

[39] Christine Meyer, Omar Squali, Heribert Lorenz, and Khaled Karrai. Slip-stick step-scanner for scanning probe microscopy. *Review of Scientific Instruments*, 76, 063706 (5pp.), 2005.

[40] C. Dubois, P. E. Bisson, A. A. Manuel, and Ø. Fischer. Compact design of a low temperature XY stage scanning tunneling microscope. *Review of Scientific Instruments*, 77, 043712–043717, 2006.

[41] Weida Wu, Ayan Guha, Suenne Kim, and Alex de Lozanne. A Compact Dual-Tip STM Design. *IEEE Transactions on Nanotechnology*, 5, 77–79, 2006.

[42] Anjan K. Gupta, Rajiv Shankar Sinha, and Reetesh Kumar Singh. Compact two-dimensional coarse-positioner for scanning probe microscopes. *Review of Scientific Instruments*, 79, 063701 (3pp.), 2008.

[43] S. H. Pan, 1993. World Intellectual Property Organization Patent WO 93/19494.

[44] S. H. Pan, E. W. Hudson, and J. C. Davis. ^{3}He refrigerator based very low temperature scanning tunneling microscope. *Review of Scientific Instruments*, 70, 1459–1463, 1999.

[45] Earle H. Kennard. *Kinetic Theory of Gases*. McGraw-Hill, 1938.

[46] Charles Kittel. *Introduction to Solid State Physics*. Wiley, 6th edition, 1986.

[47] Y. S. Touloukian, R. W. Powell, C. Y. Ho, and P. G. Klemens. *Thermal Conductivity: Metallic Elements and Alloys*, volume 1 of *Thermophysical Properties of Matter*. IFI/Plenum, 1970.

[48] J. M. Ziman. *Principles of the Theory of Solids, 2nd Ed.* Cambridge University Press, 1972.

[49] Frank Pobell. *Matter and Methods at Low Temperatures, 2nd Ed.* Springer, 1996.

[50] P. G. Klemens and G. Neuer. *Landolt-Börnstein New Series, Group III, Vol. 15, Metals: Electronic Transport Phenomena, Subvolume c:Thermal Conductivity of Pure Metals and Alloys*, chapter Thermal conductivity of alloys, pages 126–127. Springer-Verlag, 1991.

[51] K. Gloos, C. Mitschka, F. Pobell, and P. Smeibidl. Thermal conductivity of normal and superconducting metals. *Cryogenics*, 30, 14–18, 1990.

[52] L. Risegari, M. Barucci, E. Olivieri, E. Pasca, and G. Ventura. Measurement of the thermal conductivity of copper samples between 30 and 150 mK. *Cryogenics*, 44, 875–878, 2004.

[53] A. C. Anderson, W. Reese, and J.C. Wheatley. Thermal Conductivity of Some Amorphous Dielectric Solids Below 1^{o}K. *Review of Scientific Instruments*, 34, 1386–1390, 1963.

[54] Dennis S. Greywall. Thermal conductivity of normal liquid ^{3}He. *Physical Review B*, 29, 4933–4945, 1984.

[55] J. R. Olson. Thermal conductivity of some common cryostat materials between 0.05 and 2 K. *Cryogenics*, 33, 729–731, 1993.

[56] A. Kushino, M. Ohkubo, and K. Fujioka. Thermal conduction measurement of miniature coaxial cables between 0.3 and 4.5 K for the wiring of superconducting detectors. *Cryogenics*, 45, 637–640, 2005.

[57] A. C. Anderson. *Amorphous Solids: Low-Temperature Properties*, chapter Thermal Conductivity, pages 65–80. Springer-Verlag, 1981.

[58] W. Reese and J. E. Tucker. Thermal Conductivity and Specific Heat of Some Polymers between 4.5^o and 1^oK. *Journal of Chemical Physics*, 43, 105–114, 1965.

[59] T. Scott and M. Giles. Dislocation Scattering in Teflon at Low Temperatures. *Physical Review Letters*, 29, 642–643, 1972.

[60] C. L. Tsai, H. Weinstock, and Jr. W. C. Overton. Low temperature thermal conductivity of stycast 2850FT. *Cryogenics*, 18, 562–563, 1978.

[61] F. Rondeaux, Ph. Bredy, and J. M. Rey. Thermal Conductivity Measurements of Epoxy Systems at Low Temperature, 2001. http://irfu.cea.fr/Phocea/file.php?class=std&&file=Dpc/Publications/Archives/stcm-01-09.pdf (14 July 2010).

[62] J. H. McTaggart and G. A. Slack. Thermal conductivity of General Electric No. 7031 varnish. *Cryogenics*, 9, 384–385, 1969.

[63] A. C. Anderson and R. E. Peterson. Selection of a thermal bonding agent for temperatures below 1 K. *Cryogenics*, 10, 430–433, 1970.

[64] R. B. Stephens. Low-Temperature Specific Heat and Thermal Conductivity of Noncrystalline Dielectric Solids. *Physical Review B*, 8, 2896–2905, 1973.

[65] W. H. Keesom and A. P. Keesom. On the Heat Conductivity of Liquid Helium. *Physica*, 3, 359–360, 1936.

[66] O. V. Lounasmaa. *Experimental Principles and Methods Below 1 K*. Academic Press, 1974.

[67] R. M. Mazo. *Theoretical studies on low temperature phenomena*. PhD thesis, Yale University, 1955.

[68] W. A. Little. The Transport of Heat Between Dissimilar Solids at Low Temperatures. *Canadian Journal of Physics*, 37, 334–349, 1959.

[69] R. E. Peterson and A. C. Anderson. The Kapitza Thermal Boundary Resistance. *Journal of Low Temperature Physics*, 11, 639–665, 1973.

[70] E. T. Swartz and R. O. Pohl. Thermal Boundary Resistance. *Reviews of Modern Physics*, 61, 605–668, 1989.

[71] Roshdi Rashed. A Pioneer in Anaclastics: Ibn Sahl on Burning Mirrors and Lenses. *Isis*, 81, 464–491, 1990.

[72] Lawrence E. Kinsler and Austin R. Frey. *Fundamentals of Acoustics, 2nd Ed.* John Wiley & Sons, 1962.

[73] P. V. E. McClintock, D. J. Meredith, and J. K. Wigmore. *Matter at Low Temperatures*. Wiley-Interscience, 1984.

[74] Gerald L. Pollack. Kapitza Resistance. *Reviews of Modern Physics*, 41, 48–81, 1969.

[75] David Cheeke and Henry Ettinger. Macroscopic Calculation of the Kapitza Resistance between Solids and Liquid ^{4}He. *Physical Review Letters*, 37, 1625–1628, 1976.

[76] N. S. Snyder. The Kapitza Conductance of the (100) Surface of Copper. *Jounal of Low Temperature Physics*, 22, 257–284, 1976.

[77] R. Berman and C. F. Mate. Thermal Contact at Low Temperatures. *Nature*, 182, 1661–1663, 1958.

[78] Jack H. Colwell. The Performance of a Mechanical Heat Switch at Low Temperatures. *Review of Scientific Instruments*, 40, 1182–1186, 1969.

[79] I. Didschuns, A. L. Woodcraft, D. Bintley, and P. C. Hargrave. Thermal conductance measurements of bolted copper to copper joints at sub-Kelvin temperatures. *Cryogenics*, 44, 293–299, 2004.

[80] E. Gmelin, M. Asen-Palmer, M. Reuther, and R. Villar. Thermal boundary resistance of mechanical contacts between solids at sub-ambient temperatures. *Journal of Physics D: Applied Physics*, 32, R19–R43, 1999.

[81] Angel Colin. Thermal contact resistance of different materials between 0.3 K and 4.5 K. *Cryogenics*, 48, 35, 2008.

[82] Louis J. Salerno, Peter Kittel, and Alan L. Spivak. Thermal Conductance of Pressed Metallic Contacts Augmented with Indium Foil or Apiezon-N$^{\text{TM}}$ Grease at Liquid Helium Temperatures. NASA Technical Memorandum 108779, National Aeronautics and Space Administration, July 1993.

[83] R. Berman. Some Experiments on Thermal Contact at Low Temperatures. *Journal of Applied Physics*, 27, 318–323, 1956.

[84] Y. Hariharan, M. P. Janawadkar, and T. S. Radhakrishnan. Electrical and thermal conductivity of soft solder at low temperatures. *Pramana*, 13, 117–125, 1979.

[85] Jr. William A. Steyert. Thermal Transport Across Superconducting Solder Joints Near 0.1^{o}K. *Review of Scientific Instruments*, 38, 964–966, 1967.

[86] Guy K. White. *Experimental Techniques in Low-Temperature Physics*. Oxford University Press, 3rd edition, 1979.

[87] Benjamin B. Dayton. *Foundations of Vacuum Science and Technology*, chapter Kinetic Theory of Gases, pages 1–79. Wiley-Interscience, 1998.

[88] R. B. Dingle. The anomalous skin effect and the reflectivity of metals. *Physica*, 19, 311–347, 1953.

[89] C. A. Bailey. *Advanced Cryogenics*, chapter Heat Transfer and Thermal Insulation, pages 133–153. Plenum Press, London, 1971.

[90] A. B. Zorin. The thermocoax cable as a microwave frequency filter for single electron circuits. *Review of Scientific Instruments*, 66, 4296–4300, 1995.

[91] John M. Martinis, Michel H. Devoret, and John Clarke. Experimental tests for the quantum behavior of a macroscopic degree of freedom: The phase difference across a Josephson junction. *Physical Review B*, 35, 4682–4696, 1987.

[92] Akio Fukushima, Akira Sato, Akio Iwasa, Yasuhiro Nakamura, Takeshi Komatsuzaki, and Yasuhiko Sakamoto. Attenuation of Microwave Filters for Single-Electron Tunneling Experiments. *IEEE Transactions on Instrumentation and Measurement*, 46, 289–293, 1997.

[93] K. Bladh, D. Gunnarsson, E. Hürfeld, S. Devi, C. Kristoffersson, B. Smålander, S. Pehrson, T. Claeson, and P. Delsing. Comparison of cryogenic filters for use in single electronics experiments. *Review of Scientific Instruments*, 74, 1323–1327, 2003.

[94] F. P. Milliken, J. R. Rozen, G. A. Keefe, and R. H. Koch. 50 Ω characteristic impedance low-pass metal powder filters. *Review of Scientific Instruments*, 78, 024701 (5 pp), 2007.

[95] A. Lukashenko and A. V. Ustinov. Improved powder filters for qubit measurements. *Review of Scientific Instruments*, 79, 014701 (4 pp.), 2008.

[96] D. F. Santavicca and D. E. Prober. Impedance-matched low-pass stripline filters. *Measurment Science and Technology*, 19, 087001 (5 pp), 2008.

[97] D. H. Slichter, O. Naaman, and I. Siddiqi. Millikelvin thermal and electrical performance of lossy transmission line filters. *Applied Physics Letters*, 94, 192508 (3 pp), 2009.

[98] R. G. Chambers. The Anomalous Skin Effect. *Proceedings of the Royal Society of London A*, 215, 481–497, 1952.

[99] Simon Ramo, John R. Whinnery, and Theodore Van Duzer. *Fields and Waves in Communication Electronics*. John Wiley & Sons, 2nd edition, 1984.

[100] John David Jackson. *Classical Electrodynamics, Third Edition*. Wiley, 1998.

[101] NDT Education Resource Center, http://www.ndt-ed.org (Nov. 2010).

[102] Minicircuits, Brooklyn NY, USA; Coaxial low-pass filters, http://www.minicircuits.com/products (Nov. 2010).

[103] Moe Khalil, Laboratory for Physical Sciences, unpublished data.

[104] Emerson & Cuming, Inc., Billerica, MA USA.

[105] Myung-Jun Park, Jaeho Choi, and Sung-Soo Kim. Wide Bandwidth Pyramidal Absorbers of Granular Ferrite and Carbonyl Iron Powders. *IEEE Transactions on Magnetics*, 36, 3272–3274, 2000.

[106] Hélène le Sueur and Philippe Joyez. Microfabricated electromagnetic filters for millikelvin experiments. *Review of Scientific Instruments*, 77, 115102 (5 pp), 2006.

[107] D. Vion, P. F. Orfila, P. Joyez, and M. H. Devoret. Miniature electrical filters for single electron devices. *Journal of Applied Physics*, 77, 2519–2524, 1995.

[108] H. Courtois, O. Buisson, J. Chaussy, and B. Pannetier. Miniature low-temperature high-frequency filters for single electronics. *Review of Scientific Instruments*, 66, 3465–3468, 1995.

[109] H. le Sueur. *Cryogenic AFM-STM for mesoscopic physics*, volume 33 of *Annales de Physique*. Société Français de Physique, 2008.

[110] David M. Pozar. *Microwave Engineering, 3rd Ed.* John Wiley & Sons, 2005.

[111] Thermocoax, Inc., Alpharetta, GA USA.

[112] Lafe Spietz, John Teufel, and R. J. Schoelkopf. A Twisted Pair Cryogenic Filter, 2006. http://arxiv.org/pdf/cond-mat/0601316 (29 June 2010).

[113] Hendrik Bluhm and Kathryn A. Moler. Dissipative cryogenic filters with zero dc resistance. *Review of Scientific Instruments*, 79, 014703 (6 pp), 2008.

[114] J. G. Hust. Thermal Anchoring of Wires in Cryogenic Apparatus. *Review of Scientific Instruments*, 41, 622–624, 1970.

[115] SC-040/50-CN-CN Coax Co., Ltd., Kanagawa Japan. URL: http://www.coax.co.jp/english/main.html (August 2010).

[116] C. Daraio, V. F. Nesterenko, E. B. Herbold, and S. Jin. Strongly nonlinear waves in a chain of Teflon beads. *Physical Review E*, 72, 016603 (9 pp), 2005.

[117] Micro-Coax, Inc., Pottstown, PA USA, http://www.micro-coax.com/ (August 2010).

[118] Lakeshore Cryotronics, Inc, Westerville, OH USA. Technical Wire Specifications. http://www.lakeshore.com/temp/acc/am_wirets.html (20 April 2010).

[119] J. W. Gardner and A. C. Anderson. Effect of neutron irradiation on the low-temperature specific heat and thermal conductivity of magnesium oxide. *Physical Review B*, 23, 1988–1991, 1981.

[120] Glen A. Slack. Thermal Conductivity of MgO, Al_2O_3, Mg Al_2O_4, and Fe_3O_4 Crystals from 3° to 300° K. *Physical Review*, 126, 427–441, 1962.

[121] Deane K. Smith and H. R. Leider. Low-Temperature Thermal Expansion of LiH, MgO and CaO. *Journal of Applied Crystallography*, 1, 246–249, 1968.

[122] D. S. Matsumoto, Jr. C. L. Reynolds, and A. C. Anderson. Thermal boundary resistance at metal-epoxy interfaces. *Physical Review B*, 16, 3303–3307, 1977.

[123] Oxford Instruments, Concord, MA.

[124] Kadel Engineering Corp., Danville IN.

[125] American Magnetics, Inc., Oak Ridge, TN.

[126] Michael Dreyer, Jonghee Lee, Hui Wang, and Barry Barker. A low temperature scanning tunneling microscopy system for measuring Si at 4.2 K. *Review of Scientific Instruments*, 81, 053703 (6 pp), 2010.

[127] TMC Model 71-473-SPL; Technical Manufacturing Corporation, Peabody MA.

[128] ETS-Lindgren, Glendale Heights, IL.

[129] Golo Power Winch, Model 12-15 RMO, Cordem Corporation, Minneapolis MN.

[130] The cable and fittings are available from McMaster-Carr, Robbinsville, NJ.

[131] GS-11D, 4.5 Hz, 4000 Ω with 18 kΩ shunt, OYO Geospace Corp, Houston TX USA.

[132] E. I. Rivin. *Passive Vibration Isolation*. ASME Press, 2003.

[133] http://www.vibrasystems.com/data/CRMP-series.pdf; retrieved 30 Dec. 2009.

[134] Spectrum Control, Fairview, PA, USA, D-subminiature pi-filter type 56-715-003; http://www.spectrumcontrol.com (Nov. 2010).

[135] Standard Bellows Co., Windsor Locks, CT USA.

[136] W. P. Kirk and M. Twerdochlib. Improved method for minimizing vibrational motion transmitted by pumping lines. *Review of Scientific Instruments*, 49, 765–769, 1978.

[137] Roman Movshovich. *Experimental Techniques in Condensed Matter Physics at Low Temperatures*, chapter Vibration Isolation, pages 129–144. Addison-Wesley, 1998.

[138] P. Gorla, C. Bucci, and S. Pirro. Complete elimination of 1K Pot vibrations in dilution refrigerators. *Nuclear Instruments and Methods in Physics Research A*, 520, 641–643, 2004.

[139] A. Raccanelli, L. A. Reichertz, and E. Kreysa. Eliminating the vibrational noise in continuously filled 1 K pots. *Cryogenics*, 41, 763–766, 2001.

[140] Joan A. Hoffmann. *Superfluid ^{4}He: On sinϕ Josephson Weak Links and Dissipation of Third Sound*. PhD thesis, University of California at Berkeley, 2005.

[141] J. C. Davis. Electronic Wavefunction Imaging and Spectroscopy in Metallic and Magnetic Nanostructures by Millikelvin Scanning Tunneling Microscopy, Oct 2004. http://www.dtic.mil/cgi-bin/GetTRDoc?AD=ADA426959 (July 2010).

[142] J. R. Anderson, C. J. Lobb, and F. C. Wellstood. Imaging the Gauge-Invariant Phase Difference of Superconductors at the Atomic Scale. proposal to National Science Foundation, 2005.

[143] H. P. Ott O. Züger and U. Dürig. Variable-temperature ultrahigh vacuum scanning tunneling microscope: Mechanical and electronic instrumentation. *Review of Scientific Instruments*, 63, 5634–5643, 1992.

[144] Hélène le Sueur and Philippe Joyez. Room-temperature tunnel current amplifier and experimental setup for high resolution electronic spectroscopy in millikelvin scanning tunneling microscope experiments. *Review of Scientific Instruments*, 77, 123701 (5 pp.), 2006.

[145] GVL Cryoengineering, Aachen, Germany; www.GVL-Cryoengineering.de.

[146] Michael Dreyer. personal communication.

[147] Cambridge Magnetic Refrigeration, Cambridge, UK; www.cmr-direct.com.

[148] Supercon, Inc, Shrewsbury, MA USA; http://www.supercon-wire.com (August 2010).

[149] Tomohiro Matsui, Hiroshi Kambara, and Hiroshi Fukuyama. Development of a new ULT Scanning Tunneling Microscope at University of Tokyo. *Jounal of Low Temperature Physics*, 121, 803–808, 2000.

[150] T. Matsui, H. Kambara, I. Ueda, T. Shishido, Y. Miyatake, and Hiroshi Fukuyama. Construction of an ultra low temperature STM with a bottom loading mechanism. *Physica B*, 329-333, 1653–1655, 2003.

[151] H. Kambara, T. Matsui, Y. Niimi, and Hiroshi Fukuyama. Construction of a versatile ultralow temparature scanning tunneling microscope. *Review of Scientific Instruments*, 78, 073703, 2007.

[152] Kennametal, Inc., Fallon, NV USA.

[153] Superior No. 75, Superior Flux & Mfg. Co, Cleveland OH, USA.

[154] Roy Beardmore, Properties of Solids, http://www.roymech.co.uk (May 2010).

[155] R. P. Reed. *Materials at Low Temperatures*, chapter 9, Martensitic Phase Transitions, pages 295–341. American Society for Metals, 1983.

[156] D. F. Sullivan, S. K. Dutta, M. Dreyer, M. A. Gubrud, A. Roychowdury, J. R. Anderson, C. J. Lobb, and F. C. Wellstood. Measuring the Gauge-Invariant Phase Difference of a Sub-Micron Josephson Junction in an Asymmetric DC SQUID. *to be published*, 2010.

[157] O. Naaman, W. Teizer, and R. C. Dynes. Fluctuation Dominated Josephson Tunneling with a Scanning Tunneling Microscope. *Physical Review Letters*, 87, 097004 (4 pp), 2001.

[158] H. F. Hess, R. B. Robinson, and J. V. Waszczak. Vortex-core Structure Observed with a Scanning Tunneling Microscope. *Physical Review Letters*, 64, 2711–2714, 1990.